Variations latérales de sismicité le long du méga-chevauchement himalayen au Népal

Roser Hoste Colomer

▶ **To cite this version:**

Roser Hoste Colomer. Variations latérales de sismicité le long du méga-chevauchement himalayen au Népal. Sciences de la Terre. Université Paris sciences et lettres, 2017. Français. NNT : 2017PSLEE031 . tel-01797590

HAL Id: tel-01797590
https://theses.hal.science/tel-01797590

Submitted on 22 May 2018

HAL is a multi-disciplinary open access archive for the deposit and dissemination of scientific research documents, whether they are published or not. The documents may come from teaching and research institutions in France or abroad, or from public or private research centers.

L'archive ouverte pluridisciplinaire **HAL**, est destinée au dépôt et à la diffusion de documents scientifiques de niveau recherche, publiés ou non, émanant des établissements d'enseignement et de recherche français ou étrangers, des laboratoires publics ou privés.

THÈSE DE DOCTORAT

de l'Université de recherche Paris Sciences et Lettres
PSL Research University

Préparée à l'Ecole Normale Supérieure

Variations latérales de sismicité le long du méga-chevauchement himalayen au Népal

Lateral variations of seismicity along the Himalayan megathrust in Nepal

Ecole doctorale n°560

Sciences de la Terre et de l'Environnement et Physique de l'Univers

Spécialité Sciences de la Terre et de l'Environnement

Soutenue par
Roser **HOSTE COLOMER**
Le 14 septembre 2017

Dirigée par **Laurent BOLLINGER**
et Hélène LYON-CAEN

COMPOSITION DU JURY :

M. HETÉNYI György – Président du Jury
Université de Lausanne

Mme. LASSERRE Cécile - Rapporteur
Institut des Sciences de la Terre de Grenoble

M. DEVERCHÈRE Jacques - Rapporteur
Université de Bretagne Occidentale

M. GRANDIN Raphaël - Examinateur
Institut de Physique du Globe de Paris

M. BOLLINGER Laurent - Directeur de thèse
Commissariat à l'énergie atomique et aux énergies alternatives

Mme. LYON-CAEN Hélène – Directrice de thèse
École Normale Supérieure de Paris

Remerciements

Ce projet a été financé par l'Agence Nationale de la Recherche (ANR-13-BS06-0006-01) et le Commissariat à l'Energie Atomique et aux Energies Alternatives.

Je remercie les membres du jury d'avoir accepté d'évaluer ma thèse. Jacques Deverchère et Cécile Lasserre d'avoir lu avec intérêt et proposé des améliorations au manuscrit. György Hetényi pour ses remarques et les échanges antérieurs sur l'expérimentation temporaire. Raphaël Grandin, membre aussi de mon comité de thèse, d'avoir suivi ma thèse du début jusqu'à la fin avec un regard extérieur. J'ajouterais Yves Cansi, le deuxième membre du comité de thèse qui a veillé aussi au bon déroulement de celle-ci.

Je remercie mes directeurs, Hélène Lyon-Caen et Laurent Bollinger, de m'avoir donné l'opportunité d'effectuer et d'amener à bien cette thèse. Je tiens aussi à faire valoir leur engagement et investissement dans ce projet. Aussi je les remercie d'avoir partagé leurs connaissances avec moi et leurs savoirs faires sur le terrain. A Hélène pour sa sincérité et sa capacité à avoir du recul. Et Laurent dont la passion pour l'Himalaya et particulièrement le Népal est contagieuse, je le remercie pour les heures passées à discuter autour du sujet, pour sa patience devant mes moments de blocage et sa capacité à rebondir au cours des situations difficiles. Je le remercie également pour la découverte de Kathmandu.

Je remercie toutes les personnes du CEA et DMG qui, à différents niveaux, ont fait une réalité et un succès le déploiement du premier réseau sismologique temporaire aux régions *Mid et Far Western* du Népal. J'ai une gratitude particulière aux personnes du NSC et RSC qui m'ont accueilli aux laboratoires :

- Lok Bijaya Adhikari et Sudhir Rajaure pour les échanges pré-missions.
- Ramesh Pandey, Ratnamani Gupta, Mukunda Bhattarai, Thakur Prasad Kandel, Bharat Prasad Koirala, Kapil Maharjan pour leur participation et échanges sur le terrain.
- Dili Ram Tiwari et Umesh Gautam d'avoir partagé leurs connaissances et conseils.

Je remercie Ram qui, avec son 4x4 et son attitude positive, nous a amené aux endroits les plus lointains possibles tout en prenant soin de tous.

Je remercie les trois coopérants français (Tristan Didier, Eric Sauvage et Corentin Quedec) pour les gestions avant-pendant-post missions du réseau temporaire. Plus personnellement, je les remercie de m'avoir fait découvrir la vie de Kathmandu et des expat's.

Je remercie Eric Jacques et Rémy Matrau pour leur participation à la revisite des stations sismologiques.

Je remercie Jean Letort d'avoir participé à deux missions de terrain, de sa bonne compagnie lors du séisme de Gorkha et des multiples échanges sur les séismes népalais.

Je remercie Christian Baillard d'avoir participé à une mission de terrain et d'avoir passé du temps sur la définition des paramètres de Seiscomp3. Je tiens aussi à remercier Angélique Benoît pour les pointés effectués lors de son stage de M2.

Je tiens à remercier mes laboratoires d'accueil : Laboratoire de Géologie à l'ENS et le LEGA au CEA. Je souhaite étendre ce remercîment aux deux autres laboratoires du BARD avec lesquels j'ai bien interagi : le LSGO et le CSEM.

Tout d'abord, Hélène Hébert qui a fait office de tuteur pour tous les objets informatiques dont j'ai pu bénéficier et pour les aides diverses et variés apportées côté administratif. De même, Sylvia Tondeur sans qui je ne serai pas parti en mission. Je remercie Pierre Duperray pour m'avoir aidé à trouver des solutions à mes mésaventures informatiques, Jean-Paul et Nicolas pour les petites astuces pour pointer les signaux sismologiques, Jelle et Julien de m'avoir aidé à effectuer des transformations complexes des documents, et Michel Dandine pour tous les échanges sur la base de données.

Je remercie Paul, Myrtille, Amandine, Denis, Christel, Hélène et Tim d'avoir apporté de la joie dans les bureaux (ENS et CEA).

Je remercie Aline, Anne, Audrey, Bruno, Charlie, Olivier, Philipe, Alexis, Elisabeth pour les déjeuners dans une bonne ambiance et pour les activités « afterwork » comme l'escalade ou le bowling. Je remercie toute la « troupe des précaires » pour les sorties de cohésion. A Angélique de son soutien inestimable au cours des derniers mois et de son nez pour détecter les fautes d'orthographe. A ma promotion de docteurs : Adrien et Antoine pour les pauses et les soirées de détente, Claire pour les petites balades et les longues heures au laboratoire, et Dorianne pour son soutien et son énergie positive.

Le chemin parcouru jusqu'ici repose sur de bonnes bases. Pour cela, je remercie profondément ma mère, mon père, ma sœur Cèlia et le reste de ma famille qui, sans besoin de tout comprendre, m'ont toujours soutenu et ont été critique à chaque étape. Un grand merci également à mes amis les Apel · les (Mar, Sara, Marta, Núria, Kike's, Pau, Jepa i Marta), au Comando Tulipan (Mireia, Ari i Gemma) et, comme le dit la chanson, « com no, la meva gent del cau » (bien sûr, à mes gens des scouts).

Finalement, j'ai pu me dédier pleinement à ce projet de thèse grâce à Aurélien qui m'a encouragé tout au long et m'a transmis la force de donner mon mieux tous les jours.

Résumé

La sismicité présente le long du méga-chevauchement himalayen, dans la trace du fort séisme de 1505, des variations spatiales qui restaient peu résolues. Nous y avons déployé un réseau sismologique temporaire de 15 stations pour la période 2014-2016, en complément du réseau national. Nous avons effectué une détection automatique Seiscomp3 puis un pointé manuel des séismes enregistrés par le réseau, suivi par une localisation absolue Hypo71 et une relocalisation relative d'essaims HypoDD. Le catalogue résultant compte 2154 évènements dans notre zone d'étude dont les profondeurs (8-16 km) sont bien résolues. Les variations temporelles de la sismicité suggèrent des migrations de fluides. La confrontation de la sismicité avec des coupes géologiques équilibrées montre que les séismes se localisent dans le compartiment supérieur à proximité du Grand Chevauchement Himalayen au voisinage de rampes ou contacts suspectés entre écailles de moyen pays. Les variations latérales de structures associées à cette sismicité sont susceptibles de contrôler pour partie les ruptures cosismiques de séismes intermédiaires, qui viennent rompre partiellement le chevauchement, comme l'ont démontré les études du séisme de Mw7.8 de Gorkha-Népal, 2015. La segmentation qui en résulte est une donnée importante dans les études d'aléa sismique.

Mots Clés
Sismicité, cycle sismique, Himalaya, chevauchement, relocalisation, réseau sismologique temporaire.

Abstract

The seismicity located along the Himalayan mega-thrust, within the trace of the great M8+ 1505AD earthquake, displays striking spatial variations which remained poorly resolved. In order to better constrain and understand these variations, we deployed a 15-stations temporary seismological network for 2 years (2014-2016) as a complement to the national network. We first processed the data with an automatic detection with Seiscomp3, then a manual picking of earthquakes recorded by the network, followed by a Hypo71 absolute localization and HypoDD relative relocation of clustered events. The resulting catalogue contains 2154 local events, shallow to midcrustal (8 – 16 km). The seismicity presented temporal variations suggesting fluid migrations. The confrontation between the seismicity and the geologic balanced cross-sections shows that most earthquakes happen within the hangingwall of the Main Himalayan Thrust fault nearby ramps or suspected contacts between Lesser Himalayan slivers. The lateral variations of some of the structures associated to this seismicity are likely to partially control the extent of the coseismic ruptures during intermediate earthquakes that break partly the locked fault zone, in a similar way as what was reported after the Mw7.8 2015 Gorkha-Nepal earthquake. Better characterizing the segmentation of such faults is an important input for seismic hazard studies.

Keywords

Seismicity, seismic cycle, Himalaya, thrust, relocation, temporary seismological network.

Sommaire

Remerciements ... 3

Résumé ... 5

Abstract ... 6

Sommaire ... 7

Introduction ... 11

CHAPITRE 1 : Contexte sismotectonique du Népal ... 19

1.1. Contexte géologique ... 19

1.1.1. Géométrie du Main Himalayan Thrust (MHT) ... 22

1.1.2. Couplage du Main Himalayan Thrust ... 28

1.2. Sismicité ... 30

1.2.1 Réseau sismologique du Népal ... 31

1.2.1.1. Traitement des données ... 31

1.2.2. Sismicité des catalogues NSC et RSC ... 32

1.3. Questions ... 36

CHAPITRE 2 : Centre Népal ... 37

2.1. Introduction ... 38

2.2. Le séisme de Gorkha ... 39

2.2.1. La sismicité post-Gorkha 2015 ... 43

2.2.1.1. Réseau sismologique national du Népal ... 43

2.2.1.2. Catalogue du séisme de Gorkha du 25 avril 2015 au 8 juin 2015 ... 44

2.2.1.3. Distribution spatio-temporel de la sismicité post-Gorkha ... 45

2.2.2. Structure *versus* rupture ... 48

2.3. La sismicité intersismique au nord de Katmandou : variations latérales de structure et épisode transitoire ... 51

CHAPITRE 3 : West Nepal: Temporary Seismic Network and data processing ... 65

3.1. Temporary Seismological Network ... 65

3.1.1. Network Geometry ... 66

3.1.2. Sites characteristics ... 68

3.1.3. Stations components and monument....70
3.1.4. Station performances....72
3.2. Data used in this study....74
3.3. Data Processing....74
3.3.1. Seiscomp3 automatic data processing....74
3.3.1.1. Detection and association of phases....74
3.3.1.2. Parameters....75
3.3.1.3. Preliminary results....76
3.3.1.4. Limits....77
3.3.2. Seiscomp3 manual post-processing....79
3.3.2.1. Manual picking....79
3.3.2.2. Hypo 71 plugin profiles....79
3.3.2.3. Preliminary results....80
3.3.2.4. Limits....84
3.3.2.5. Magnitude MLv....84
3.3.3. Hypo71 – Localization Program....88
3.3.3.1. Procedure....88
3.3.3.2. Preliminary results....89
3.3.4. HypoDD....92
3.3.4.1. Procedure....94
3.3.4.2. Preliminary Results....95
3.3.4.2.1. Zone S....95
3.3.4.2.1.1. Cluster KS....95
3.3.4.2.1.2 Cluster DK....96
3.3.4.2.2. Zone W....96
3.3.4.2.2.1. Cluster A....96
3.3.4.2.2.2. Cluster B....96
3.3.4.2.2.3. Cluster C....96
3.3.4.2.2.4. Cluster D....96
3.4. Comparison between RSC catalogue and our study....97

CHAPITRE 4 : West Nepal: Results and seismotectonics implication 101
4.1. Seismicity TSN catalogue analysis 101
4.1.1. The Bajhang seismic belt 106
4.1.1.1. Cluster A 110
4.1.1.2. Cluster B 114
4.1.1.3. Cluster C 118
4.1.1.4. Cluster D 122
4.1.2. The South Karnali seismic belt 125
4.1.2.1. Cluster KS 129
4.1.2.2. Cluster DK 132
4.1.3. Main characteristics of the seismic clusters 135
4.2. Temporal distribution of the clusters 138
4.3. Seismicity and the geological structures 141
4.3.1. Darchula 144
4.3.2. Bajhang 144
4.3.3. South Karnali 146
4.3.4. North Karnali 150
4.4. Interpretation 151
4.4.1. Full or partial locking and related stress build up along the MHT 151
4.4.2. Behavior of the MHT related to the topography, the thermal structure and fluids 154
4.5. Implications on the segmentation of the MHT 157
Conclusions et Perspectives 161
References 165
ANNEXES 177
Annexe A: 179
Annexe B: 187
Annexe C: 203

Introduction

Les plus forts séismes connus à la surface du globe (méga-séismes de M8.5+ e.g. Chili 1960 M9.5, Alaska 1964 M9.2 ; Sumatra-Andaman 2004 M9.1-9.3; Tohoku-Oki 2011 M9.0 mais aussi Assam 1950 M8.5) se sont tous produits au niveau des zones de convergences inter-plaques, le long des grandes subductions océaniques et continentales : ceinture de Feu du Pacifique, fosses de subduction autour de l'Océan Indien (voir Figure i.1), mais aussi dans les régions les plus affectées par la convergence Inde-Eurasie.

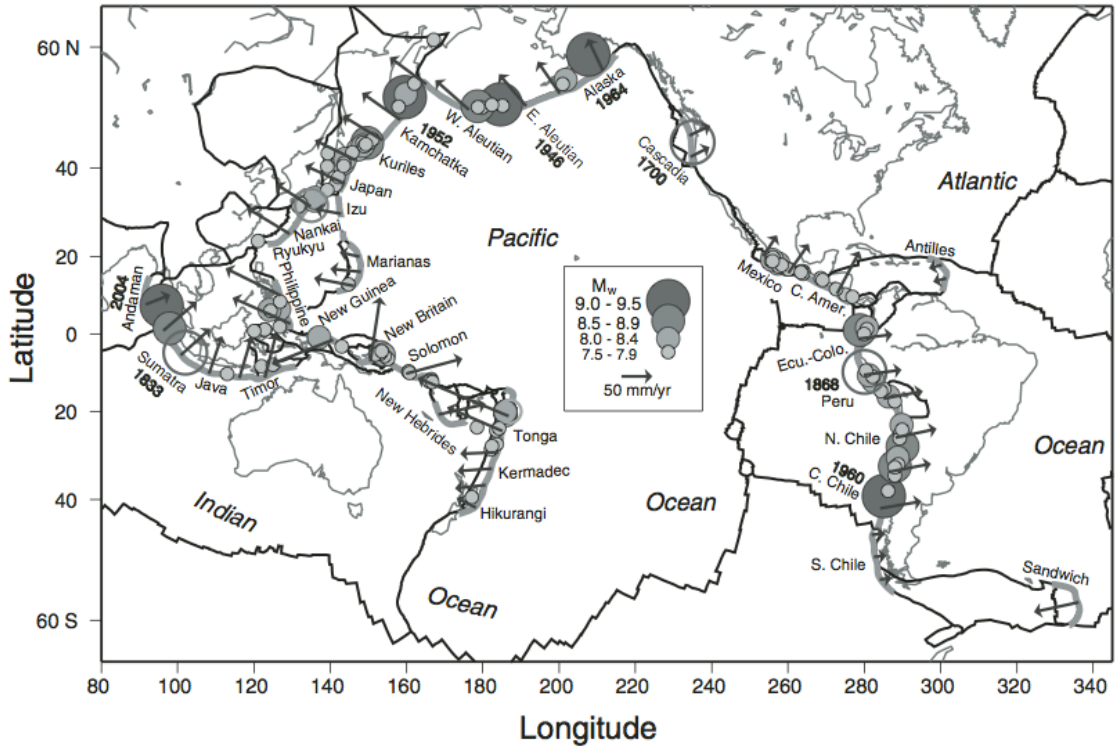

Figure i.1. Distribution des forts séismes instrumentaux et historiques autour du Pacifique (McCaffrey et al., 2008).

Ces méga-séismes ont rompu des plans de chevauchement de plusieurs centaines de kilomètres de long, et sont donc associés à la rupture de « méga-chevauchements ». Tous ces séismes se sont produits dans des zones de déformation rapide et donc de forte activité sismique. Pour cette raison, certaines de ces régions ont été affectées par des forts séismes plusieurs fois à l'échelle historique. Ces séismes n'ont pour autant pas toujours rompu des surfaces identiques. En effet, certaines régions ont vu le développement de séquences de forts séismes (M7-M8) qui sont venus rompre le mégachevauchement par morceau (Figure i.2.a). C'est le cas par exemple au large du Japon, le long du prisme de Nankai, dans la trace du méga-séisme de Hoei (1707) (Figure i.2.b) mais aussi dans la trace du séisme de Tohoku-Oki (M9.0) qui

correspondent à des zones rompues lors de séismes de magnitude inférieure dans les décennies/siècles qui ont suivis ou précédés les plus forts événements. On peut aussi citer les séismes de Nicobar 1881 M8 et Andaman 1941 M8 dans la trace du méga-séisme de Sumatra-Andaman 2004 ou des nombreux séismes chiliens dans la trace du grand séisme de 1960.

(a) (b)

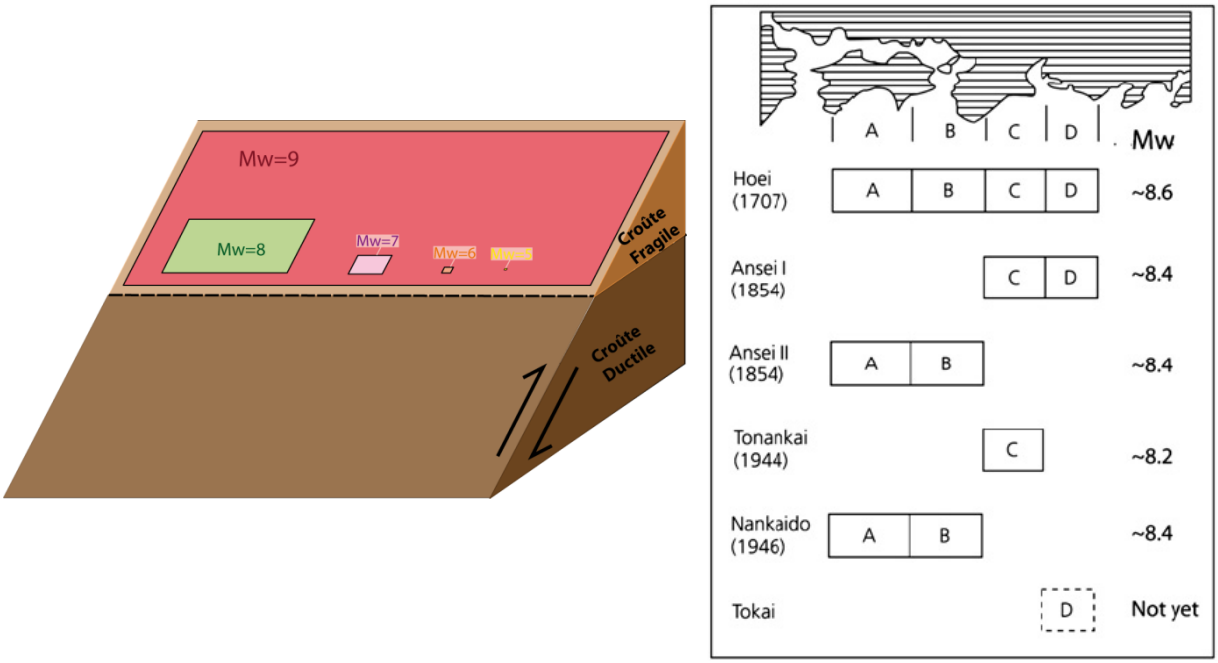

Figure i.2. (a) Dimension des ruptures de plusieurs classes de séismes (Mw 5 à 9) sur le long de la zone bloquée d'un méga-chevauchement utilisant les loi d'échelle empiriques qui associent les dimensions de la rupture avec le moment sismique (Wells and Coppersmith, 1994; Blaser et al., 2010). (b) Trace des ruptures des forts séismes historiques et instrumentaux le long du prisme de Nankai (Ando, 1975).

Les séquences de forts séismes ou le méga-séisme ne présentent pas les mêmes impacts, ni sur le niveau de l'aléa sismique considéré, ni sur le risque qui en découle, surtout si ce risque est estimé sur des échéances courtes devant le temps de retour des plus forts événements sismiques.

Or, l'exposition des populations à ces forts séismes en chevauchement est très importante. En effet, un grand nombre de ces régions présentent de fortes densités de population le long des côtes et dans les bassins aux pieds des montagnes. Le nombre de personne exposées aux forts séismes le long de ces structures est par ailleurs de plus en plus important (Bilham, 2004 ; Jackson, 2006). C'est particulièrement vrai dans les régions où les villages s'agrègent en ville puis en méga-villes (Bilham, 2009). C'est le cas à l'échelle du sous-continent indien, une région dans laquelle la population a triplé depuis le séisme d'Assam 1950 (e.g. Sapkota et al., 2016).

A l'échelle globale, plus de 1,5 millions de personnes ont péri au 20e siècle à cause d'un tremblement de terre. Depuis le début des années 2000, ce chiffre est d'environ 750.000 personnes (les morts par tsunami inclus) dont environ 64% sont dus à un séisme sur un méga-chevauchement (subduction océanique : Mw9.1 2004 Sumatra-Andaman (Indonésie) et Mw9.0 2011 Tohoku-Oki (Japon) ; subduction continentale : Mw7.6 2005 Muzzaffarabad (Pakistan), Mw7.9 2008 Wenchuan (China), et Mw7.8 2015 Gorkha (Népal)).

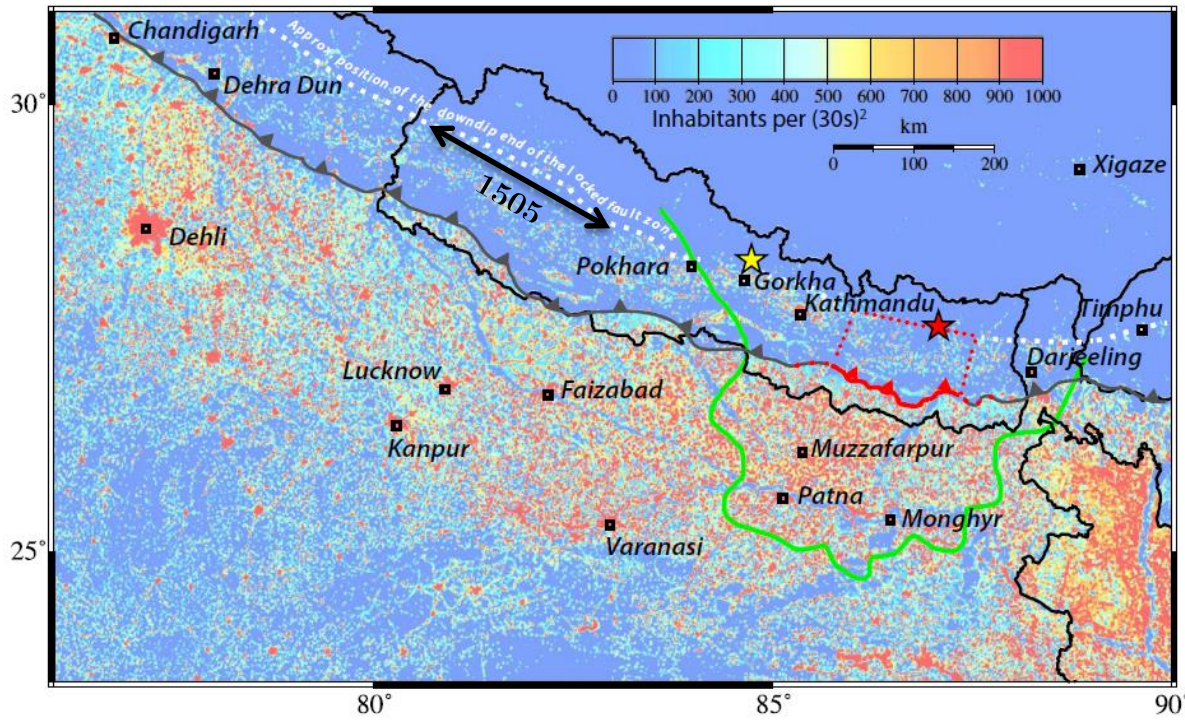

Figure i.3. Densité de population et exposition aux forts séismes. Etoile jaune, épicentre du séisme de Gorkha, Etoile rouge et rectangle rouge, épicentre et extension de la rupture du séisme de M8.3 de Bihar-Nepal 1934. En vert, isoséiste VII couvrant les régions très affectées par le séisme de 1934 (Sapkota et al., 2016). La flèche noire indique la longueur supposée du grand séisme de 1505 à l'ouest du Népal (Bollinger et al., 2016).

La proximité de la source sismogénique avec les populations fait accroître le risque (Figure i.3). C'est particulièrement vrai en domaine de subduction continentale où les populations vivent au droit des segments de failles à la rupture ou à proximité de la trace de surface des chevauchements (Figure i.3). Les séismes de M7+ dans ces régions y sont bien souvent beaucoup plus meurtriers qu'en domaine de subduction océanique. Pour exemple, le séisme de Wenchuan de Mw7.9 en 2008 qui a rompu jusqu'à la surface aux pieds de la chaîne de montagne de Longmenshan (Xu et al., 2009) est responsable de près de 80000 décès et disparition en plaine comme en montagne. Un autre exemple est le séisme de Muzzafarabad (Kashmir), Pakistan de Mw7.6 en 2005 responsable de plus de 80.000 décès. Ce séisme, initié sur le méga-chevauchement himalayen (*Main Himalayan Thrust* - MHT), a atteint la surface au niveau du *Main*

Boundary Thrust à l'intérieur de la chaîne de l'Himalaya (Kaneda et al., 2008). Plus récemment, le séisme de Gorkha de Mw7.8 au Népal, qui a fait 9000 victimes, a également eu lieu sur ce méga-chevauchement himalayen mais la rupture n'est pas arrivée en surface (Avouac et al., 2015; Grandin et al., 2015 ; Kobayashi et al., 2015).

Le *Main Himalayan Thrust*, responsable de ces deux forts séismes récents, est un exemple de méga-chevauchement qui rompt partiellement ou totalement - de l'extension profonde de la zone bloquée à la surface. En effet, tous les séismes dévastateurs au Népal ne font pas la taille du séisme de Gorkha. Le segment voisin à l'est a rompu jusqu'en surface en 1934 lors d'un très grand séisme (magnitude M8.3 ; plan de rupture de plus de 90 x 150 km2 de faille) (Figure i.3). Des séismes encore plus gros sont connus (le séisme d'Assam 1950 M8.6) ou ont été décrits dans les tranchées paléosismiques (Lavé et al., 2005 ; Yule et al. , 2006) et sont attendus dans la région sur la base du bilan de moment sismique (Stevens and Avouac, 2016). En revanche, du fait de la mauvaise connaissance des séismes anciens, cette segmentation reste largement méconnue. La segmentation est très probablement reliée pour partie à la présence de variations latérales des structures géologiques dans les compartiments supérieurs et inférieurs de la faille, des structures qui peuvent constituer des barrières à la propagation de la rupture. Des variations de couplage ou de structure thermique peuvent influencer les ruptures sismiques. La circulation de fluides est aussi un facteur qui pourrait influer sur la sismicité. La segmentation peut être étudiée à la suite des ruptures cosismiques, par l'imagerie de la source (grâce aux données sismologiques, géodésiques, et à l'imagerie spatiale de la déformation) et l'étude des répliques. Le séisme de Gorkha 2015 est le meilleur exemple de séisme himalayen bien étudié par ces techniques (e.g. Adhikari et al., 2015 ; Avouac et al., 2015 ; Grandin et al., 2015 ; Duputel et al., 2016 ; Elliott et al., 2016, Letort et al., 2016 and Baillard et al., 2017). Cependant ces techniques étant assez récentes, elles limitent l'application à des séismes contemporains. De plus, l'occurrence d'un séisme de M7+ reste rare sur une même zone ou sur des zones consécutives à l'échelle de temps humaine. Afin d'étudier des séismes plus anciens, on peut s'appuyer sur des chroniques régionales qui apportent des informations sur l'aire affectée par les plus fortes intensités et renseigne indirectement sur la position des ruptures. De plus, certains de ces séismes historiques dévastateurs ont atteint la surface et peuvent être étudiés au front de la chaîne par des études paléosismologiques. Ces études permettent de localiser les zones affectées par des ruptures de surface anciennes, d'estimer leur glissement associé et leur magnitude. Plusieurs études de ce type ont été conduites en Himalaya (Wesnousky et al., 1999 ; Lavé et al., 2005 ; Yule et al., 2006 ; Sapkota et al., 2013 ; Bollinger et al., 2014 ; Leroux-Mallouf et al., 2016). Les extensions des ruptures des plus anciens séismes restent toutefois toujours très débattues au Népal de par le faible nombre d'observations et l'incertitude sur les âges des ruptures (Mugnier et al., 2013 ; Bollinger et al., 2016 ; Wesnousky et al., 2017) (Figure i.3 et i.4).

Les variations latérales de structures responsables de la segmentation peuvent aussi être étudiées par imagerie géophysique associée à la cartographie géologique. Plusieurs études complémentaires de ce type ont été conduites le long de l'Himalaya (Nabelek et al., 2009 ; Schulte-Pelkum et al., 2005). Elles ne permettent pas systématiquement de résoudre les variations de structure profonde avec la résolution souhaitée. L'analyse des variations latérales de la sismicité intersismique pourrait s'avérer très complémentaire (voir Figure i.4 pour ce qui concerne la confrontation entre la sismicité et les ruptures passées).

Si à l'échelle du globe la sismicité a été un des premiers indices pour détecter les limites des plaques, c'est-à-dire des structures tectoniques actives, cette relation devrait aussi être présente à l'échelle d'un méga-chevauchement. Ainsi on peut se demander si:

- Ces variations latérales de sismicité sont-elles réelles? Ou résultent-elles pour certaines de biais de localisation et de variations de magnitude de complétude ?
- Est-ce que la sismicité est constante au cours du temps?
- Est-ce que la sismicité a une distribution spatiale particulière ?
- Est-ce que les variations spatiales de sismicité peuvent être reliées à des variations de géométrie du *Main Himalayan Thrust* ? Et/ou à de variations des structures au droit du mégachevauchement? A des variations de contraintes locales (orientation du champ de contrainte et/ou valeur de la variation de contrainte statique depuis le précédent séisme). Correspondent-elles à des variations de couplage ? Ou bien à des variations de structure thermique ?
- Si ces variations spatiales sont réelles, comment affectent-elles les ruptures cosismiques ?

L'objectif de cette thèse est d'apporter autant que possible des éléments de réponses à ces questions à l'issu d'un travail sur la sismicité régionale et ses relations probables aux structures tectoniques en profondeur. La zone ciblée est l'Himalaya et plus particulièrement sa partie centrale, le Népal. D'un côté, l'étude de la segmentation sur une subduction continentale présente des avantages par rapport à l'étude des subductions océaniques : accès à la zone d'étude et donc à la structure géologique, accès aux ruptures de surface ou encore la possibilité d'instrumenter au zénith du méga-chevauchement. D'un autre côté, le Népal est une des zones de l'Himalaya très largement documentée et étudiée par la communauté scientifique depuis des décennies et donc présentant une grande quantité d'observations géodésiques, sismologiques, géologiques entre autres. De plus, la sismicité intersismique qui est très abondante au Népal a été enregistrée depuis 1994 de façon homogène par deux sous-réseaux du réseau sismologique national du Népal: le réseau du *National Seismological Centre* (NSC) qui couvre le centre et l'est du pays et le *Regional Seismological Centre* (RSC) qui couvre l'ouest du territoire national (Figure i.4).

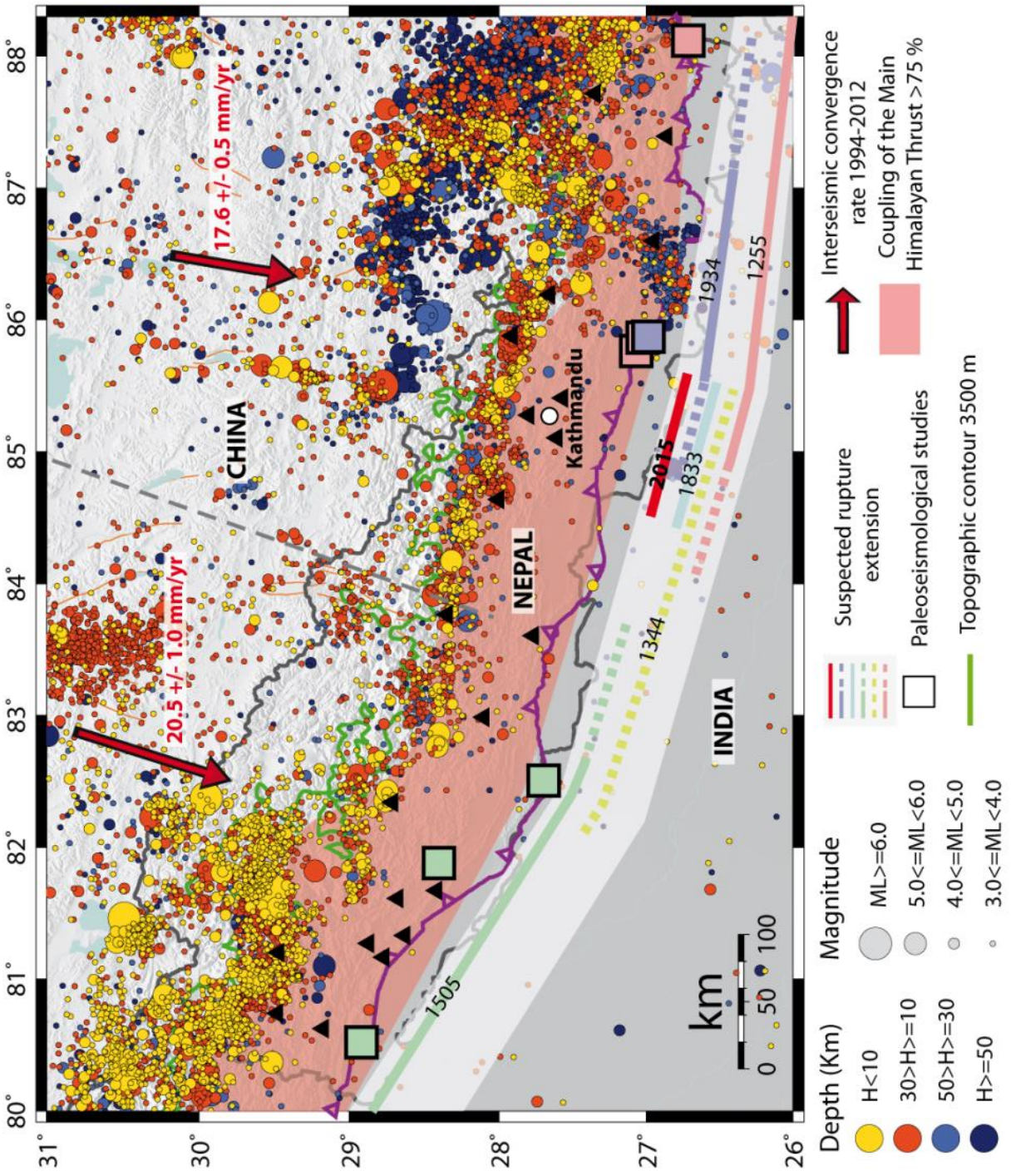

Figure i.4. Contexte sismotectonique du Népal. Le taux de convergence mesuré par le GPS est de Ader et al., 2012 et le couplage de Stevens and Avouac, 2015. Les sites d'études paléosismologiques est de Bollinger et al., 2016. Les cercles sont la sismicité intersismique de 1990 -2015 du catalogue du *National* et *Regional Seismological Centres of Nepal* (NSC and RSC) enregistrée par les stations séismologiques du réseau national (triangles noirs). La ligne violette est le Main Frontal Thrust (MFT). Les lignes orange sont les failles normales.

En général la sismicité intersismique liée au *Main Himalayan Thrust* au Népal est localisé entre 80-100 km au nord de la trace en surface du MHT, le *Main Frontal Thrust* (MFT), situé au pied de la haute chaîne de l'Himalaya (Pandey et al., 1995 ; Pandey et al., 1999 ; Cattin and Avouac, 2000) (Figure i.4). Elle est située à des profondeurs micrustales entre 10 et 20 km, c'est pour cela qu'elle est appelée communément sismicité micrustale (Figure i.5). Elle se situe également au niveau de la limite fragile-ductile (isotherme 350°C) au niveau de la rampe micrustale du méga-chevauchement MHT (Cattin and Avouac, 2000 ; Bollinger et al., 2006 ; Herman et al., 2010 ; Ader et al., 2012) (Figure i.5). Alors que cette description semble appropriée au premier ordre pour le centre du pays, la sismicité de l'ouest du Népal présente de fortes variations latérales (e.g. Pandey et al., 1999) auxquelles je vais m'intéresser particulièrement (Figure i.4).

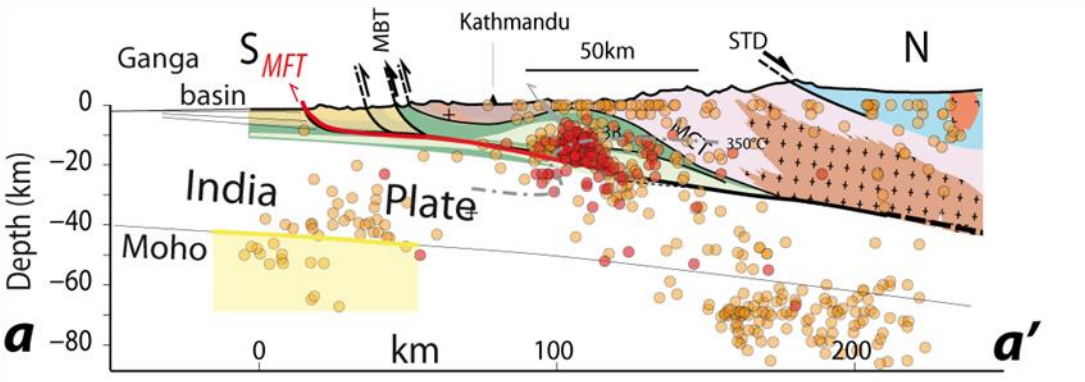

Figure i.5. Coupe géologique simplifié N018°E du Centre Népal (modifié de Bollinger et al., 2006 et Bollinger et al., 2014). Le trait discontinu gris correspond à la limite fragile-ductile de la structure thermique de Bollinger et al., 2006. Les cercles rouges et oranges correspondent à la sismicité instrumentale sous la klippe de Katmandou de juillet à décembre 1995 (Cattin et Avouac, 2000) et de l'est du Népal de septembre 2001 à avril 2003 (Monsalve et al., 2006), respectivement. MFT est le *Main Frontal Thrust*, MBT est le *Main Boundary Thrust*, MCT est le *Main Central Thrust* et STD est le *South Tibetan Detachment*. Voir Figure 1.2 pour l'échelle de couleur des zones tectonostratigraphiques.

Ce manuscrit de thèse se divise en quatre chapitres. Le **Chapitre 1** présente le contexte tectonique et sismique du Népal ainsi que le réseau sismologique du Népal. Le **Chapitre 2** est consacré aux variations latérales du MHT évoquées par le séisme de 2015 Gorkha et ses répliques, et la sismicité intersismique du catalogue du *National Seismological Centre* du Népal (NSC). J'y présente un résumé des études qui ont eu lieu, ayant apporté de l'éclaircissement à la question de la segmentation. Mon travail d'analyse du premier mois de la crise sismique y est également présenté, travail ayant été réalisé en support de celui effectué par les collègues du NSC. De plus, je reprends les données disponibles du NSC et analyse la distribution spatio-temporelle d'une crise

sismique qui a eu lieu en 1997 dans la zone de rupture du séisme de Gorkha. Les résultats semblent indiquer la présence d'un évènement transitoire à l'échelle de l'Himalaya. De plus, la relocalisation relative d'un des essaims de sismicité de la crise permet de mettre en évidence des complexités structurales au niveau du MHT au nord de Katmandou. Ces complexités ont été aussi relevées par les études après le séisme de Gorkha en 2015. Les **Chapitres 3** et **4** portent sur l'analyse de la sismicité à l'ouest du Népal, à l'aide d'un réseau temporaire de 15 stations sismologiques et son interprétation d'un point de vue sismotectonique. Cette expérience sismologique est présentée avec une première partie technique au **Chapitre 3** sur l'installation des stations et le fonctionnement des stations au cours du temps. Le traitement des données avec des logiciels tels que Seiscomp3, Hypo71 et HypoDD comprenant une discussion sur les paramètres et la qualité des résultats sont également discutés. Les résultats sont confrontés aux études existantes dans le **Chapitre 4**, notamment les coupes géologiques équilibrées et la discussion portent sur la relation entre la sismicité et les structures tectoniques. Enfin, le dernier chapitre est axé sur les conclusions principales de cette thèse ainsi que les perspectives qui s'en suivent.

CHAPITRE 1

Contexte sismotectonique du Népal

Avant-propos

Le Chapitre 1 a pour but d'introduire le contexte géologique et plus particulièrement le contexte tectonique au voisinage du grand chevauchement himalayen (MHT). Il a aussi pour objectif de présenter la sismicité de l'Himalaya au Népal, en particulier la sismicité de l'Ouest Népal. Cette présentation est suivie par une batterie de questions concrètes qui s'ajoutent à celles posées dans l'Introduction.

1.1. Contexte géologique

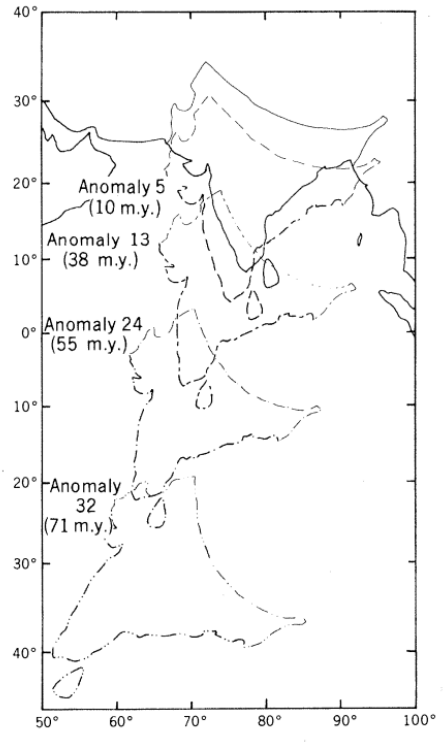

Figure 1.1. Migration de la plaque Inde vers le nord jusqu'à atteindre la plaque Eurasie (extrait de Molnar and Tapponnier, 1975).

L'Himalaya est la chaîne de montagne avec les plus hauts sommets de la Terre qui s'étale sur 2500 km de long traversant le Pakistan, l'Inde, le Népal, le Bhoutan et le Tibet. Elle est le résultat de la collision entre les plaques Inde et Eurasie qui commença il y a ~55 Ma et se poursuit de nos jours (e.g. Molnar et Tapponnier, 1975) (Figure 1.1). La vitesse de convergence Inde-Eurasie, initialement à 10-18 cm.an^{-1} est actuellement de 4 cm.an^{-1} (Molnar et Tapponnier, 1975 ; Bettinelli et al., 2006), dont la moitié est accommodée au travers de l'Himalaya, sur le grand chevauchement Himalayen (e.g. Bilham et al., 1997 ; Lavé et Avouac, 2000 ; Ader et al., 2012).

Au travers de la chaîne himalayenne on distingue quatre zones tectonostratigraphiques (*Subhimalaya*, *Lesser Himalaya* ou moyen pays himalayen, *Greater Himalaya* ou Haut Himalaya et le *Tibet Himalaya* ou Himalaya Téthysien) séparées par des grands chevauchements crustaux (le *Main Frontal Thrust* (MFT), le *Main Boundary Thrust* (MBT) et le *Main Central Thrust* (MCT)) et le *Southern Tibet Detachment* (STD) (e.g. Gansser, 1964) (Figure 1.2). Les chevauchements s'enracinent

en profondeur sur le *Main Himalayan Thrust* ou Grand Chevauchement Himalayen (MHT) (e.g. Hauck et al., 1998).

La **zone Subhimalayenne** est formée par le Groupe des Siwaliks qui est constitué par des roches sédimentaires molassiques syntectoniques datant du Miocène moyen au Pliocène (e.g. Upreti et al., 1999; Dhital, 2015) (Figure 1.2). Cette zone est limitée par le MFT au sud et le MBT au nord. A l'heure actuelle, des sédiments analogues sont déposés dans le bassin du Gange au sud du MFT sur la plaque Inde plongeante (e.g. Lyon-Caen and Molnar, 1985).

Le ***Lesser Himalaya*** ou moyen pays est limité au sud par le MBT et au nord par le MCT (actif à partir de 23-20 Ma (e.g. Hubbard and Harrison, 1989)) (Figure 1.2). L'histoire géologique de cette zone est un sujet d'actualité qui évolue au fur et à mesure que la connaissance des formations géologiques qui la compose progresse. Robinson et al., 2006 classifie la zone en trois séquences:

1) La séquence du moyen pays (*Lesser Himalaya*) est formée principalement par des roches sédimentaires du Protérozoïque, d'origine plaque Inde, accrétées à l'Himalaya, et affectées par un faible degré de métamorphisme. Elle est souvent divisée en deux unités tectono-stratigraphiques (e.g. DeCelles et al., 2001; Khanal and Robinson, 2013): moyen pays inférieur (*Lower Lesser Himalaya*) et moyen pays supérieur (*Upper Lesser Himalaya*), formés par des roches du Protérozoïque inférieur et moyen respectivement.

2) La séquence Gondwana comprend de roches sédimentaires Permiennes à Paléocène très fortement déformées.

3) La séquence de Bassin d'Avant-Pays du Tertiaire est le témoin le plus ancien de roches sédimentaires syntectoniques qui sont très fortement déformés.

Il convient de souligner que l'unité du moyen pays supérieur et les séquences Gondwana et Bassin d'Avant-Pays du Tertiaire sont chevauchées par le chevauchement Ramgarh (Pearson and DeCelles, 2005) qui met en place une unité du moyen pays inférieur au sommet de la pile du moyen pays. Pour cela et suivant les représentations de la littérature (e.g. Khanal and Robinson, 2013), nous assimilerons l'ensemble au moyen pays supérieur (Figure 1.2).

La zone du ***Greater Himalaya*** ou Cristallin du Haut Himalaya, limitée au sud par le MCT et au nord par le STD, est formée par des roches sédimentaires et ignées datant du Protérozoïque supérieur à l'Ordovicien et sont affectées par un métamorphisme de degré élevé (Figure 1.2).

Finalement, la zone ***Tibetan Himalaya*** ou Himalaya Téthysien est formée par des roches sédimentaires riches en fossiles marins de la marge passive de la plaque Inde de l'époque de l'océan Téthys. Au nord, la zone de suture Indus-Tsangpo marque la limite avec la plaque Eurasie (Figure 1.2).

Les zones Greater Himalaya comme Tibetan Himalaya, décrites le long et sur le flanc nord de la haute chaîne, ont parfois été préservées plus au sud, au sein des klippes posées sur le moyen pays. C'est le cas de la klippe de Katmandou, au centre Népal ou de la klippe de Dadeldhura à l'ouest du pays (Figure 1.2). Ces klippes ont été localement préservées de part et d'autres de régions affectées par d'épais empilements d'écailles de moyen pays.

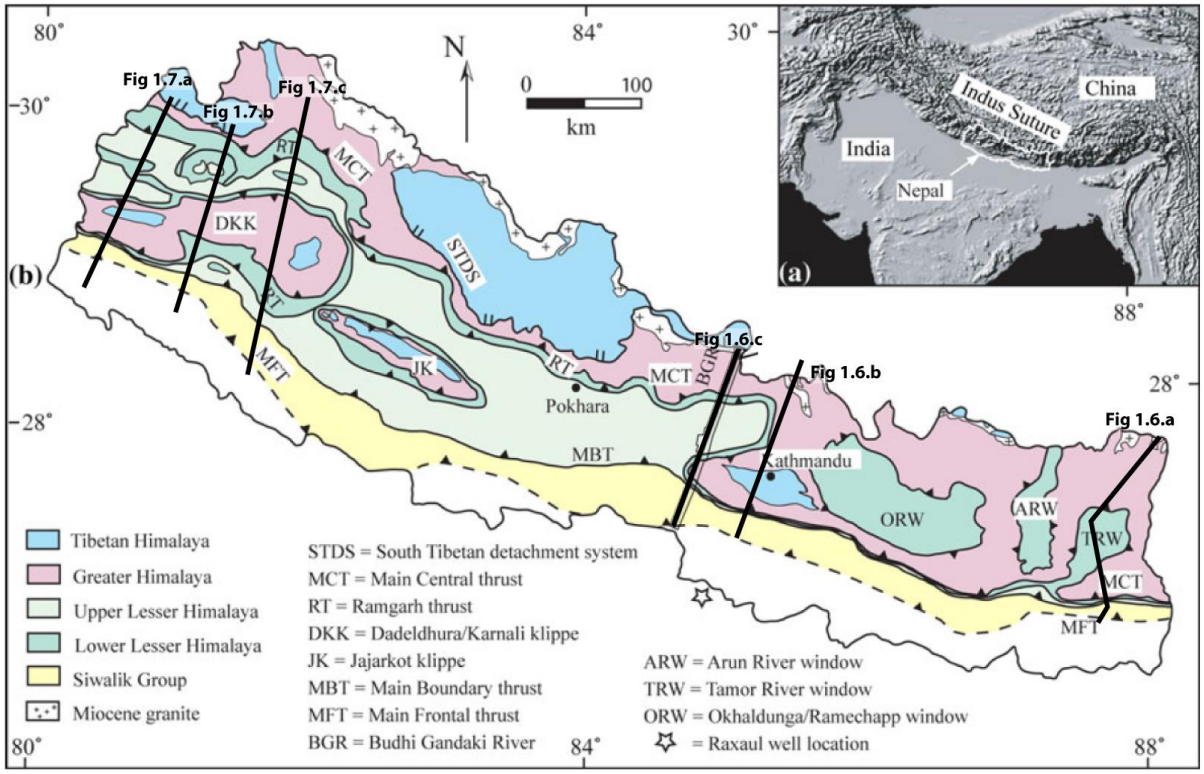

Figure 1.2. Carte des principales structures et zones stratigraphiques. Extrait de Khanal and Robinson, 2013. Les lignes noires correspondent aux traits des coupes des Figures 1.6 et 1.7.

1.1.1. Géométrie du Main Himalayan Thrust (MHT)

La géométrie du grand chevauchement Himalayen a tout d'abord été déduite des observations géologiques de surface. Les coupes géologiques qui en sont déduites présentent dans leur majorité une rampe frontale raide (typiquement 30° de pendage) puis un plat à très faible pendage (2°-5°) et environ 100 km au nord du front, au droit de l'antiforme de moyen pays principal, une rampe micrustale (e.g. Schelling and Arita, 1991; Avouac et al., 2001).

Le grand chevauchement himalayen n'a été imagé par la géophysique que plus tard. Le projet INDEPTH a réalisé des profils de sismique réflexion au travers du Plateau Tibétain à l'est du Népal (Zhao et al., 1993). Cette expérience a permis de mettre en évidence le Moho et le MHT qui s'approfondissent avec un faible pendage (~10°) vers le nord de 60 à 70 et de 25 à 39 km respectivement au droit de la haute chaîne et de la partie méridionale du plateau Sud-Tibétain (Figure 1.3) (Hauck et al., 1998).

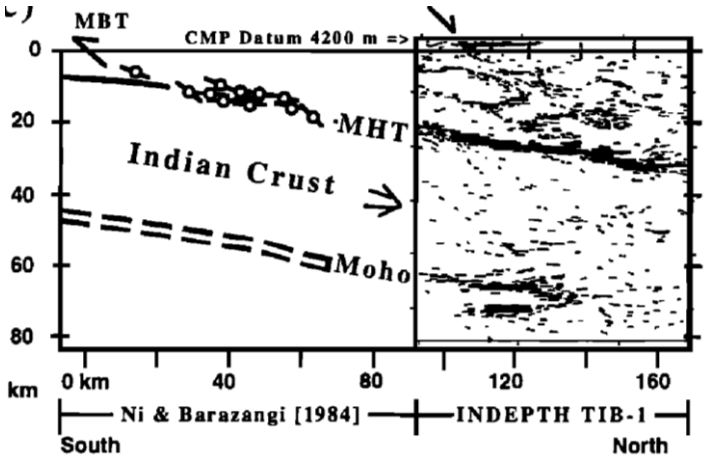

Figure 1.3. Profil de sismique réflexion à la longitude du Sikkim, Inde (à côté de la frontière est du Népal). Les deux plus fortes réflexions suivent la prolongation du MHT et du Moho de Ni and Barazangi, 1984. Extrait de Hauck et al., 1998.

Depuis, plusieurs profils fonction récepteur le long de l'Himalaya ont été réalisés à l'aide de réseaux sismologiques temporaires (Schulte-Pelkum et al., 2005; Nabelek et al., 2009 ; Acton et al., 2011 ; Caldwell et al., 2013). Ces profils ont imagé le plat du MHT et le Moho à des profondeurs moyennes respectives de 10-15 km et 40-50 km sous le moyen pays et la haute chaîne (Figure 1.4).

(a)

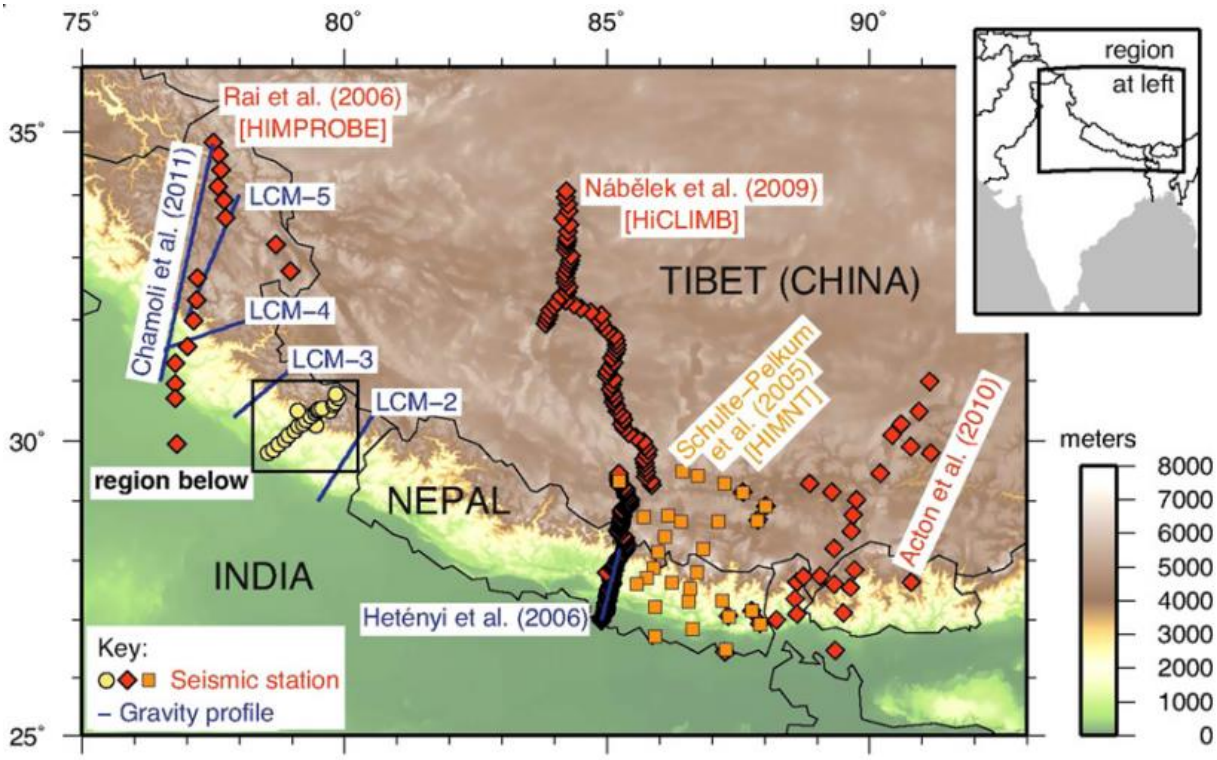

(b)

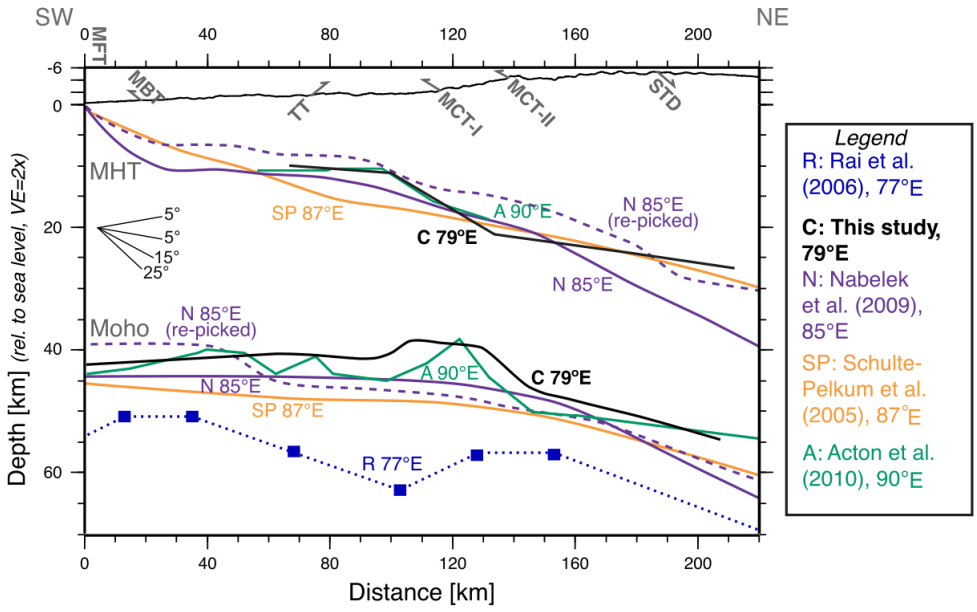

Figure 1.4. (a) Carte des réseaux temporaires déployés jusqu'à 2013 et (b) trace du Moho et géométrie du Main Himalayan Thrust d'après les images fonction-récepteur des profils sismologiques en Himalaya (extraites de Caldwell et al., 2013). La ligne noire (C :This study, 79°E) correspond aux tracés de Caldwell et al., 2013.

Parmi ces études, deux ont permis d'imager les structures au Népal, les projets HIMNT et HiCLIMB :

Le projet HIMNT était une expérience sismologique temporaire (2001-2003) de 29 stations large bande couvrant l'est du Népal et le sud du plateau Tibétain pendant 18 mois. Le profil déduit de 40 à 250 fonctions récepteurs par station a mis en évidence un Moho relativement plat sous la chaîne himalayenne (~40 km de profondeur) qui s'approfondit au Nord ainsi qu'un MHT à des profondeurs de 8 km au niveau des Siwaliks et environ 20 km sous la haute chaîne (Schulte-Pelkum et al., 2005) (Figure 1.4 et 1.5.a).

Le projet Hi-CLIMB a consisté en un déploiement sismologique temporaire (2002-2005) de plus de 200 stations le long d'un profil sud-nord de la chaîne, avec pour objectif d'imager les structures à l'aide d'un profil fonction récepteur. Ce profil s'est étendu vers le nord depuis le MFT, le long de la rivière Trisuli, à l'ouest de la klippe de Katmandou puis plus au Nord au Tibet, sur 800 km (Nabelek et al., 2009) (Figure 1.4 et 1.5). Les auteurs de cette étude ont identifié une zone à faible vitesse (LVZ – *Low Velocity Zone*) très superficielle à proximité du bassin du Ganges et à des profondeurs entre 10-15 km sous la Haute Chaîne qui correspondrait à la zone broyée du MHT (Nabelek et al., 2009) (Figure 1.5). Les auteurs proposent que la présence des fluides ou la fusion partielle participent à faire de cette zone une LVZ.

(a)

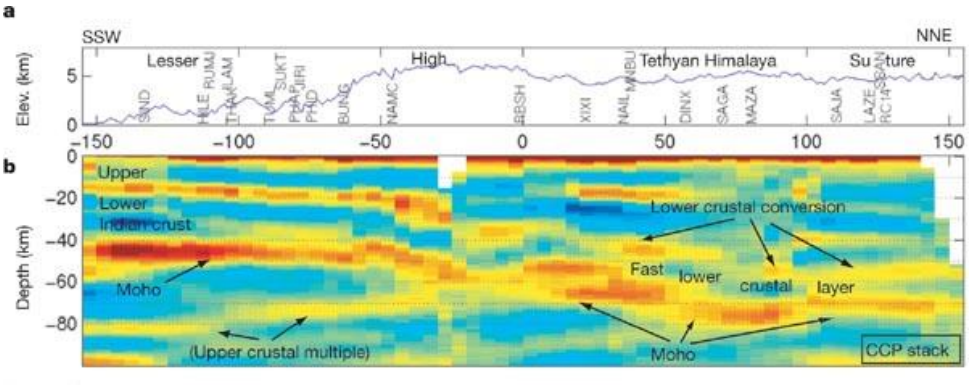

(b)

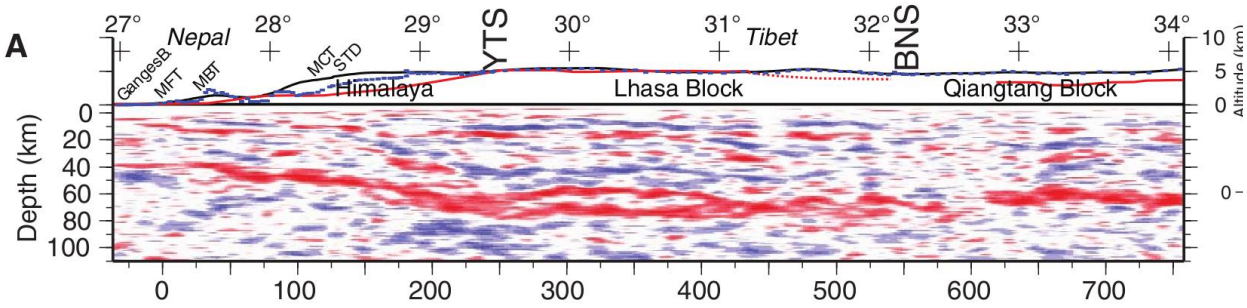

Figure 1.5. Coupes fonction récepteur des expériences (a) HIMNT à l'est du Népal (extrait de Schulte-Pelkum et al., 2005) et (b) Hi-CLIMB à l'ouest de Katmandou (extrait de Nabelek et al., 2009). Voir Figure 1.4.a pour la localisation des coupes.

Les géométries de premier ordre du Moho et du MHT déduites de ces études géophysiques apparaissent relativement homogènes latéralement. L'examen de la géologie régionale suggère toutefois l'existence de variations latérales de la position et de l'extension de rampes mi-crustales.

Dans l'Est Népal, Schelling and Arita, 1991 suggèrent, sur la base des coupes géologiques, l'existence d'une rampe micrustale en avant de l'antiforme de moyen pays (Figure 1.6.a), une rampe qui n'a pas été imagée par la coupe fonction récepteur (Schulte-Pelkum et al., 2005) (Figure 1.5). Au niveau de la klippe de Katmandou, une rampe micrustale au droit de la haute chaîne est suspectée, tandis qu'une seconde rampe, d'extension plus limitée, a été décrite au nord du Mahabarat (Khanal and Robinson, 2013 ; Hubbard et al., 2016) (Figure 1.6.b et 1.6.c). Plus à l'ouest, au pied des Annapurnas la rampe micrustale présente à nouveau au pied de la haute chaîne une histoire récente complexe: un saut récent de la rampe (unique) a été mis en évidence en comparant le soulèvement transitoire et à long terme (Grandin et al., 2012).

Au Far West Népal, la géométrie et la cinématique du moyen pays apparaissent encore plus complexe :

D'importantes variations latérales de la position de rampes sont suggérées par les coupes équilibrées (e.g. DeCelles et al., 2001 ; Robinson et al., 2006) (Figure 1.7). Certains auteurs proposent l'activité d'une seule rampe très frontale (~45 km au nord du MFT) (Berger et al., 2004) tandis que d'autres suspectent une activité tectonique plus au nord (cf. Harvey et al., 2015). La tectonique récente de cette région de l'Himalaya reste en effet encore très peu documentée.

(a)

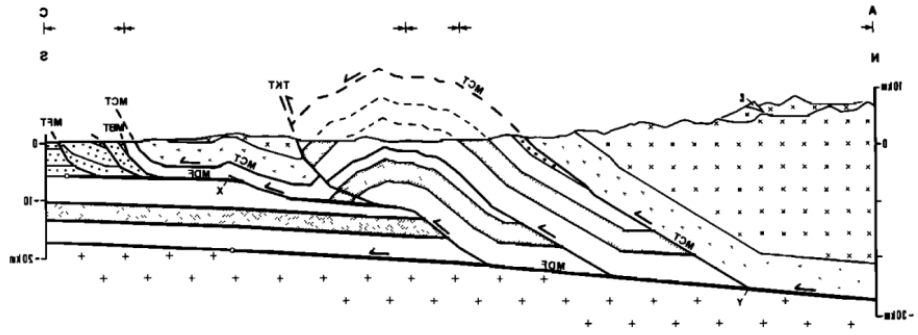

(b)

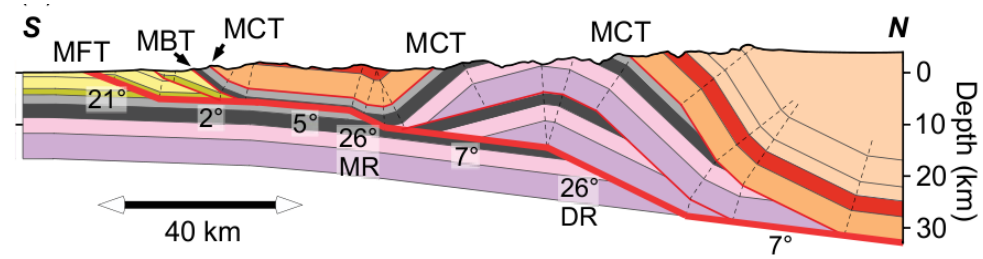

(c)

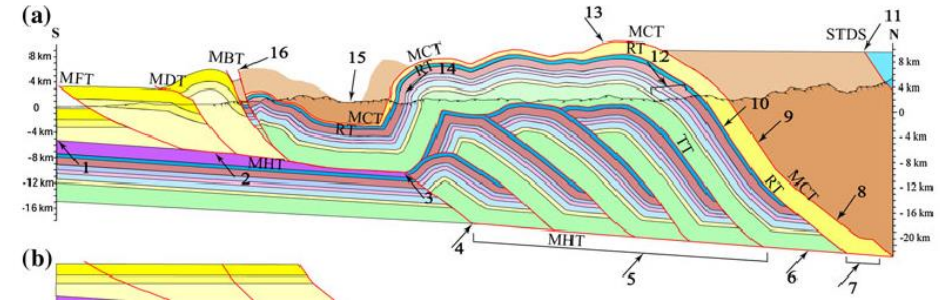

Figure 1.6. Coupes équilibrées d'est au centre Népal (voir les traits des coupes sur la Figure 1.2). Elles sont localisées à (a) Extrémité est (longitude 87.5°E), extrait de Schelling and Arita, 1991, (c) Extrémité ouest de la klippe de Katmandou (longitue 84.7°E), extrait de Khanal and Robinson, 2013 et (b) centre-ouest de la klippe de Katmandou, extrait de Hubbard et al., 2016.

(a)

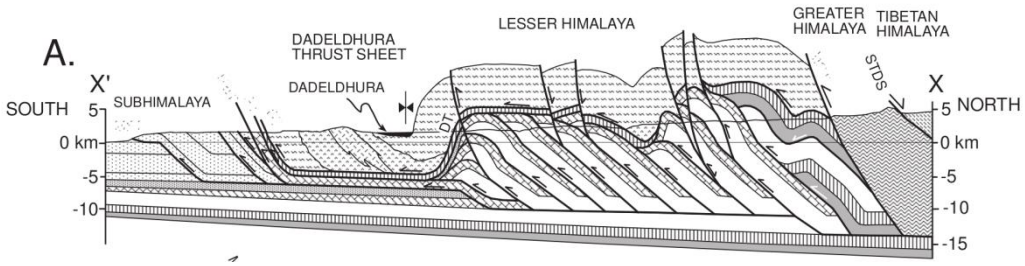

(b)

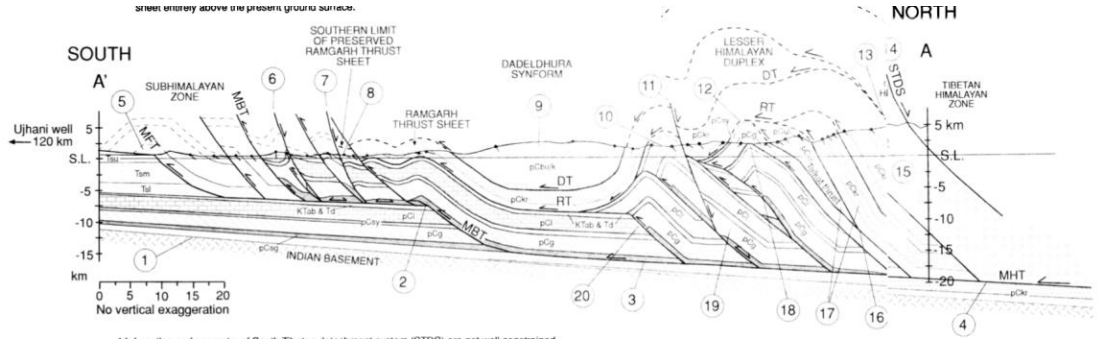

(c)

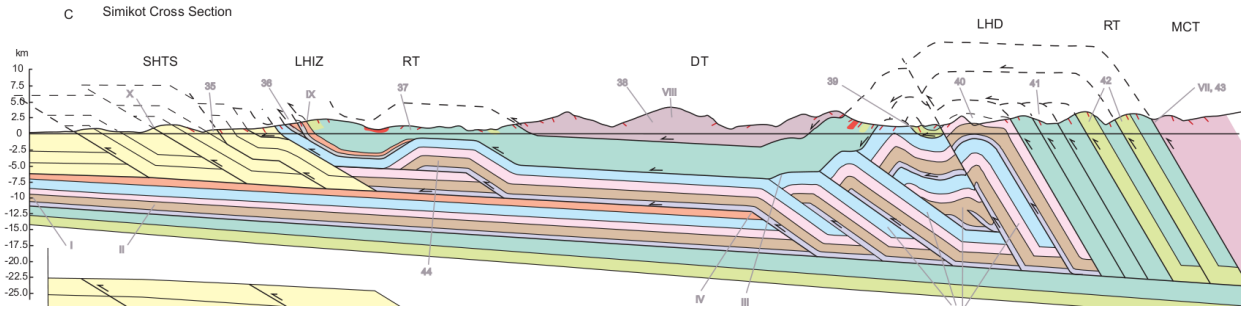

Figure 1.7. Coupes équilibrées au travers des regions *Far* et *Mid West Nepal* (voir les traits des coupes sur la Figure 1.2). Elles sont localisées à (a) extrémité ouest du Népal (longitude 80.9°E), extrait de DeCelles et al., 1998, (b) extrémité ouest du Népal (longitude 81.1°E) , extrait de DeCelles et al., 2001 et (c) est de la rivière Karnali (longitude 81.5°E), extrait de Robinson et al., 2006.

1.1.2. Couplage du Main Himalayan Thrust

Le taux de convergence actuel entre les plaques Inde et Eurasie est de ~40 mm/an dont 10-20 mm/an sont accommodés par le MHT (Banerjee and Bürgmann, 2002 ; Paul et al, 2001). Au Népal, le MHT accommode environ ~16-21 mm/an (Bettinelli et al., 2006, Jouanne et al., 2004, Ader et al., 2012, Grandin et al., 2012) qui est similaire à l'estimation long terme de ~21 mm/an (Lavé et Avouac, 2000). Pendant la période intersismique, les modèles de déformation montrent que le glissement sur la faille est nul, le MHT est bloqué de sa trace de surface actuelle (MFT) jusqu'à l'aplomb de la haute chaîne, 80-100 km au nord (Ader et al., 2012, Stevens and Avouac, 2015) (Figure i.4 et 1.8). La partie plus profonde du MHT, au nord du haut Himalaya, accommode ces ~20 mm/an de façon asismique (Figure i.4 et 1.8).

Ce segment bloqué constitue la partie sismogénique du MHT. Ce segment casse lors des plus forts séismes, relâchant les contraintes accumulées en période intersismique (e.g. Cattin et Avouac, 2000) (Figure i.4).

La limite entre le segment bloqué du MHT et le segment qui glisse continûment en profondeur apparait localisée au voisinage de l'emplacement suspecté d'une rampe mi-crustale, au front de la haute chaîne, à l'aplomb de l'antiforme de moyen pays. Les modèles thermo-cinématiques prédisent que l'extension profonde de la zone bloquée se situe au voisinage de l'isotherme 350°C, une température proche de celle qui contrôle le fluage du Qz, constituant majoritaire de la croûte continentale (Bollinger et al., 2006; Herman et al., 2010; Ader et al., 2012).

L'accumulation de contraintes au voisinage de cette zone de transition est exprimée par une sismicité mi-crustale intense (Cattin et Avouac, 2000). L'extension vers le nord de cet essaim semble suivre le contour 3500 m du relief (Bollinger et al., 2004a) (Figure i.4). Au-delà d'un relief moyen de 3500 m, la contrainte principale maximum, N-S sous cette limite, devient verticale. Cette orientation du champ de contrainte est cohérent avec la présence de failles normales et la sismicité mi-crustale sur des plans de chevauchement à faible pendage est inhibée (Bollinger et al., 2004a).

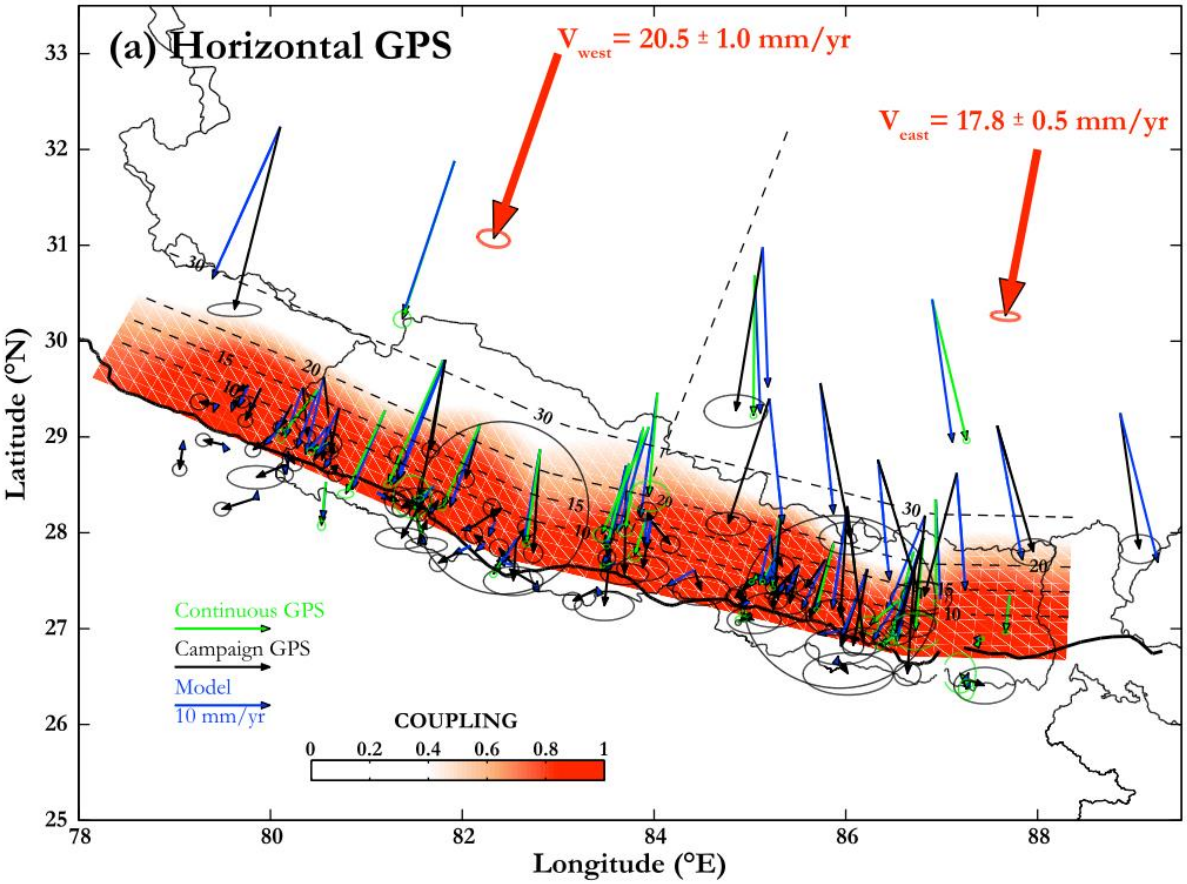

Figure 1.8. Carte GPS horizontal et modèle de couplage sismique en rouge. La ligne noire continue en gras est le MFT. Les lignes noires en pointillé avec des numéros sont les contours en profondeur du MHT en kilomètres du modèle de couplage. Extrait de Ader et al., 2012.

1.2. Sismicité

A l'échelle de l'Himalaya, la sismicité souligne toute la zone de collision entre les plaques Inde et Eurasie au pied des reliefs de l'Himalaya (Figure 1.9). En effet, la sismicité se concentre sur une bande étroite suivant la trace de la chaîne himalayenne ; de part et d'autre de la chaîne, les syntaxes de la collision sont très présentes avec une sismicité très abondante et au nord la sismicité sur le plateau Tibétain témoigne de l'activité, –extension – extrusion, liée à la collision (Figure 1.9). L'activité sismique apparait être très faible au cœur de la plaque Inde, comparativement à l'Himalaya. La ceinture étroite de sismicité à la frontière entre la plaque Inde et les zones affectées par la collision correspond pour l'essentiel à la sismicité mi-crustale liée au MHT.

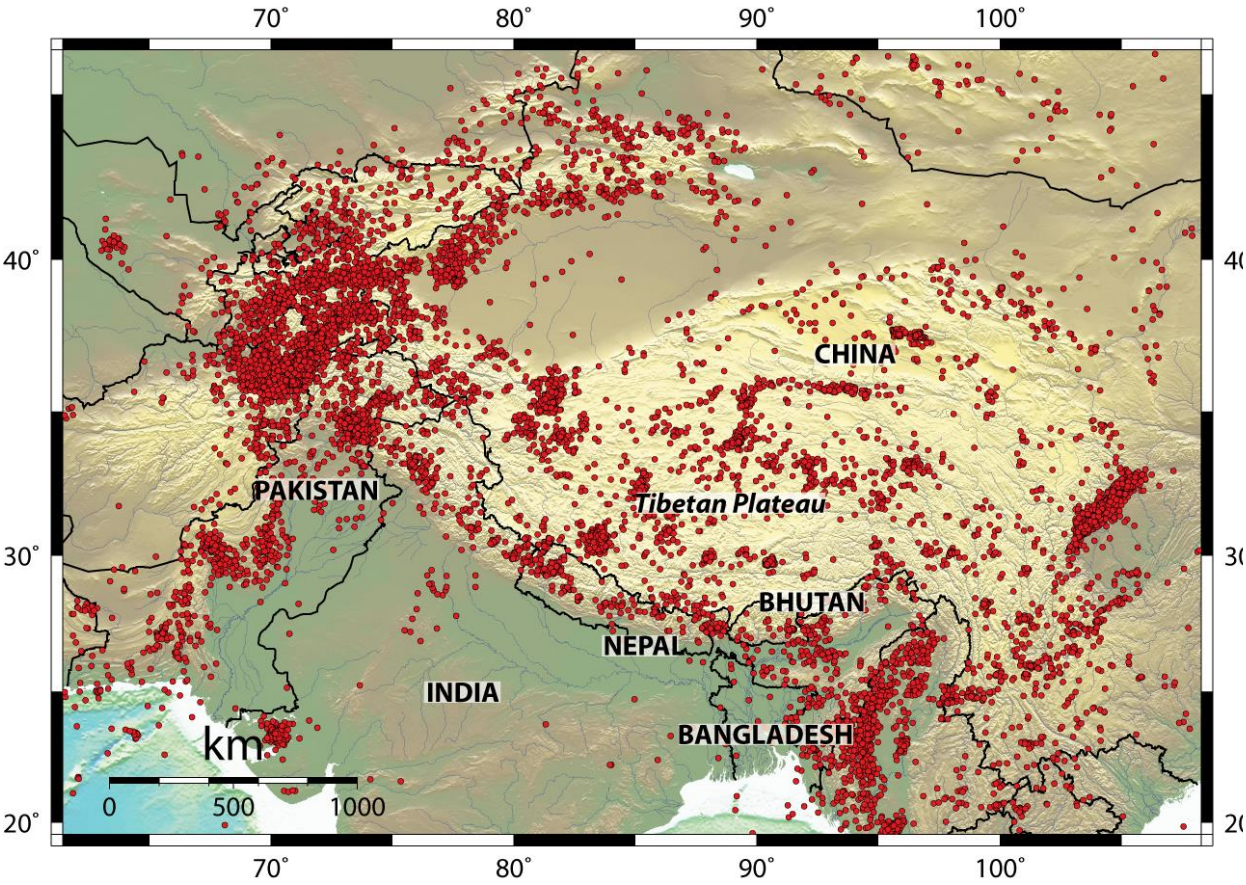

Figure 1.9. Sismicité du catalogue *International Seismological Centre* - ISC (1964 – 2011) des magnitudes 1.5 à 7.8 à l'échelle de l'Himalaya.

1.2.1 Réseau sismologique du Népal

Le réseau séismologique du Népal est opéré par le *Departement of Mines and Geology* (DMG) en collaboration avec le Département Analyse Surveillance Environnement (DASE). Ce réseau est dédié à l'alerte sismique afin de transmettre les informations nécessaires aux organismes gouvernementaux pertinents afin d'organiser les secours si besoin. De même, les données sont stockées ce qui permet son exploitation à des fins scientifiques. Il est constitué de 21 stations courte période (1s) une composante (ZM500) et deux stations large bande distribuées au long du pays (Figure i.4). Les données sont transmises des stations aux deux centres séismologiques (NSC – *National Seismological Centre* et RSC – *Regional Seismological Centre*) où elles sont traitées. Le NSC est situé à Katmandou et s'occupe de la surveillance de l'est et du centre du pays à l'aide de 12 stations sismiques analogiques depuis 1994 de façon homogène. En mai 2016, le réseau a été modernisé avec des stations digitales. Le RSC se trouve à Birendranagar dans le district de Surkhet et se charge de l'alerte sismique de l'ouest du Népal. Les données étaient enregistrées par des stations sismiques analogiques de 1994 jusqu'à 2014. Depuis les stations du réseau ouest ont été remplacées par des stations digitales (Adhikari et al., 2015).

1.2.1.1. Traitement des données

Les deux centres utilisent la même chaîne de traitement à l'aide du logiciel Jade-Onyx et avec le modèle de vitesse 1-D de Pandey, 1985 (Table 1.1). Les données sismiques sont pointées manuellement par les analystes des centres.

Couches (km)	Vp (km/s)	Vs (km/s)
0-23	5.56	3.18
23-55	6.50	3.71
>55	8.10	4.63

Table 1.1. Modèle de vitesse de Pandey, 1985.

La magnitude calculée est une magnitude locale M_{L_NSC} spécifique pour le Népal (Adhikari et al., 2015) :

$$M_{L_{NSC}}(i) = log\left[\frac{A(i)}{T}\right] + B[\Delta(i)] + C(i)$$

Où A est l'amplitude maximale de la phase S à la station i, T est la période, B correspond à la loi d'atténuation, $C(i)$ la correction appliquée à chaque station et $\Delta(i)$ la distance épicentrale à la station. La magnitude $M_{L_{NSC}}$ est obtenue à partir de la moyenne arithmétique des magnitudes $M_{L_{NSC}}(i)$.

Afin d'éviter des biais de magnitude liés à des effets de source ou de trajet, seules les stations dont la distance à l'épicentre est supérieure à 100 km sont utilisées pour ce calcul (Adhikari et al., 2015) . Cette magnitude n'est adaptée qu'aux séismes de magnitude inférieure à 6. En effet, tous les séismes de forte magnitude, quelle que soit leur localisation sur le territoire népalais, saturent l'intégralité des voies gain faible du réseau national.

1.2.2. Sismicité des catalogues NSC et RSC

A l'échelle du Népal, nous distinguons une sismicité située à proximité des grabens sud-tibétains au nord du Népal et une agglomération de sismicité profonde (Monsalve et al., 2006) à l'est du pays qui se situe où a eu lieu le séisme M6.6 Udaypur le 20/08/1988 (Pandey and Nicolas, 1991) (Figure i.4 et 1.10). La sismicité mi-crustale, entre 10 – 20km de profondeur (voir Introduction), est constituée d'évènements individuels mais aussi d'essaims de sismicité (plus d'une cinquantaine en 20 ans) (exemple *Chapitre 2* – section *2.3. La sismicité intersismique au nord de Katmandou : variations latérales de structure et épisode transitoire*, article Figure 2). De plus, elle se présente sous la forme de ceinture au long du Népal à l'exception des extrémités est et ouest du pays (Figure i.4).

A l'est, l'étude de Monsalve et al., 2006 qui a exploité l'expérience HIMNT a mis en évidence que la sismicité la plus superficielle est distribuée de façon discontinue à des profondeurs entre 0 et 20 km (Figure 1.10). Toutefois, une particularité de cette région est la présence de sismicité profonde qui affecte la plaque Inde plongeante entre 30 et 70 km de profondeur (Figure 1.10). Les modèles multiparamétriques d'Hétényi et al., 2007 localisent à cette profondeur la croûte inférieure et le manteau de la plaque Inde où il y a des processus métamorphiques (« éclogitisation ») avec des réactions de déshydratation. Ces processus libèrent des fluides qui augmentent la pression de pore jusqu'à la rupture, et donc des séismes (Hétényi et al., 2007).

(a)

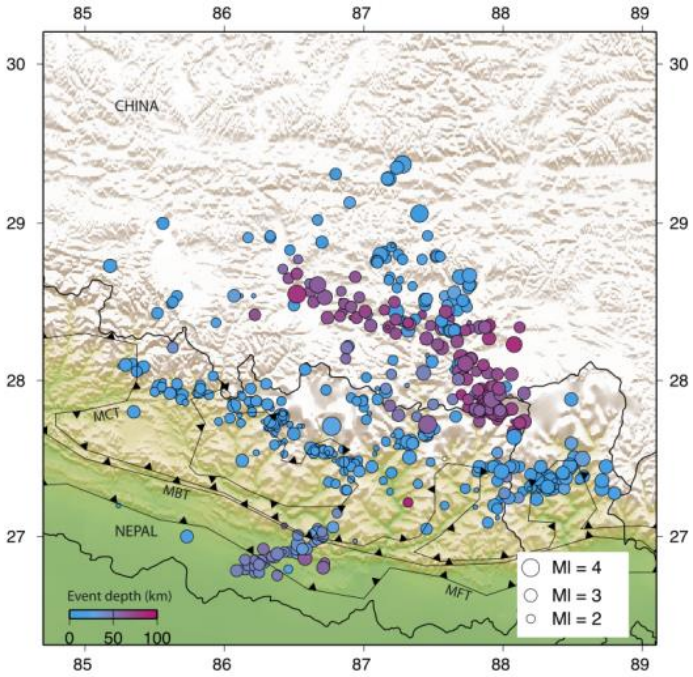

(b)

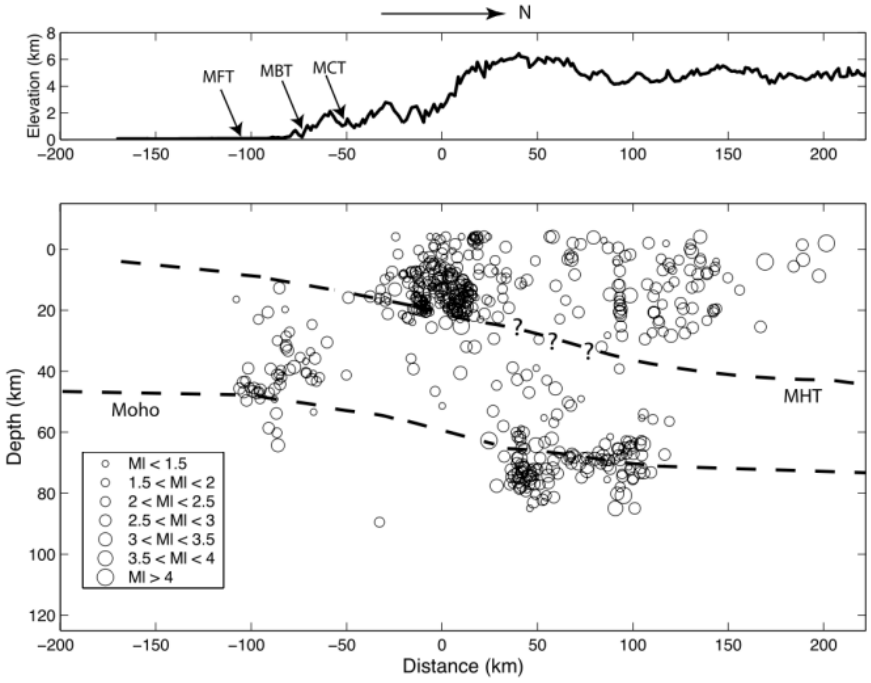

Figure 1.10. Sismicité de l'est Népal de l'expérience HIMNT en (a) carte et (b) coupe du catalogue de sismicité pour la période de septembre 2001 à avril 2003 de Monsalve et al., 2006.

A l'ouest du Népal (Région *Mid West* et *Far West Nepal*) se trouvent deux ceintures parallèles de sismicité distantes de 60 km identifiées pour la première fois par Pandey et al., 1999 avec seulement 5 ans de données du réseau sismologique du RSC. La distribution de la sismicité du catalogue du RSC pour la période 1993-2012 dessine une forme de fourche sur une distance de 105 km vers l'est. Elle présente une sismicité dont les profondeurs restent peu contraintes entre 0 et 50 km (Figure 1.11). On distingue 3 zones:

1) La ceinture de sismicité de l'ouest ou **ceinture de sismicité de Bajhang** a une largeur de ~50 km et se trouve à 60 km au nord du MFT (Figure 1.11).

2) La ceinture sud de sismicité ou **ceinture de sismicité Karnali Sud** a une largeur de 20 km et se trouve à ~40 km du MFT (Figure 1.11).

3) La ceinture nord de sismicité ou **ceinture de sismicité Karnali Nord** avec ces 43 km de largeur est la plus éloignée du MFT des trois ceintures à plus de 100 km (Figure 1.11).

(a)

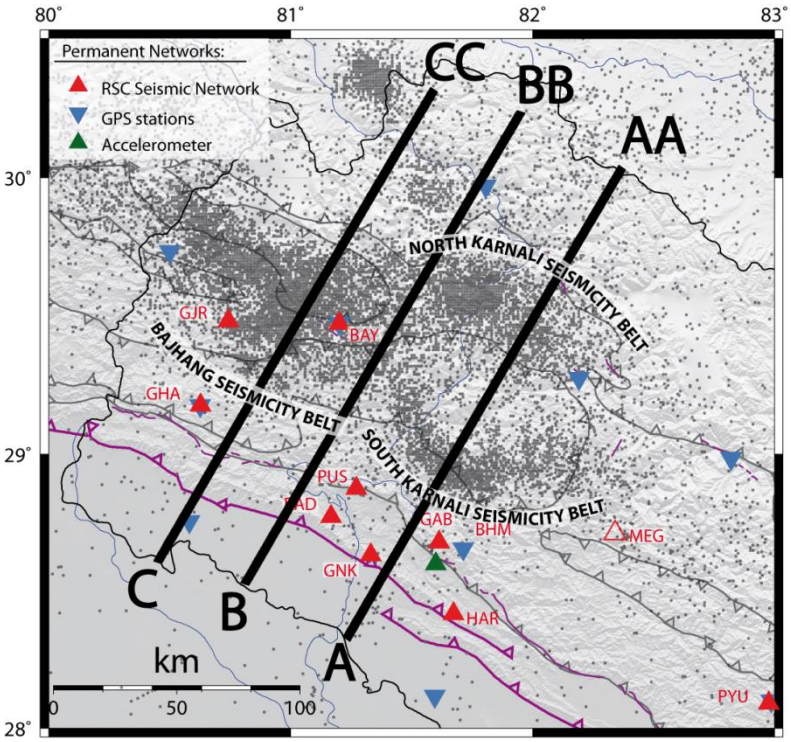

(b)

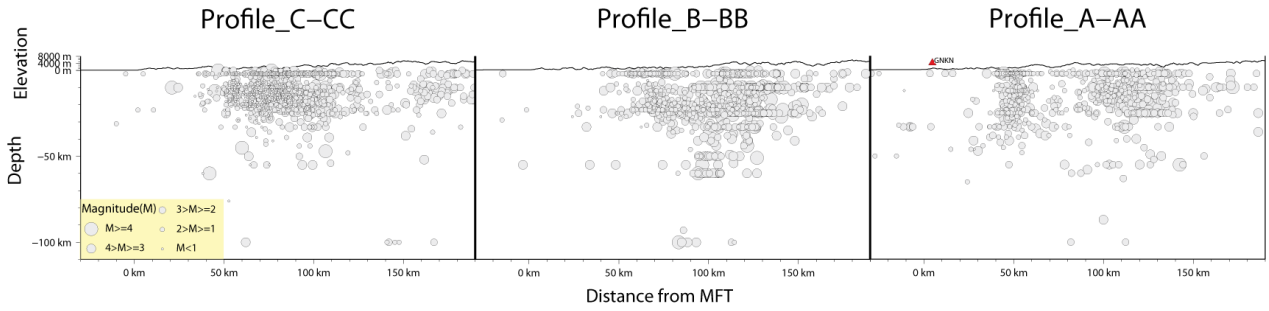

Figure 1.11. Sismicité du catalogue du RSC (1993-2012) en (a) carte et (b) coupe. Magnitudes entre 0.1≤ML≤6.8. Les lignes violettes correspondent aux traces en surface des failles actives (le MFT (ligne endentée) et les failles identifiés par Nakata, 1982 (lignes fines) et les lignes grises aux anciennes traces en surface du MHT.

Il est à noter que le catalogue RSC n'est pas complet depuis 1993 pour l'ouest Népal : en tout 6 années, marquées par la guerre civile, le démantèlement de certaines stations et relais, sont manquantes. Toutefois cela est suffisant pour s'apercevoir de l'intense activité dans la zone. En effet, lorsque l'ouest du Népal compte ~1790 séismes de ML≥3.0 entre 1994-2015, le centre du Népal en compte ~800 séismes de ML≥3.0 pour une surface similaire pour le même temps.

1.3. Questions

La sismicité de l'ouest du Népal suscite des interrogations spécifiques que nous énumérons ci-dessous.

Les premières questions concernant la précision des données dont nous disposons :

1) Les différences entre la sismicité du centre et de l'ouest du Népal sont-elles bien réelles ? Ou bien sont-elles pour partie liées à la géométrie du réseau sismologique?

2) Les profondeurs des hypocentres des séismes de l'ouest Népal sont-elles justes ? Distribuées entre 0 à 50 km comme suggérées par les coupes au travers du catalogue RSC?

Alors que la sismicité micrustale dans l'est et le centre Népal se localise normalement à l'endroit où se produit l'accumulation des contraintes entre le segment bloqué et débloqué du MHT, à la transition fragile-ductile et au pied de la haute topographie de la chaîne himalayenne ; la sismicité à l'ouest du Népal s'étale sur une large surface :

3) Comment la sismicité est-elle distribuée relativement au MHT pendant la période intersismique à l'ouest du Népal ? Se trouve-t-elle principalement sur le plan de chevauchement? Y a-t-il des séismes profonds dans la plaque Inde ? Y a-t-il de la sismicité localisée sur des failles actives secondaires ?

4) Quelle est la relation, si elle existe, entre les deux ceintures de sismicité parallèles (Karnali Sud et Karnali Nord) et les variations latérales de géométrie du MHT en profondeur ?

5) Quelle est la relation avec le contexte de l'ouest du Népal (topographie, couplage, ...) ?

Une meilleure localisation de la sismicité permettrait de répondre à beaucoup de ces questions. Par le passé, les expériences séismologiques temporaires menées à l'échelle régionale le long de l'Himalaya ont permis d'avoir une meilleure estimation de la profondeur de la sismicité et en conséquence d'établir la relation avec les structures environnantes (Monsalve et al., 2006 ; Mahesh et al., 2013 ; Diehl et al., 2017). Le succès de ces réseaux temporaires a été de localiser les stations au-dessus de la zone d'étude afin de localiser au mieux les hypocentres. L'ouest Népal présente un intérêt scientifique majeur comme je l'ai montré auparavant mais il n'y a jamais eu d'expériences séismologiques temporaires. Un réseau séismologique supplémentaire couplé aux stations du RSC, situées principalement au sud des ceintures de sismicité, améliorerait la localisation hypocentrale de la sismicité et donc notre connaissance des relations entre structures tectoniques et sismicité. Ceci permettrait d'ouvrir la discussion sur la segmentation du MHT à l'ouest du Népal. Le fort taux de sismicité annuel permet de garantir le succès d'une expérience temporaire au droit de l'essaim de sismicité, un déploiement envisagé dans le cadre de l'ANR Bhutanepal.

CHAPITRE 2

Centre Népal

Avant-propos

Au début de la thèse je me suis intéressée à la distribution spatiale et temporelle du catalogue préexistant (NSC et RSC). Je me suis focalisée sur l'étude d'une crise sismique survenue simultanément -pendant l'hiver 1996-1997- à trois endroits distants les uns des autres au Népal. L'essaim de sismicité le mieux documenté parmi les 3 était situé au centre du Népal, à proximité de plusieurs stations du réseau sismologique permanent du NSC. L'étude des variations spatiales de sismicité intersismique dans la région touchée par l'essaim a révélé la présence de possibles variations de géométrie du Main Himalayan Thrust à proximité de l'extension profonde de la zone bloquée. L'analyse de la sismicité post-séisme de Gorkha révèle des variations spatiales et temporelles aux mêmes positions ce qui rend l'interprétation « structurale » des variations latérales de sismicité tout à fait crédible. Ce travail m'a amené à étudier les variations spatio-temporelles de la sismicité pendant deux périodes différentes du cycle sismique et à les comparer aux études de la rupture cosismique. L'ensemble révèle l'existence de complexités géométriques du MHT, et d'un possible contrôle de la rupture cosismique par ces structures profondes, une idée peu documentée auparavant. Cette relation entre sismicité intersismique, rupture en profondeur et sismicité postsismique m'amène à présenter dans ce chapitre un certain nombre d'informations sur le séisme de Gorkha et le Centre Népal.

Avant de rentrer dans le vif du sujet, je voulais vous faire part de mon vécu, en quelques mots, du séisme de Gorkha qui a eu lieu lors de ma troisième mission de terrain dans l'ouest Népal.

Le 25 avril 2015 à 11h56, j'étais sur la « route » qui relie Gamgadhi et Sinja, 370 km au nord-ouest de Katmandou, avec Ram et Thakur Kandel. Une heure plus tard, nous apprenions que la terre « avait tremblé » dû à un « séisme au voisinage de Katmandou » (80 km nord-ouest de Katmandou), sans que nous en ressentions les conséquences. Le lendemain Thakur, chef du RSC, a réussi à communiquer avec le centre ce qui a précipité notre retour à Surkhet avant la fin de la mission. Nous y sommes arrivés deux jours et demi après le séisme. C'est seulement à ce moment que j'ai appris la vraie ampleur du séisme et de la crise sismique qui était en cours. Les jours qui ont suivi, il n'était pas question de rentrer à Katmandou, en plein cœur de la zone mésoséismale, je me suis donc rendue utile en produisant quelques cartes avec les données qui arrivaient du NSC à Katmandou au RSC à Surkhet.

A mon retour en France, j'ai participé à l'exploitation du catalogue postsismique dans le cadre de la collaboration entre le DASE et le DMG. Du fait de mon travail sur la crise sismique au nord de Katmandou en 1997 (section 2.3 de ce Chapitre 2), j'ai pu mettre à profit ma connaissance de la sismicité et du contexte sismotectonique local. J'ai aussi contribué aux travaux sur le séisme Mw7.8 2015 Gorkha au travers de la réalisation de cartes et figures pour les publications ci-après:

Bhattarai, M., Adhikari, L.B., Gautam, U.P., Laurendeau, A., Labonne, C., ***Hoste-Colomer, R.****, Sèbe, O., and Hernandez, B., 2015. Overview of Large 25 April 2015 Gorkha, Nepal, Earthquake from Accelerometric Perspectives, Seismological Research Letters, 86 (6), 1540-1548, doi: 10.1785/0220150140.*

Dans cet article, j'ai collaboré au travers de ma connaissance du contexte géologique et du terrain avec des collègues sismologues qui pour certains ne travaillaient pas initialement sur le contexte népalais. Cet article n'est pas présent dans ma thèse car je considère qu'il est éloigné de mon domaine d'expertise.

Adhikari, L.B., Gautam, U.P., Koirala, B.P., Bhattarai, M., Kandel, T., Gupta, R.M., Timsina, C., Maharjan, N., Maharjan, K., Dahal, T., ***Hoste-Colomer, R.****, Cano, Y., Dandine, M., Guilhem, A., Merrer, S., Roudil, P. and Bollinger, L., 2015. The aftershock sequence of the 2015 April 25 Gorkha-Nepal earthquake, Geophysical Journal International, 203, 2119-2124, doi: 10.1093/gji/ggv412.*

Dans cet article, j'ai collaboré à l'analyse spatio-temporelle de la sismicité. Une partie de mon travail, inclus dans la section 2.2 de ce Chapitre 2, a été joint à l'article. L'article complet est disponible dans l'Annexe A.

2.1. Introduction

Les variations spatiales et temporelles de sismicité le long du *Main Himalayan Thrust* (MHT) s'observent à différentes échelles –de temps et d'espace- au centre Népal. Elles sont révélées autant par l'étude des périodes cosismiques et postsimiques (du séisme de Gorkha) et celle de l'intersismique grâce au catalogue de sismicité du *National Seismological Centre* (NSC).

Dans ce Chapitre 2 nous présentons les découvertes récentes sur les variations spatiales et temporelles de sismicité le long du MHT au travers :

1) des études effectuées par différentes équipes, notamment sur la rupture cosismique (Section 2.2).

2) notre étude sur les répliques du séisme de Gorkha en étroite collaboration avec le *Department of Mines and Geology* (DMG) du Népal (Adhikari et al., 2015) (Section 2.2).

3) notre étude sur la sismicité intersismique focalisée sur la crise sismique de 1997 (Hoste-Colomer et al., 2017) (Section 2.3).

2.2. Le séisme de Gorkha

L'épicentre du fort séisme de 2015 était localisé au voisinage du village de Barpak, dans le district de Gorkha, à 80 km au nord-ouest de Kathmandu, la capitale du Népal (Figure 2.1). Le moment sismique dissipé de 7.2-7.7*10^{20} Nm correspond à une magnitude de moment de Mw=7.8 (Avouac, et al., 2015; Grandin et al., 2015). Les premières données géodésiques et satellitaires ont montré que la zone de rupture avait une longueur de 120-160 km et une largeur de 35-50 km (Galetzka, et al., 2015, Grandin et al., 2015, Kobayashi et al., 2015) avec un glissement maximal déterminé entre 4 et 7 m (Avouac et al., 2015, Grandin et al., 2015) (Figure 2.2). La solution du tenseur de moment obtenu par phase W (Duputel et al., 2016) ou Global Centroid Moment Tenseur propose un plan ~E-W avec un très faible pendage vers le nord. Cependant, leurs déterminations des profondeurs présenter des fortes variations (8 à 20 km de profondeur). L'étude conjointe des solutions CMT et fonction-récepteur de l'expérience Hi-Climb a montré que le séisme de Gorkha s'est produit à 12 km de profondeur sur un plan à 7° de pendage vers le nord (Figure 2.1.b)(Duputel et al., 2016). La rupture s'est initiée à l'ouest de la klippe de Kathmandu et s'est donc propagée en profondeur sur le Main Himalayan Thrust jusqu'à la terminaison nord-ouest de la surface de rupture supposée du grand séisme de 1934 (Sapkota et al., 2013, Bollinger et al., 2014) (Figure 2.1 and 2.2). Les mesures géodésiques et sismologiques ont rapidement fait suspecter que la rupture n'avait pas atteint la surface et qu'elle s'était arrêtée quelque part sous la vallée de Kathmandu (Figure 2.2).

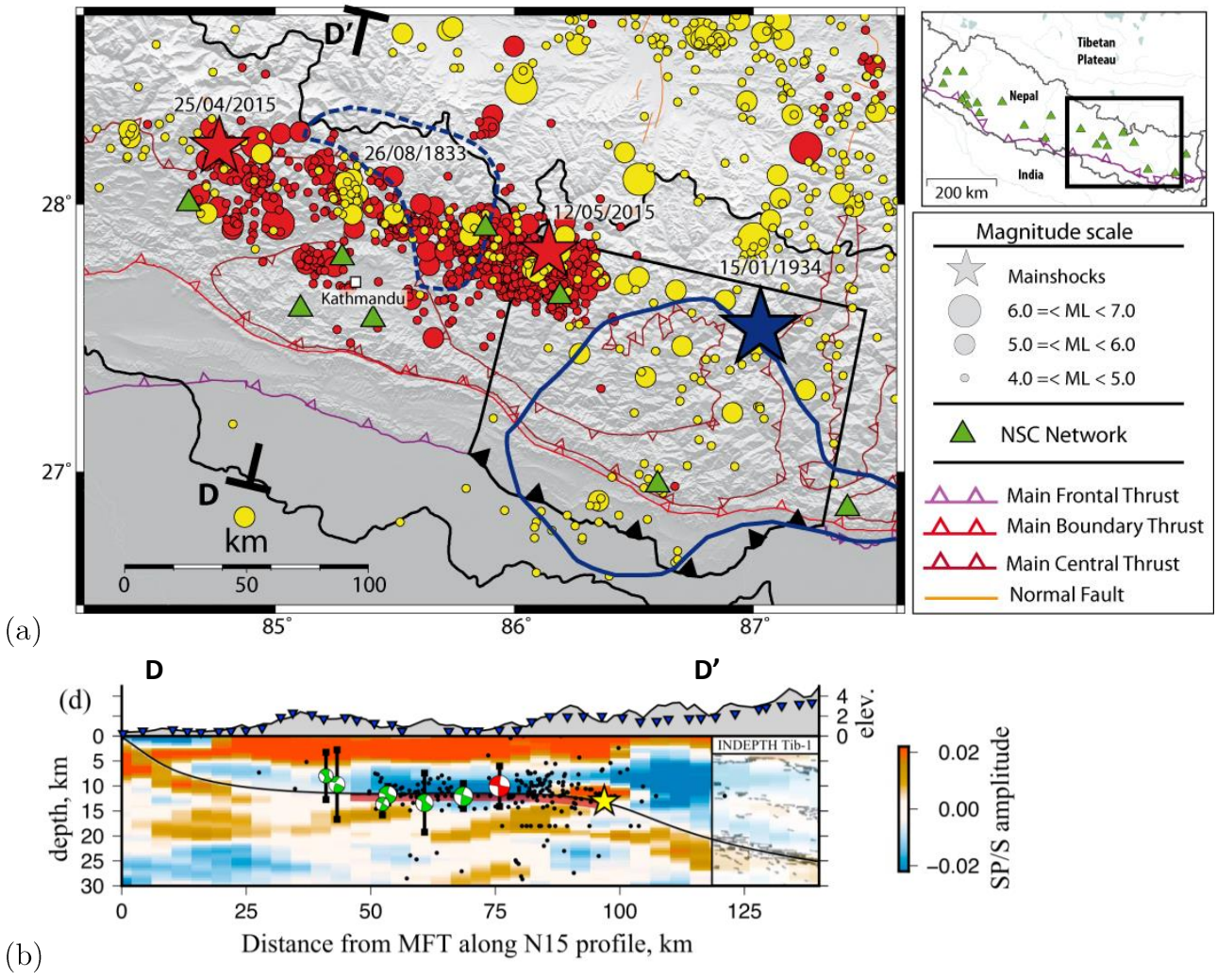

Figure 2.1. (a) Carte générale du centre et de l'est du Népal avec les principales répliques (cercles rouges) du séisme de Gorkha du 25 avril 2015. Répliques localisées par le NSC au cours des 45 jours qui ont suivi le choc principal. Les deux étoiles rouges correspondent au séisme de Gorkha à l'ouest et au séisme de Kodari (M7.3 du 12/05/2015) à l'est. Les cercles jaunes représentent la sismicité intersismique enregistrée depuis 1994 par le NSC. Les polygones bleus sont les isoséistes macrosismiques MSK64-VIII des forts séismes du 26/08/1833 (pointillé) et 15/01/1934 (continue) d'après Ambraseys and Douglas, 2004 et Sapkota, 2011. L'étoile bleue correspond à l'épicentre instrumental du séisme de 1934 (Chen et Molnar, 1977). Le rectangle noir est la surface de rupture présumée déduite des isoséistes macrosismiques et de la longueur minimale de la rupture de surface au niveau du MFT en 1934 (ligne noire avec triangles noirs) (Sapkota et al., 2013 ; Bollinger et al., 2014). Extrait de Adhikari et al., 2015. (b) Coupe fonction récepteur D-D' imageant le MHT à la longitude du profile Hi-CLIMB (Figure 1.4). En noir, la sismicité d'après Adhikari et al., 2015 de la carte Figure 2.1.a situé à ±40 km du profil avec les mécanismes focaux du séisme de Gorkha (rouge) et des répliques principales (vert). L'étoile est l'épicentre du séisme de Gorkha de l'USGS projeté sur le MHT proposé par les auteurs (ligne noire). Au nord, le profil INDEPTH Tib-1 (Hauck et al., 1998) (Figure 1.3). Extrait de Duputel et al., 2016.

(a)

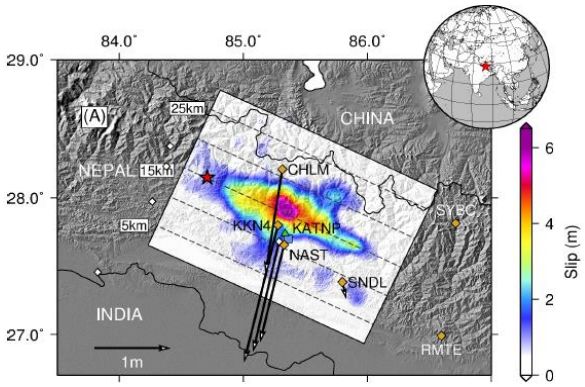

(b)

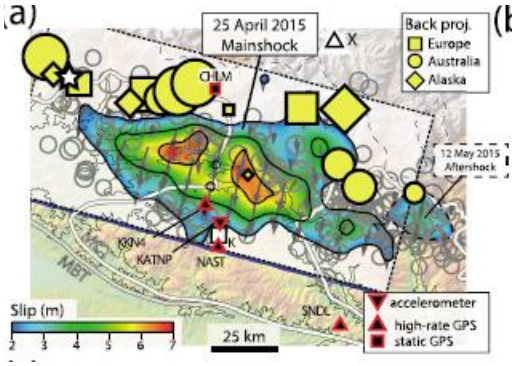

(c)

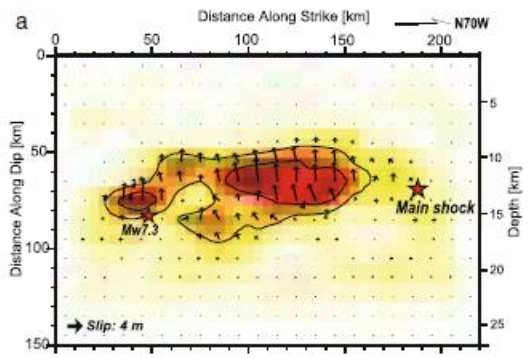

Figure 2.2. Glissement de la rupture du séisme de Gorkha (étoiles). (a) Inversion des données GPS du réseau permanent du Népal (losange orange) de Galetzka et al., 2015. (b) Inversion des données géodésiques et sismologiques avec des contours (ligne noire) de 2m de glissement de Grandin et al., 2015. (c) Inversion de déplacement InSAR avec des contours de 2m de glissement (lignes noires) de Kobayashi et al., 2015. Les flèches sont les vecteurs de glissement pour le compartiment supérieur par rapport au compartiment inférieur.

En regardant plus en détail, la rupture révèle des particularités en termes de propagation et de glissement. Les études de rétroprojection à des distances télésismiques utilisant des ondes P à haute-fréquence (Avouac et al., 2015 ; Fan et Shearer, 2015) montrent que la rupture s'est propagée unilatéralement vers l'est (Figure 2.3.a and 2.3.b). Le même type d'étude mais utilisant les ondes P à basses fréquences a mis en évidence une rupture par étapes : d'abord vers le nord, ensuite vers l'est et finalement vers le sud (Fan and Shearer, 2015) (Figure 2.3.c). Le glissement cosismique présente deux pics à 6-7 mètres résolus par l'étude conjointe de l'InSAR, du GPS et de l'inversion sismologique (Grandin et al.,2015 et Kobayashi et al., 2015) (Figure 2.2.b and 2.2.c). Ces variations observées au sein de la rupture ont conduit à proposer que des complexités structurales pouvaient être à l'origine de telles observations.

Les variations latérales de glissement cosismique sont susceptibles d'être soulignées par des variations latérales dans la distribution des répliques. Dans ce sens et par le sujet

de ma thèse, je me suis intéressée à l'exploitation du catalogue de répliques et le rapprochement entre ses variations latérales et leurs relations avec la structure en profondeur, et avec la sismicité intersismique (Hoste-Colomer et al., 2017 ; voir section *2.3. La sismicité intersismique au nord de Katmandou : variations latérales de structure et épisode transitoire*). La connaissance de la profondeur de la sismicité est donc un enjeu majeur, puisque les hypocentres doivent être confrontés aux structures. Tous les efforts menés pour mieux contraindre les profondeurs (e.g. Letort et al., 2016) sont donc importants. L'article de Letort et al., 2016 porte sur la détermination des profondeurs avec des phases détectées à des distances télésismiques et est amené à confronter par la suite les profondeurs issues de leur travail avec les localisations hypocentrales locales ; ceci est un des objectifs du déploiement du réseau sismologique Bhutanepal à l'ouest Népal.

(a)

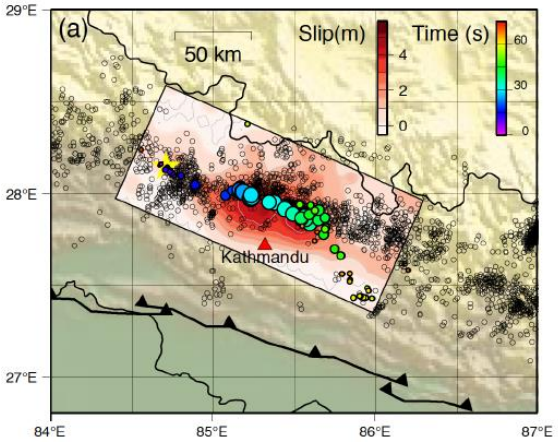

(b)

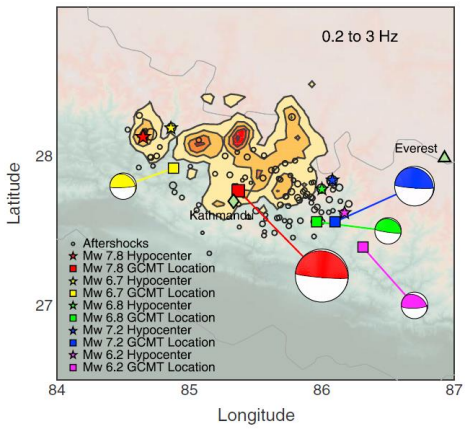

Figure 2.3. Cinématique de la rupture issue de techniques de rétroprojection des ondes P à des distances télésismiques : (a) Ondes haute fréquence (0.5 - 2.0 Hz) (Avouac et al., 2015) ; (b) Ondes haute fréquence (0.2 - 3.0 Hz) (Fan and Shearer, 2015) ; (c) Ondes basse fréquence (0.05 – 0.2 Hz) (Fan and Shearer, 2015).

(c)

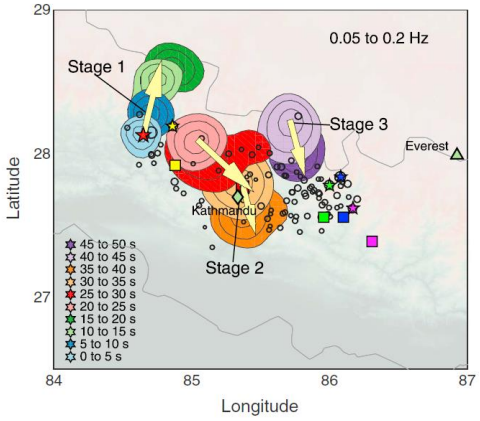

2.2.1. La sismicité post-Gorkha 2015

Le séisme de Gorkha a été suivi par plusieurs milliers de répliques localisées le long de la rupture dans les mois qui ont suivi le choc principal. Pour la première fois au Népal, les répliques d'un fort séisme himalayen généré par la rupture partielle du MHT ont été enregistrées et en plus par un réseau séismologique local, le réseau séismologique national du Népal.

L'étude de cette crise sismique de Gorkha permet d'ores et déjà de mieux connaître les grands séismes himalayens et leurs répliques au travers de la connaissance des relations entre les segments de failles qui ont rompu et les répliques, de l'évolution spatio-temporelle des répliques, et du bilan de moment sismique (Jouanne et al., 2011 ; Gualandi et al., 2016). Une des premières inconnues suite au séisme principal qui n'avait pas rompu jusqu'à la surface, était de savoir où pouvaient se situer les répliques. Leur étude était très attendue par les autorités népalaises d'une part et par la communauté scientifique de l'autre particulièrement parce que le séisme de Gorkha n'était pas le *Big One* attendu sur la région. En effet, plusieurs segments de faille en périphérie de la rupture n'ont pas rompu depuis des centaines d'années et pourraient être, de ce fait, des régions propices au développement de séismes futurs. L'étude de la distribution des hypocentres pourrait éventuellement donner des indices sur une activité sismique préférentielle sur des zones plus sollicitées suite au choc principal. Pour exemple, l'ouest ou la partie frontale de la rupture pourraient être affectés par un transfert de contraintes statiques, des régions où la sismicité se doit d'être particulièrement étudiée. Une autre question importante (et récurrente de la part des népalais) est relative à l'estimation de la durée de la crise sismique (Adhikari et al., 2015).

Ces questions se sont révélées d'autant plus pertinentes que le 12 Mai 2015, un séisme de Mw=7.3 est survenu à proximité de Kodari, à l'est de la rupture de Gorkha (Figure 2.1 et 2.5). Ce séisme a été suivi lui aussi par un nombre très important de répliques. Il a été suivi de tout un ensemble de questions: cet évènement est-il un séisme déclenché au sein d'une séquence de forts séismes ou une simple « réplique » ? Où se situe le segment à la rupture par rapport à la rupture de Gorkha ? Ce séisme et ses répliques révèlent t'ils des complexités géologiques / structurales ?

2.2.1.1. Réseau sismologique national du Népal

Dans le cas de la crise sismique de Gorkha, seules les stations du NSC ont servi à la localisation des évènements. Par contre, parce que les signaux aux stations proches étaient saturés lors des plus fortes répliques (ML >5), beaucoup de magnitudes ont été obtenues avec les stations en bordure du réseau NSC, ou les stations du réseau RSC.

2.2.1.2. Catalogue du séisme de Gorkha du 25 avril 2015 au 8 juin 2015

Le catalogue produit par le NSC, présenté ci-dessous et détaillé dans Adhikari et al., 2015, est le catalogue de sismicité qui nous a permis par la suite d'analyser la distribution de la sismicité et particulièrement ses variations spatio-temporelles.

En tout, 4401 évènements comprenant 55778 phases pointées manuellement (P et S) ont été localisés les 45 premiers jours de la crise sismique dont 1802 évènements de M_L supérieure à 3.0.

Les localisations épicentrales sont bien contraintes pour les séismes de $M_L \geq 3.0$. Ils ont été localisés avec un nombre important de phases (15-20 phases/séisme), des distances courtes entre l'évènement et les stations (≤30 km pour 75% des séismes) et une relativement bonne couverture azimutale. Cependant les séismes localisés à l'est de la crise, notamment les répliques du séisme de Kodari Mw=7.3, présentent une mauvaise couverture azimutale qui influence la résolution de la localisation. Cette mauvaise couverture fait suite à la défection temporaire d'un relais de transmissions des 3 stations situées plus à l'extrême est du réseau.

Malgré la bonne résolution des épicentres, les profondeurs obtenues dans un premier temps sont des profondeurs par défaut du logiciel de d'acquisition et localisation Jade-Onyx (2/10/25/30/40/50 km) (Figure 2.4.a). Dans le but d'avoir une estimation des profondeurs plus fine, les évènements ont été relocalisés avec ISClocator (voir Adhikari et al., 2015 pour plus de détails) (Figure 2.4.b). Les résultats de cette relocalisation absolue amène à penser que les répliques étaient localisées principalement dans le compartiment supérieur de la faille.

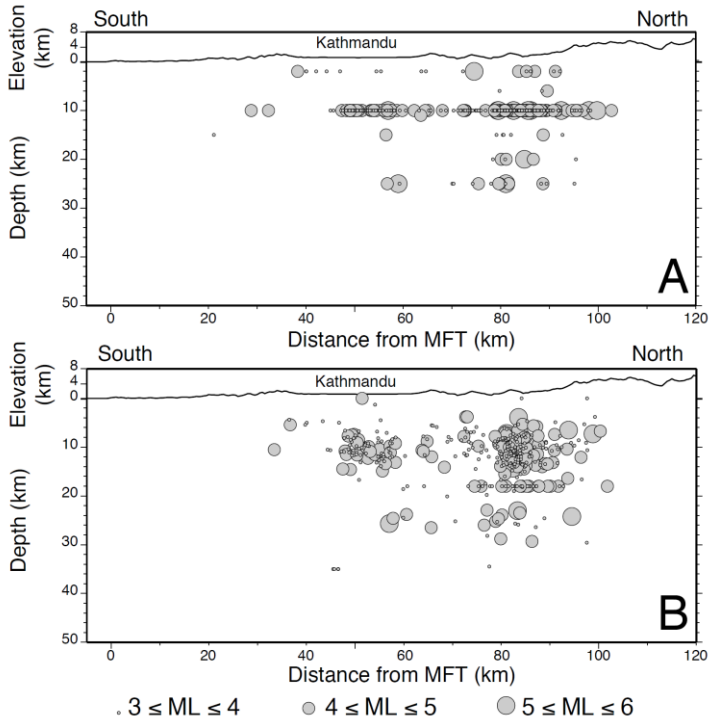

Figure 2.4. Coupe A-A' de la Figure 2.5.(a) Localisation NSC and (b) Relocalisation ISClocator. Extrait d'Adhikari et al., 2015.

2.2.1.3. Distribution spatio-temporel de la sismicité post-Gorkha

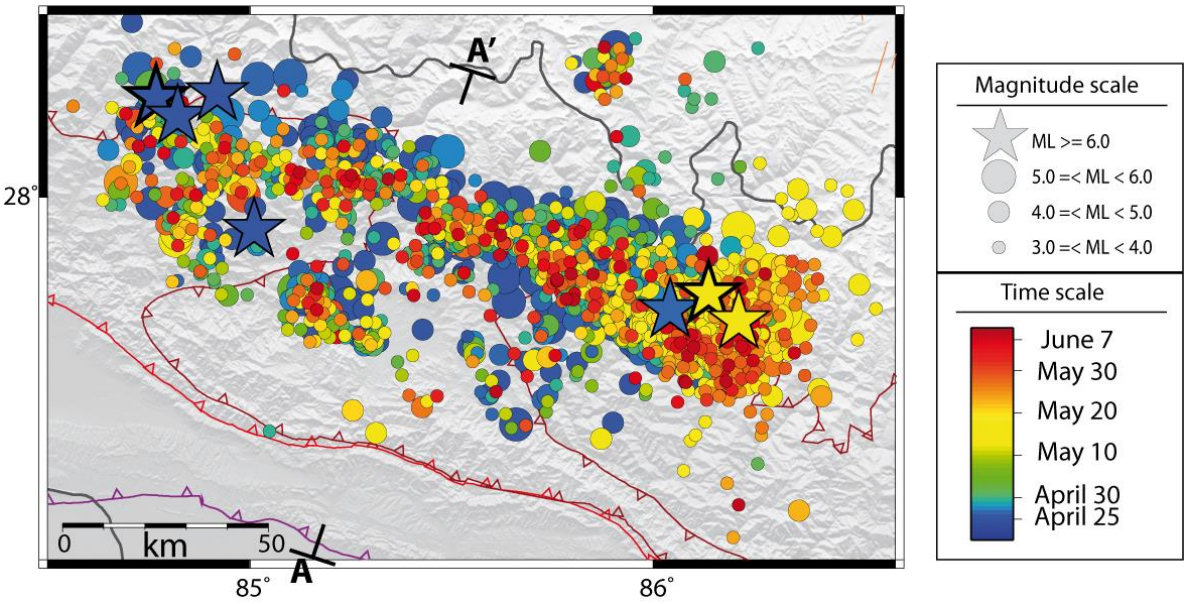

Figure 2.5. Carte de sismicité localisée par le NSC en fonction du temps d'occurrence des premiers 45 jours après le séisme de Gorkha (étoile bleue contour gras). L'étoile jaune à contour gras correspond au séisme de Kodari du 12 mai 2015. Les lignes endentées violette, rouge et grenat correspondent respectivement au MFT, MBT et MCT.

Les répliques du séisme de Gorkha se sont manifestées rapidement après le choc principal (Figure 2.5). Elles se sont concentrées depuis la région épicentrale jusqu'à 120 km à l'est et sur environ 40 de km de large (Figure 2.5), correspondant à la zone rompue. Les répliques les plus importantes ont eu lieu les premiers deux jours et se sont localisées aux extrémités de la rupture. Le nombre de répliques a diminué normalement les 17 jours suivants, moment où le séisme de Kodari Mw=7.3 a eu lieu. Ce séisme a été suivi par un nombre très important de répliques sur une zone de 60 km autour de l'épicentre (Figure 2.5).

La plupart des répliques ont été localisées au voisinage des hypocentres de la sismicité intersismique, au sud de la haute topographie (Figure 2.1). En revanche, plusieurs essaims de répliques ont aussi été localisés beaucoup plus au sud, à proximité de l'extension Sud de la rupture du séisme de Gorkha; en particulier autour de la vallée de Kathmandu (Figure 2.5). Enfin, une forte concentration des répliques a été localisée au niveau de la bordure est de la rupture.

La sismicité au voisinage de la vallée de Kathmandu a attiré particulièrement notre attention (1) parce qu'elle était proche de la capitale et donc très ressentie, (2) parce qu'elle se développe dans une région, loin de l'extension profonde de la zone bloquée,

qui ne présente pas de sismicité intersismique (Figure 2.1), (3) parce qu'une partie de cette sismicité se situe au niveau de l'extension sud de la rupture. Nous avons distingué dans cette région deux essaims de sismicité, un au nord de la vallée de Kathmandu et un au niveau de la bordure sud de la rupture à des profondeurs de 8-14 km. La forte concentration des hypocentres dans cette région nous amène à penser que des structures secondaires ont été sollicitées. En effet, ces essaims se trouvaient à proximité des failles de Kalphu et Chobar où Sakai et al., 2006 et Saijo et al., 1995 respectivement y avaient trouvé des indices d'activité quaternaire. Il est difficile de confirmer la relation entre ces failles actives et l'activité sismique aux alentours sur la seule base du catalogue de sismicité actuel, cependant il est tentant de proposer que ces failles puissent être activées suite à des forts séismes sur le MHT. De même, elles pourraient être activées pendant la période intersismique et montrer des variations spatiales de la sismicité. Ce scénario est une des hypothèses pour la distribution spatiale de la sismicité à l'ouest du Népal que nous allons revoir au Chapitre 4.

Concernant les répliques à la hauteur de la sismicité intersismique, l'étude de Baillard et al., 2017 a montré une zone avec une absence de sismicité à la longitude 85.4° (Figure 2.6.b), à laquelle nous avons dédié une étude (Hoste-Colomer et al., 2017, voir section *2.3. La sismicité intersismique au nord de Katmandou : variations latérales de structure et épisode transitoire*).

Dans notre étude nous avons observé une sismicité distribuée depuis des profondeurs micrustales (typiquement 14 km) jusqu'à la surface. Toutefois, la sismicité autour de la rupture de Gorkha s'est révélée plus superficielle que celle autour du séisme de Kodari (Figure 2.6.a). Cet approfondissement de la sismicité à l'est a aussi été observé suite à l'étude de signaux enregistrés à des distances télésismiques (Letort et al., 2016) (Figure 2.6.c) et confirmé par l'étude de Baillard et al., 2017 (Figure 2.6.b). De plus, le séisme de Kodari a été précédé par une forte activité à la bordure est de la rupture du Gorkha et une absence de sismicité sur la zone rompue. Tous ces indices semblent indiquer un transfert de contraintes très important à l'est de la rupture de Gorkha qui aurait déclenché le séisme de Kodari.

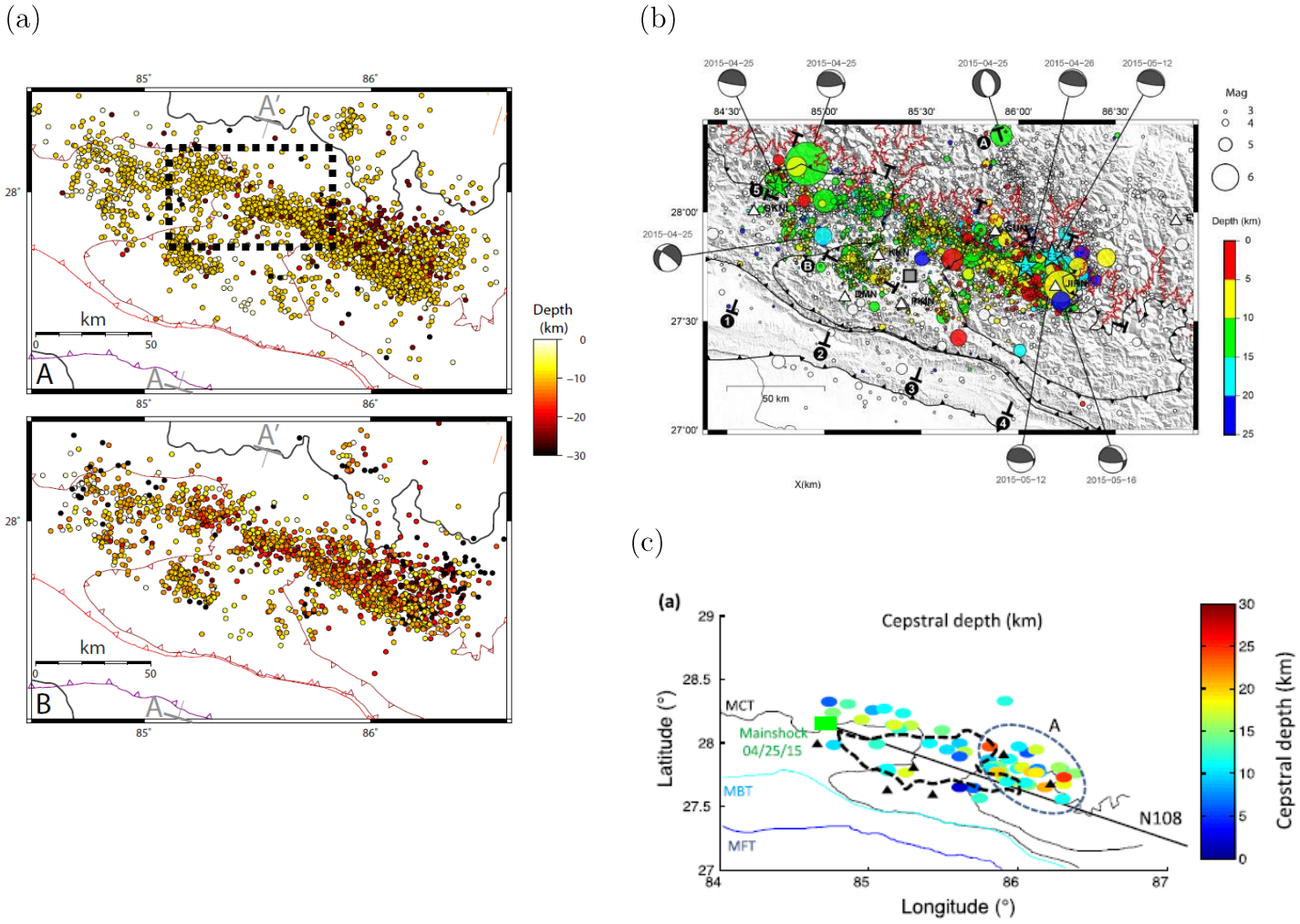

Figure 2.6. Estimation des profondeurs des répliques des séismes de Gorkha et Kodari à l'aide de différentes méthodes. (a) a. localisation NSC et b. relocalisation ISClocator (Bondar and Storchak, 2011) avec des données des stations du NSC (extrait de Adhikari et al., 2015)(rectangle noir est la zone d'étude de Hoste-Colomer et al., 2017), (b) logiciel Seiscomp3 (Weber et al., 2007) suivi par un filtre Kurtosis (Baillard et al., 2014) avec des données des stations du NSC (extrait de Baillard et al., 2017) et (c) technique d'analyse cepstrale de Letort et al., 2015 avec des données des stations CTBTO à distances télésismiques (extrait de Letort et al., 2016).

2.2.2. Structure *versus* rupture

Les études conduites suite au séisme de Gorkha Mw=7.8 ont permis d'avancer sur la connaissance de la géométrie profonde du MHT et de son influence (1) sur le contrôle des ruptures cosismiques et (2) sur la répartition des répliques.

En effet, l'étude de la rupture cosismique dans son ensemble, son initiation, son évolution et son arrêt ainsi que la crise sismique qui a suivi ont amené à considérer que la rupture avait été contrôlée structuralement (Hubbard et al., 2016, Hoste-Colomer et al., 2017).

Jusqu'au séisme de Gorkha, la klippe de Katmandou n'était pas considérée comme ayant un rôle actif dans la modulation des forts tremblements terre sinon comme une relique isolée des roches du Haut Himalaya (roches très fortement métamorphiques) dûe à la croissance des duplex de moyen pays en profondeur au niveau de la rampe et qui ont été charriés vers l'avant avec l'évolution de l'orogène. La morphologie de la klippe aurait contraint la surface de la rupture du séisme de Gorkha (Hubbard et al., 2016).

La rupture s'est initiée à l'ouest de la klippe de Katmandou et s'est propagée jusqu'à l'extrémité ouest de la surface de rupture supposée du grand séisme de 1934 (Sapkota et al., 2013 ; Bollinger et al., 2014). La géométrie de premier ordre au travers de la coupe de Katmandou est une géométrie en plat-rampe-plat (i.e. Jackson and Bilham, 1994 ; Cattin and Avouac, 2000) cohérente avec la géométrie du moyen pays (présence d'un anticlinorium et d'un empilement d'écailles au sein d'un duplex de moyen pays au droit de la rampe). A cette géométrie de premier ordre, s'ajoute la présence d'une seconde rampe plus au sud. Cette rampe décrite par Khanal et Robinson, 2013 au sud-ouest de la klippe de Katmandou serait aussi présente plus à l'est, au voisinage de la vallée de Katmandou (Hubbard et al., 2016) (Figure 2.7). Ces auteurs proposent en effet, sur la base d'une nouvelle coupe équilibrée qu'une rampe intermédiaire se développe au nord du Mahabarat (Figure 2.7). Hubbard et al., 2016 proposent que la rupture du séisme soit venue buter au pied de cette rampe, empêchant sa propagation vers l'avant sous le Mahabarat. D'autre part, l'extension latérale de la rupture aurait été contrôlée par la présence d'un segment de faille plate, présentant une géométrie « pincée » terminée par des « pinch points » où les deux rampes de la klippe fusionnent en une seule rampe (Hubbard et al., 2016) (Figure 2.8). La structure en double rampe le long d'une région d'extension latérale limitée serait responsable du confinement de la rupture et de son contrôle structural (Hubbard et al., 2016).

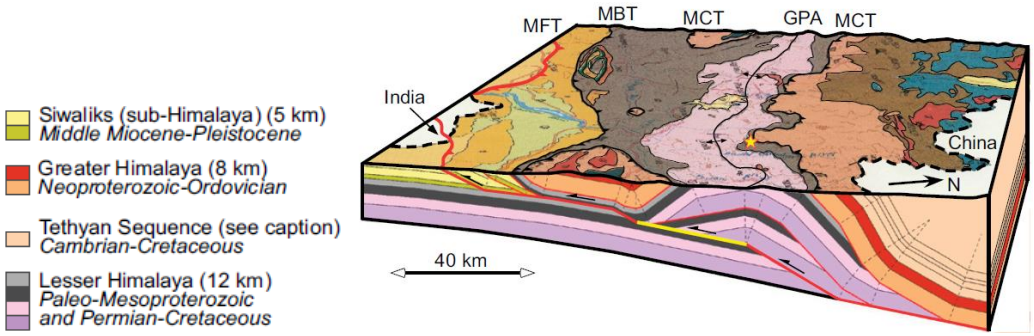

Figure 2.7. Modèle 3D de l'Himalaya du centre Népal de Hubbard et al., 2016 à partir de la carte géologique du *Department of Mines and Geology of Nepal*. L'étoile jaune et la ligne jaune montrent l'épicentre et la largeur de la rupture du séisme de Gorkha, respectivement. GPA est l'anticlinorium de Gorkha-Pokhara.

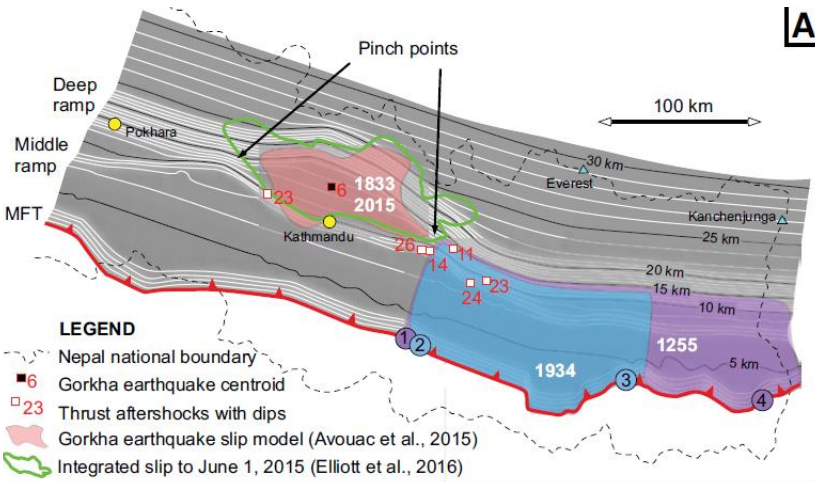

Figure 2.8. Carte du MHT au centre et est Népal de Hubbard et al., 2016. Les contours représentent la profondeur du décollement. Les surfaces colorées représentent la possible extension des séismes passés avec les sites où ils ont été étudiés.

Grâce à l'inversion des données géodésiques, Qiu et al., 2016 ont pu reproduire la rupture et montrer que les deux rampes jouent un rôle de barrière. De plus, il est fortement possible que le séisme de 1833 ait rompu le même segment. Ils proposent donc de considérer cette zone rompue comme une aspérité permanente (Qiu et al., 2016, Hubbard et al., 2016) (Figure 2.9).

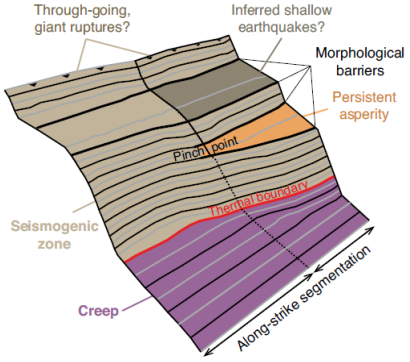

Figure 2.9. Modèle de la segmentation et comportement de la rupture du séisme de Gorkha prenant en compte le contexte et les barrières morphologiques de Qiu et al., 2016.

De son côté, le séisme de Kodari dont la rupture est estimée à de plus fortes profondeurs que le séisme de Gorkha (18 contre 15 km à l'hypocentre) aurait activé un segment plus profond du MHT (Baillard et al. 2017) (Figure 2.10).

La localisation d'une partie des répliques au droit de la rupture, dans le compartiment chevauchant du MHT, a mis en évidence que des structures secondaires pouvaient être réactivées à la suite de la rupture principale. Cela semble particulièrement vrai au voisinage de la rupture du séisme de Kodari qui a été suivi par beaucoup de répliques localisées dans toute la zone couverte par les écailles du duplex de moyen pays en champ proche de l'extension sud de la rupture (i.e. cela semble particulièrement vrai au droit du pied de rampe micrustale) (Baillard et al., 2017) (Figure 2.10).

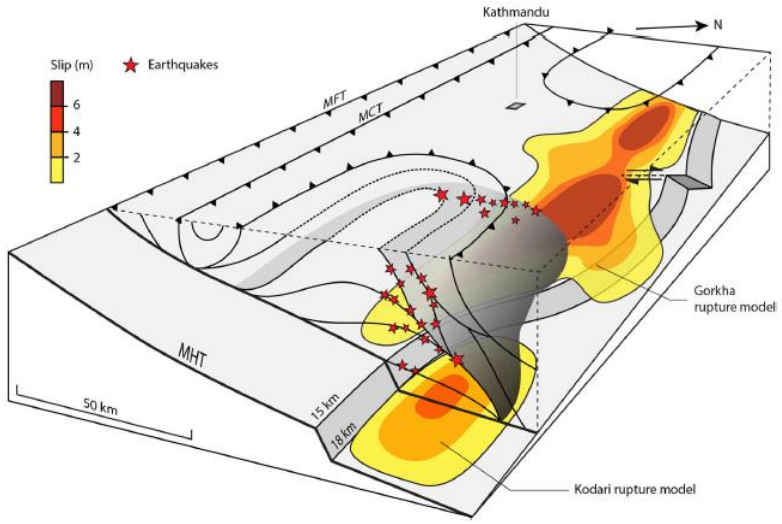

Figure 2.10. Interprétation sismotectonique de la rupture des séismes de Gorkha et Kodari et ses répliques de Baillard et al., 2017.

2.3. La sismicité intersismique au nord de Katmandou : variations latérales de structure et épisode transitoire

Ce paragraphe présente un résumé en Français des travaux présentés dans l'article Hoste-Colomer et al., 2017 qui suit.

Comme nous venons de le voir, l'extension de la rupture du séisme de Gorkha suggère l'existence d'un contrôle structural. La segmentation du MHT qui en est déduite peut être confrontée d'une part (1) à l'organisation spatio-temporelle des répliques mais aussi (2) à celle des hypocentres des essaims de sismicité de la période intersismique qui précède le séisme. Cette sismicité pourrait refléter en effet les variations latérales de géométrie du MHT et la segmentation.

Cette section présente une étude dans laquelle j'ai travaillé sur la relocalisation de la sismicité micrustale au voisinage de l'extension profonde de la zone bloquée. Cette étude m'a amenée à analyser les variations spatio-temporelles de la sismicité depuis 1994 dans la trace du séisme de Gorkha, et plus particulièrement au nord de Katmandou dans une région qui présente (1) des variations latérales de glissement (entre les 2 pics de glissement cosismique du séisme) et (2) des variations latérales des répliques.

Les résultats de mon travail ont été publiés en 2016 dans le numéro spécial « Gorkha earthquake » de Tectonophysics (*Hoste-Colomer et al., 2017. Lateral structure variations and transient swarm revealed by seismicity along the Main Himalayan Thrust north of Kathmandu, Tectonophysics, http://dx.doi.org/10.1016/j.tecto.2016.10.004*) et son brièvement décrits ci-après (et présent sous forme d'article complet dans ce chapitre):

Au nord de Katmandou, la sismicité intersismique (antérieur à 2015) se situe à des profondeurs micrustales au sein d'une ceinture de sismicité permanente. L'activité permanente est accompagnée de temps en temps par des essaims transitoires dont le plus important a eu lieu en 1997 (article Figure.2). Cet essaim de 1997 a été localisé aux alentours de la longitude 85.4° (comme les variations détectés lors du séisme de Gorkha) au voisinage du village de Sarshin, épicentre du séisme principal de la séquence. Ce séisme de magnitude M_{L_NSC}=5.8 présente un mécanisme au foyer en chevauchement oblique. Ce séisme dit de « Sarshin » a été suivi par plus de 160 séismes localisés par le NSC. La géométrie de l'essaim est peu précise avec la localisation NSC, c'est pour cette raison que nous effectuons une relocalisation relative à l'aide de la méthode de relocalisation double différence d'HypoDD.

Les résultats de la relocalisation montrent la présence de 2 essaims de sismicité distincts à des profondeurs micrustales lors de l'épisode de 1997 (article Figure 4). Au nord-ouest, un cluster orienté ~N050 avec un pendage de 70-80° vers le sud-est qui inclut le séisme de Sarshin (article Figure 4). Le mécanisme au foyer de ce séisme de

M_{L_NSC}=5.8, en chevauchement oblique, présente un plan nodal raide similaire au plan défini par la sismicité. Au sud-est, un essaim plus petit et plus superficiel. La sismicité entre ces deux essaims dessine un plan sub-vertical d'orientation ~N155 (article Figure 4).

Nous interprétons le premier essaim comme étant le résultat de l'activation d'un rétro-chevauchement NE-SW avec un pendage très raide vers le sud-est. Le reste de la sismicité relocalisée présente une géométrie en baïonnette : alignement de sismicité NW-SE sur une vingtaine de kilomètres puis, un nouvel essaim diffus de sismicité au sud-est. Cette géométrie, la position des essaims par rapport aux cartes locales de couplage sismique, l'activation du rétro-chevauchement oblique au NW suggèrent la présence d'une faille de transfert (*tear fault*) séparant 2 segments de rampe micrustale en échelon. Ces structures, d'extension plurikilométrique ont probablement influencé la propagation de la rupture cosismique : cette région est localisée entre les 2 pics de glissements du séisme de Gorkha, et présente une géométrie de l'essaim de répliques similaires (décalage d'~ 20 km vers le sud-est des répliques).

La structure temporelle se révèle être particulièrement intéressante: la sismicité dans la région présente une période de quiescence prolongée de quelques mois –mousson 1996 jusqu'en décembre 1996 (article Figure 5). L'activité sismique s'initie ensuite au niveau de la faille de transfert avant de se développer au nord-ouest, au voisinage du choc principal de Sarshin (article Figure 5). Une activité sismique est donc bien présente avant le choc principal. L'activité se poursuit avec les répliques du séisme de Sarshin. Dans le même temps, l'activité sismique augmente à l'est de la faille de transfert, sur ce que nous interprétons comme le segment est de la rampe micrustale (article Figure 5).

Ce développement particulier d'essaim micrustal de sismicité au voisinage de l'extension profonde de la zone bloquée n'est pas unique : au cours des années 1996-1997 deux autres essaims de sismicité de structure temporelle similaire, ont été localisés au Népal, simultanément à l'essaim de Sarshin (article Figure 6). Ces essaims étaient situés un à l'est du Népal et l'autre à l'extrémité ouest du Népal (article Figure 6). Malheureusement, la localisation des évènements n'est pas assez bien résolue pour effectuer le même exercice de relocalisation relative que dans la zone de Sarshin.

Le contexte tectonique de la zone de Sarshin nous amène à proposer que la sismicité de 1997 soit la conséquence de (1) un chargement irrégulier local ou (2) un transfert local de contraintes au voisinage de la transition bloquée – fluage du MHT. La coexistence de deux autres essaims très distants nous amène à proposer (3) un glissement transitoire à grande échelle le long du MHT.

L'évènement transitoire de 1997 pourrait être lié à un épisode de glissement lent sur le MHT du Népal. Bien que nous manquions de preuves directes (absence d'augmentation de la sismicité entre les 3 essaims, absence de trémors non volcaniques, absence de mesures GPS continues denses), le catalogue de sismicité apporte des indices indirects

tels que la production simultanée de sismicité le long du MHT (trois essaims distants aux structures temporelles atypiques – augmentation de la sismicité pre-mainshock simultanée puis séquence en choc principal et répliques). La sismicité micrustale est sensible à l'état de contraintes locales qui dépend de la contrainte tectonique et de la topographie et contrôlent l'orientation des plans préférentiels à la rupture. En effet, du sud au nord, on passe d'un régime inverse à un régime normal au niveau des Grabens Tibétains. Entre les deux domaines, l'état de contraintes régional devrait favoriser l'existence de failles décrochantes, or, c'est la cinématique de la faille de transfert activée avant le séisme de Sarshin qui casse un rétrochevauchement à la géométrie et à la cinématique cohérente avec le coulissage dextre attendu sur la faille de transfert. L'activité sismique sur cette faille de transfert crée une variation de contraintes statiques aux extrémités, déclenchant la sismicité au niveau du chevauchement et du rétro-chevauchement (article Figure 7).

Note: (1) les références ne sont pas écrites dans le Résumé. (2) le *Supplementary data* de l'article est dans l'Annexe B.

Tectonophysics 714–715 (2017) 107–116

Contents lists available at ScienceDirect

Tectonophysics

journal homepage: www.elsevier.com/locate/tecto

Lateral structure variations and transient swarm revealed by seismicity along the Main Himalayan Thrust north of Kathmandu

R. Hoste-Colomer [a,b,*], L. Bollinger [a], H. Lyon-Caen [b], A. Burtin [c], L.B. Adhikari [d]

[a] CEA, DAM, DIF, F-91297 Arpajon, France
[b] Laboratoire de Géologie, Ecole Normale Supérieure/CNRS UMR 8538, PSL Research University, Paris 75005, France
[c] Institut de Physique du Globe de Paris, Sorbonne Paris Cité, Université Paris Diderot, UMR 7154 CNRS, Paris, France
[d] Department of Mines and Geology, National Seismological Center, Kathmandu, Nepal

ARTICLE INFO

Article history:
Received 16 February 2016
Received in revised form 21 September 2016
Accepted 4 October 2016
Available online 5 October 2016

Keywords:
Seismicity
Main Himalayan Thrust
Fault segmentation
Relative relocation

ABSTRACT

The midcrustal seismicity along the Main Himalayan Thrust in Nepal presents lateral variations along the rupture of the 2015 Gorkha earthquake. In order to resolve these variations, we relocate the seismicity north of Kathmandu, during a period well covered by the Nepal National Seismological Network, using a double-difference algorithm. The 550 relocated events highlight a complex pattern of clustered seismicity within the unstable-stable transition zone. Part of the seismicity is densely clustered on a southward dipping plane which ruptured on January 31st 1997 (ML = 5.8), activating a backthrust with a geometry consistent with the centroid moment tensor of this event calculated in this study. At its eastern end, the midcrustal cluster is offset by 20 km to the south suggesting the presence of a tear fault. The analysis of the time sequence allows constraining a scenario involving stress transfer between these local midcrustal structures, beginning more than one month before the 1997 main shock. The temporal evolution of the seismicity is strikingly similar for two other transient seismic swarm episodes which developed hundreds of kilometers apart along the Main Himalayan Thrust at the same time. The local stress field appears responsible for the higher sensitivity of these regions to subtle strain transients developing along the Main Himalayan Thrust.

© 2016 Elsevier B.V. All rights reserved.

1. Introduction

Along-strike variations of seismic activity on a fault can result from lateral variations in the geometry of the locked fault zone, spatial heterogeneity in frictional parameters or from unsteady loading during the interseismic period. Variations in seismicity rates along the downdip end of a locked megathrust may reveal that the structure is segmented, and these segment boundaries may correspond to the barriers that delimit major seismic ruptures (e.g. Schwartz et al., 1989; Collot et al., 2004; Métois et al., 2012; Holtkamp et al., 2011; Holtkamp and Brudzinski, 2011). The Main Himalayan Thrust (MHT) fault in Nepal qualifies as one interesting fault to document in terms of seismicity variations given its seismogenic potential and the possible control of the coseismic ruptures by persistent structural features (e.g. Grandin et al., 2015; Hubbard et al., 2016). Indeed, despite the apparent homogeneity of the stress build up revealed by geodesy (Ader et al., 2012; Stevens and Avouac, 2015) significant variations of the seismic rate have been reported along strike (Pandey et al., 1999). Some of the variations in seismic rate are persistent in time and might reveal lateral heterogeneity in terms of seismic coupling and/or tectonic structures along strike of the MHT. Others are temporary, related to transient episodes including swarm activity or mainshock-aftershock sequences.

On April 25 2015 at 11 h56 Nepal Standard Time (06 h11 UTC), the Mw 7.8 Gorkha earthquake ruptured a 120 km-long and 35–50 km wide fault segment of the MHT (e.g., Avouac et al., 2015; Grandin et al., 2015; Kobayashi et al., 2015; Elliott et al., 2016) (Fig. 1), abutting the great M8.2 1934 earthquake rupture. The propagation of the rupture and the slip along the fault plane were heterogeneous, leading some authors to suggest possible along strike variations of the structure at depth (Grandin et al., 2015, Fan and Shearer, 2015).

The aftershocks near the trace of the rupture in the vicinity of Kathmandu are heterogeneously distributed (Adhikari et al., 2015; Bai et al., 2015). Some aftershocks are clustered under Kathmandu valley, a place where no seismicity has been observed during the interseismic period (Fig. 1). In the meantime, north of the Nepalese capital, the aftershocks epicenters coincide with the location of the midcrustal interseismic cluster (10–20 km depth) (Fig. 1). The heterogeneous distribution of the Gorkha earthquake aftershocks and the seismicity during interseismic period north of Kathmandu could be due to structural complexities or a transient event. The goal of our study is to use small earthquakes prior to the 2015 Gorkha event to resolve structural and frictional characteristics that might control the rupture parameters of the main shock.

* Corresponding author at: CEA, DAM, DIF, F-91297 Arpajon, France.
E-mail address: roser.hoste-colomer@cea.fr (R. Hoste-Colomer).

http://dx.doi.org/10.1016/j.tecto.2016.10.004
0040-1951/© 2016 Elsevier B.V. All rights reserved.

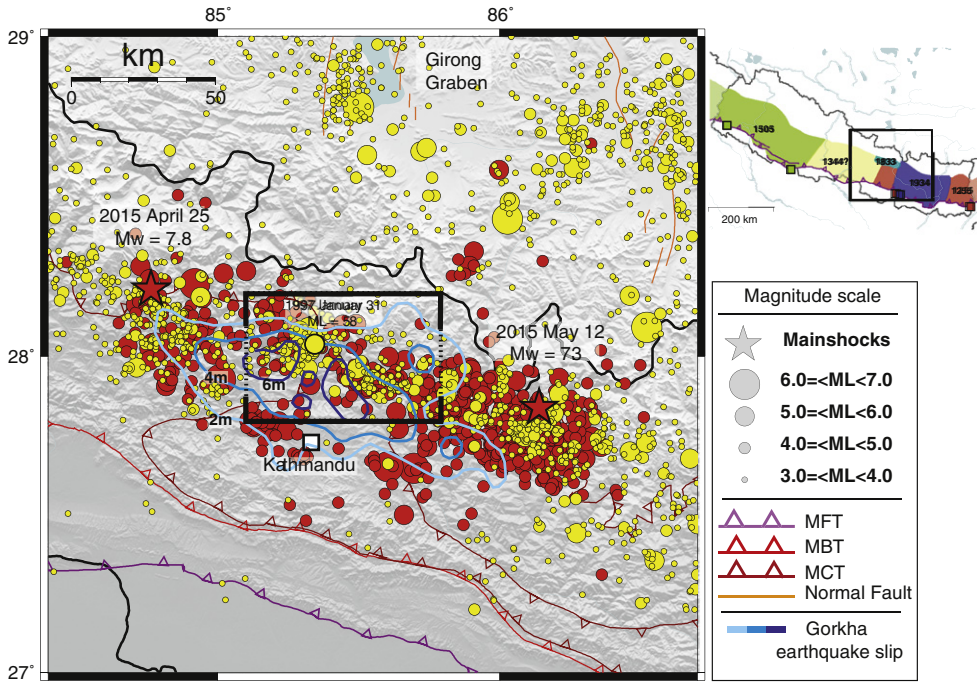

Fig. 1. Seismicity map of Central Nepal from the National Seismological Center of Nepal (Modified from Adhikari et al., 2015). Red dots are the aftershocks of the Gorkha earthquake and the yellow dots indicate epicenters prior to the Gorkha event since 1994. The iso-slip contours of the Gorka earthquake are from Grandin et al., 2015. The black rectangle indicates the area used for Figs. 2 and 4. Past earthquakes rupture areas (top right) from Bollinger et al., 2016. MFT: Main Frontal Thrust, MBT: Main Boundary Thrust, MCT: Main Central Thrust. The orange thin lines are the traces of the Southern Tibetan Grabens (Armijo et al., 1986).

In order to test such a hypothesis, we analyze the spatio-temporal variations of the seismicity during the interseismic period north of Kathmandu, a region well covered by the Nepalese national seismological network. We first relocate the seismic events using a double-difference algorithm (Waldhauser and Ellsworth, 2000) and perform a Centroid Moment Tensor inversion of the largest instrumentally recorded event in the region, ML = 5.8 on January 31st 1997. We then interpret the spatial pattern of seismicity in terms of geological structures at depth, and finally focus on the temporal variation of the seismicity rate along this structure.

2. Data description

2.1. Regional network

The seismicity of central and eastern Nepal has been continuously monitored since the 1990s by the National Seismological Center of Nepal (NSC) with a national network composed of 21 short period vertical component seismic stations (Fig. S1). Among them 12 high gain stations have been operational since 1994 in central and eastern Nepal providing a completeness of the seismic catalogue for that region around local magnitude ML = 2.0 (Pandey et al., 1999). Their records are processed using Jade-Onyx acquisition-treatment software in which a 1D velocity model is used to locate earthquakes using the phases picked manually at NSC (Pandey, 1985; Pandey et al., 1995, Adhikari et al., 2015). A complementary network of 3 stations was deployed temporarily, from July 1995 to December 1996. The addition of these stations facilitated improved locations for the small earthquakes generated at midcrustal depths below the front of the high topography (Cattin and Avouac, 2000) in the vicinity of the Main Himalayan shear zone (Nábelek et al., 2009).

2.2. Earthquake catalogue

North of Kathmandu, the interseismic activity appears concentrated at midcrustal depths within a permanent seismic cluster (Pandey et al., 1995; Cattin and Avouac, 2000) (Fig. 1) modulated by a few transient seismicity bursts (Fig. 2). The most important seismicity burst was recorded in 1997. Indeed, 30% of the ML ≥ 4.0 events of the catalogue in this region occurred in that year (Fig. 2). The sequence culminated after the occurrence of the "Sarshin earthquake" an ML = 5.8 event which happened on January 31st 1997 (Table 1), an event preceded 3 h before by a foreshock of ML 5.1. This event resulted in a maximum shaking intensity of MMI VII and was felt in Kathmandu 40 km SE from its epicenter. It caused significant impact (MMI VI) over a region 1800 km^2 in size (Sapkota, 2011). Given its magnitude, this event was also recorded at teleseismic distances by international institutions, which assigned a body-wave magnitude (mb) around 5.2 and depths between 17 and 23 km (Table 1).

The Sarshin earthquake was followed by >160 aftershocks in a region spanning 50 × 30 km^2, a surface significantly larger than the

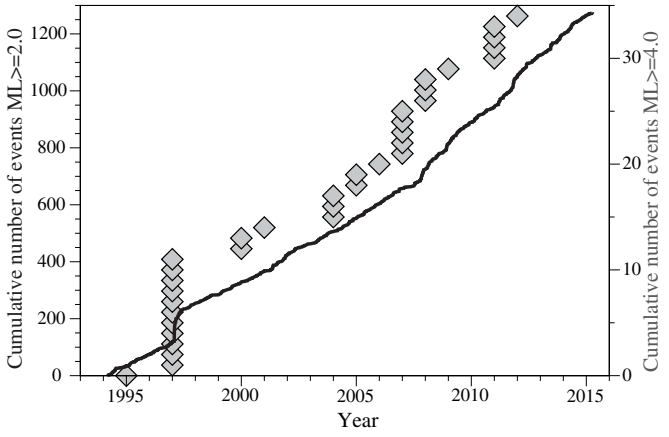

Fig. 2. Cumulative number of events during the interseismic period recorded by the NSC from 1994 to 2015 in the area delimited in Fig. 1. The black line corresponds to the events of magnitude ML ≥ 2.0 scaled on the left side. The gray diamonds correspond to the events of magnitude ML ≥ 4.0 scaled on the right side. 30% of the events of ML ≥ 4.0 occurred in 1997.

Table 1
Description of the main shocks of the three swarms of 1997. Origin time and epicentral location are from the NSC.

						Magnitude			Focal mechanism					
									NP1			NP2		
Main shocks of swarms	Date	Time	Longitude	Latitude	Depth (km)	ML (a)	mb (b)	Mw	Strike (°)	Dip (°)	Rake (°)	Strike (°)	Dip (°)	Rake (°)
Sarshin	31/01/1997	20:02:14	85.34°E	28.04°N	20.3(a), 7.0 (fixed)(b), 17(c), 23(d), 22.2(e), 21(f), 17.6(g)	5.8	5.2	4.8(c)	74.6(c)	84.8	66.4	332.2	24.1	67.1
Darchula	05/01/1997	08:47:24	80.42°E	29.90°N	13 24.9 15(h)	6.3	5.4	5.4(e) 5.5(h)	279(h)	19	68	122	73	97
Gudelhongu	30/12/1996	11:18:19	86.91°E	27.22°N	25 33(f)	5.8	4.8	–						

(a) National Seismological Center of Nepal (NSC).
(b) International Seismological Center, UK (ISC).
(c) Centroid Moment Tensor (in this article).
(d) Geophysical Survey of Russian Academy of Science (MOS).
(e) National Earthquake Information Center, USGS (NEIC).
(f) Experimental (GSETT3) International Data Center, USA (EIDC).
(g) Engdahl, van der Hilst and Buland, USA (EHB).
(h) Global Centroid Moment Tensor.

expected rupture extension. The orientation of the seismic cluster based on NSC locations is unclear and we expect that relocated aftershocks will help to constrain the geometry of the structure activated by the Sarshin earthquake.

3. Method

3.1. Centroid moment tensor at regional scale

Seismic data of the 1997 Sarshin earthquake recorded by stations at distances up to 1700 km and of good quality are used to calculate a Centroid Moment Tensor. This includes data from stations LSA (Tibetan plateau), HYB (central India), WUS (northern China) and CHTO (Thailand) (Fig. 3).

The centroid moment tensor solution is retrieved from the inversion of regional long-period seismic waves (40–100 s). The procedure is taken from Nábelek (1984) and is adapted to a low-frequency inversion (Nábelek and Xia, 1995). For the centroid moment tensor inversion, a 1-D velocity structure should be chosen to compute synthetic Green's functions and model the observed waveforms at seismic stations. Processing a large number of events (29 earthquakes in (Burtin, 2005) and 107 earthquakes in (Baur, 2007) in the Himalaya and Tibetan Plateau regions) we failed to correctly invert the seismic waveforms at stations with a single velocity model. Seismic signals from sources occurring along the Himalayan arc were recorded at stations located around the Tibetan plateau and the India plate. Therefore, velocity structures through which seismic waves travel can drastically change. For instance when a velocity model with a Moho depth fixed at 35 km (ex. India path) is used, the modeled waveforms for northern Tibetan stations will systematically arrive sooner than the observed ones. To overcome this issue, each ray path is associated with a specific 1-D structure. For the Indian station HYB, the model is from Saul et al. (2000) with a Moho depth at 35 km. For the Tibetan station LSA and northern China station WUS, the model is modified from Haines et al. (2003) with a

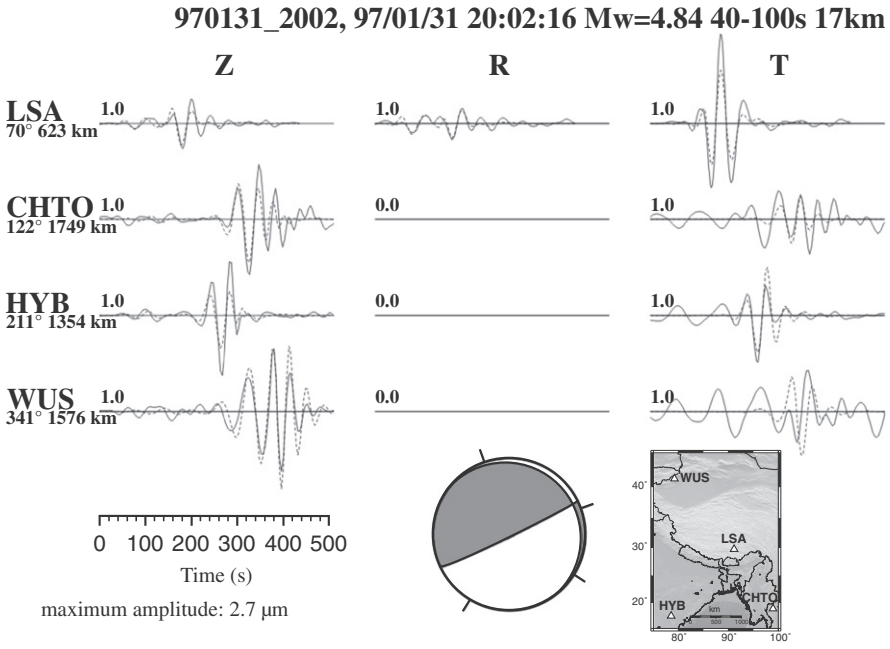

Fig. 3. Centroid Moment Tensor solution for the Sarshin earthquake occurred on January 31st 1997. For each station, observations are shown with solid lines and synthetics with dotted lines. Z, R and T are the vertical, radial and transverse components respectively. Radial components of CHTO, HYB and WUS were discarded because of the high signal-noise ratio. 1 and 0 are the weights used in the inversion.

Moho depth at 65 km. In this latter model, we had to remove the 5 km thick sedimentary layer because otherwise the synthetic inverted seismic waves were delayed too much. Finally, the model for the Thai station CHTO was set to an intermediate model between the Indian and Tibetan models with a Moho depth at 45 km. These velocity models were tested using a trial and error procedure on the 29 focal mechanisms studied (Burtin, 2005); we retained those models that resulted in synthetics that best matched the observed seismic data (Fig. 3) – See Burtin, 2005 for further information. Furthermore, for each earthquake analyzed in Burtin (2005), including the Sarshin earthquake, the centroid moment tensor source depth was constrained through a grid search algorithm that minimized the waveform misfit, using at first a coarse step size (10 km) followed by a finer step size (1 km).

3.2. Relative relocation at local scale

We calculate relocations using the double-difference algorithm HypoDD (Waldhauser and Ellsworth, 2000) for the seismicity clustered north of Kathmandu, in the trace of the Gorkha earthquake. We use data from the NSC bulletin for the period 1996–1999 and the whole bulletin from the temporary experiment of 1995–1996. Relative locations are resolved by solving an inverse problem using a damped least-square technique, minimizing the residuals between observed and calculated phase delay times between a pair of adjacent earthquakes recorded at common stations. This procedure reduces the biases induced by velocity model errors along the paths from hypocenters to seismic stations. The velocity model considered hereafter is the 1-D model of Pandey (1985) with a Vp/Vs of 1.73. We initially attribute to each seismic event the origin time and hypocenter of the NSC seismic bulletin. We also allocate location errors corresponding to the average of the longitudinal and latitudinal uncertainties as well as depth uncertainties documented in the bulletin. Undetermined depths in the database are fixed to 0. The second set of inputs includes the arrival times of P and S phase arriving at a station for a given event. The weight for the P phases is fixed to 1 and for the S phases to 0.3.

Given the very high density of events located immediately in the vicinity of the Sarshin earthquake, compared to the more diffuse spatial and temporal pattern of the seismicity elsewhere, we divide the catalogue of events in two, a western and an eastern region (respectively zones 1 and 2 hereafter) separated at 85.4E (Fig. S2 and S5.). This division will enable us to better optimize the relocation process.

We select pairs of phases at every station considering (1) a maximal separation between hypocenters of 20 km and (2) a minimum number of links between two neighbor events of 8 for Zone 1 and of 4 for Zone 2.

The relocation is performed in both cases with P and S phases when available and with three sets of iterations taking into account the seismic bulletin parameters. We set the damping at 20 in a LSQR inversion. The first set iterates four times using only P waves. The second set iterates also four times with P and S waves. The third set iterates 8 times taking into account P and S waves, limiting the residuals to 5 s and the maximum distance between linked pairs to 10 km. The relocation of Zone 1 considers 8 as the minimum number of links per pair to form a continuous cluster. There is no clustering a priori parameter for the relocation of Zone 2.

We tested the most influential parameters for both the pair-phase selection and the relocation process. In the pair-phase selection, we tested values at 4, 8, and 12 for the minimum number of links between two neighbor events. We also tested maximum separation between hypocenters at 20 and 50 km. The number of pair-phases created increase considering either a larger number of minimum links per pair or a larger maximum separation distance between hypocenters, however there are more events weakly linked. The minimum number of links between two neighbor events tested changes in Zone 1 and 2 because of the density of events. We also tested various numbers of iterations (4 and 8 for each set) in the relocation process. The RMS misfit decreases for the first two sets until it stabilizes after 4 iterations. The solution becomes unstable with 8 iterations, resulting in a centroid shift and in an unstable RMS misfit. In the third step, 8 iterations are needed to stabilize the RMS misfit. Geometrically, the relative relocations were similar for any iteration scheme.

The tests results support the parameters we chose for Zone 1 and 2.

4. Results

In Zone 1 (Fig. 4), the seismic bulletin includes 230 events with 2408 phases from which 20140 P-phases pairs and 12469 S-phase pairs are found. 80% of P-phase pairs and 84% of S-phase pairs are selected. The event pairs have an average of 10 links with an average offset of 6.04 km. After event pair selection, 167 events are successfully relocated, with <1500 m of 2-sigma-relative location errors in x, y, z and a RMS misfit reduction of 60% (Fig. S2, S3, S5, and S6).

The seismic bulletin covering Zone 2 (Fig. 4) includes 548 events with 4886 phases from which 45938 P-phase and 39002 S-phase pairs are determined. Respectively, 49% and 45% of P- and S-phase pairs are selected. The event pairs have an average of 6 links with an average offset of 6.9 km. 477 events are selected, from which 384 events are successfully relocated with <100 m of 2-sigma-relative location errors in x, y, z. The RMS misfit reduction, following the integration of the phases picked at the temporary 3 component stations, is close to 90% (Fig. S2, S3, S4, S5, S6, and S7).

The relocation of Zone 1 and Zone 2 seismicity indicates the presence of two separate clusters during the 1997 seismic episode (Fig. 4). The westernmost seismic cluster is located between 85.3° and 85.4°, covering an area of 7×11 km^2 (Fig. 4, map), just above the January 31st Sarshin earthquake hypocenter (Fig. 4, cross-section). The visual inspection of 3D plots shows that the seismicity lies on a plane that strikes N050 $\pm$ 20 E dipping steeply southeast (70–80°). The other seismic cluster is smaller (6×8 km^2) and is located between 85.4° and 85.5°. It describes an almost vertical plane striking N155 $\pm$ 20 E (Fig. 4). No large event is associated with this cluster. The remaining relocated seismic events do not show a particular geometry. Most of them are located in a 10 km-wide band east of 85.5°.

The centroid moment tensor solution for the January 31st Sarshin earthquake indicates a best centroid depth at 17 km and a reverse motion with a slight strike-slip component. One nodal plane (NP1) strikes N075 and dips 85°SE, and the second (NP2) strikes N152 and dips 24°NE. Although it is difficult to quantify uncertainties on the centroid moment tensor solution, the azimuthal coverage being decent and the changes in centroid moment tensor being small in the vicinity of the best depth, we consider the uncertainties to be moderate ($\pm$20°) (Zahradnik et al., 2008). In particular NP1, which dips at a high angle, is quite stable in the inversions. The NP1 plane is the closest to the plane defined by the relocated aftershocks of the Sarshin earthquake. The moment magnitude obtained is Mw = 4.8.

The depths of the relocated events range from 15 to 26 km in the western cluster, with the main shock at 24 km depth which is slightly deeper than previous determinations (Table 1). NSC gives a hypocenter at 20.3 km while the centroid moment tensor centroid depth is at 17 km. Although the relocation allows us to place constraints on the relative positions of hypocenters leading to a fairly well defined geometry for the cluster, the centroid depth of the cluster (~22 km) is less well constrained as the closest station that recorded these events is located at ~25 km, and thus the centroid could move by a few kilometers. Both hypocenter depths and centroid moment tensor centroid depths being within $\pm$5 km, we think the differences may not be significant. In addition, as most crustal earthquakes nucleate at depth and propagate towards the surface (e.g., Das and Scholz, 1983; Huc et al., 1998), we expect the hypocenter depth of the mainshock to be larger than its centroid moment tensor depth. This will be particularly true if the coseismic slip is small and the ruptured area large for a Mw4.8 event. Indeed, the source of a Mw4.8 can be either 2×2 km^2 with 10 cm of slip or 5×5 km^2 with 2 cm of slip.

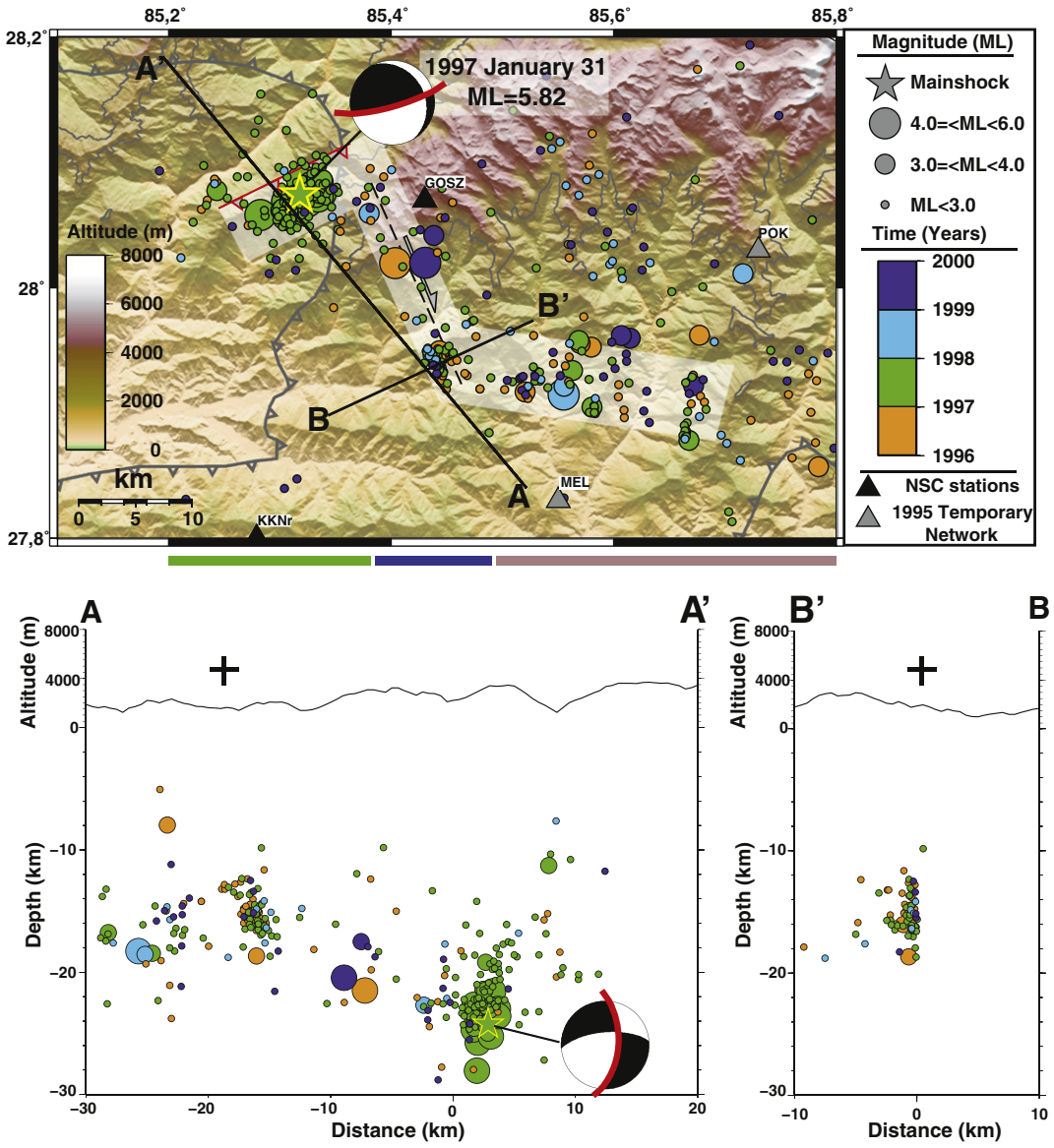

Fig. 4. Spatial distribution of the seismic episode of 1996–1999, north of Kathmandu (see Fig. 1): The map shows the relocated seismicity as a function of time and magnitude of Zone 1 and 2 (zones boundary: longitude 85.4°). The main shock corresponds to the 1997 January 31st ML = 5.8 (Mw 4.8) earthquake with the preferred focal mechanism plane in red. The cross-sections include the relocated seismicity. A-A′ and B′-B cross-sections are orientated N140 and N065, respectively. They stack seismicity located 10 km for A-A′ and 3 km for B′-B from each side of the track. The area highlighted in light white correspond to the suspected fault segments at depth activated by the 1997 episode (see Fig. 7 for interpretation).The intersection between A-A′ and B-B′ cross-sections are indicated with a black cross. The green, blue and pink-brown lines at the bottom of the map are western, central and eastern respectively used in Fig. 5.

5. Interpretation

5.1. Spatial distribution of the Sarshin Swarm

Most of the 1996–2000 Sarshin Swarm seismicity is located at midcrustal depths, with centroid depths at 22 and 15 km respectively for the two clusters (Fig. 4). These depths roughly correspond to the depth of the Main Himalayan shear zone, as interpreted on images obtained along profiles based on receiver function analysis (Schulte-Pelkum et al., 2005; Nábelek et al., 2009; Duputel et al., 2016).

The westernmost cluster develops after the main shock of the Sarshin earthquake over a 7×11 km^2 region. Given the geometry of the cluster and the fault plane solution parameters of its main shock, the January 31st 1997 Sarshin earthquake, we associate this seismic swarm to the activation of a NE-SW backthrust, steeply dipping to the southeast. Assuming that the aftershock distribution corresponds to the maximum extent of the fault segment ruptured by the main shock, a Mw 4.8 ($M0 = 2.3 * 10^{16}$ Nm deduced from the centroid moment tensor determination), and assuming a shear modulus of 32 GPa we obtain an average minimum slip of 1 cm. Considering that aftershocks may more likely extend beyond the edges of the ruptured plane, its surface is likely overestimated. A surface overestimation by 100% will lead to doubling the average slip, at 2 cm. This amount of slip at depth induces infra-mm displacements at the surface GPS sites around, values below the resolution capacity of the campaign GPS available at that time (Jouanne et al., 2004).

A rupture on a steep south-eastward dipping - northwestward verging thrust at mid-crustal depths below the front of the high topography may correspond either to the activation of (a) a fault segment at the forelimb of the lesser Himalayan duplex (e.g. Pearson and DeCelles, 2005; Khanal and Robinson, 2013), or (b) a local shear zone within the hinge above the flat-decollement/ramp, as predicted by mechanical

models (e.g. Souloumiac et al., 2009) (Fig. 7D). We prefer the latter interpretation, as the depth seems more consistent with the downdip end of a midcrustal ramp than the passive roof-thrust of the duplex.

The relocated seismicity appears offset by 20 km from west to east, describing an eastward right-stepping strand. Note that this step is not an artifact due to the location of the boundary between the two zones considered in the relocation process: alternative relocations considering only one zone, keeping the same relocation parameters, produced similar spatial patterns, with the seismic cluster stepping to the south in this area. This offset could be explained by the presence of a tear fault between two ramps or structural discontinuities within the Main Himalayan shear zone such as a stepover of the fault. We prefer the former hypothesis given the absence of overlapping seismicity along strike. In addition, the vertical NW-SE plane described by the second cluster (85.4° and 85.5°) identified in the relocation results is consistent with tear faulting although we could not compute any fault plane solution to prove this. Such tear faults are required because of the topology of the MHT flat/ramp system and its lateral variations (Fig. 7). The right lateral tear fault suspected to develop at depth within the trace of the second cluster is aligned with an active dextral fault system reaching the surface along the 20 km-long NNW-SSE Jhiku Khola fault (Kumahara et al., 2016).

We propose that the backthrust and tear fault activated during the 1997 seismic episode, and in a more general way every significant variation of the structure at depth along the MHT, might influence its behavior. It could affect the propagation of the co-seismic rupture (e.g. Béjar-Pizzarro et al., 2010), influencing the co- and post-seismic slip distribution as well as the location of the aftershocks. Note that the structure we studied is located in between two patches of maximum slip of the Gorkha earthquake proposed by some authors (e.g. Avouac et al., 2015; Grandin et al., 2015) (Fig. 1).

5.2. Temporal distribution of the seismicity at local and regional scales

The time structure of a seismic episode gives a dynamic sense and evolution of the phenomenon that the spatial distribution does not. Both are essential to interpret our results.

The time structure of the seismicity in this area (Fig. 4) exhibits complex variations in the period covered by our study. The seismicity rate decreases first in mid-1996 (Figs. 2 and 5). This relative quiescence is difficult to ascertain, being concurrent with the monsoon arrival, a period during which the seismic noise level and therefore the completeness magnitude of the catalogue is higher than on average, a period during and slightly after which the seasonal load of the India plate has a genuine influence on the seismicity (Bollinger et al., 2007; Bettinelli et al., 2008; Burtin et al., 2008). The seismic rate remains low until December, far after the monsoon period, and is followed by a sharp increase. The seismic events are then clustered between 85.4° and 85.5° (Central zone in Fig. 4), mostly along a 6 km-long vertical plane oriented N155. This activity, decreasing at the beginning of 1997, is followed by the development of another cluster 15 km to the northwest in January (Figs. 4, 5). The swarm in the area begins before the Sarshin main shock which occurred at 20:02 (local time) on January 31st and was preceded by a ML5 and smaller events a few hours earlier. The seismic cluster that developed within the next three months within 10 km from the hypocenter is typical of an aftershock sequence. In the meantime, the seismicity rate east of 85.5°E increased significantly (Fig. 5).

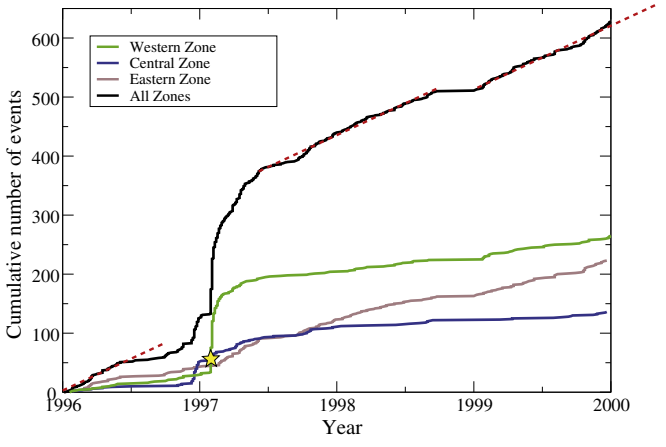

Fig. 5. Time sequence of the seismicity north of Kathmandu. The zones are indicated at the bottom of the map in Fig. 4. The Sarshin earthquake is indicated by the yellow star. The red dashed line is the average rate of seismicity (108 events per year).

Surprisingly, this unusual transient seismic activity is not exceptional in the Himalaya region. Indeed, in eastern Nepal, a seismic swarm developed between 86.8 and 87°E, generating 80 events south of Mount Everest, between November 1996 and May 1997. No main shock was detected prior to the onset of the seismic swarm but a larger shock, with a ML 5.8, occurred on the 30/12/1996 (Table 1) and was followed by aftershocks (Fig. 6). In western Nepal, between 80.5° and 81°E, a similar swarm developed with a main shock on 05/01/1997 of ML = 6.3 (Table 1).The location of the seismicity in these two areas is not sufficiently resolved to perform an analysis similar to what has been done here. The time structure of these two swarms is very similar to that of Sarshin as illustrated on Fig. 6.

Altogether, the 3 clusters contribute to 40% of the yearly midcrustal events detected along the front of the range in Nepal. Their cumulative along strike development accounts for ~10% of the length of the midcrustal cluster making this event the most important seismicity burst of the interseismic period recorded by the Nepal National Seismological Network. No significant seismic rate variations were detected in between the three clusters (Fig. 6).

6. Discussion

Complex spatial and temporal variations of seismicity have been revealed at local and regional scales. Locally, north of Kathmandu, the spatial distribution of the seismicity coincides with a back-thrust and a thrust segment separated by a proposed 20 km-long tear fault. Their consecutive activation follows the development of a seismic swarm on the tear fault. The geometry of the fault system is consistent with a right lateral slip on the tear fault. This scenario is compatible with the topology of the thrust system as well as with the kinematics of the dextral NNW-SSE Jhiku Khola fault described in continuity to the south (Kumahara et al., 2016). The en-echelon segments of the MHT there are close to the unstable-stable transition zone USTZ (e.g. Jackson and Bilham, 1994; Bettinelli et al., 2006). This behavior was confirmed recently by the determination of the seismic coupling that falls there between 0.4 and 0.6 (Ader et al., 2012; Grandin et al., 2012; Stevens and Avouac, 2015).

The seismic activity in 1997 in this region could result from (1) a local unsteady loading or (2) a local strain transfer in the vicinity of the USTZ. However, rather than just a local strain transient, the development in 1996–97 of 2 other clusters hundreds of kilometers apart, depicting similar temporal variations, may imply (3) a large scale unsteady loading. The unsteady loading could be due, among others, to a lithospheric response to the water mass redistribution after the monsoon or to a slow slip event. However, in 1996, the precipitation records were fairly typical (e.g., Shrestha et al., 2000; Yatagai et al., 2012). This leads us to propose that the 1997 seismic episode may be related to a slow slip event. A transient slip event with a slip amplitude of tens of centimeters is precluded due to the absence of measurable changes in the seismicity rate between the clusters (Fig. 6A). Indeed, a seismicity change would likely occur after a centimetric to decimetric scale slow slip event, which would in turn release years of stress build up and therefore most probably induce years of midcrustal seismicity along strike. The lower end of the slip amplitude expected, i.e. 1 cm, would

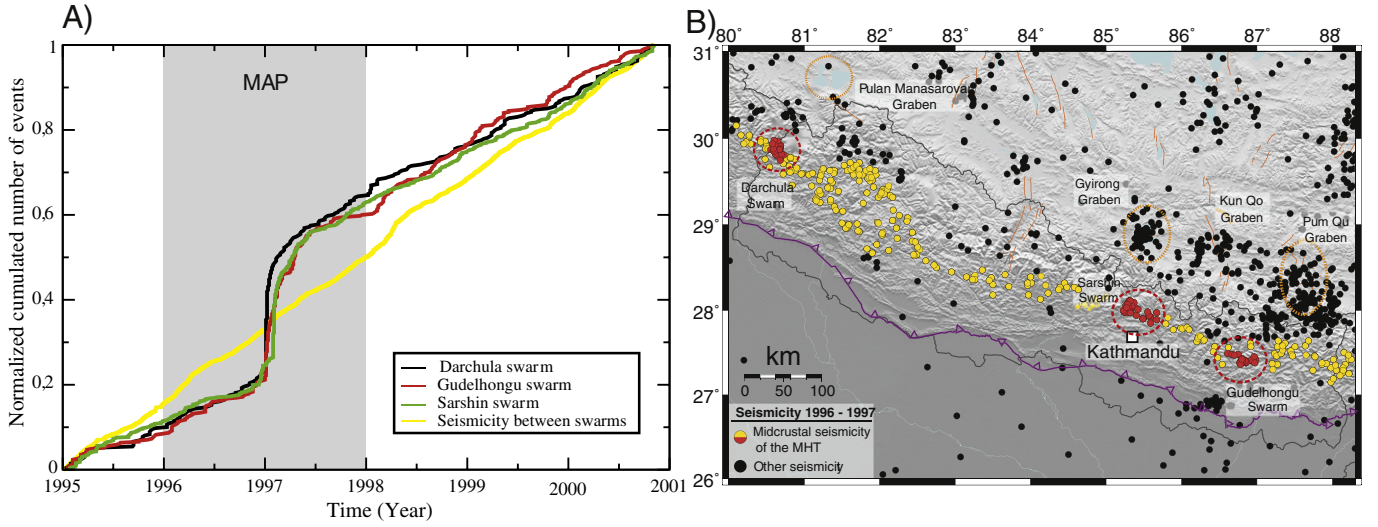

Fig. 6. Spatio-temporal variations of the seismicity. A) Normalized time sequence of the midcrustal seismicity along the MHT. The curves correspond to the three swarm areas and the yellow one to the inter-swarms area. Gray shadow zone is the time covered in the map. B) Midcrustal seismicity for the period 1996–1997 in yellow, swarm seismicity in red. Orange circles are the Southern Tibetan Grabens north of the swarms.

correspond roughly to the seismic slip accommodated during the Sarshin earthquake (see previous section for estimation). In Sarshin area, such an amount of slip at midcrustal depths generates only infra-milimetrical displacements at RAM0 and SYA0, regional GPS stations respectively 17 and 20 km from the updip-end of the ruptured fault plane. These stations were surveyed briefly in 1995 and 1998 (1 to 4 days/sessions). They were translated in 3 years by 19 ± 6 mm and 21 ± 7 mm respectively in an India fixed reference frame (Jouanne et al., 2004). The large uncertainties of the measurements preclude resolving the infra-milimetrical displacements induced by the Sarshin earthquake as well as those induced by any strain transient with similar amplitudes. We further note that the displacements uncertainties for both stations amounts to one third of the measurements, a value comparable to one year of strain above the Main Himalayan Thrust. The thrust accommodates, at depth, on average, a shortening of 18 mm/yr (Ader et al., 2012). Detecting a transient slip event at depth on the creeping part of the MHT of <18 mm therefore seems impossible. This result is corroborated by the absence of any major change in the shortening rates estimated elsewhere in Nepal by campaign GPS data, and by the continuous DORIS time series available at Everest.

Several of the large transient events elsewhere in the world were accompanied by tremors and low frequency earthquakes (Schwartz and Rokosky, 2007). Such kinds of seismic events have not been observed in 1997 in Nepal, a period during which the continuous seismic signals recorded by National Seismological Network was not stored. Further analysis of these signals to detect tremors or low frequency earthquakes is therefore limited to the cut signals of seismic events which, according to a preliminary analysis, present a typical spectra.

Despite the lack of direct evidence that tremors and low frequency earthquakes occurred, we think the seismic catalogue contains other indirect evidences of this process.

A subtle transient slip event may generate heterogeneous seismicity along strike due to the geometry and state of stress changes along strike of the MHT. Indeed, the midcrustal seismicity under the front of the Himalayas appears sensitive to the local state of stress which depends mainly on the regional tectonic stress and the topography, through their influence on the preferred orientation of the failure planes (Bollinger et al., 2004a). In between the Main Frontal Thrust and the front of the High range, S3 and S1, the minimal and maximal principal stresses, are respectively vertical and north-south. S1 increases during interseismic deformation due to slip at depth on the MHT, promoting failure on EW striking thrust planes (Fig. 7A(area 2)). Further north, in the Southern Tibetan grabens (Fig. 6B), S1 is vertical while S3 is horizontal, striking approximately east-west. S3 might decrease during interseismic deformation (Fig. 7A(area 3)), since east-west extension increases in the Southern Tibetan Graben due to the divergence of thrusting along the Himalayan Arc (Bollinger et al., 2004a). This promotes failure on north-south oriented normal faults (i.e.: the southern Tibetan grabens). In between these two domains (i.e. south of the range, Tibetan Plateau: between area 2 and 3 on Fig. 7A) the regional state of stress might promote the existence of NW-SE and NE-SW strike slip faults. This is valid for a range of depths in the cluster which depends on both S1 and S3 and the local non compensated topography. In this area, the intermediate stress component is vertical, while the maximum and minimum principal stresses correspond respectively to the north-south and east-west stress values (Fig. 7A(area 1)). The strike slip faults in this region are very sensitive to the simultaneous N-S and E-W stress variations (Fig. 7A). The lack of strike slip Centroid Moment Tensor solutions for intermediate events (M > 5.5) during the last decades along the Himalaya demonstrate that strike slip faulting is infrequent along strike, probably due to the restriction to a small depth range of the corresponding state of stress. Besides the presence of large scale active strike-slip faults affecting the lesser Himalayas (Nakata, 1989), interpreted as resulting from large scale strain partitioning (Nakata, 1989; Murphy et al., 2014) or from the presence and migration of lateral ramps (Bollinger et al., 2004b), few active strike-slip fault segments were described at the foot of the High range (Nakata, 1989). However, tear-faults are suspected at midcrustal depths because of the lateral variations of the midcrustal ramps along the strike of the Main Himalayan thrust (e.g. Robinson et al., 2001; Bollinger et al., 2004b; Grandin et al., 2012). Despite the publication of balanced cross sections immediately west of Sarshin area (e.g. Pearson and Decelles, 2005; Khanal and Robinson, 2013), the present-day positions of the midcrustal ramps in the vicinity of the seismic cluster studied here are still unresolved. Assuming the cluster represents the edge of the MHT locked segment (e.g. Cattin and Avouac, 2000; Bollinger et al., 2004a; Ader et al., 2012, Grandin et al., 2015), a dextral NW-SE transform structure is required for the sake of geometrical continuity (Figs. 4 and 5, Central zone in blue). Assuming that this swarm is located on such a right lateral strike slip segment, its activity in December 1996 creates static stress changes at its extremities. It leads to the generation of 2 positive Coulomb stress variations (DeltaCFF) lobes on its NW and SE sides (while NE and SW would see a negative DeltaCFF(Fig. S8 to S11 and Table S1 and S2). This static stress change scenario accounts for

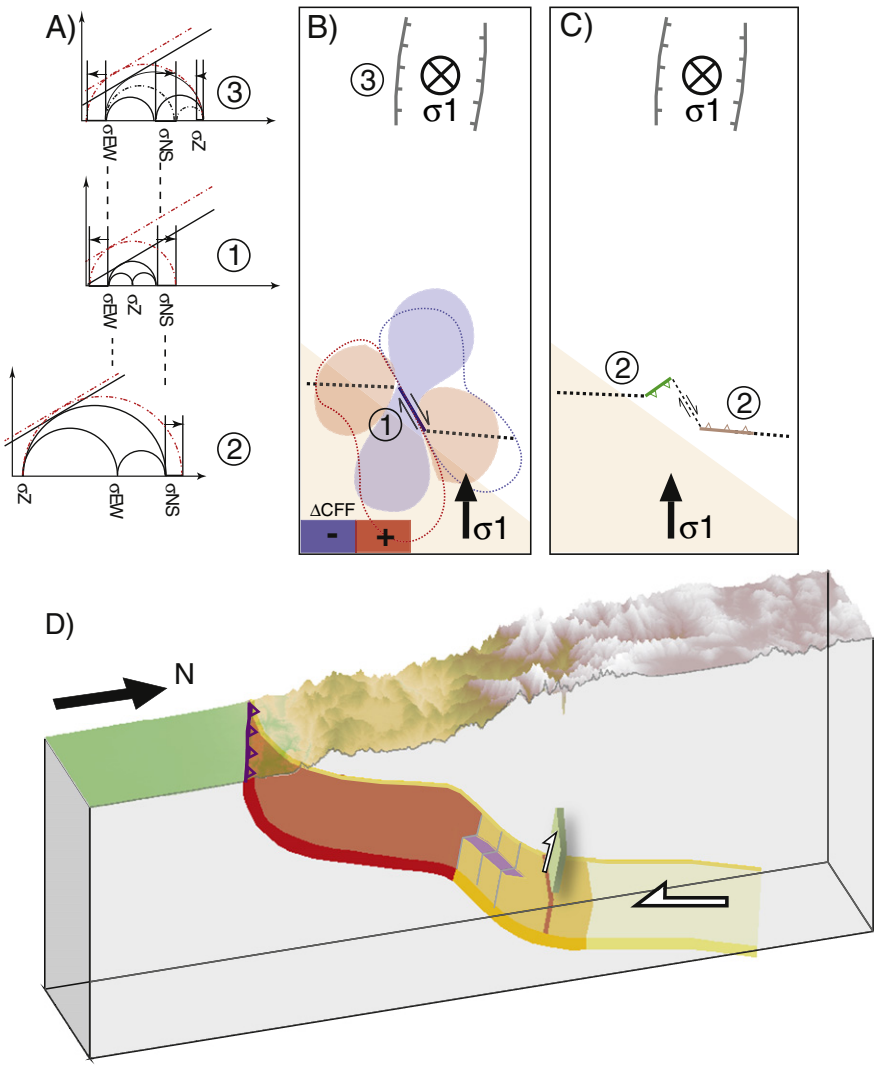

Fig. 7. Schematic evolution of the stress field and structure activation. A) Variation of shear stress and normal stress associated with a transient slip event on the Main Himalayan Thrust in a region with midcrustal tear faults and southern Tibetan grabens. The initial state is shown in black and is assumed tangent to the failure envelope represented by the straight line. 1, 2, and 3 refer to the different areas indicated in B and C. In area 1, s1 and s3 are horizontal, increasing and decreasing respectively, promoting failure. In area 2, s1 is horizontal, striking about north-south and increasing during interseismic deformation and transient slip events, promoting failure. In area 3, s3 is horizontal, striking approximately east-west and decreasing during interseismic deformation, promoting failure. B) and C) Kinematical evolution north of Kathmandu in 1996–1997; orange surface corresponds to the area with a coupling >50–80% depending on source (Ader et al., 2012; Grandin et al., 2015). B) Static stress change induced by slip on the tear fault is schematized by Coulomb stress lobes, respectively blue and red for DCFF < 0 and >0. Dotted lines and filled areas correspond respectively to the DCFF calculated for receiver faults with the backthrust and the thrust orientation (more information in Table S1, Table S2, and Fig. S8 to S11). C) Activation of the backthrust (in green) and the thrust fault (in salmon) as a consequence of static stress change induced by the tear fault (B). D) Schematic three dimensional block, with vertical exaggeration, of the MHT with the backthrust (green) and the tear fault (purple). Colors on the MHT correspond to the coupling: red: total coupling (>50–80%), orange: transition zone (60%–40%), Yellow: completely decoupled (0%) (Ader et al., 2012; Grandin et al., 2015). White arrows show the kinematics of the structures.

the generation of seismicity along the backthrust to the NW and the thrust to the SE as well as with the lack of microseismic activity along its NE and SW extremities (Fig. 7B and C). Furthermore it is consistent with Sarshin focal mechanism depicting a NE-SW oriented fault plane solution (Fig. 4).

Whether similar kinematics and mechanisms are involved in the generation of the Far western and eastern Nepal seismic swarms is unknown. Unfortunately, the seismicity in these regions cannot be analyzed with a similar relocation approach due to the less optimal geometry of the seismic network and completeness of the database. But the 3 swarms are located in similar settings, within the midcrustal cluster at similar distances from the USTZ and within the trace of southern Tibetan Grabens (Fig. 6B). Another similarity is their time sequence that begins with a weak but detectable decrease of seismicity prior to the swarms' development (Fig. 6A). These rate decreases begin about 6 months prior to each swarm, during the onset of the monsoon. That the higher level of seismic noise during the monsoon is responsible for the seismic rate decrease is possible (Bollinger et al., 2007), but the rate remains low after the end of the monsoon and the decrease of the seismic noise generated by landsliding and rivers (Burtin et al., 2008). An alternative interpretation could be that the seismicity was partially inhibited and then promoted due to the response of the crust to a loading/unloading of continental water (Bettinelli et al., 2008; Chanard et al., 2014) in 1996. Whatever the scenario, the simultaneous development of these swarms may have resulted from a transient slip event similar to those detected along other subduction zones (e.g. Cascadia, Mexico, Japan, …) with an affected area between 30 and 600 km along strike, and transient slip lasting 6 days to about a year with amplitudes between 5 mm and 5.6 cm (e.g. Dragert et al., 2001; Schmidt and Gao, 2010; Schwartz and Rokosky, 2007; Szeliga et al., 2008).

Such a slow slip event occurring on the Main Himalayan Thrust could play a role in the seismic cycle of the locked segment of the fault. Indeed, such transient events bring the locked fault zone closer

to failure by several months (Dragert et al., 2001), besides the interseismic loading on the fault.

7. Conclusion

The first conclusion to be drawn from this work is that the downdip end of the locked section of the Main Himalayan Thrust exhibits lateral seismicity variations that may reveal the presence of structural complexities at midcrustal depths. The right-stepping geometry of the seismicity, north of Kathmandu, is interpreted as resulting from the activation of a tear fault between a backthrust and a thrust segment. This structural complexity might have influenced the slip distribution during the Gorkha earthquake rupture as revealed by a local minima in the region of high slip of some published slip models. A second major conclusion is that the time sequence of the seismic swarm which developed there in 1996–97 is consistent with a propagation of a local strain transient, from the tear fault to the backthrust and thrust. Finally, the temporal coincidence between this swarm and two others at far distances leads us to suspect the development of a larger-scale transient slip event on the Main Himalayan Thrust. The local stress field appears responsible for the higher sensitivity of these areas to strain transients and needs therefore to be monitored to ascertain the presence of infrequent subtle slow slip events along the Himalaya.

Acknowledgements

This project is funded by the French Agence Nationale de la Recherche (ANR-13-BS06-0006-01) and the Comissariat à l'Energie Atomique et aux Energies Alternatives. We thank the National Seismological Center, Sudhir Rajaure and Soma Nath Sapkota for early exchanges on the seismic catalogue and macroseismic field of the Sarshin earthquake. The authors also thank the two anonymous reviewers and Gavin P. Hayes for their helpful comments that improved the paper.

Appendix A. Supplementary data

Supplementary data to this article can be found online at http://dx.doi.org/10.1016/j.tecto.2016.10.004.

References

Ader, T., Avouac, J.P., Liu-Zeng, J., Lyon-Caen, H., Bollinger, L., Galetzka, J., Genrich, J., Thomas, M., Chanard, K., Sapkota, S.N., Rajaure, S., Shrestha, P., Ding, L., Flouzat, M., 2012. Convergence rate across the Nepal Himalaya and interseismic coupling on the Main Himalayan Thrust: implications for seismic hazard. J. Geophys. Res. 117, B04403. http://dx.doi.org/10.1029/2011JB009071.

Adhikari, L.B., Gautam, U.P., Koirala, B.P., Bhattarai, M., Kandel, T., Gupta, R.M., Timsina, C., Maharjan, N., Maharjan, K., Dahal, T., Hoste-Colomer, R., Cano, Y., Dandine, M., Guilhem, A., Merrer, S., Roudil, P., Bollinger, L., 2015. The aftershock sequence of the 2015 April 25 Gorkha-Nepal earthquake. Geophys. J. Int. 203, 2119–2124. http://dx.doi.org/10.1093/gji/ggv412.

Armijo, R., Tapponnier, P., Mercier, J.L., Han, T.L., 1986. Quaternary extension in southern Tibet: field observations and tectonic implications. J. Geophys. Res. Solid Earth 91 (B14), 13803–13872.

Avouac, J.P., Meng, L., Wei, S., Wang, T., Ampuero, J.P., 2015. Lower edge of locked Main Himalayan Thrust unzipped by the 2015 Gorkha earthquake. Nat. Geosci. 8, 708–711.

Bai, L., Liu, H., Ritsema, J., Mori, J., Zhang, T., Ishikawa, Y., Li, G., 2015. Faulting structures above the Main Himalayan Thrust as shown by relocated aftershocks of the 2015 Mw7.8 Gorkha, Nepal, earthquake. Geophys. Res. Lett. 43. http://dx.doi.org/10.1002/2015GL066473.

Baur, 2007. Seismotectonics of the Himalayas and the Tibetan Plateau. Moment Tensor Analysis of Regional Seismograms. Oregon State University, p. 298.

Béjar-Pizzarro, M., Carrizo, D., Socquet, A., Armijo, R., Barrientos, S., Bondoux, F., Bonvalot, S., Campos, J., Comte, D., de Chabalier, J.B., Charade, O., Delorme, A., Gabalda, G., Galetzka, J., Genricj, J., Nercessian, A., Olcay, M., Ortega, F., Ortega, I., Remy, O., Ruegg, J.C., Simons, M., Valderas, C., Vigny, C., 2010. Asperities and barriers on the seismogenic zone in North Chile: state-of-the-art after the 2007 Mw 7.7 Tocopilla earthquake inferred by GPS and InSAR data. Geophys. J. Int. 183, 390–406. http://dx.doi.org/10.1111/j.1365-246X.2010.04748.x.

Bettinelli, P., Avouac, J.P., Flouzat, M., Jouanne, F., Bollinger, L., Willis, P., Chitrakar, G.R., 2006. Plate motion of India and interseismic strain in Nepal Himalaya from GPS and DORIS measurements. J. Geod. 80, 567–589. http://dx.doi.org/10.1007/s00190-006-0030-3.

Bettinelli, P., Avouac, J.P., Flouzat, M., Bollinger, L., Ramillien, G., Rajaure, S., Sapkota, S., 2008. Seasonal variations of seismicity and geodetic strain in the Himalaya induced by surface hydrology. Earth Planet. Sci. Lett. 266, 332–344. http://dx.doi.org/10.1016/j.epsl.2007.11.02110.

Bollinger, L., Avouac, J.P., Cattin, R., Pandey, M.R., 2004a. Stress buildup in the Himalaya. J. Geophys. Res. 109, B11405. http://dx.doi.org/10.1029/2003JB002911.

Bollinger, L., Avouac, J.P., Beyssac, O., Catlos, E.J., Harrison, T.M., Grove, M., Goffé, B., Sapkota, S., 2004b. Thermal structure and exhumation history of the Lesser Himalaya in central Nepal. Tectonics 23, TC5015. http://dx.doi.org/10.1029/2003TC001564.

Bollinger, L., Perrier, F., Avouac, J.P., Sapkota, S., Gautam, U., Tiwari, D.R., 2007. Seasonal modulation of seismicity in the Himalaya of Nepal. Geophys. Res. Lett. 34, L08304. http://dx.doi.org/10.1029/2006GL029192.

Bollinger, L., Tapponnier, P., Sapkota, S.N., Klinger, Y., 2016. Slip deficit in central Nepal: omen for a repeat of the 1344 AD earthquake? Earth Planets Space 68, 12. http://dx.doi.org/10.1186/s40623-016-0389-1.

Burtin, A., 2005. Seismotectonics of the Himalayan Arc from regional seismogram moment tensor inversion. Internship Report. Oregon State University.

Burtin, A., Bollinger, L., Vergne, J., Cattin, R., Nábělek, J.L., 2008. Spectral analysis of seismic noise induced by rivers: a new tool to monitor spatiotemporal changes in stream hydrodynamics. J. Geophys. Res. 113, B05301. http://dx.doi.org/10.1029/2007JB005034.

Cattin, R., Avouac, J.P., 2000. Modeling mountain building and seismic cycle in the Himalaya of Nepal. J. Geophys. Res. 105 (B6), 13389–13407.

Chanard, K., Avouac, J.P., Ramillien, G., Genrich, J., 2014. Modeling deformation induced by seasonal variations of continental water in the Himalaya region: sensitivity to Earth elastic structure. J. Geophys. Res. Solid Earth 119. http://dx.doi.org/10.1002/2013JB010451.

Collot, J.Y., Marcaillou, B., Sage, F., Michaud, F., Agudelo, W., Charvis, P., Graindorge, D., Gutscher, M.-A., Spence, G., 2004. Are rupture zone limits of great subduction earthquakes controlled by upper plate structures? Evidence from multichannel seismic reflection data acquired across the northern Ecuador–southwest Colombia margin. J. Geophys. Res. Solid Earth 109, B11103.

Das, S., Scholz, C.H., 1983. Why large earthquakes do not nucleate at shallow depths. Nature 305, 621–623.

Dragert, H., Wang, K., James, T.S., 2001. A silent slip event on the deeper Cascadia subduction interface. Science 292 (5521), 1525–1528.

Duputel, Z., Vergne, J., Rivera, L., Wittlinger, G., Farra, V., Hetényi, G., 2016. The 2015 Gorkha earthquake: a large event illuminating the Main Himalayan Thrust fault. Geophys. Res. Lett. 43. http://dx.doi.org/10.1002/2016GL068083.

Elliott, J.R., Jolivet, R., Gonzalez, P.J., Avouac, J.P., Hollingsworth, J., Searle, M.P., Stevens, V.L., 2016. Himalayan megathrust geometry and relation to topography revealed by Gorkha earthquake. Nat. Geosci. 9 http://dx.doi.org/10.1038/NGEO2623.

Fan, W., Shearer, P.M., 2015. Detailed rupture imaging of the 25 April 2015 Nepal earthquake using teleseismic P waves. Geophys. Res. Lett. 42, 5744–5752. http://dx.doi.org/10.1002/2015GL064587.

Grandin, R., Doin, M.-P., Bollinger, L., Pinel-Puyssegur, B., Ducret, G., Jolivet, R., Sapkota, S.N., 2012. Long-term growth of the Himalaya inferred from interseismic InSAR measurement. Geology 40 (12), 1059–1062. http://dx.doi.org/10.1130/G33154.1.

Grandin, R., Vallée, M., Satriano, C., Lacassin, R., Klinger, Y., Simoes, M., Bollinger, L., 2015. Rupture process of the Mw = 7.9 2015 Gorkha earthquake (Nepal): insights into Himalayan megathrust segmentation. Geophys. Res. Lett. 42. http://dx.doi.org/10.1002/2015GL066044.

Haines, S.S., Klemperer, S.L., Brown, L., Jingru, G., Mechie, J., Meissner, R., Ross, A., Wenjin, Z., 2003. INDEPTH III seismic data: from surface observations to deep crustal processes in Tibet. Tectonics 22 (8), 1001.

Holtkamp, S.G., Brudzinski, M.R., 2011. Earthquake swarms in circum-Pacific subduction zones. Earth Planet. Sci. Lett. 305 (1), 215–225.

Holtkamp, S.G., Pritchard, M.E., Lohman, R.B., 2011. Earthquake swarms in south America. Geophys. J. Int. 187 (1), 128–146.

Hubbard, J., Almeida, R., Foster, A., Sapkota, S.N., Bürgi, P., Tapponnier, P., 2016. Structural segmentation controlled the 2015 Mw 7.8 Gorkha earthquake rupture in Nepal. Geology 44 (8), 639–642. http://dx.doi.org/10.1130/G38077.1.

Huc, M., Hassani, R., Chéry, J., 1998. Large earthquake nucleation associated with stress exchange between middle and upper crust. Geophys. Res. Lett. 25 (4), 551–554.

Jackson, M., Bilham, R., 1994. Constraints on Himalayan deformation inferred from vertical velocity fields in Nepal and Tibet. J. Geophys. Res. Solid Earth 99 (B7), 13897–13912.

Jouanne, F., Mugnier, J.L., Gamond, J.F., Le Fort, P., Pandey, M.R., Bollinger, L., Flouzat, M., Avouac, J.P., 2004. Current shortening across the Himalayas of Nepal. Geophys. J. Int. 157, 1–14. http://dx.doi.org/10.1111/j.1365-246X.2004.02180.x.

Khanal, S., Robinson, D.M., 2013. Upper crustal shortening and forward modeling of the Himalayan thrust belt along the Budhi-Gandaki River, central Nepal. Int. J. Earth Sci. 102, 1871–1891.

Kobayashi, T., Morishita, Y., Yarai, H., 2015. Detailed crustal deformation and fault rupture of the 2015 Gorkha earthquake, Nepal, revealed from ScanSAR-based interferograms of ALOS-2. Earth, Planets and Space 67, 201. http://dx.doi.org/10.1186/s40623-015-0359-z.

Kumahara, Y., Chamlagain, D., Upreti, B.N., 2016. Geomorphic features of active faults around the Kathmandu Valley, Nepal, and no evidence of surface rupture associated with the 2015 Gorkha earthquake along the faults. Earth, Planets and Space 68 (1), 1–8.

Métois, M., Socquet, A., Vigny, C., 2012. Interseismic coupling, segmentation and mechanical behavior of the central Chile subduction zone. J. Geophys. Res. 117, B03406. http://dx.doi.org/10.1029/2011JB00736.

Murphy, M.A., Taylor, M.H., Gosse, J., Silver, C.R.P., Whipp, D.M., Beaumont, C., 2014. Limit of strain partitioning in the Himalaya marked by large earthquakes in western Nepal. Nat. Geosci. 7 (1), 38–42.
Nábelek, J., 1984. Determination of earthquake source parameters from inversion of body waves. Ph. D. Thesis. Massachusetts Institute of Technology, Cambridge, MA.
Nábelek, J., Xia, G., 1995. Moment-tensor analysis using regional data: application to the 25 March, 1993, Scotts Mills, Oregon, earthquake. Geophys. Res. Lett. 22 (1), 13–16.
Nábelek, J., Hetényi, G., Vergne, J., Sapkota, S.N., Kafle, B., Jiang, M., Su, H., Chen, J., Huang, B.-S., Hi-CLIMB Team, 2009. Underplating in the Himalaya-Tibet collision zone revealed by the Hi-CLIMB experiment. Science 325, 1371–1374.
Nakata, T., 1989. Active faults of the Himalaya of India and Nepal. Geol. Soc. Am. Spec. Pap. 232, 243–264.
Pandey, M.R., 1985. Seismic model of central and eastern lesser Himalaya of Nepal. Journal of Nepal Geological Society 3 (1–2), 1–11.
Pandey, M.R., Tandukar, R.P., Avouac, J.P., Lavé, J., Massot, J.P., 1995. Interseismic strain accumulation on the Himalayan Crustal Ramp (Nepal). Geophys. Res. Lett. 22, 751–754.
Pandey, M.R., Tandukar, R.P., Avouac, J.P., Vergne, J., Héritier, T., 1999. Seismotectonics of the Nepal Himalayas from a local seismic network. J. Asian Earth Sci. 17 (5–6), 703–712.
Pearson, O.N., DeCelles, P.G., 2005. Structural geology and regional tectonic significance of the Ramgarh thrust, Himalayan fold-thrust belt of Nepal. Tectonics 24, TC4008 (doi: 10/1029/2003TC001617).
Robinson, D.M., DeCelles, P.G., Patchett, P.J., Garzione, C.N., 2001. The kinematic evolution of the Nepalese Himalaya interpreted from Nd isotopes. Earth Planet. Sci. Lett. 192 (4), 507–521. http://dx.doi.org/10.1016/S0012-821X(01)00451-4.
Sapkota, S.N., 2011. Surface rupture of 1934 Bihar-Nepal earthquake: implications for seismic hazard in Nepal Himalaya. Ph.D Thesis. Institut de Physique du Globe de Paris, France, pp. 2–292.
Saul, J., Kumar, M.R., Sarkar, D., 2000. Lithospheric and upper mantle structure of the Indian shield, from receiver functions. Geophys. Res. Lett. 27, 2357–2360.
Schmidt, D.A., Gao, H., 2010. Source parameters and time-dependent slip distributions of slow slip events on the Cascadia subduction zone from 1998 to 2008. J. Geophys. Res. Solid Earth 115, B00A18. http://dx.doi.org/10.1029/2008JB006045.
Schulte-Pelkum, V., Monsalve, G., Sheehan, A., Pandey, M.R., Sapkota, S., Bilham, R., Wu, F., 2005. Imaging the Indian subcontinent beneath the Himalaya. Nature Letters 435. http://dx.doi.org/10.1038/nature03678.
Schwartz, S.Y., Rokosky, J.M., 2007. Slow slip events and seismic tremor at circum-Pacific subduction zones. Rev. Geophys. 45 (3).
Schwartz, S.Y., Dewey, J.W., Lay, T., 1989. Influence of fault plane heterogeneity on the seismic behavior in the southern Kurile Islands Arc. J. Geophys. Res. Solid Earth 94 (B5), 5637–5649.
Shrestha, A.B., Wake, C.P., Dibb, J.E., Mayewski, P.A., 2000. Precipitation fluctuations in Nepal Himalaya and its vicinity and relationship with some large scale climatological parameters. Int. J. Climatol. 20, 317–327.
Souloumiac, P., Leroy, Y.M., Maillot, B., Krabbenhoft, K., 2009. Predicting stress distributions in fold-and-thrust belts and accretionary wedges by optimization. J. Geophys. Res. 114, B09404. http://dx.doi.org/10.1029/2008JB005986.
Stevens, V.L., Avouac, J.P., 2015. Interseismic coupling on the main Himalayan thrust. Geophys. Res. Lett. 42, 5828–5837. http://dx.doi.org/10.1002/2015GL064845.
Szeliga, W., Melbourne, T., Santillan, M., Miller, M., 2008. GPS constraints on 34 slow slip events within the Cascadia subduction zone, 1997–2005. J. Geophys. Res. vol. 110 (Solid Earth), 113, B04404. http://dx.doi.org/10.1029/2007JB004948.
Waldhauser, F., Ellsworth, W.L., 2000. A double-difference earthquake location algorithm: method and application to the Northern Hayward Fault, California. Bull. Seismol. Soc. Am. 90 (6), 1353–1368.
Yatagai, A., Kamiguchi, K., Arakawa, O., Hamada, A., Yasutomi, N., Kitoh, A., 2012. Aphrodite. Constructing a long-term daily gridded precipitation dataset for Asia based on a dense network of rain gauges. Am. Meteorol. Soc., Q07023 http://dx.doi.org/10.1029/2011GC003513.
Zahradnik, J., Jansky, J., Plicka, V., 2008. Detailed waveform inversion for Moment Tensor of M ~ 4 events: examples from Corinth Gulf, Greece. Bull. Seismol. Soc. Am. 98 (6), 2756–2771. http://dx.doi.org/10.1785/0120080124.

CHAPITRE 3

West Nepal: Temporary Seismic Network and data processing

3.1. Temporary Seismological Network

The deployment of a temporary seismological network (TSN) was an unprecedented experiment in western Nepal. Initially planned to cover a two-year period, from spring 2014 to spring 2016, the network was finally deployed in November 2014 due to transport and custom delays. Because of the occurrence of the Gorkha earthquake in April 2015, after a few months of deployment, we got the opportunity to extend the deployment until October 2016. The original project was to install 20 seismological stations, but finally there were 17 stations available. In order to benefit from spare parts, we decided to install only 15 monuments, 2 stations being kept as spare for the revisits. These instruments belonged to SisMob which is the French national pool of terrestrial mobile seismological instruments.

I took part in the project from the very beginning. I made a proposition of sites according to the scientific requirements (limited background noise level, good azimuthal coverage, at least 3 stations above the most interesting clusters, optimized distances between stations ...) but also according to the logistic requirements. Indeed, the area covered by the project is not very accessible. Furthermore, the local road conditions were poorly known by our collaborators in France and in Nepal because the area was under road network development. I therefore tried to identify from the laboratory with a few documents made available if routes or tracks were allowing an access with a vehicle to the regions, and if not how much time would be necessary to walk to targeted places. Afterwards, I organized a first mission in May 2014 (initially planned for equipment reception) to survey potential sites in Dailekh, Bajhang and Bajura Districts with Ramesh Pandey from NSC. My stay in May 2014 was valuable: we discovered accesses that were not spotted on the maps, estimated "travel-times" between villages and had a first contact with local people. This mission was very helpful afterwards when installing.

I also participated in the preparation of the equipment, deployed 10 stations during the installation mission (November-December 2014) (Laurent Bollinger and Ratnamani Gupta installed 3 stations; Mukunda Bhattarai, Ramesh Pandey and me installed seven stations. Other participants: Hélène Lyon-Caen and Bharat Prasad Koirala. We installed four stations together) and participated in the first visit organized to

download the first months of data available (April-May 2015) (Jean Letort and me with Mukunda Bhattarai and Thakur Prasad Kandel). I later exchanged with the different teams which revisited the network and helped organized the revisit schedules in October 2015 (Jean Letort and Mukunda Battharai, Christian Baillard and Ratnamani Gupta) and April 2016 (Eric Jacques and Rémy Matrau with Thakur Prasad Kandel and Ratnamani Gupta). The dismantling mission was entirely handled by our Nepalese colleagues of the RSC and NSC (Mukunda Battharai, Ratnamani Gupta and Kapil Maharjan). Together with Hélène Lyon-Caen and Laurent Bollinger, we remained in contact with the teams in the field during every mission.

This section presents the sites, stations and their performance during the seismological experiment.

3.1.1. Network Geometry

The network geometry was defined according to the distribution of the seismicity and taking into account an efficient logistics to install and revisit the sites (Figure 3.1). The goal was to cover the three belts of seismicity in order to better resolve the lateral variations in the seismicity and their relations with the local tectonic structures. In each area the best inter-stations distance was set to the expected depth of the earthquakes (~10-20 km). This condition was well respected for the western and southern belts. However, because of the difficult accessibility to the northern area as well as because we had a limited number of stations, we privileged a group of 3 stations as close as possible to the seismicity of the northern cluster as well as an additional station north in order to bring the aperture of the network.

The three zones targeted were:

Zone 0 located in Bajhang District to record the Bajhang seismicity belt (Figure 3.1). Six stations were deployed in Bijgada (BJ01), Deura (DE02), Matela (ML04), Chainpur (CH06), Wariana (WA07) and Talkot (TK08).

Zone 1 located in Dailekh District to record the South Karnali seismicity belt (Figure 3.1). Here, the belt is narrower than elsewhere, so four stations were deployed in Kusapani (KS11), Dullu (DU12), Dailekh (DK13) and Naumule (NU14)

Zone 2 spread out in Humla, Mugu, Jumla and Bajura Districts to record the North Karnali seismicity belt (Figure 3.1). A total of five stations were installed in Martadi (MA10), Simikot (SM15), Gamgadhi (GH25), Sinja (SJ26) and Jumla (JL27).

See the Annex C for further information on the stations.

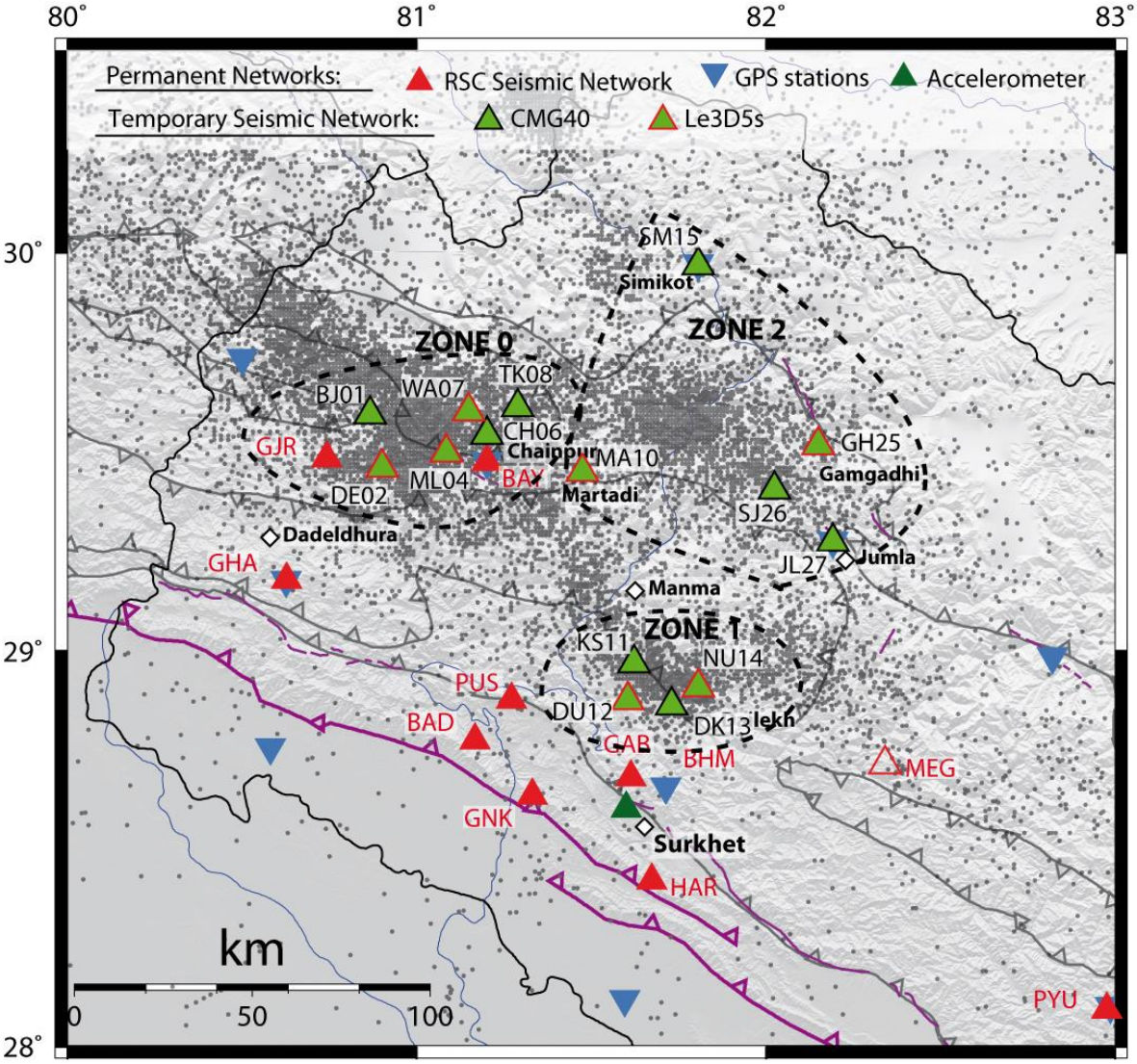

Figure 3.1. Map of western Nepal (Mid and Far Western Regions) with the stations of the permanent networks (seismological in red, GPS in blue and accelerometer in dark green) and the stations of our temporary seismological experiment (November 2014 – October 2016) in green. Note that Simikot station (SM15) was only deployed on April the 25th 2015, a few minutes after the Gorkha earthquake. Black points are the earthquake epicenters located at RSC for the period 1993-2012; the active faults are indicated in purple (MFT – thick line and active faults of Nakata, 1982 – thin lines) and the trace of ancient MHT surface traces in gray. The main cities around the experiments are signalized by the white diamonds.

3.1.2. Sites characteristics

The choice of the type of sites was largely discussed with H. Lyon-Caen and with the National Seismological Centre (NSC) collaborators who had numerous experiences of temporary deployment. The first mission was entirely dedicated to the research of potential sites.

We selected sites which follow some or all of the following characteristics, which we tried to stick with as much as possible:

1) Permanent stations of the Nepalese seismological network are on bedrock. Because a good compromise between soil thickness and bedrock distance is required to record a good signal, we selected sites as close as possible from the bedrock.

2) South orientated sites were selected most of the time to optimize the solar energy supply.

3) Whenever possible, far from roads, villages or rivers. The minimum distance considered between a 100 inhabitant's village and a station was considered to be between 200 and 300 m (Figure 3.2).

4) Private properties (11 stations) or Government land (4 stations) are highly recommended for safety reasons for the station (Figure 3.2).

(a)

(b)

(c)

Figure 3.2. Representative examples of station sites with its noise sources. (a) BJ01, Zone 0, with a rather short distance to the river (200 m), a potential source of high frequency seismic noise (Burtin et al., 2008). A steep slope, as in most of the sites considered. (b) and (c) DU12 and KS11 respectively, Zone 1, illustrate the short distances of most of the stations to human activity.

3.1.3. Stations components and monument

The stations were composed by a seismometer (CMG40 or Le3D5s), a Taurus digitizer recording the signals in the original format on a compact flash card (CF store) as well as miniseed on an additional CF card (Figure 3.3). The digitizer is connected to a Global Positioning System (GPS) antenna for precise time acquisition. The Taurus digitizer is connected to a battery that was connected to two solar panels for energy supply (Figure 3.3).

The architecture of the station monuments was another largely discussed subject. We took into account the advices from officers and technical staff of the NSC who benefited from the feedback of several field experiences (including the Himnt (e.g. Schulte-Pelkum et al., 2005) and HiCLIMB projects during which more than one hundred stations were deployed (Nabelek et al., 2009)). We also benefited from the experience of György Hetényi, partner in the ANR Bhutanepal, who deployed a temporary seismological network in Bhutan. His recent experience was very useful on the choices we made.

The main hazards that could affect the monuments include among others water and animals. The monsoon is source of heavy rains across the Himalayas and soils become saturated in water. We therefore tried to limit the influence of water and moisture on the digitizer, the battery and the seismometer. The seismometers were buried in agricultural lands mostly. In order to keep the seismometer in a flat position and well coupled to the underlying basement, the instrument was put on a concrete basement with a ceramic slab leveled horizontal and covered with a hard plastic barrel then sealed (Figure 3.3.c and d). Because the digitizer and battery needed to remain accessible during the revisits, they were kept inside a plastic bucket under the solar panels (Figure 3.3.d). The GPS wire was protected with a wire protection to limit the exposure to hungry rodents and monkeys.

The sites being located in areas where the main activity is agriculture and livestock, animals were likely to generate seismic noises and/or damage the instruments. For that reason, the monument was protected by a fence, barrier to intruders and extra noises in the immediate vicinity of the seismometer (Figure 3.3.e).

(a)

(b)

(c)

(d)

(e)

Figure 3.3. Station components and monument. (a) Seismometer CMG40. (b) Taurus digitizer and the battery. (c) Seismometer monument: a bottom-opened hard plastic barrel sunk in the concrete with a ceramic slab inside. The hole made with the metal rod in the barrel is necessary for inserting a cable that connects the seismometer and the digitizer. (d) The seismometer is then isolated after sealing the cable in the hole and closing the plastic barrel which is buried during the whole experiment. The digitizer and the battery were kept in a plastic bucket and placed under the solar panels. (e) The station was protected by a thick plastic sheet.

3.1.4. Station performances

The seismometers were intermediate period instruments CMG40 and Le3D5s, from which we installed 8 and 7 respectively. The sampling rate was set to 100 samples per second.

Because telemetry was not an option given the telecommunication availability in the remote regions covered by the network, the status of the stations and the signals recorded were only known after revisits of the stations (we planned 3 revisits in April 2015, October 2015 and April 2016 before dismantling in order to limit the amount of data lost because of station unavailability).During the first year, almost all stations recorded continuously during the dry season while 1/3 of them failed after the first revisit or during the summer monsoon (Figure 3.4.a and b). The second year of deployment, most of the stations recorded continuously even during the summer monsoon (Figure 3.4.c). Technically, the stations functioned quite well all along the experiment, with minor problems. For example BJ01 had a clock problem due to the fact that the GPS cable was cut probably because of a hungry rodent; SJ26 met unidentified digitizer problems despite the visits.

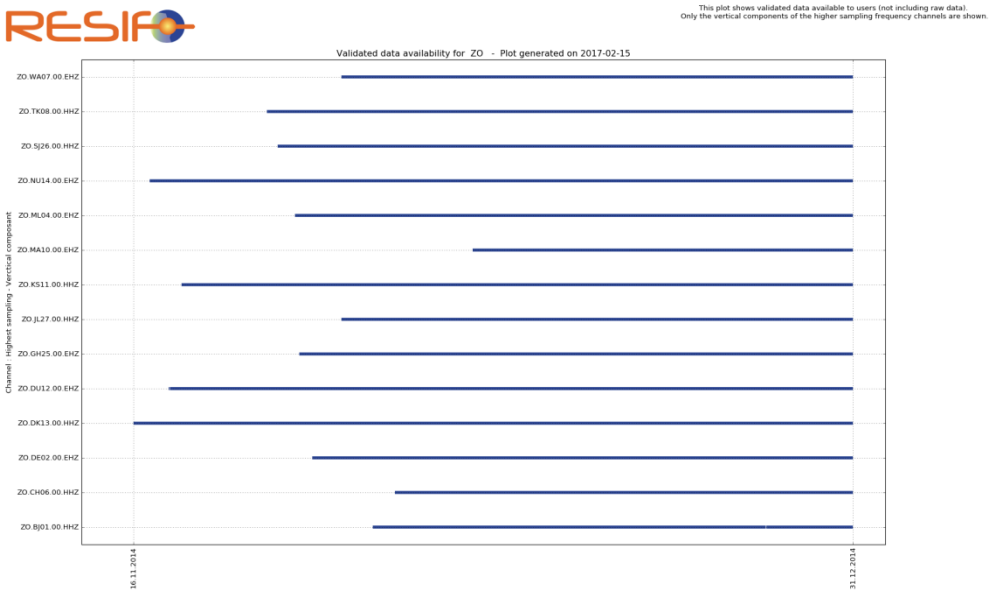

(a)

(b)

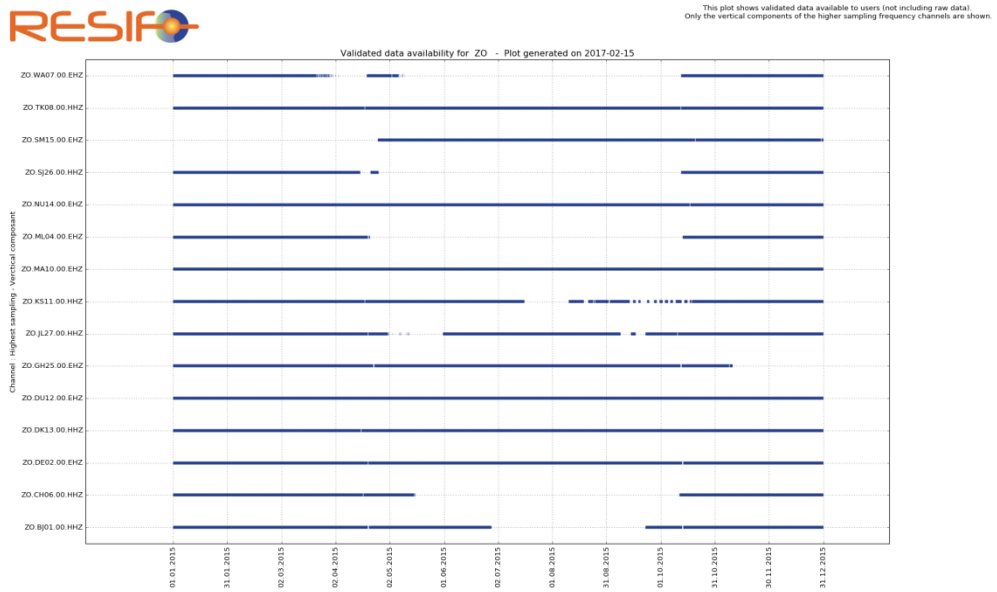

(c)

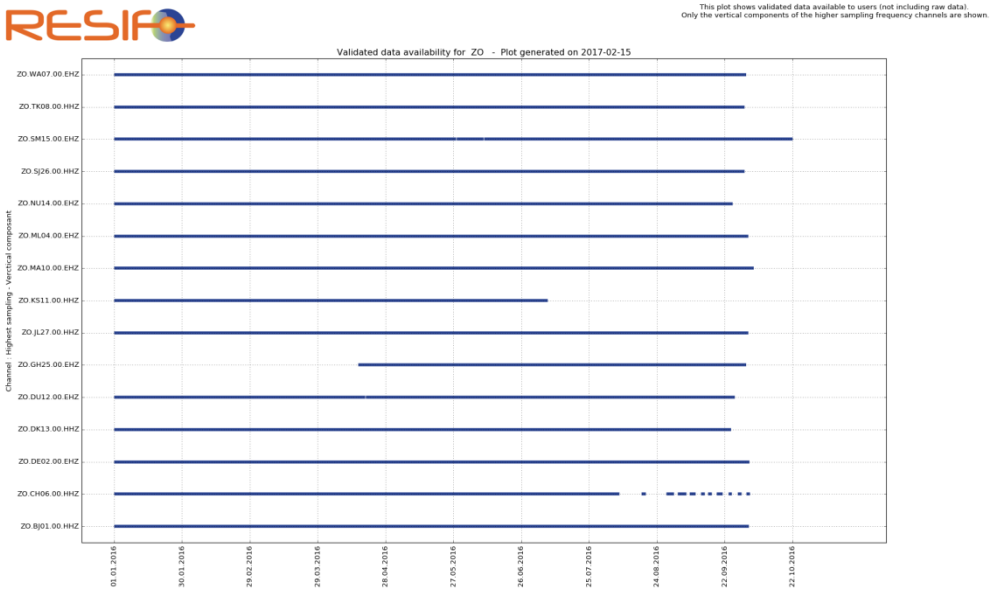

Figure 3.4. Timelines of seismological data recorded per station by the Temporary seismic stations. Blue lines correspond to the period covered by the data. (a) From the installation until the end of 2014. (b) Entire year 2015. (c) From January 2016 until dismantling in Autumn 2016.

3.2. Data used in this study

Because the network was deployed till the last year of my thesis, I limited my work to the first year of acquisition: from December 2014 until October 2015.

In addition to the signals acquired at the temporary stations, we benefited from the data recorded at the seismic stations of the permanent seismological network of RSC for the same period. Combining both networks we increased the number of stations to 24. The seismic catalogue produced by the RSC was further used in order to evaluate the performance of our data processing.

3.3. Data Processing

Several seismological software solutions are available to acquire and process the seismic signals. We used Seiscomp3 which is software that brings together the acquisition, the processing and the analysis of seismic data. It has been developed by GEOFON program, Helmholtz Centre Potsdam, GFZ German Research Centre for Geosciences and gempa GmbH. Seiscomp3 is largely used in the seismic and tsunami alert centers on the world (ex. CENtre d'Alerte aux Tsunami). Commonly used to treat the data flow in real-time, it offers also the possibility to process the data in off-line mode which was best-suited to our needs. In addition, the input and output file format (miniSEED and XML respectively) are standard formats that allows an easy exchange with other partners.

Seiscomp3 is divided into multiple modules connected to a master. We used the processing modules and the post-processing analysis modules which will be explained in the two following sections.

3.3.1. Seiscomp3 automatic data processing

3.3.1.1. Detection and association of phases

This first step focused on detecting the maximum number of events in our area of interest. For that, three main modules are used to obtain an automatic catalogue: scautopick, scanloc and scevent.

Scautopick detects P and S phases. It uses an automatic picker based on an STA/LTA algorithm(Short Time Average – Long Time Average) that consists in sliding two time windows (1,10[1]) along the signal and detect changes on the average amplitudes of the signal; the picker will be triggered over a certain threshold (2[1]) (Allen, 1982). The final pick of the phase is refined by the Akaike Information Criterion (AIC) which is a static method applied to the seismic signal. The picker is triggered when the AIC reaches a

[1] Value of parameter in our case of study.

certain value of signal-to-noise ratio minSNR, 3 in our case (Akaike, et al.,1973). Scanloc creates origins associating close P-phases using a cluster search method and calculating a location with LocSAT locator with iasp91 as velocity model (Kennett and Engdahl, 1991). Finally Scevent determines which origins present a good enough quality to be declared as event.

3.3.1.2. Parameters

The modules of Seiscomp3 have a default configuration adapted for teleseismic events. No Seiscomp3 configuration was optimized before for the Nepalese seismological network. In order to detect the maximum number of events, we needed to adapt the software configuration to our study. This task took time due to the large number of parameters taken into account in all modules (>100 parameters). We focused on the most critical parameters which are those related to the detector and picker, and the association of picks to create an origin. For example, in the case of the phase detection (detect filter, STA/LTA windows and triggers), we optimized the values by trial and error until the picks were satisfactory for most of the seismic network / epicenter configurations (Figure 3.5). The association of picks was highly influenced by the maximum search distance allowed to take picks into account and create an origin. If this value was kept to 60 seconds (default value), picks of different origins could be linked together; to solve this problem, we tested other values (20, 15, 10 seconds) that increased the association of picks to form origins (from 29 events for 60 seconds to a maximum of 47 events with 15 seconds). Another example is the *minsize* which is a minimum number of phases required to create an origin. We had to set the *minsize* to the low value of 3 phases in order to improve the performance on the association of phases, despite the larger number of stations picked.

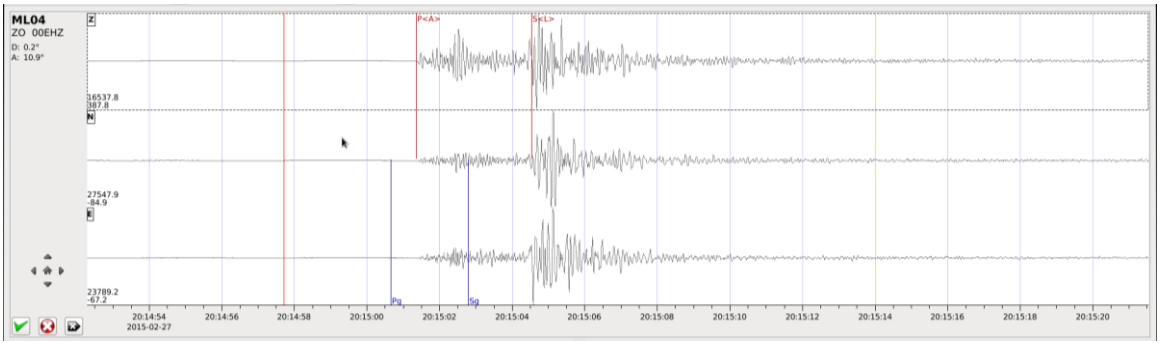

Figure 3.5. Example of a signal in ML04 station with an automatically picked event by Seiscomp3 in dark red. P-phase is picked on the vertical component and S-phase is picked on the horizontal components. The blue line corresponds to theoretical arrivals after localization. The velocity model is not adapted to the area of study because it predicts a phase arrival too early.

3.3.1.3. Preliminary results

The first automatic processing carried out in Seiscomp3 allowed detecting and localizing 6529 events. These events are mainly located in our area of study (See Figure 3.6 for an illustration covering the first months of acquisition). The seismicity appeared very dense inside the network especially in the Zone 0 and 2 (Figure 3.6). The seismicity spreads on a 60-70 km-wide area with a southern limit ~50 km north from the MFT. The depth of the hypocenters falls mostly between 0 and 30 km (Figure 3.6).

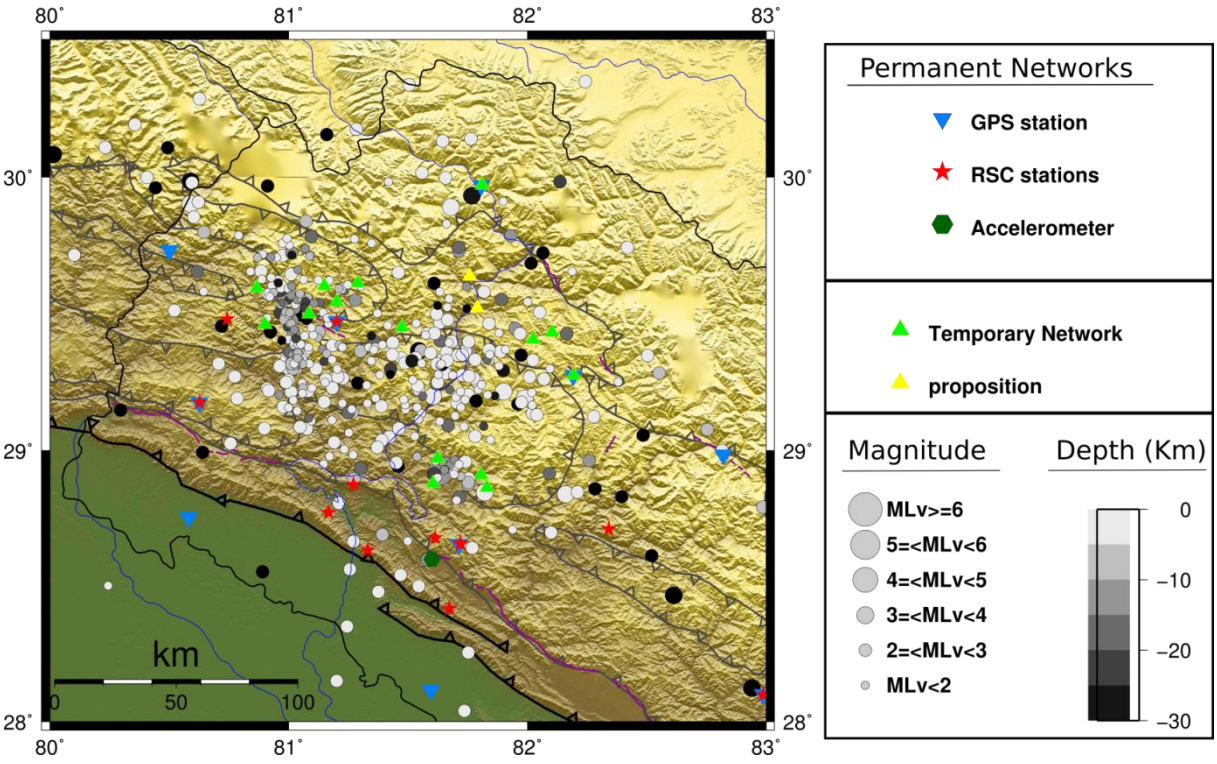

Figure 3.6. Map of the seismicity processed automatically under Seiscomp3. This map covers the period January – March 2015. 401 events were detected by Seiscomp3 in this frame whereas the RSC catalogue integrate 260 events for the same period and frame. Black line is the Main Himalayan Thrust. Gray lines are MBT and MCT. Purple lines are the active faults of Nakata, 1982.

3.3.1.4. Limits

The number of events detected appears satisfying when comparing to the RSC catalogue (Figure 3.6).The number of events detected is twice larger than the number of events detected by the RSC for the same period of time. The comparison between the two catalogues will be presented later on in section *3.4 Comparison between RSC catalogue and our study*.

Nevertheless, looking closely at the signals and at the results of the automatic data processing, we noticed that:

1- There are stations where the signal of the event stands out from the seismic noise but no pick has been done or phases are wrongly identified (Figure 3.7).

2- The automatic picks include neither the weight of the pick itself nor the polarity of first arrival. These are important information to consider a pick on the localization process and an eventual focal mechanism attempt.

3- The LocSAT locator does not allow associating weights to the picks, despite the interest to weight them as a function of the distance to the epicenter. This could be interesting because the arrivals of phases are usually "clearer" at the closest stations than at the distant ones. Hypo71 program differs from LocSAT because it does a weight in function of the quality of the picking, distinguishing P and S picks, and a weight in function of the distance of the station to the epicenter (see section *3.3.2.2. Hypo 71 plugin profiles*).

(a)

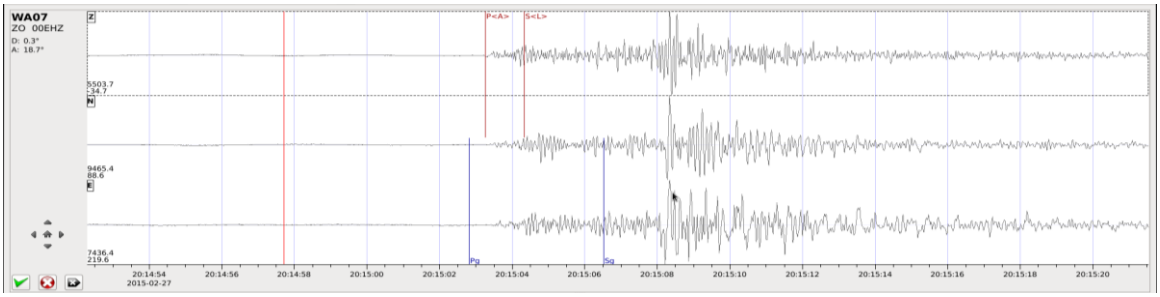

(b)

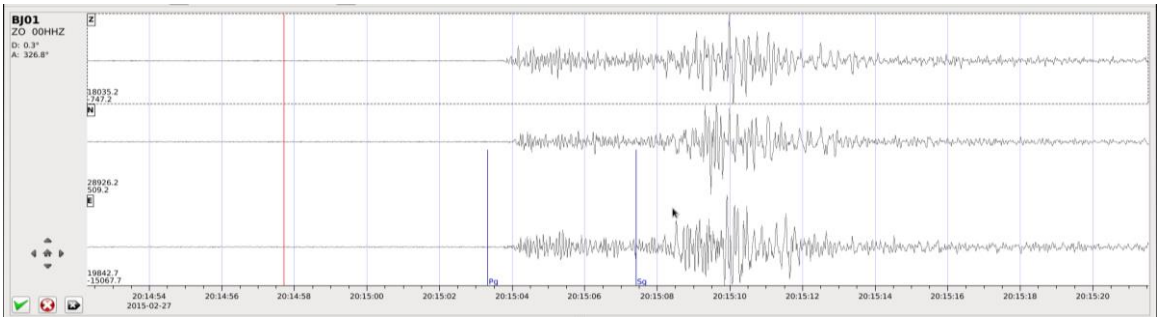

(c)

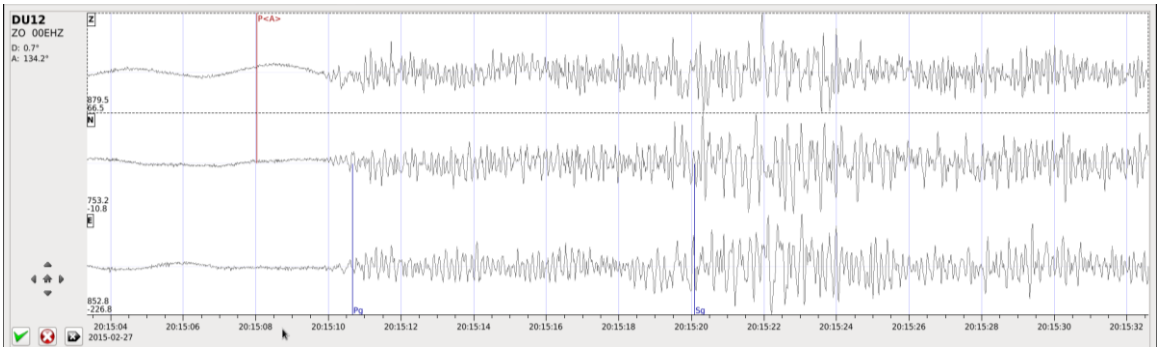

Figure 3.7. Example of signals at WA07, BJ01 and DU12 stations with wrong automatic picks in dark red. (a) S-phase is picked too early from the S-phase arrival. (b) Absence of automatic picks. (c) P-phase is picked too early from the P-phase arrival.

3.3.2. Seiscomp3 manual post-processing

A reliable location of the events, associated with quantified uncertainties, is critical for the seismotectonic interpretation. That is why we considered a manual revision of each event detected in the previous section as well as an alternative location algorithm.

3.3.2.1. Manual picking

We used the module scolv to revise manually each event detected. We distinguished and tagged 3 types of events:

- *Earthquake*: regional seismic event with a delay P-S inferior to 20 seconds.
- *Out of Network of Interest* (ONI): seismic events with a delay P-S superior to 20 seconds.
- *Others*: includes duplicate events, fake events and not locatable events.

ONI and *Others* were not picked nor localized. We only revised events of *Earthquake* type.

We first filtered the data between 1-15 Hz and 1-25 Hz using a Butterworth filter of 3rd order. Then we picked P- and S- phase when possible assigning an uncertainty in time on the location of the pick and a polarity sense (positive or negative) (Figure 3.8).

Again, we used this module in off-line mode which is the only way to read the .xml files. Unfortunately, this mode only allows the effective revision of events declared as "Associated". If an event is declared as "Unassociated" or has not been picked, it will not be possible to add them into the XML file. The loss is approximately of 2%.

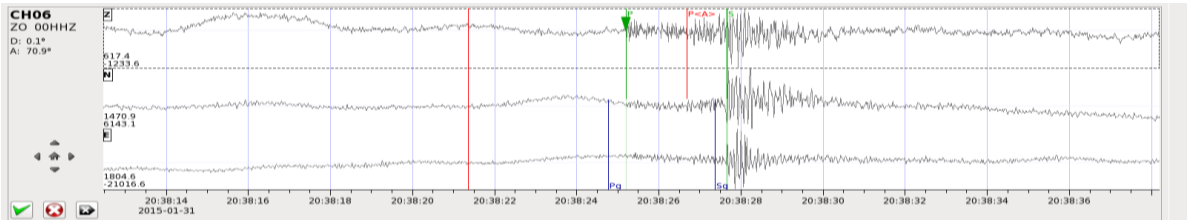

Figure 3.8. Example of signal of CH06 station with a manually revised picks in green. The green triangle represents the polarity. Light red pick is the automatic pick.

3.3.2.2. Hypo 71 plugin profiles

Hypo71 is a program that determines hypocenter, magnitude and angle of incidence of local earthquakes (Lee and Lahr, 1975) in which the user can fix a weight to the picks as a function of the epicentral distance. This is a useful functionality, the best picks being usually determined at the shortest epicentral distances, whereas the picks at the stations far from the epicenter may add errors to the hypocenter calculation. The

Observatoire Volcanologique et Sismologique de Martinique (OVSM-IPGP) developed a plug-in of Hypo71 for Seiscomp3. This program has mainly two advantages for us: (1) the weighting according to epicentral distance and (2) the use of a regional velocity model which is more adapted than the global earth velocity model iasp91, in our case we used the velocity model obtained by Pandey, 1985 based on local seismicity in east and central Nepal (Table 1.1).

We created three profiles in the plug-in:

Profile C is useful for the closest events to the seismic stations. The stations located up to 20 km from the source will have the maximum weight on the localization process. On the contrary, the stations farther than 60 km will be weighted to 0 and so they will not be used to locate the event. In this case, the events are more likely to be located by one of the sub-networks rather than the whole network.

Profile B has been conceived to locate events far from the stations but in the area of interest like the Zone 2. The stations located up to 50 km from the source will have the maximum weight on the localization process. On the contrary, the stations farther than 150 km will be weighted to 0 and so they will not be used to locate the event.

Profile A is a modified Profile C for events close to the stations but recorded by a small number of stations around. The stations located up to 20 km from the source will have the maximum weight on the localization process. On the contrary, the stations farther than 80 km will be weighted to 0 and so they will not be used to locate the event.

3.3.2.3. Preliminary results

The manual data processing helped to distinguish real events in the area of interest and *ONI* and *Others* (Table 3.1). The distribution of *Earthquake*, *ONI* and *Others* during the months is very interesting (Figure 3.9). We can see that the number of events in our area of study is high from December 2014 to March 2015. The amount of *Earthquake* decreases from April to August and increases again around September (Figure 3.9). During the months of April and May, the sudden increase of the number *ONI* is due to the large number of aftershocks following the April 25th Gorkha earthquake and the 12th May Kodari earthquakes. Finally, during June, July, August and September the number of *Others (fake/duplicate/non locatable events)* is higher than during the first months of the experiment (Figure 3.9). This is partly due to the fact that one third of the seismic stations were not recording during that period (Figure 3.4). Further note that during this period the area is affected by the monsoon and its effects (high river discharge, motion of the bed load on the river bedrock, landslides …) responsible for an increase of the high frequency seismic noise (Burtin et al., 2008; 2009). These effects are also partially responsible of the increase in "fake" or "not locatable" events ("Others" type).

Most of the events could be relocated with Profile C, and a minority of events had to be relocated with the other profiles (Table 3.2).

Type of event	Number of events
Earthquake	2245
ONI	3201
Other	1081

Table 3.1. Total number of each type of events defined for the revision.

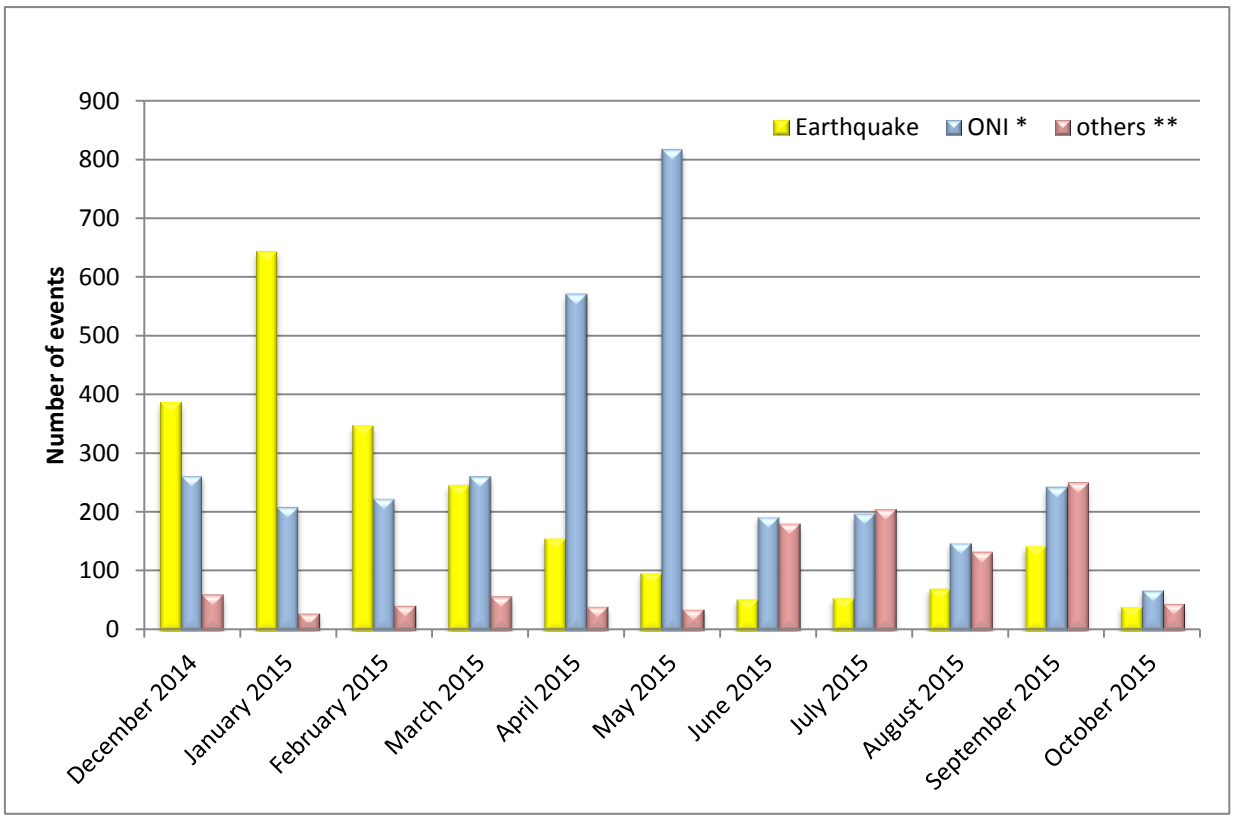

Figure 3.9. Histogram of the number of events detected per month depending on the manual revision classification: local earthquakes (Earthquake -yellow), *out of network of interest (ONI blue), **Others – including duplicate, fake events and not locatable events (salmon). Note the increase of the number of these events from June to September, a period during which (1) one third of the stations were not recording (Figure 3.4) and (2) high frequency seismic noise increases following the high river discharge, associated bedload transport, and landslide generation.

Profile	Number of events localized
Profile C	1877
Profile B	186
Others	182
Total	2245

Table 3.2. Number of events relocated with each profile. Others include events located with Profile A and events that could only be relocated with LocSAT locator and Iasp91 velocity model.

The spatial distribution of the events after the Seiscomp3 manual post-processing reminds the shape of pitch-fork that we expected (Figure 3.10). The results observed in Figure 3.6 were definitely perturbed by the presence of events of type *ONI* and *Others*, especially in Zone 2 where there is a lower number of events than in the catalogue generated after the Seiscomp3 automatic data processing.

More than 60 % of the events are localized with at least 10 phases, reaching a maximum of >40 phases (Figure 3.11). Finally, the root mean square (RMS) misfit is inferior or equal to 0.2 seconds for almost all events (Figure 3.12). The horizontal uncertainties of the events are below 1 km inside the network because of the good station coverage (Figure 3.10.a). The depth of the events is well resolved, with uncertainties below 1 km, for events very close to the stations (Figure 3.10.b). However, the events outside of the network or inter-subnetwork are associated to depth uncertainties higher than 2.5 km (Figure 3.10.b).

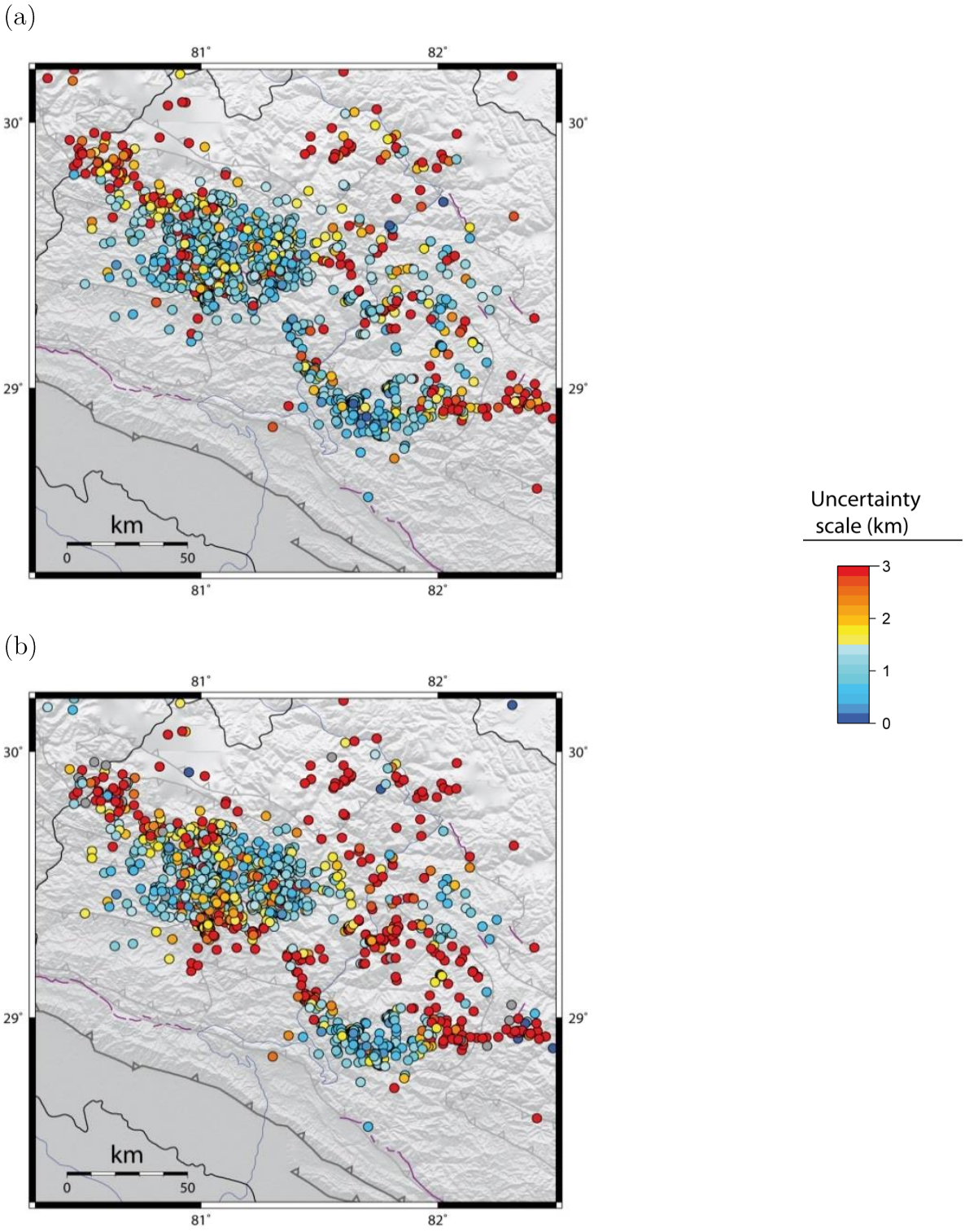

Figure 3.10. Map of the seismicity manually revised tagged as *Earthquake*. The color scale represents the (a) horizontal uncertainty and (b) depth uncertainty in kilometers.

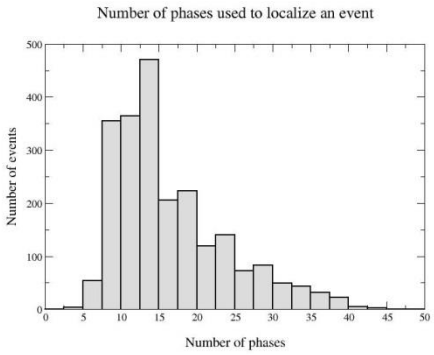

Figure 3.11. Histogram of the number of picks (P- and S- phases) per event manually revised and tagged as *Earthquake*.

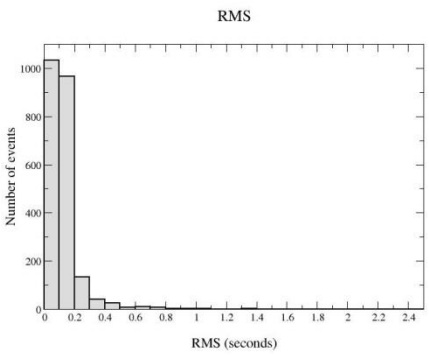

Figure 3.12. Histogram of the RMS per event manually revised and tagged as *Earthquake*.

3.3.2.4. Limits

The weight of the pick in Seiscomp3 represents the uncertainty in time of the emplacement of the pick. Hypo71 integrates a weight for the picks which depends on the analyst confidence, a confidence rated from 0 to 4, with 0 full weight, 1 ¾ weight, 2 ½ weight, 3 ¼ weight and 4 no weight. However, in the plugin Hypo71 in Seiscomp3 the weights of the phases are defined relatively only to the weights of phases in that event, weighting the lowest uncertainty 0 and the highest uncertainty 4. The result of this way of weighting is a heterogeneous calculation uncertainty in the catalogue and then the events cannot be compared. We solve the problem using the source program of Hypo71 (see section *3.3.3. Hypo71 – Localization Program*)

3.3.2.5. Magnitude MLv

Seiscomp3 calculates automatically a magnitude MLv for each event. The MLv is the Richter, 1935 magnitude but the amplitude is measured on the vertical component (Seiscomp3, 2013).

The distribution of magnitudes in our catalogue of local earthquakes covers the range 0 to 5.2, with a 93% of events under MLv≤2.0 which do not contribute much to seismic moment released (Figure 3.13). The number of the smallest events (with magnitudes between 0 and 1) varies in time (Figure 3.13). Indeed, from December 2014 to March 2015, the minimal magnitude is close to 0 and increases afterwards until the beginning of July 2015 reaching a value of 1.0. The minimal magnitude MLv starts decreasing from August 2015 until the end of our period of study, October 10th. Nevertheless, it does not reach the minimal values of the first period studied. Therefore, we would need to process the rest of the data acquired by the temporary network to see if the tendency continues.

Independently from the magnitude, the number of events in the local earthquake catalogue is low during the summer monsoon 2015 (July and August) compared to

other periods (this is probably partially due to the low number of stations acquiring during this period). Another important feature is the intense activity during the first's months, specifically between December 2014 and February 2015, with a seismic activity clustered in time.

(a)

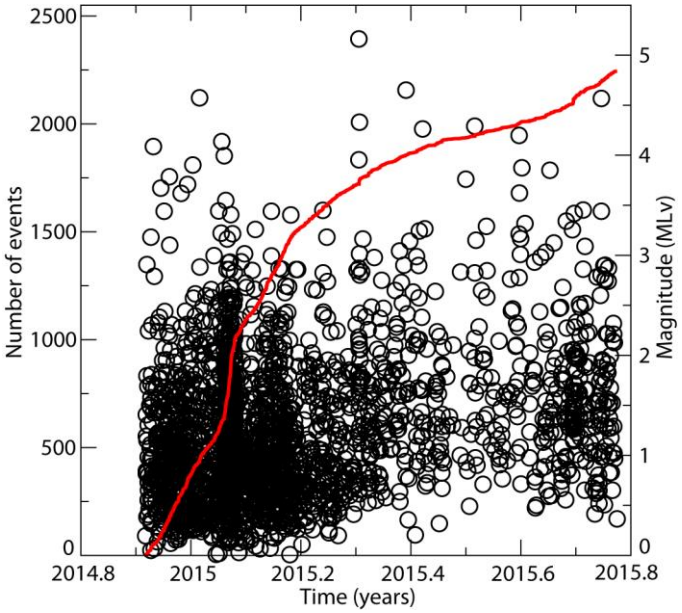

(b)

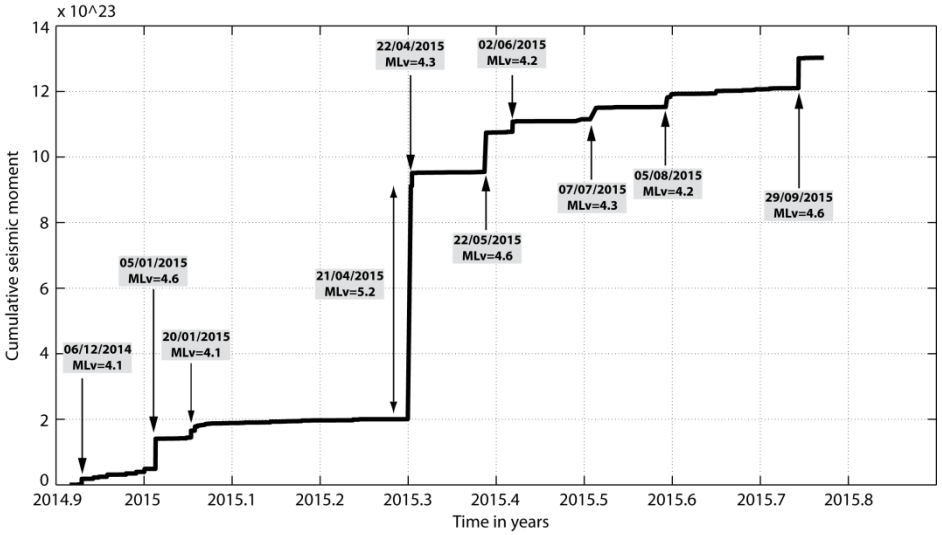

Figure 3.13. (a) Distribution of the local earthquakes as a function of time of the TSN catalogue. The red line represents the cumulative number of events (left y-axis). The black circles represent the magnitude M_{Lv} (scaled on the right y-axis). See Figure 3.19 for a histogram of the magnitudes. (b) Estimation of cumulative seismic moment of the events of Figure 3.13.a assuming that MLv is equivalent to Mw. Events of magnitude MLv≥4.0 in gray boxes.

The Seiscomp3 MLv calculated for western Nepal local events can be compared with the ML of the RSC catalogue (see *Chapter 1* section *1.2.1.1. Traitement des données*) and the mb of events determined by the International Data Centre, CTBTO.

The Seiscomp3 catalogue and the RSC catalogue share 467 common events with a determined magnitude. We calculate a linear regression in the cloud of points that leads to a relation between MLv and ML of: $ML = 0.97137 + 0.86866 \times MLv$ (Figure 3.14.a). The difference between the MLv and the ML is inversely proportional to the magnitude, in other words, the difference between MLv and ML is greater with small magnitudes and smaller for larger magnitudes (Figure 3.14.a).

The relation between the MLv and the mb_IDC is not as robust because only 23 events are common between both catalogues (Figure 3.14.b). In addition, some events of magnitude MLv~3.4 and others at mb~4.8 do not follow the general tendency of the rest of the events. We have tested the linear relation between both types of magnitude taking into account: (1) the 23 events, (2) events with MLv≥3.5 and (3) events with 3.5≤MLv≤4.8 (Figure 3.14.b). Depending on the set, the relation between MLv and mb_IDC is different. In general the relation can differ from ~0.1 to ~0.2 on the magnitudes. We consider the relation poorly constrained with the actual TSN catalogue.

(a)

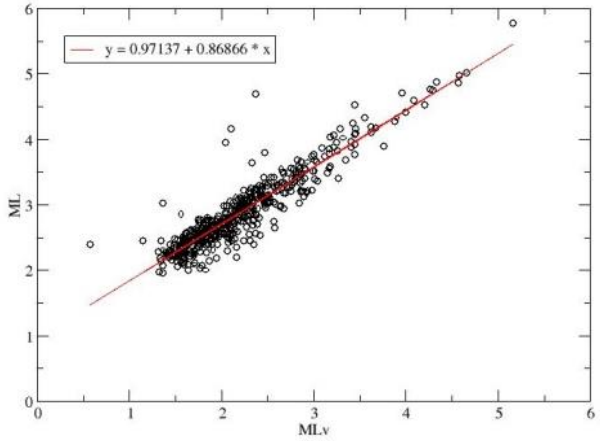

(b)

(1)

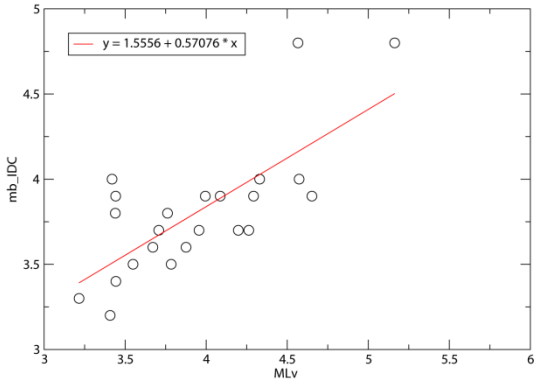

(2)

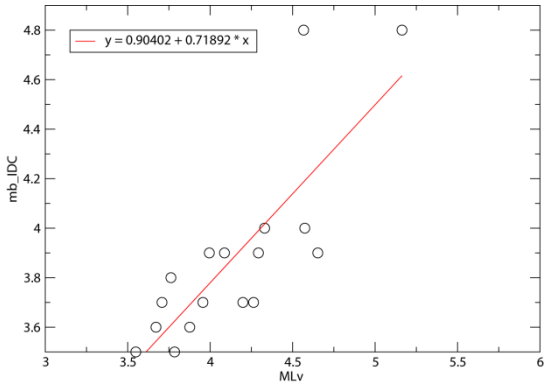

(3)

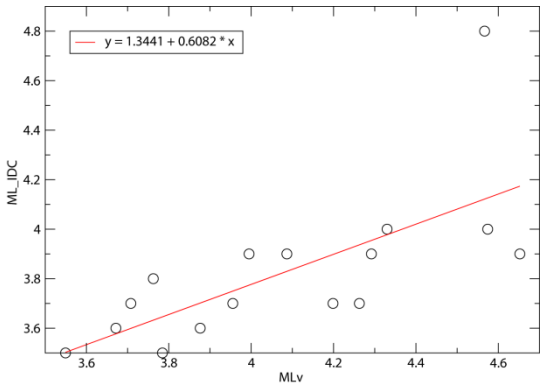

Figure 3.14. Magnitude relationship for events common to our study, to the RSC catalogue, and to the ISC catalogue. (a) RSC magnitude in function of Seiscomp3 magnitude MLv, (b) IDC magnitude mb of the International Seismological Centre in function of Seiscomp3 magnitude MLv for (1) the 23 events, (2) events with MLv≥3.5 and (3) events with 3.5≤MLv≤4.8.

3.3.3. Hypo71 – Localization Program

The aim of localizing the events with Hypo71 was to add a coefficient to station in the localization process depending on the epicentral distance and a differential weighting between P and S picks. The plug-in Hypo71 in Seiscomp3 presented a problem of homogeneity in the weighting along the catalogue. We thus used the source program of Hypo71 (Lee and Lahr, 1975) to localize the events picked manually in Seiscomp3.

3.3.3.1. Procedure

Before starting, we first transformed the Seiscomp3 weights into Hypo71 weights.

The difference between the plug-in and the program Hypo71 is that the program accepts only one set-up/profile at a time. There were different ways to approach the problem, either localize all the events with only one of the profiles, localize the events depending on the profile used in the plug-in Hypo71 in Seiscomp3, or localize a maximum number of events with the Profile C (phase weight = 1 up to 20 km; phase weight = 0 over 60 km) and the rest with the Profile B (phase weight = 1 up to 50 km; phase weight = 0 over 150 km).

We localized the whole set of data with only one set-up (i.e. profile C). We rapidly realized that some of the events localized with Profile B in Seiscomp3 can actually be localized with Profile C (Table 3.3).

Profile	**Number of events localized**	**Percentage of events localized**
Profile C	2156	95.5 %
Profile B	2232	98 %

Table 3.3. Number of events relocated with each profile using the whole set of data in each case.

We then compared the events localized with both profiles and looked at the differences to see if relocating with different profiles makes a real difference. For that we split the results depending on their localization and we kept only the events with at least 6 P-phases and 3 S-phases in profile B, a maximum RMS misfit of 0.4 and a maximum horizontal and depth error of 2 km. This selection helps to compare the Profiles with the best located events which represent 40% of the common events between Profile C and B.

We defined two sub-zones in Zone *W* (663 events) and Zone *S* (194 events) where we expect the best locations with Profile C and Zone *The Rest* (35 events) where Profile B should obtain better results.

In general, most of the events have been localized with a minimum of 12 phases independently of the Profile used (Figure 3.15.h). If we look to the epicenters location and origin time differences, there is no significant difference on using one profile or another to localize (Figure 3.15.a and c). The Zone *W* does not show any remarkable difference between both profiles except for the residual time (RMS) that is favorable to Profile C (Figure 3.15.b). However, the comparison of profiles in Zone *S* shows that the use of one profile or the other does make a difference: the RMS, the horizontal errors (ERH) and the vertical errors (ERZ) are clearly smaller in Profile C, so the short epicenter-station distance data is better explained (Figure 3.15.b, d and f). It reveals as well that Profile B tends to locate the events deeper than Profile C (Figure 3.15.e). This tendency is also observed in Zone *The Rest*. But it contains only few events so a robust conclusion cannot be given. Nevertheless, the depth error, the phases used to localize an event and the azimuthal gap support Profile B (Figure 3.15.f-h). With Profile C, too many stations are far away and not taken into account.

3.3.3.2. Preliminary results

The tests performed on the results depending on the Profile showed clearly a better quality of localization with Profile C at a very local scale (Zone S). On the contrary, events located in the network but distant to a station are better located with Profile B (Zone *The Rest*). According to these results, we localized the events in the closest areas to the westernmost and southernmost stations of the temporary network with Profile C and the rest of the events with Profile B (Figure 3.16).

We now obtain a reliable catalogue of events with a good estimation of the uncertainties. Looking at the best localized events, we observe that the horizontal and vertical uncertainties on the parameters are low (≤1.5 km) and so we consider the results to be the most reliable (Figure 3.16). We will consider later the catalogue generated by this approach as the most accurate in term of absolute earthquake location.

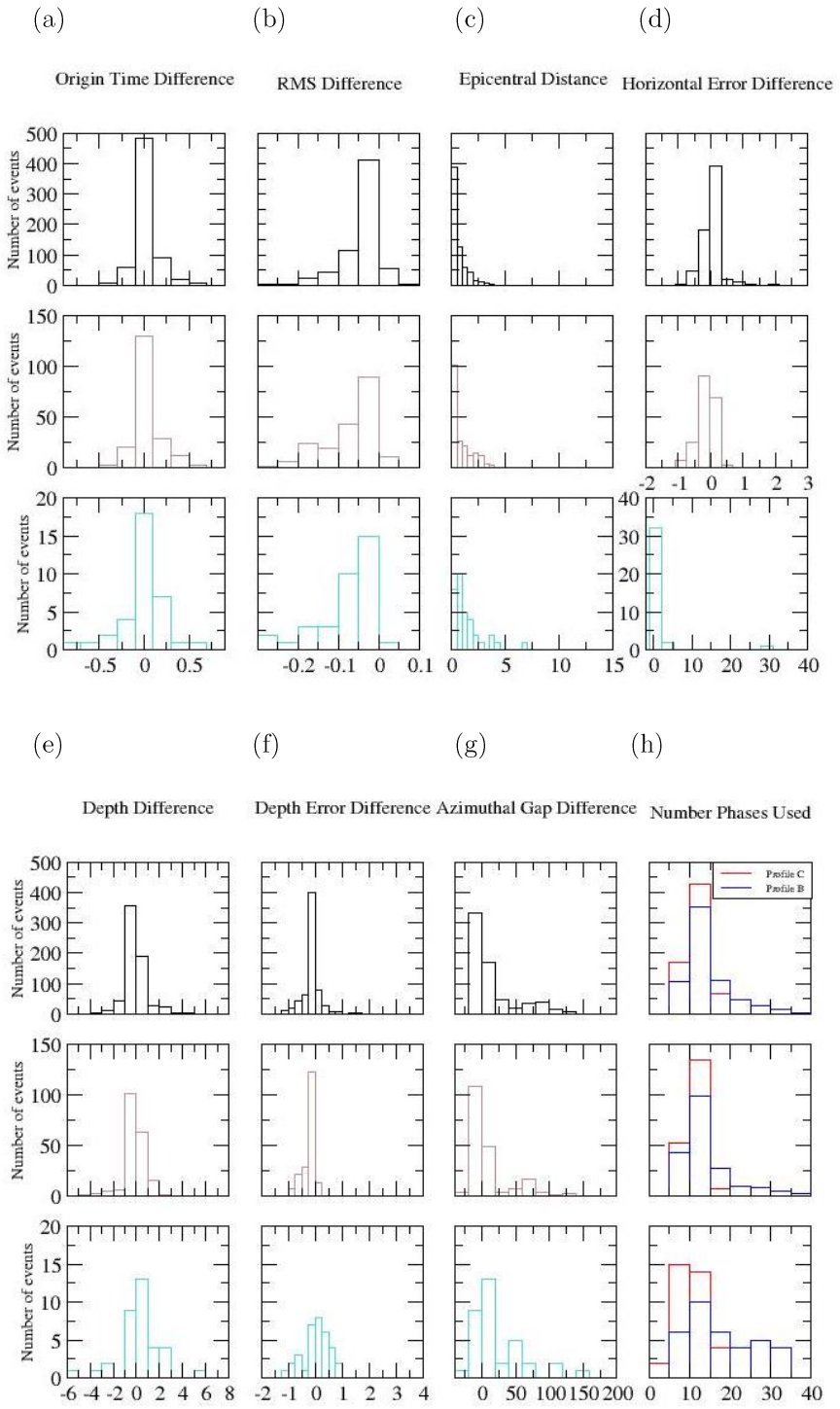

Figure 3.15. Differences between locations obtained using Profile C and Profile B for the three identified zones. Results for Zone *W* are shown in black, for Zone *S* in brown and for Zone *The Rest* in turquoise. (a) origin time difference, (b) RMS misfit difference, (c) epicentral distance between Profile C and Profile B solution, (d) horizontal error ERH difference, (e) depth difference between Profile C and Profile B solution, (f) depth error ERZ difference, (g) azimuthal gap difference and (h) number of phases used per Profile.

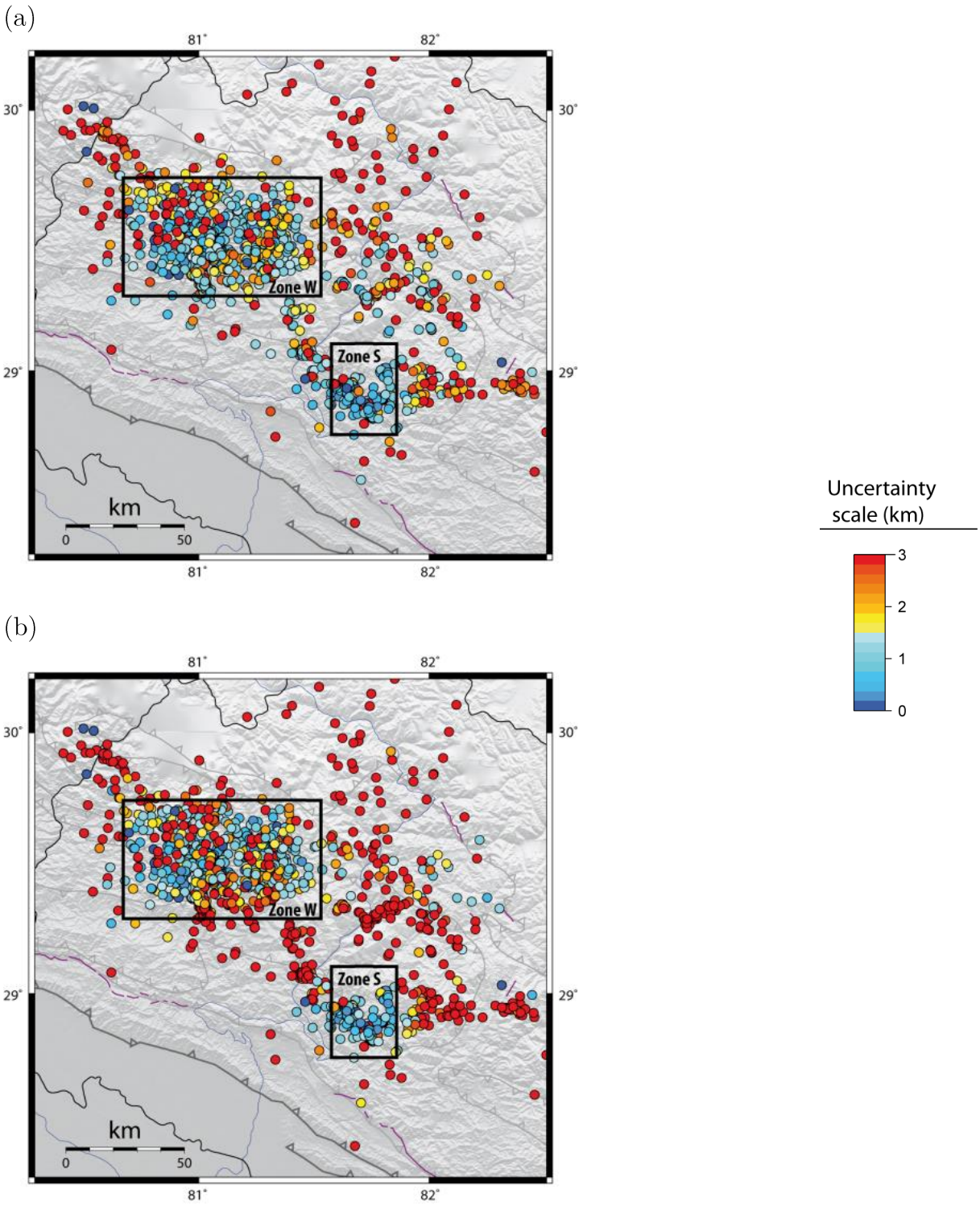

Figure 3.16. Map of the seismicity located with Hypo71 program. The color scale depends on the (a) horizontal uncertainty and (b) depth uncertainty in kilometers.

3.3.4. HypoDD

We used previously in Chapter 2 the double-difference algorithm HypoDD (Waldhauser and Ellsworth, 2000), in order to improve the relative location of the earthquakes and eventually relate their occurrence to the activation of a tectonic structure. We decide to use again this technique of relative relocation for Zone *S* and Zone *W* where multiple seismic clusters are present (Figure 3.17). Indeed, 2 main seismic clusters develop in Zone S, 4 in Zone W.

In both regions, the seismic stations are located above the seismicity and we are confident with the absolute location of the events. The configuration is therefore less challenging than in the case described in Chapter 2 where few stations at large epicentral distances recorded the events leading to large uncertainties on the absolute location. However, note that in both cases we were confident in the picked phases. We took advantage of the knowledge acquired in Chapter 2 to relocate the catalogue.

(a)

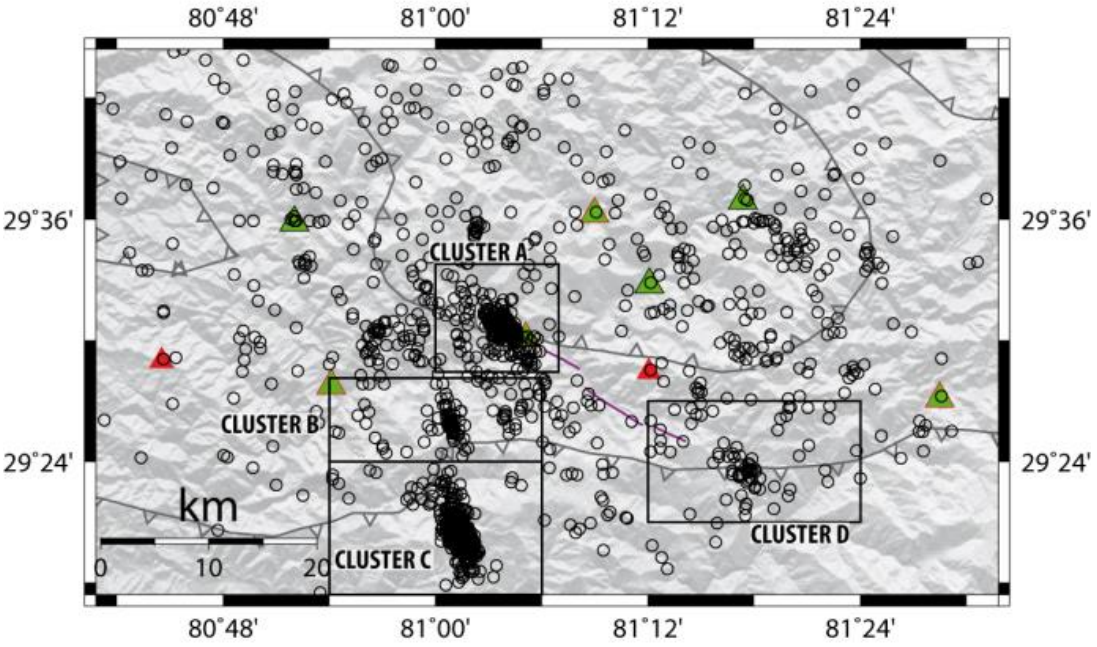

(b)

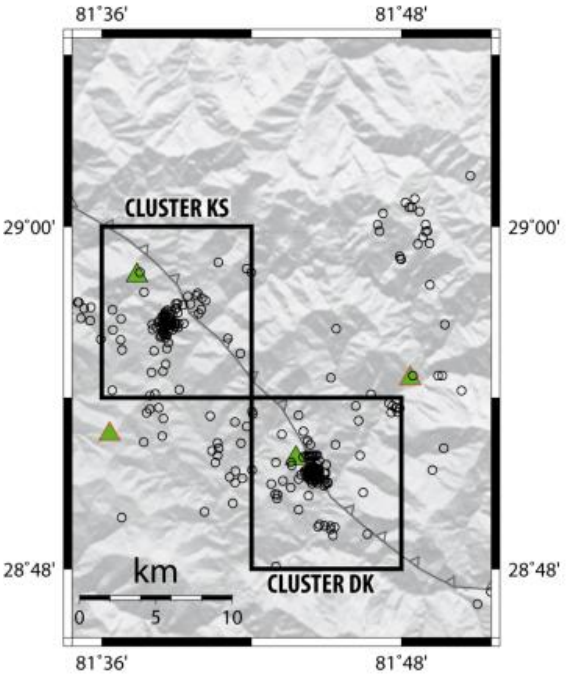

Figure 3.17. Zoom on the seismicity maps obtained after location with Hypo71 Program in Figure 3.16. Boxes (a) Zone W with 4 clusters and (b) Zone S with 2 clusters. Triangles are the seismological stations with the same color code than on Figure 3.1. Purple lines are the active faults of Nakata, 1982. Gray lines are the MCT.

3.3.4.1. Procedure

We parameterized separately Zone W and Zone S for two reasons: (1) the number of close stations to the clusters and (2) the mean number of average links per pair, higher in Zone W than in Zone S.

The first step in the relative relocation is the selection of pairs of phases at every station. We select for both Zones pairs of events with a maximum distance between the hypocenters of 5 km and a maximum number of neighbors per event of 10, limiting as much as possible the pairs to the closest neighbors. Moreover, in order to define an event as a neighbor, we set a minimum number of links of 12 for Zone W and 10 for Zone S. These values are rather conservative. The set of stations taken into account also influences the relocation process. In Hypo71, we weighted the stations depending on their epicentral distance. In order to be coherent with it, here we limited the distance between the event pair and the station to 80 km in Zone W and 70 km in Zone S. These distances are suitable to focus on the data of the closest stations and to keep a good azimuthal coverage of stations over an event pair.

The second step is the relocation itself that was parameterized equally for Zone W and Zone S. We performed the relocation using P- and S-phases, the velocity model and Vp/Vs of Pandey, 1985, and we resolve the relative relocation using the LSQR inversion (detailed in Chapter 2). The main parameters to test here are the iteration parameters. We define three sets of iterations described in Table.3.4 which are very similar to those used in Chapter 2. The two first sets work very well for the data of the temporary network; with a calculation converging rapidly to a solution. We then tested different values for the residual threshold (WRCT) in the last set of iterations. We first set this threshold at 5 seconds, leading to a rapidly converging solution. Despite that, the relative uncertainties remain relatively high (order of magnitude of hundreds of meters for both Zones). We tried also WRCT=2 which never converged and finally we set WRCT to 3 seconds, which is a good compromise between the convergence of the iterations and the relative uncertainties (~100 m for Zone W and <40 m for Zone S); it is also the minimum value recommended by Waldhauser and Ellsworth, 2000. We also tested the maximum event separation, but it did not make a big difference once the WRCT was set.

Finally, we relocated individually every cluster from each Zone in order to avoid small clusters to be attracted by large ones in their vicinity.

Number of iterations per set	Weight for P-wave	Weight for S-wave	Residuals threshold (seconds)	Maximum event separation (km)	Damping
4	1	0.1	-9	-9	20
4	1	1	-9	-9	20
8	1	1	3	5	20

Table 3.4. Iteration scheme used to relocate the seismicity with HypoDD. -9 is a default value set when the parameter is not used in the iteration. The weight for S-phase cannot be set to the default value of -9 because makes S-phases to disappear for good. So it is set to the low value of 0.1 in the first set of iterations in order to have a minimum weight possible in these iterations and can be used in the following set of iterations.

3.3.4.2. Preliminary Results

The results of the pair selection of each cluster show a selection of ~70% of the initial events, except for cluster A which is in the middle of the network and contains a large number of very small events. However, the set-up results in very well linked event pairs with an average of links per pair ranging from 10 to 15 links and an average offset between linked events of ~1 km, except for cluster D with offset >2 km. Nearly the totality of events selected are relocated. The results show a very slight reduction of the RMS misfit (~10%) and <100 m of 2-sigma-relative relocation in x, y, z for the clusters under seismological stations (Cluster KS, Cluster DK, Cluster A and Cluster B) whereas Cluster C and D show a reduction of the RMS misfit around 23 % and a more important 2-sigma-relative relocation in x, y, z.

The reduction of the RMS misfit is lower than those obtained in Chapter 2, around 60%. It could indicate that the relative relocation using the catalogue does not make much difference with respect to the Hypo71 localization. Chapter 4 will describe the clusters and their geometry in order to discuss whether the HypoDD relocation has improved practically the relative relocation inside the clusters.

3.3.4.2.1. Zone S

3.3.4.2.1.1. Cluster KS

The cluster KS was initially formed by 96 events and 1355 phases from which 6116 P-phases and 3438 S-phases. 69% P-phase pairs and 71% S-phase pairs are selected. The event pairs have an average of 12 links. The average offset between linked events is

1.15 km. From the 78 events selected, 77 events were successfully relocated with ~80 m of 2-sigma-relative relocation in x, y, z and a RMS misfit reduction of 15%.

3.3.4.2.1.2 Cluster DK

The cluster DK was initially formed by 139 events and 1519 phases from which 8340 P-phases and 4916 S-phases. 57% P-phase pairs and 61% S-phase pairs are selected. The event pairs have an average of 10 links. The average offset between linked events is 1.12 km. From the 106 events selected, 101 events were successfully relocated with ~45 m of 2-sigma-relative relocation in x, y, z and a RMS misfit reduction of 8.3%.

3.3.4.2.2. Zone W

3.3.4.2.2.1. Cluster A

The cluster A was initially formed by 313 events and 2419 phases from which 22767 P-phases and 14779 S-phases. 31% P-phase pairs and 32% S-phase pairs are selected, representing 148 events. This important loss is explained by the presence of very small events with very few phases. The event pairs have an average of 13 links. The average offset between linked events is 1.30 km. From the 148 events selected, 133 events were successfully relocated with ~50 m of 2-sigma-relative relocation in x, y, z and a RMS misfit reduction of 10.1%.

3.3.4.2.2.2. Cluster B

The cluster B was initially formed by 105 events and 1122 phases from which 4598 P-phases and 2668 S-phases. 64% P-phase pairs and 68% S-phase pairs are selected. The event pairs have an average of 13 links. The average offset between linked events is 1.39 km. From the 67 events selected, 54 events were successfully relocated with ~55 m of 2-sigma-relative relocation in x, y, z and a RMS misfit reduction of 12.4%.

3.3.4.2.2.3. Cluster C

The cluster C was initially formed by 431 events and 6560 phases from which 29978 P-phases and 14035 S-phases. 69% P-phase pairs and 75% S-phase pairs are selected. The event pairs have an average of 15 links. The average offset between linked events is 0.8 km. From the 317 events selected, 304 events were successfully relocated with ~190 m of 2-sigma-relative relocation in x, y, z and a RMS misfit reduction of 23.6%.

3.3.4.2.2.4. Cluster D

The cluster D was initially formed by 74 events and 1092 phases from which 3716 P-phases and 1952 S-phases. 69% P-phase pairs and 69% S-phase pairs are selected. The event pairs have an average of 14 links The average offset between linked events is 2.23 km. From the 59 events selected, 49 events were successfully relocated with ~265 m of 2-sigma-relative relocation in x, y, z and a RMS misfit reduction of 29%.

3.4. Comparison between RSC catalogue and our study

One purpose of the temporary experiment was to improve the hypocentral locations and increase the number of events detected in western Nepal, in order to better interpret the local seismicity, eventually associating it with local tectonic structures. 2190 local events were located (out of a total of 2245 events) between longitude 80.3°E and 82.5°E, and latitude 28.3°N to 30.2°N using the methods described before. For the same period and frame, the RSC detected 513 events from which 467 are common with our catalogue (Table 3.5). The result is satisfying, given also that most of the events hypocentral locations have been significantly improved, thanks to the addition of the 15 temporary 3-components stations to the permanent network. This work allowed also to test and validate a new workflow involving an automatic data processing with Seiscomp3.

Catalogue	Number of events	Percentage
Both catalogues	467	20.9%
RSC catalogue exclusively	46	2.1%
TSN catalogue exclusively	1723	77.0%

Table 3.5. Comparison of number of events in the TSN catalogue that has been obtained using TSN data and RSC data, and the RSC catalogue that only used RSC data for the frame of the area of study e.g. Figure 3.18.

The events of the RSC catalogue are concentrated to the west and south of the zone of study. Depths of the RSC catalogue are not well constrained, so they are set to a default superficial depth (~2 km) (Figure 3.18.b). The earthquake hypocenters of our catalogue is now resolved. The depths range roughly between 10 and 15 km (Figure 3.18.a). Moreover, the density of events is very high compared to the RSC catalogue.

The position of the stations with respect to the hypocenters of the permanent stations and the temporary network and the good solutions on the location processing make us feel confident on the improvement of the results we obtained. For that, we consider our depths to be better resolved than the catalogue RSC that only used the permanent stations.

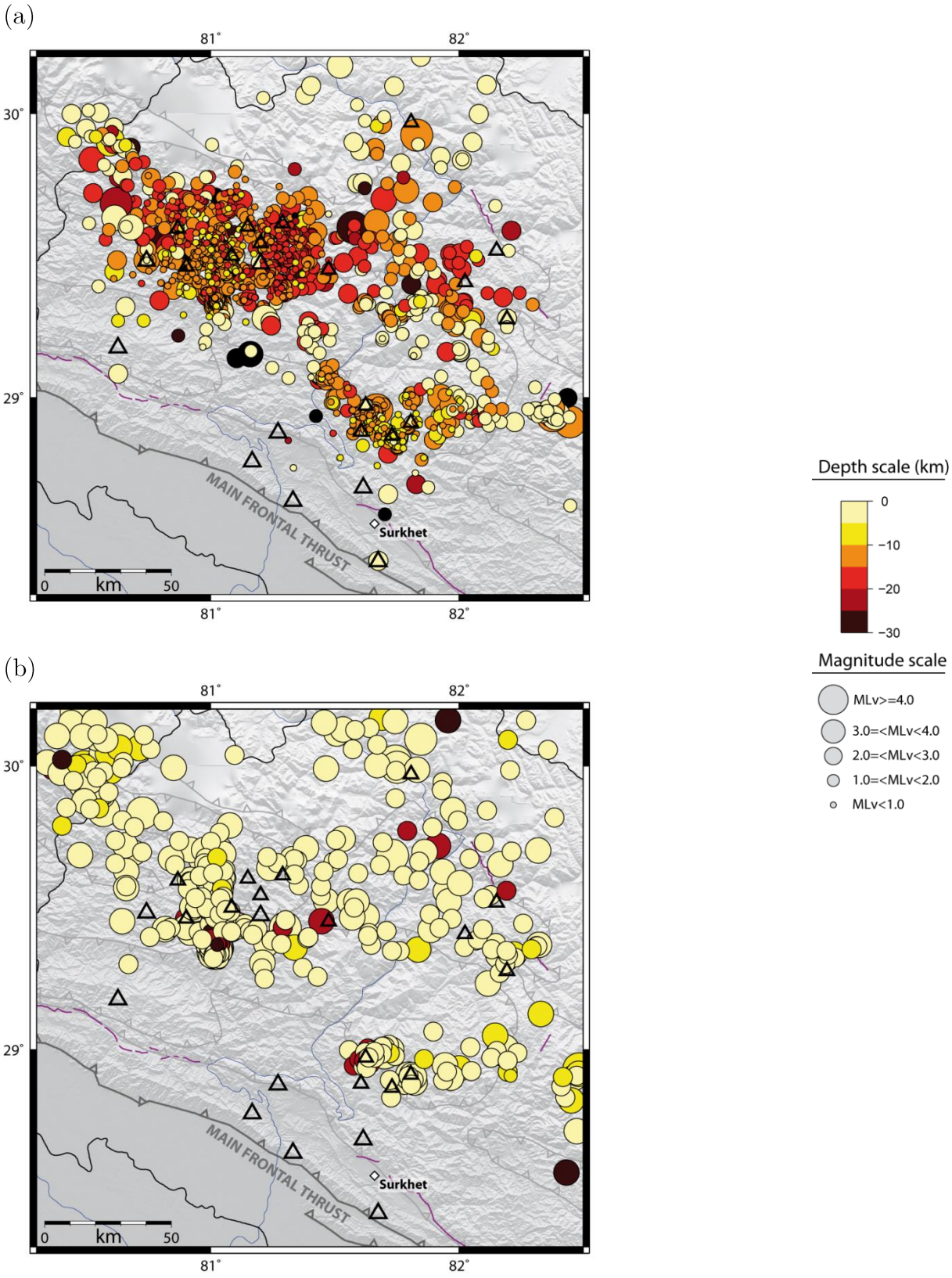

Figure 3.18. Maps of seismicity where the circle size depends on the magnitude and the color depends on depth. (a) Seismicity detected by this study. (b) Seismicity detected by the RSC. Black triangles are the seismological stations. Purple lines are the active faults of Nakata, 1982.

The RSC catalogue appears complete above a local magnitude ML 2.5 (Figure 3.19). Complementarily, the new earthquake catalogue shows a peak on the events of magnitude 0.75≤MLv≤1.0 where the completeness magnitude is likely to be. Even taking into account the difference between both types of magnitudes (example: ML≥2.0 in the RSC catalogue is equivalent to MLv≥1.2 in our catalogue), the RSC does not reach this level of detection for small magnitudes ML<2.0 (Figure 3.19).

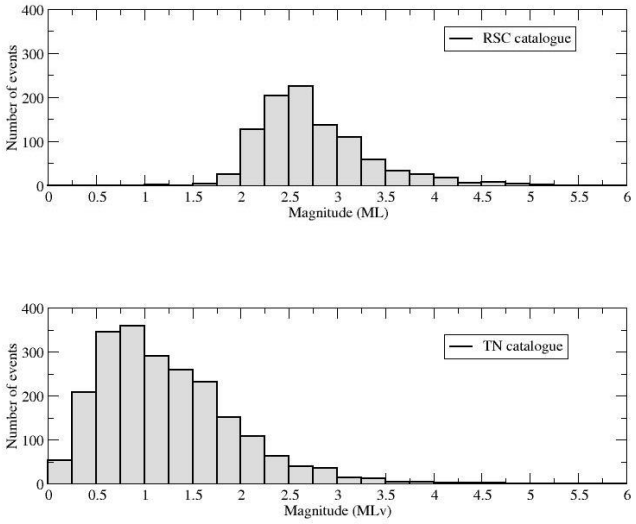

Figure 3.19. Number of events in function of its magnitude. (a) RSC catalogue accounts 467 events with magnitude determined. (b) Temporary network catalogue accounts 2187 events with magnitude determined.

CHAPITRE 4

West Nepal: Results and seismotectonics implication

4.1. Seismicity TSN catalogue analysis

The TSN network has detected 2190 events in the area of interest between December the 1st 2014 and October the10th 2015. All these events do not benefit from the same location uncertainties. Both the quality of the location and density of the events are highly dependent on the position of the subnetworks. Indeed, the best located events and the highest rates of events are in Zone W and Zone S, two regions with respectively 9 and 4 seismic stations (Figure 4.1).

The spatial distribution of the epicenters confirms the presence of a wide belt of seismicity in the west (named Bahjang seismic belt hereafter, from the eponymous district) and a southern narrower belt of seismicity in southern Karnali area reaching Dailekh district (named South Karnali seismic belt hereafter) (Figure 4.1). Their distance to the MFT, their northern extent and the depth of the events are significantly different. On the one hand, the Bajhang seismicity begins ~65 km north from the MFT and extends northward over ~45 km wide (Figure 4.1), presenting hypocenters ranging from 10 to 18-20 km with an average around 13 km (Figure 4.2 A-AA and B-BB). On the other hand, the South Karnali seismicity is located southward, about 40 km north from the MFT and extends northward through a ~15 km-large belt (Figure 4.1) presenting hypocenters with shallower depths ranging from 8 to 15 km with an average around 10 km (Figure 4.2 C-CC).

In addition, we observe a lack of seismicity between the South Karnali seismicity belt and a more scattered seismic region that develops in north Karnali (named North Karnali seismicity belt hereafter) (Figure 4.1). The seismicity from this area and vicinity is less resolved (lower quality of the location and higher completeness magnitude) due to its location relative to the network. MA10, SM15, GH25, SJ26 and JL27 are farther from the midcrustal cluster there than elsewhere within the seismic network (Figure 4.1).It is therefore more difficult to characterize the geometry of this North Karnali seismicity belt with the data available(Figure 4.2 C-CC). Part of the seismicity is located at depth in ranges between 10 and 20 km, similar to the cross-section B-BB, but we find as well seismicity set to the default depth of 5 km of the localization program (Figure 4.2 B-BB and C-CC). The fact that SM15 was installed in

April 2015 could influence the results. It is possible that processing in the future the second year of the records, this area may be better resolved.

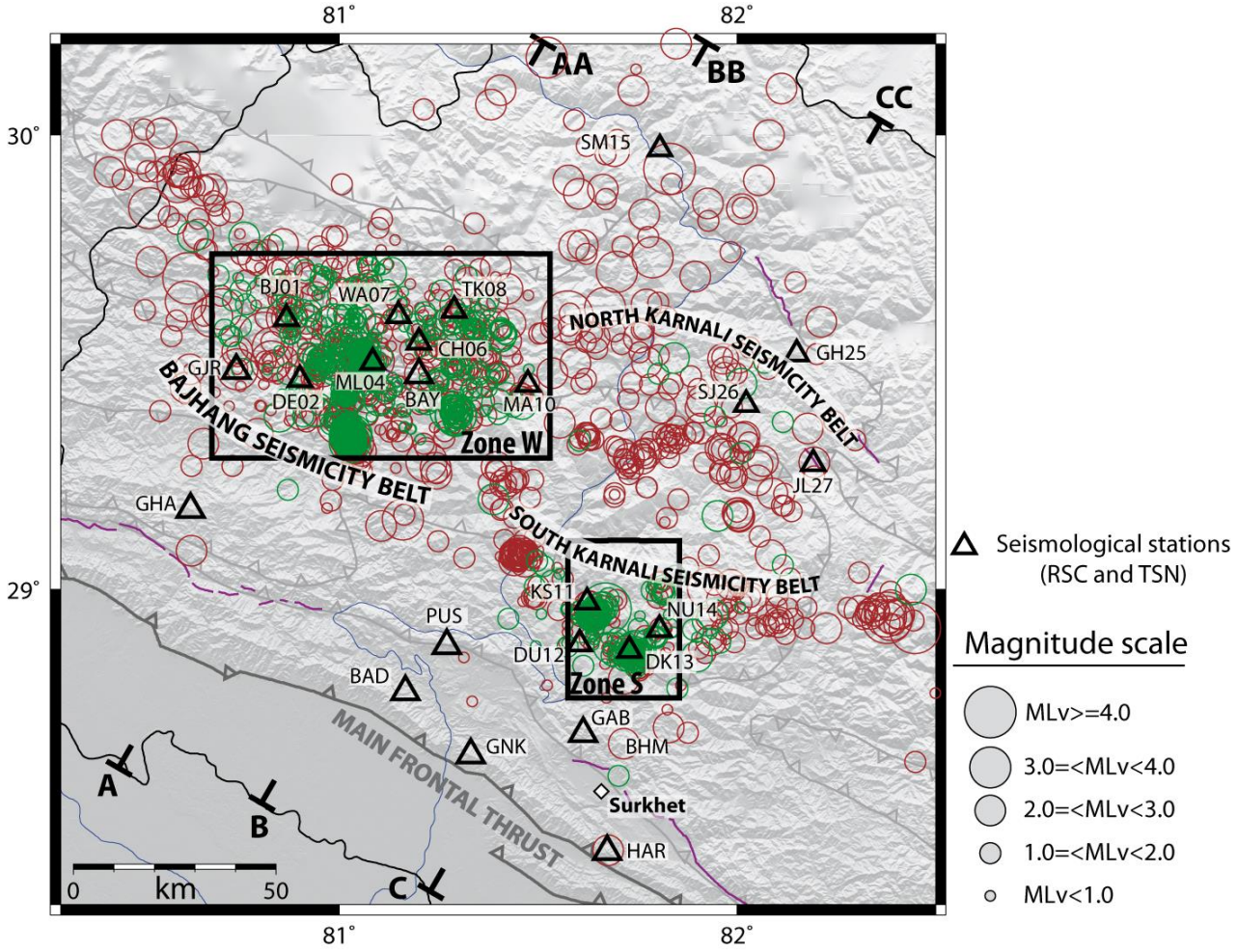

Figure 4.1. Map of the seismicity of the TSN catalogue resulting from the absolute localization by Hypo71. Green circles represent the high quality HQ events (P-phases $\geq$ 6, S-phases $\geq$ 3, RMS $\leq$ 0.4 and ERH and ERZ $\leq$ 2 km), brown circles are the low quality events (P-phases $<$ 6, S-phases $<$ 3, RMS $>$ 0.4 seconds and ERH and ERZ $>$ 2 km). A-AA, B-BB, C-CC are the 3 cross sections through the seismicity represented in Figure 4.2. Purple lines are the active faults of Nakata, 1982 and light gray are the ancient MHT surface traces.

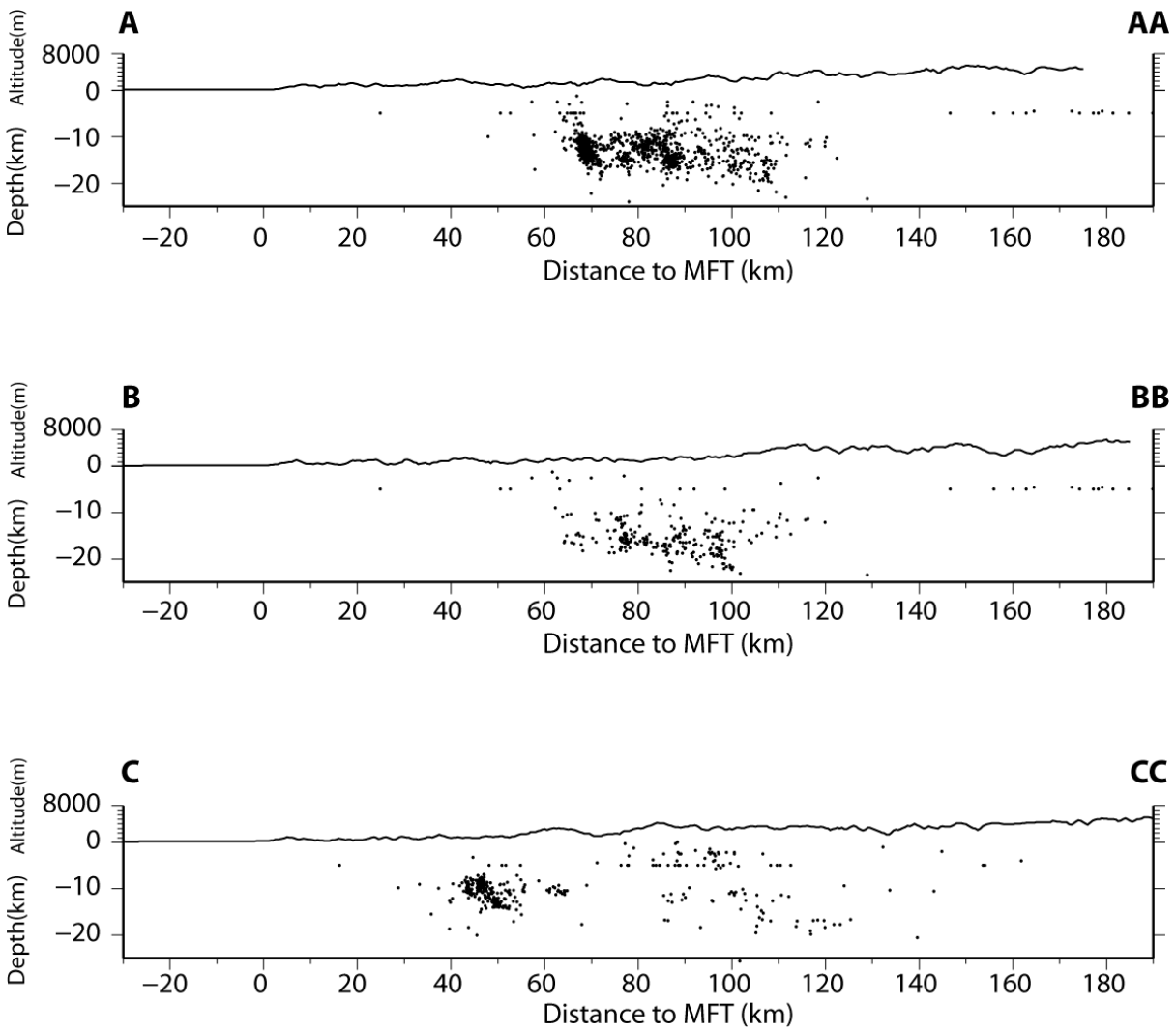

Figure 4.2. Cross-sections of Figure 4.1 oriented perpendicular to the trace of the MBT, extending from the MFT to 180 km and stacking seismicity located 20 km apart from the cross-section track.

The magnitude MLv of the events ranges from 0 to 5.2. During the period of this study, 93 % of the events in the catalogue have magnitudes MLv≤2.0 and are therefore smaller than the completeness magnitude (Mc) of the RSC catalogue (Pandey, 1999), demonstrating the potential of the temporary network (see *Chapitre 3* section *3.3.2.5. Magnitude MLv* for the relation between MLv et ML) (Figure 4.3). The histogram shows a maximum number of events MLv~1.0, which means that the Mc is necessarily above MLv≥1.0 (Figure 4.3.a). Moreover, the Gutenberg-Richter (GR) distribution is linear from MLv=4.4 until MLv=1.4 (Figure 4.3.b) where the curve present a breaking slope; under MLv=1.4 the number of events predicted by the prolongation of the slope or b-value are greater than the catalogue data. Therefore we estimate that the completeness magnitude of the catalogue in MLv is approximately 1.4. The b-value

obtained for the entire catalogue is 0.75+/-0.03, which is in the range of b-value (0.75-0.95) obtained by Pandey et al, 1999.

In order to detect temporal changes of the seismic activity, we evaluate the cumulative number of events for local earthquakes with a magnitude above Mc (Figure 4.4). We observe a sudden increase of the number of events at the beginning of 2015 which is preceded by a high rate of earthquakes (Figure 4.4). From March to September 2015, the activity slows down with approximately ~50 events per month (Figure 4.4). We finally observe an increase of the activity in October 2015. Note than the main surges in seismicity rate are not consecutive to the largest earthquakes recorded by the networks (e.g. events with ML>4 on Figure 4.4).

The number of events with MLv above the completeness magnitude (MLv≥1.4) represents only 34% of the total number of events in our catalogue. However, this completeness magnitude might not be representative for all the regions covered by the network. Indeed, important variations of the Mc in space and time are expected due to the location of the stations, their failures during the first year of acquisition (see Figure 3.4), and the temporal variations of the high frequency seismic noise (influenced in Nepal by landslides, floods and sediment transport in rivers (Burtin et al., 2008), among other sources of high frequency seismic noise).

In order to illustrate the spatio-temporal variations of the seismicity, we analyze the results at the subnetworks in the following sections, they account for 1745 events out of the total 2190 events.

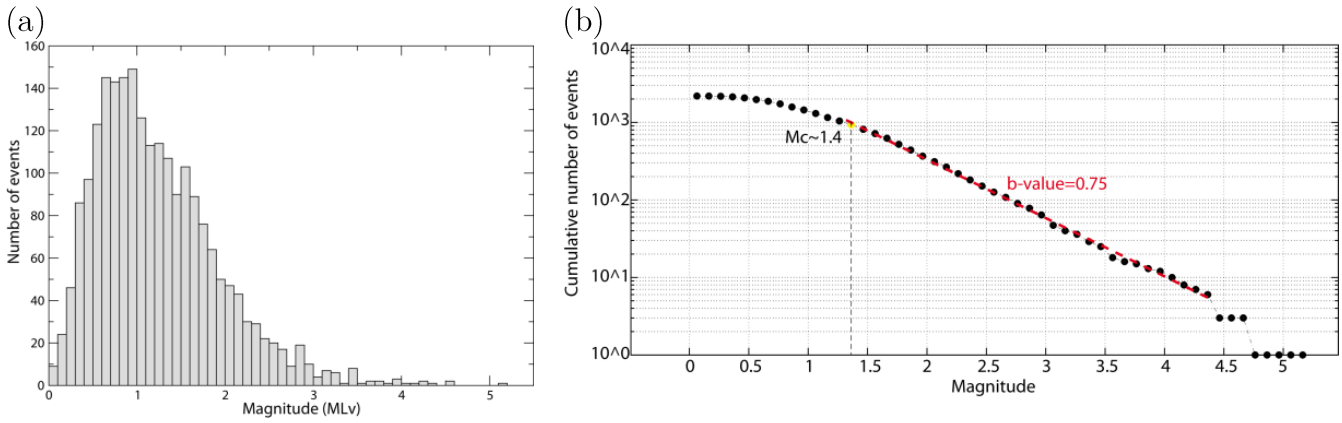

Figure 4.3. Magnitude distribution for the whole catalogue. (a) Magnitude histogram of the events in MLv. (b) Gutenberg-Richter distribution for the whole catalogue. b-value=0.75±0.03. The completeness magnitude Mc is estimated at Mc~1.4.

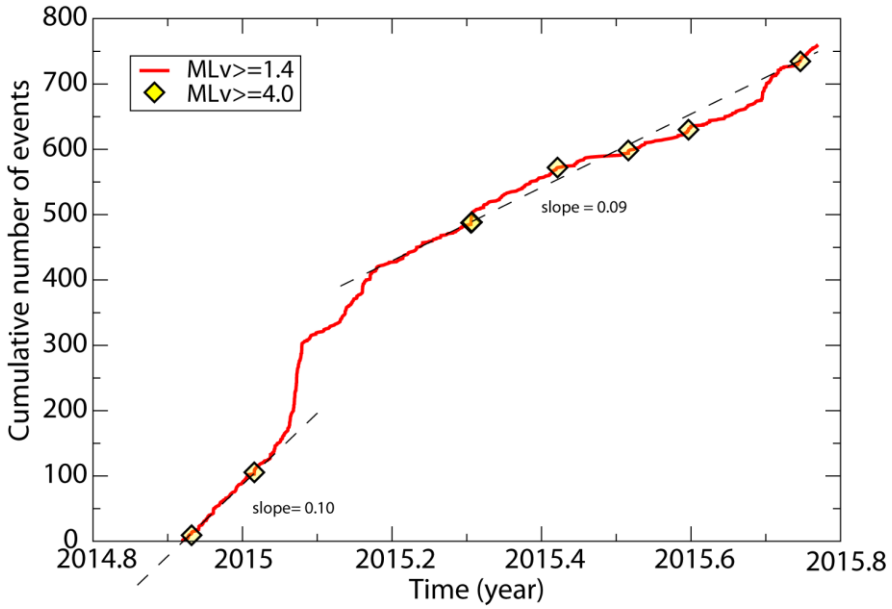

Figure 4.4. Cumulative number of events for local earthquakes with magnitude MLv above the completeness magnitude Mc=1.4.

4.1.1. The Bajhang seismic belt

1451 events were located in the Bajhang seismic belt covering the entire area and continuous along time (Figure 4.5). The high quality events represent 57% of the total events (Figure 4.5). The events are densely spread over the area either as individual events or as agglomeration of events (Figure 4.5). Most of the hypocentral depths for these events are midcrustal (10 ~18-20 km) (Figure 4.5.b and 4.6) but these depths vary laterally. Indeed, in the eastern most part of this region, we distinguish several small groups of clustered events with depths ranging between 15 and 20 km, while the central part of the area is formed by larger size clusters with larger depth ranges (Figure 4.5.b).

(a)

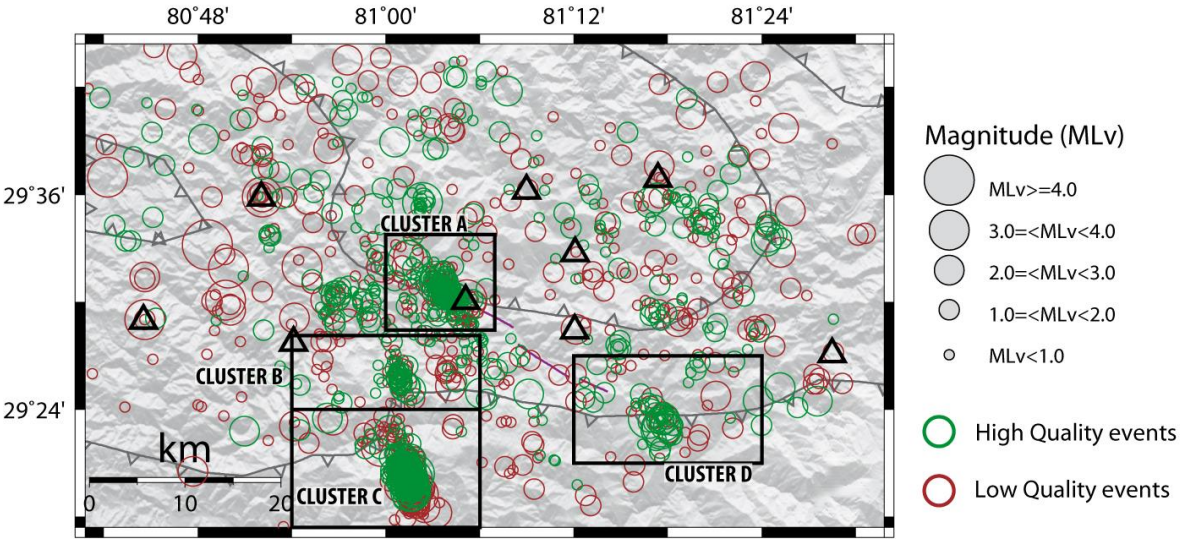

(b)

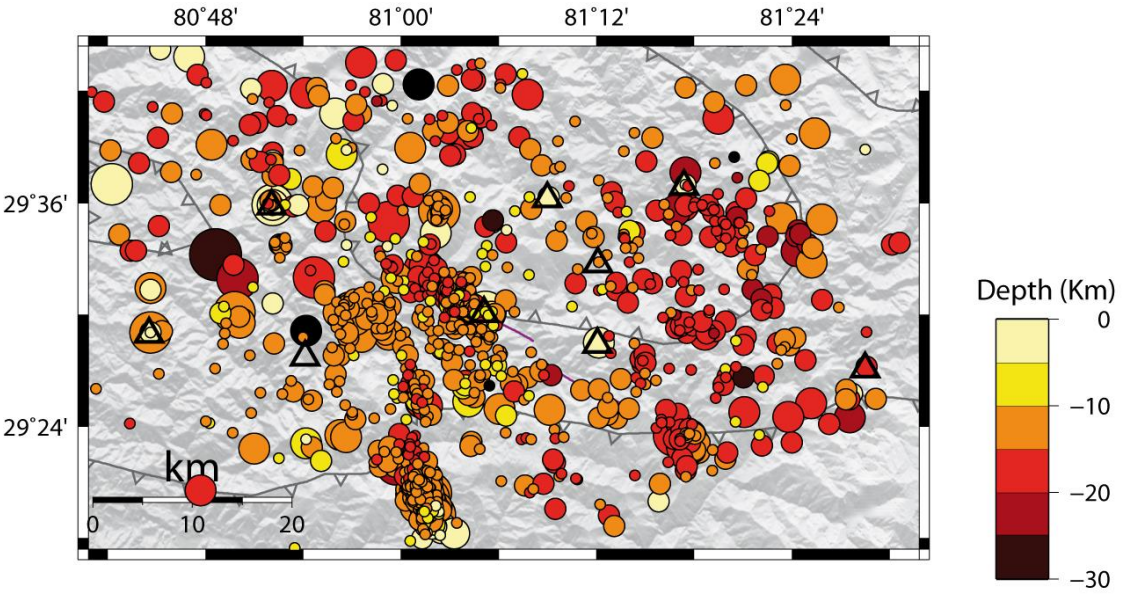

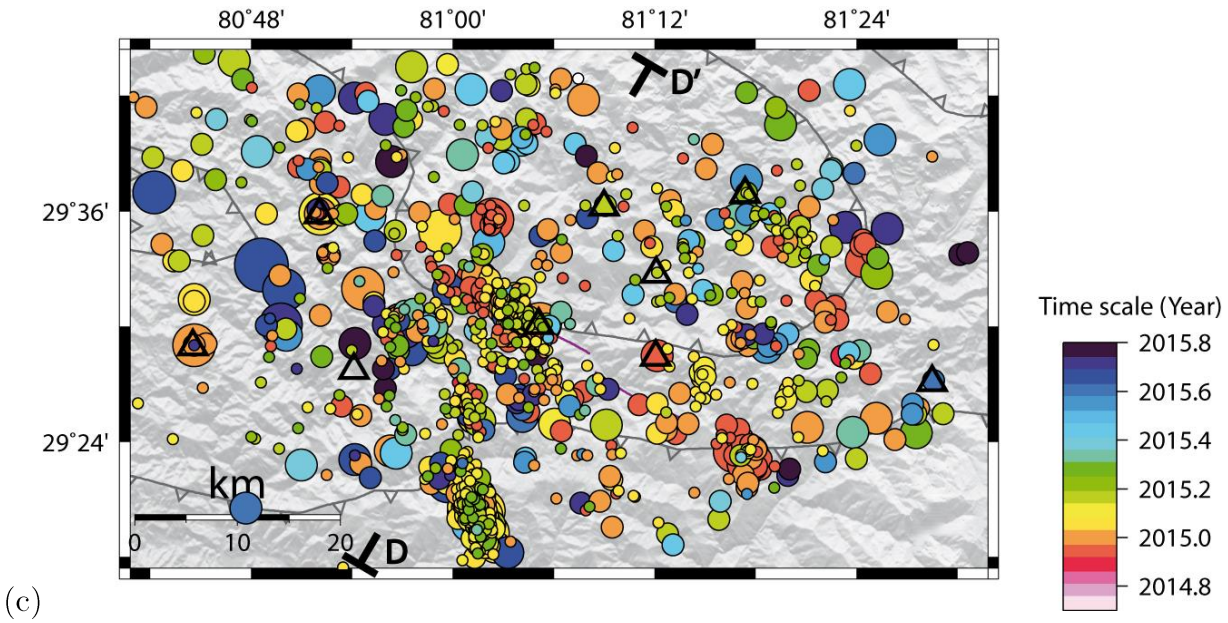

(c)

Figure 4.5. Map of the seismicity of the Bhajang seismic belt with circle size depending on magnitude MLv. The color of the events depends on (a) their quality: green circles represent the high quality HQ events (P-phases $\geq$ 6, S-phases $\geq$ 3, RMS $\leq$ 0.4 and ERH and ERZ $\leq$ 2 km), brown circles are the low quality events (P-phases $<$ 6, S-phases $<$ 3, RMS $>$ 0.4 seconds and ERH and ERZ $>$ 2 km); (b) their depth and (c) their date of occurrence. D-D' is the cross sections through the seismicity represented in Figure 4.6. Purple lines are the active faults of Nakata, 1982. Gray lines are the MCT.

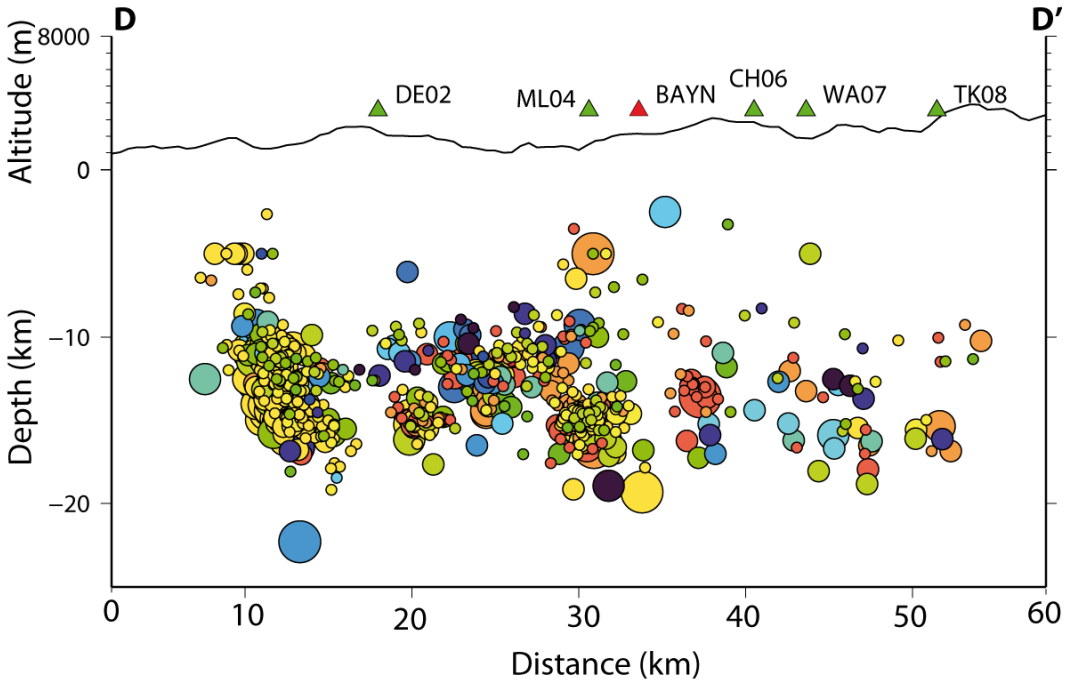

Figure 4.6. N030E cross-section within the seismicity of Figure 4.5.c. The events within a +/-10 km swath from the track are stacked. See Figure 4.5 for exact location and magnitude scale.

The magnitude histogram presents a maximum around MLv~0.7 (Figure 4.7.a). Before comparing this value to the break-in-slope in the GR distribution, we explore the GR distribution to see if any spatio-temporal variations of the network capacity had impact on the seismic catalogue. This is particularly crucial for this region because, as shown in Chapter 3, 4 out of 7 stations of the TSN in Zone W did not record data for few months in 2015 (Figure 3.4). We perform a GR distribution for the period of the study (December 2014 – October 2015) and a second GR distribution using only the period when all stations were functioning correctly (December 2014 – March 2015) (Figure 4.7.b and c). The GR distributions do not seem affected by the malfunctioning of WA07, ML04, CH06 and BJ01 during spring and summer. Indeed, the difference on the productivity 'a-value' of the GR distribution is of a ~30 events per month; and the completeness magnitudes estimated for both periods differ only by 0.1 (MLv~1.0 for the entire period, MLv~0.9 for the truncated period) (Figure 4.7.b and 4.7.c) . So, we cut the catalogue to MLv=1.0 to analyze the time sequence (Figure 4.8). The time sequence of the seismicity reveals a sudden increase of events at the beginning of 2015 that participates much to the seismicity surge present in the whole catalogue. On each side of the time-clustered activity, two different tendencies appear (Figure 4.8). From the installation until the early January, the rate of seismicity is very high, whereas from March to September the activity is clearly decreased (Figure 4.8). Because we are looking to a small period of time, it is difficult to know whether the high or low rates are representative of the average seismic rate.

A closer look at the spatio-temporal sequence of the seismicity is therefore required. To go forward, on that topic, I relocated the four denser seismic clusters of the area, four clusters labeled A to C, from north to south, and D for the fourth cluster located eastward (Figure 4.5.a). Hereafter, I present the detailed geometry with the results of the relative relocation of each cluster as well as its time sequence confronting the results with the ones deduced from the analysis of the whole catalogue of events.

(a)

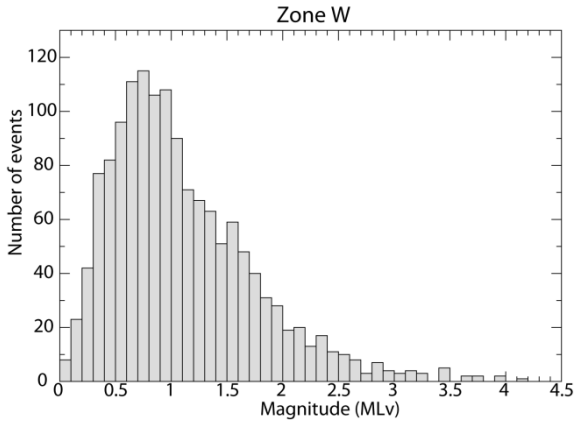

(b)

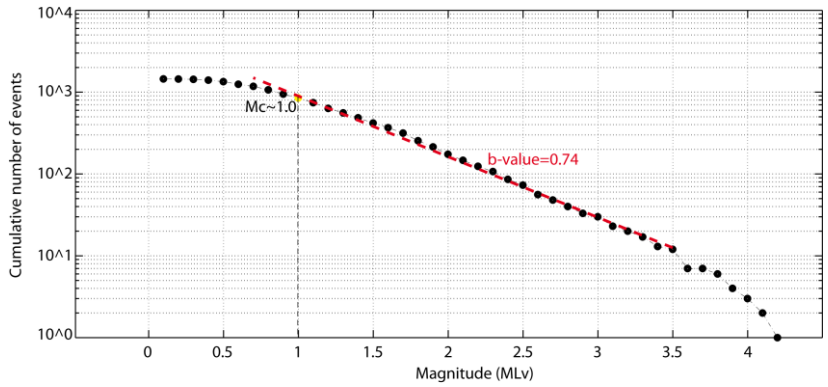

(c)

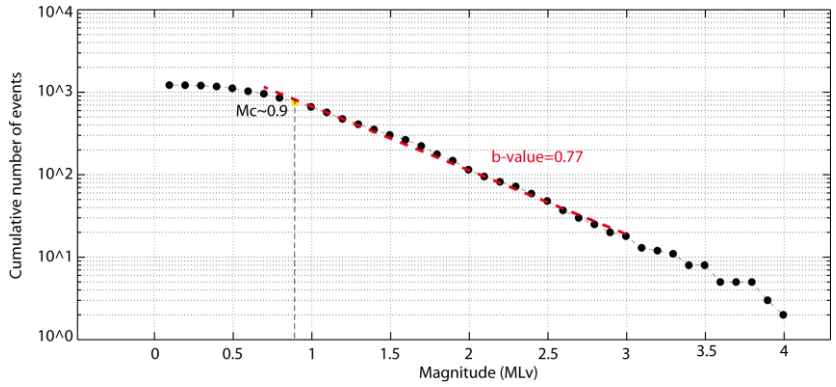

Figure 4.7. Magnitude distribution for the Bajhang seismic belt. (a) Magnitude histogram of the events from 01/12/2014 – 10/10/2015 in MLv. (b) Gutenberg-Richter distribution of the zone of study with a b-value=0.74±0.04 and Mc=1.0 from 01/12/2014 – 10/10/2015. (c) Gutenberg-Richter distribution of the zone of study with a b-value=0.77±0.03 and Mc~0.9 from 01/12/2014 – 28/03/2015.

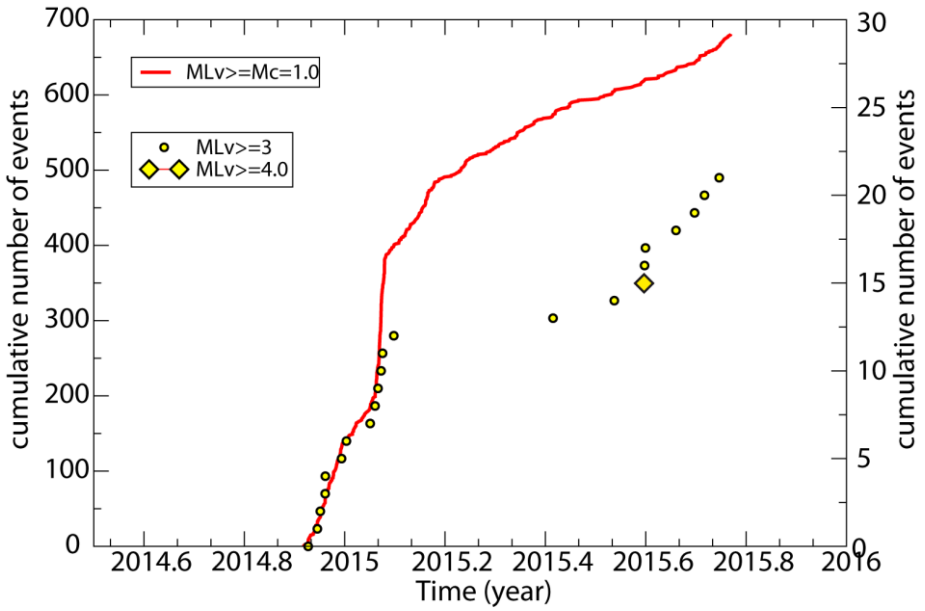

Figure 4.8. Time sequence of the seismic events with MLv≥1.0 in Bajhang seismic belt. Yellow circles correspond to the earthquakes with a magnitude MLv≥3.0. Yellow diamond is the M=4.19 event that occurred on the 05/08/2015.

4.1.1.1. Cluster A

Cluster A is situated in the middle of the network. Its southeastern end is located one kilometer from station ML04 (Figure 4.9). It is formed by more than 300 events (~130 events were relocated) with magnitudes mainly MLv≤2.0 except for three events with MLv>3.0. The activity of the clustered seismicity is principally between December 2014 and early March 2015 (Figure 4.9).

After relocation, we distinguish two distinct clusters: the main one (92 events relocated) and a smaller cluster northwards that was part of the main cluster before relocation (6 events relocated) (Figure 4.9). I focus hereafter my interest on the main seismic cluster.

The relocated epicenters (without the event of magnitude MLv=3.7) describe a 3 km-long shallow-dipping plane (~10 WNW) striking in the WNW-SSE direction (~N110) (Figure 4.9.b and 4.10.b). The width of the fault plane is about 0.5 km and for 1 km deep. We observe that the largest-magnitude event in the cluster is located just under the agglomeration of earthquakes (Figure 4.10). This earthquake with magnitude MLv=3.7 occurred the 28/12/2014 and was preceded by 2 events just above its hypocenter. The earthquakes that occurred afterwards were located on both sides. More events occurred to its eastern side (Figure 4.9 and 4.10). The analysis of this cluster has shown its geometry to be more close to a line than a plane (Figure 4.9.b and 4.10.b).

The magnitude-frequency distribution has a b-value of 0.85 with a standard deviation of 0.03 when determined on a [0.5-1.8] MLv window, linear section of the GR distribution, above the completeness magnitude (Mc), estimated here to be ~0.5 (Figure 4.11). The GR distribution for events MLv≥1.8 presents an erratic tendency maybe due to the small probability of occurrence (5% for events of MLv≥2.0) (Figure 4.11.a). The estimated Mc for cluster A is lower than the Mc of the entire Zone W (Mc~1.0) maybe owing to the close distance to the stations. We cut the full catalogue to MLv≥0.5 to analyze this local time sequence. There is a major activity from late 2014 until early March 2015 (Figure 4.11). A lower seismic activity was detected during the network installation, prior to the occurrence of the main cluster. However, this seismicity is rather difficult to characterize because of the limited period of time covered by the catalogue. However the activity in this cluster stops clearly at the beginning of March, before the failure of the nearby stations; the time structure of the end of this seismic crisis is therefore not affected by any biases related to the network geometry/ capacity.

We see a three-phase surge in the rate of earthquakes following the onset of the main cluster seismicity. Note that the largest-magnitude events occur at the beginning of the second stage. After that the activity decreases slowly from early February until early March.

Finally, the spatio-temporal sequence of Cluster A does not present characteristics of a typical mainshock-aftershock sequence but is more probably related to the development of a swarm that migrates with time.

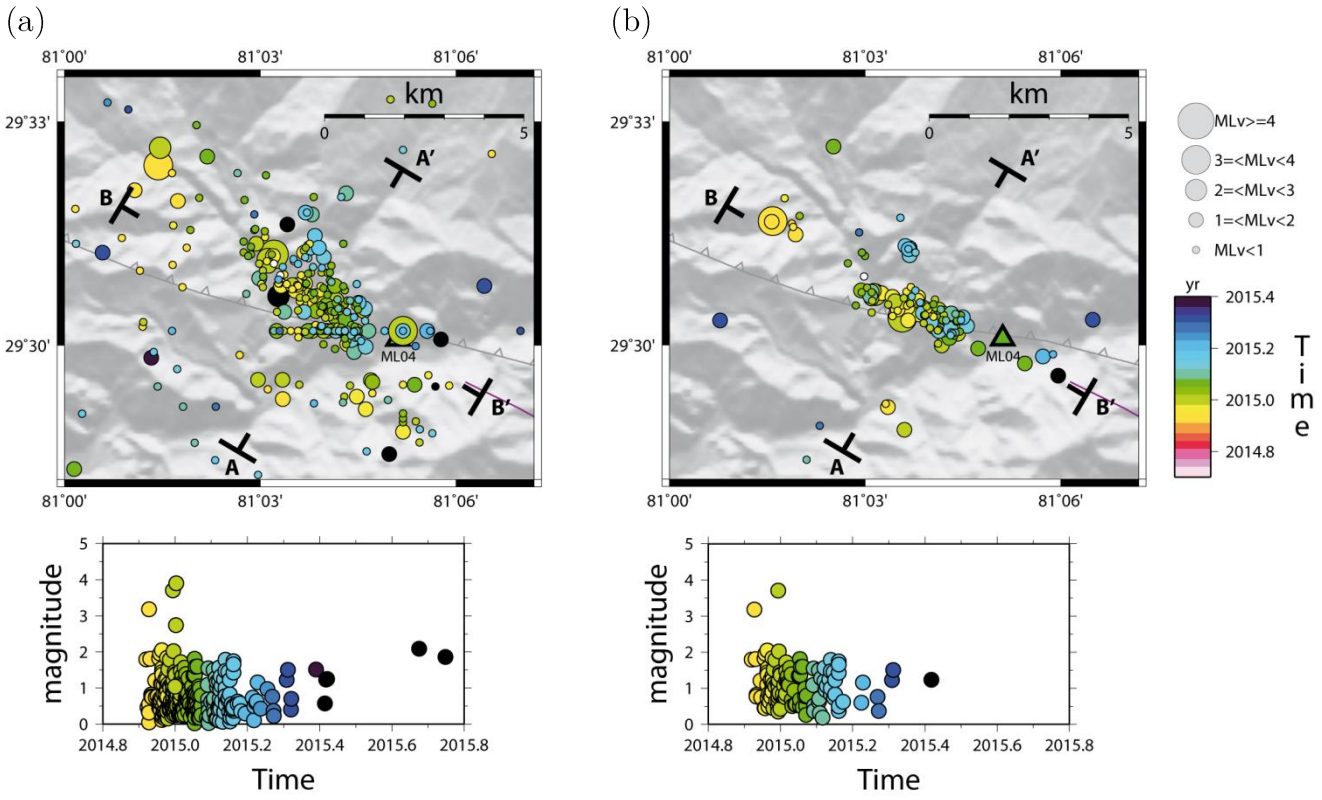

Figure 4.9. Spatio-temporal evolution of seismic cluster A in map view – Black triangle for ML04 (upper figures) - and magnitude-time plot of the cluster (lower figures). (a) Catalogue of the absolute localization of the events. (b) Catalogue of the relative relocated events. Purple lines are the active faults of Nakata, 1982. Gray line is the MCT.

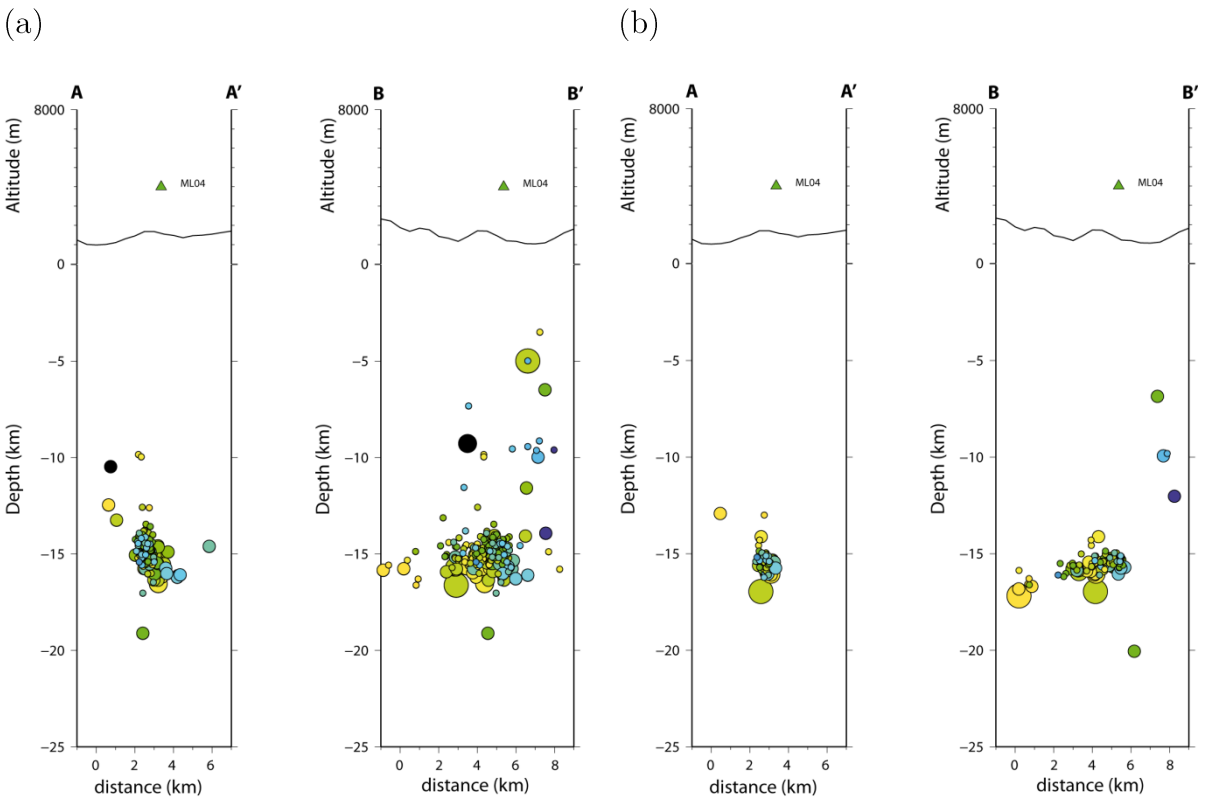

Figure 4.10. Cross-sections within +/- 1km from A-A' and B-B' (see Figure 4.9). A-A' is 8 km-long striking N030E. B-B' is 10 km-long striking N118E. (a) Catalogue of the absolute localization of the events. (b) Catalogue of the relative relocated events.

(a)

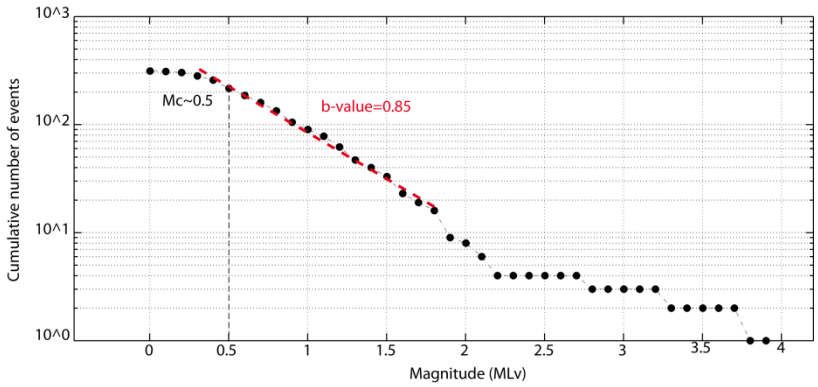

(b)

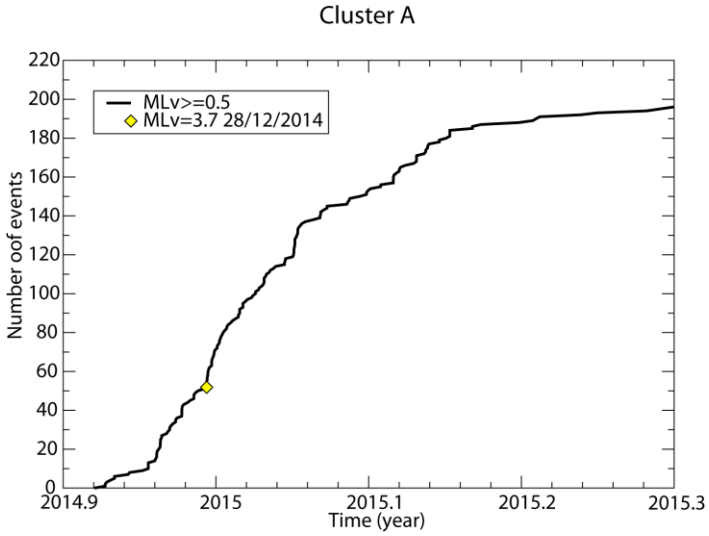

Figure 4.11. Evolution in time of the seismicity above the estimated Mc in cluster A of Figure 4.9.a. (a) Gutenberg-Richter distribution with a b-value=0.85±0.03 and a Mc~0.5. (b) Cumulative number of events with MLv≥0.5 in function of the time with the highest rate of activity of the cluster.

4.1.1.2. Cluster B

Cluster B is situated southward, around 29.25°N, between ML04 and DE02 (Figure 4.5). It is composed by 105 events (54 events were relocated) with magnitudes MLv<3.0 (Figure 4.12). The seismicity developed there between the instrumentation in December 2014 and mid-March 2015 (Figure 4.12).

The ~50 hypocenters relocated with HypoDD are distributed along a 13 km-deep 1.5 km-long NNW-SSE (~N155E) plane (Figure 4.12.b and 4.13.b). The downdip extent and dip of the plane are difficult to ascertain given the rather small depth range and lateral extent of the cluster (respectively scattered 0.5-0.7 km and 0.6 km).

The first events occurred along the northern part of the cluster (Figure 4.12.b, yellow), then the seismicity appears at the southernmost part after the occurrence of the two largest earthquakes of the cluster (Figure 4.12.b, green). Finally, the seismicity locates in the eastern side of the cluster (Figure 4.12.b, blue).

The GR distribution shows a b-value of 0.69±0.01 under MLv=1.7 with a break-in-slope around MLv=0.7 which we estimate to be the completeness magnitude (Figure 4.14). The seismic rate for events above magnitude 0.7 was very elevated at the moment of the installation of the stations until early January (Figure 4.14). From then until late February 2015, there is a slowdown of the activity. After that the rate of earthquakes increase for a few days to finally decreases to zero mid-March (Figure 4.14). The increase of the activity on the last three months is mainly related to the events located eastwards from the cluster (Figure 4.12).

Because the seismic cluster began prior to the installation of the temporary network, more information on this crisis could come from the examination of the seismic catalogue of the permanent seismic network. Figure 4.14.c illustrates the time sequence of both seismicity catalogues for the same frame starting in March 2014 for RSC. The increase of the seismic activity in the area started the 30/11/2014, 1 day before the beginning of TSN catalogue. The largest event that occurred then is an earthquake of magnitude ML=2.4 (MLv=1.6) which is therefore not the largest event that occurred in the cluster (and is rather small to generate a kilometric-long aftershock activity). We therefore do not consider it to be the mainshock of the crisis. Without any significant mainshock, we suspect the clustered seismicity in the area result from a swarm activity related to other processes that the coseismic rupture of a significant earthquake.

(a)

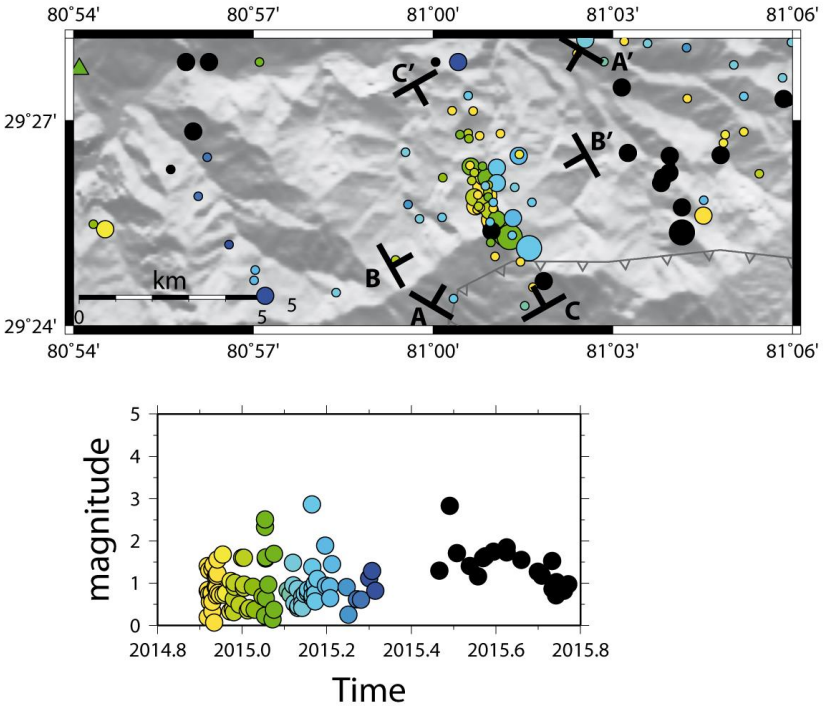

(b)

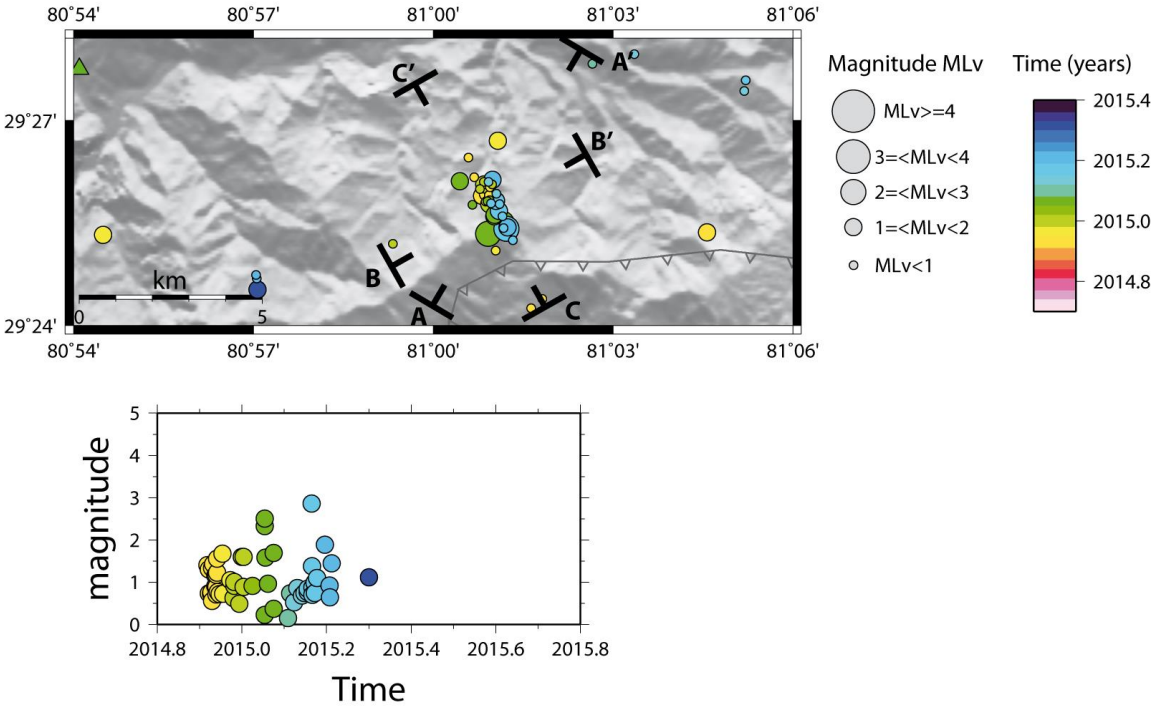

Figure 4.12. Spatio-temporal evolution of cluster B in map view (upper figures) and magnitude-time plot of the cluster (lower figures). (a) Catalogue of the absolute localization of the events. (b) Catalogue of the relative relocated events. Gray line is the MCT.

(a) (b)

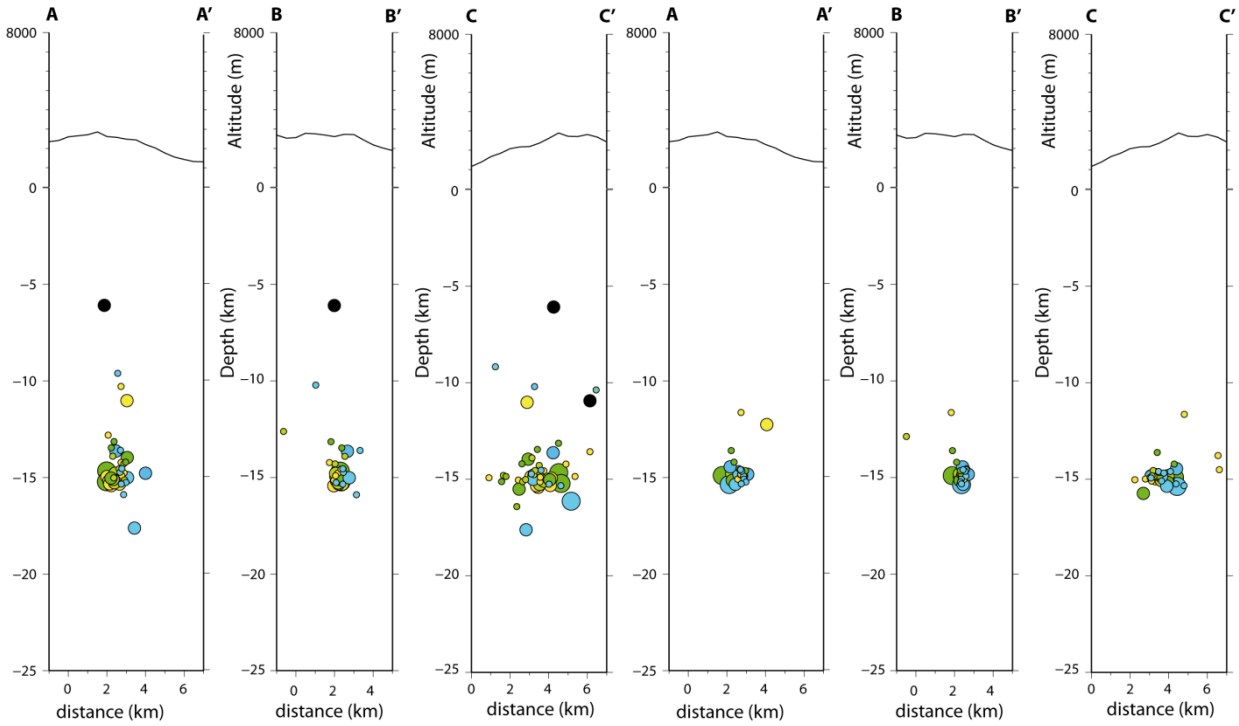

Figure 4.13. Cross-sections within +/- 1km from A-A', B-B' and C-C' (see Figure 4.12). A-A' is 8 km-long striking N030E. B-B' is 6 km-long striking N060E. C-C' is 7 km-long striking N150E. (a) Catalogue of the absolute localization of the events. (b) Catalogue of the relative relocated events.

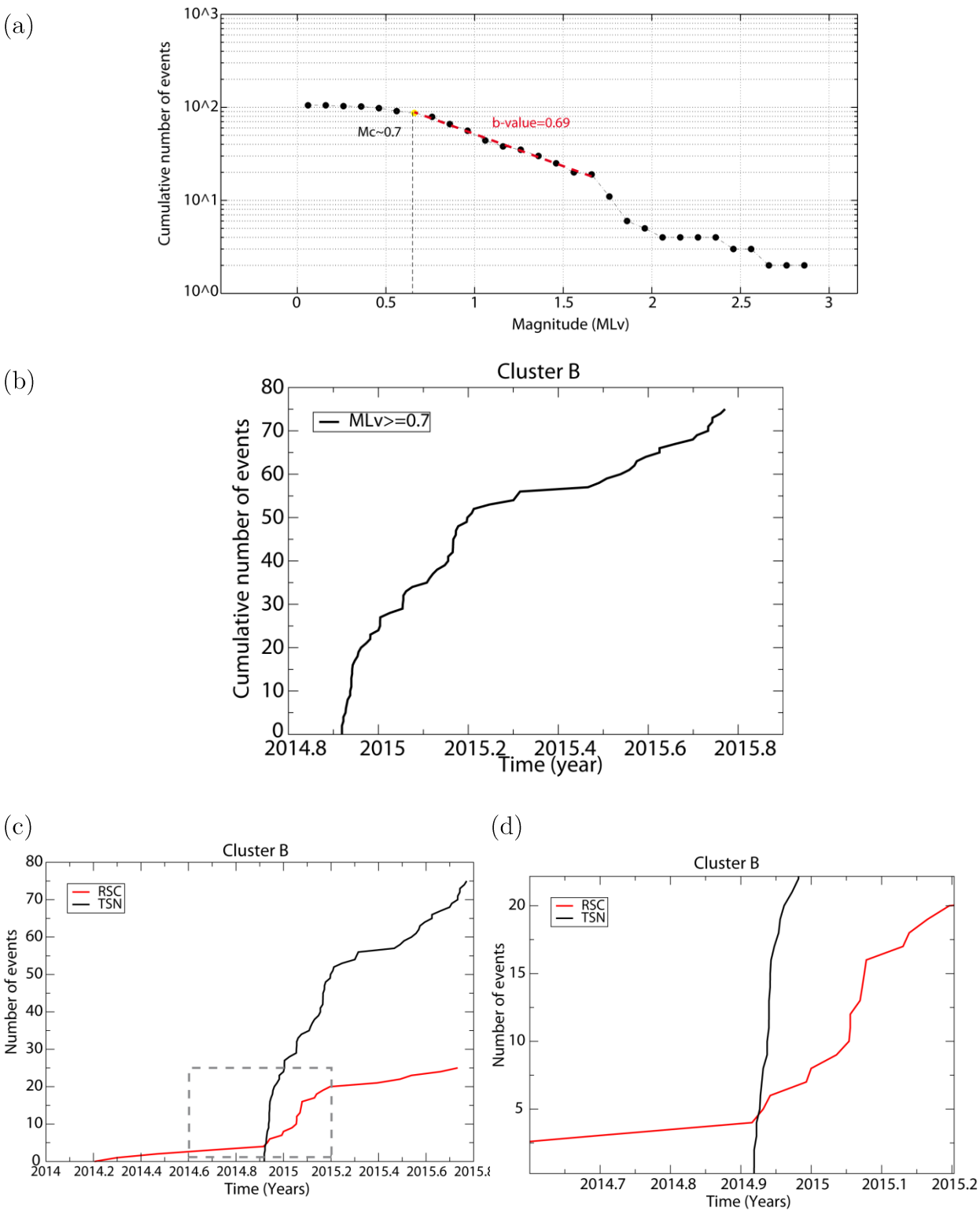

Figure 4.14. Evolution in time of the seismicity above the estimated Mc in cluster B of Figure 4.12.a. (a) Gutenberg-Richter distribution with a b-value=0.69±0.01 and a Mc~0.7. (b) Cumulative number of events with MLv≥0.7 in function time. (c) Comparison between cumulative number of events in function of time of RSC catalogue and TSN catalogue for Figure 4.12 frame. (d) Zoom of Figure 4.12.c.

4.1.1.3. Cluster C

Cluster C is the most earthquake-producing cluster recorded during the first year of the temporary network. A total of 430 events (~300 events were relocated) clustered south of the western subnetwork within a few days at the end of January 2015 (Figure 4.15).

The hypocenters there were relocated between 9 and 18 km (average depth at 14 km) along a 7 km-long segment orientated in a NNW-SSE direction (~N150) (Figure 4.15) These hypocenters get deeper towards the NNW describing a steeply-dipping plane at about 60° NNW (Figure 4.16). The dimensions of the cluster are at least 7 km x 1.5-2 km x 1.7 km (Figure 4.16). However, the position north of the closest stations respect to the cluster might influence on the depth and epicentral location.

The magnitudes of the events range from 0.2 to 4.0. The magnitude histogram shows a more progressive distribution than usual, with a plateau between 0.6 and 1.1, instead of a peak. This suggest that the completeness magnitude is somewhere around or slightly above MLv=1. A ledge is also visible between 1.4 and 2 (Figure 4.17.a).

Strikingly, the magnitude-frequency distribution shows also two break-in-slopes at MLv~0.7 and MLv~1.7 (Figure 4.17.b). The b-value obtained between magnitudes 0.7 and 1.9 is 0.5 (Figure 4.17.c.2) and would imply that we missed magnitudes between 2 and 3 whereas the b-value obtained by using the larger magnitudes is 0.86 (Figure 4.17.c.2) which would seem more coherent because the catalogue is more likely to miss small magnitudes rather than larger ones. However, taking the second break in-slope-along the GR distribution would suggest a Mc at ~1.7 which appear very high given the capacity of the network to detect there small events either. Furthermore, cutting the catalogue above 1.7 would leave few earthquakes for analyzing the spatio-temporal sequence of events, depleting a lot the catalogue. We therefore decide to cut the catalogue at MLv=1.0, Mc for Zone W.

The time sequence of events presents an abrupt raise on the seismicity rate after the occurrence of the MLv=4.0 on 22/01/2015 that lasts few days (Figure 4.17.d.1). After that, the seismicity decays progressively (Figure 4.17.d.1). This seems a typical pattern for a mainshock-aftershock sequence. Nevertheless, there are reasons to think the opposite:

1) Looking closer at the period between January 22 and 31, we can see that the sequence starts with the mainshock and increases progressively, and then there is a step meaning a decrease of the activity and two stages with the highest increase of the seismic rate (Figure 4.17.d.2).

2) The decay-day rate of seismicity fitting to this cluster presents parameters values that are too high (decay exponent p=2.6, constant c=8.7, the slope k=14996 of the modified Omori law).

3) The mainshock of MLv=4.0 and the rupture size: an event of such magnitude corresponds to a magnitude ML=4.4 (relation in *Chapitre 3* section *3.3.2.5. Magnitude MLv*) which is equivalent to Mw=3.9 (Ader et al., 2012). We can use the scaling relations to have a big picture of the correspondence between the magnitude and the surface ruptured. The moment magnitude depends on the seismic moment by the moment magnitude scale of Hanks and Kanamori, 1979, and then the seismic moment (M_0) is related to the slip and the surface on the fault by the empirical relation of Kanamori and Anderson, 1975: $M_0 = \mu S\overline{D}$ where μ is the shear modulus (32 GPa for the crust (USGS)), S is the surface of the fault and D is the slip on the fault. Using this relation with a surface equivalent to the cluster dimensions we obtain a slip of 3 mm in depth that is highly dependent on the surface of the fault. Indeed, the slip will increase if the surface decreases for the same M_0. Therefore, we can use alternatively the empirical scaling relation between moment magnitude and length and width of the area affected (Blaser et al., 2010; Wells and Coppersmith, 1994). Note that these empirical relations are meaningful for events at least Mw≥4.8, so they give us in the present case an idea of the surface rupture assuming that small earthquakes follow the same relations. Using the relationship of Blaser et al., 2010 for a reverse fault we obtain an estimation of 0.8 km x 0.9 km. If we make the hypothesis that the size of the cluster is more or less the rupture surface, the surface predicted by the empirical relations is very small compared to the actual size of the cluster.

Consequently, the MLv=4.0 will not be considered as a mainshock but as a significant event in the cluster and add to the gradual increase of the activity on the cluster, we estimate that it more likely corresponds to a swarm structure rather than a mainshock-aftershock sequence.

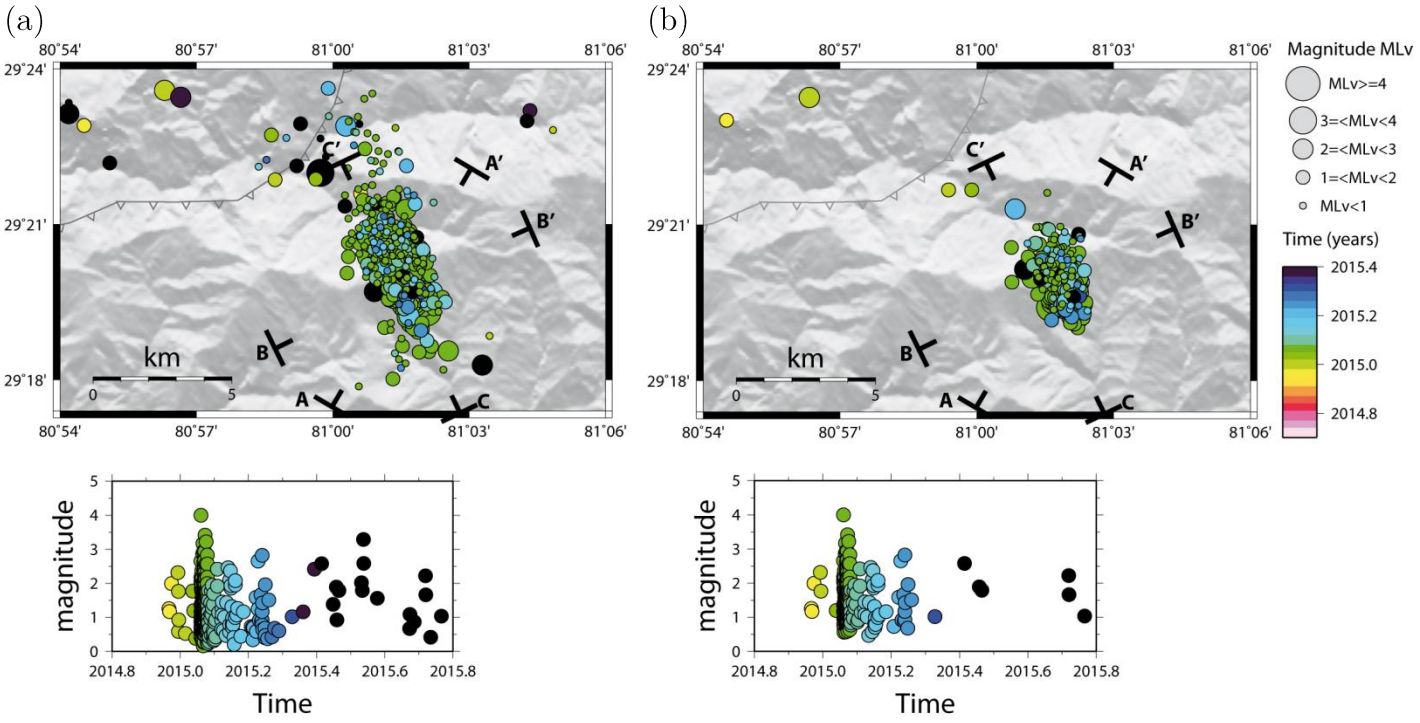

Figure 4.15. Spatio-temporal evolution of cluster C in map view (upper figures) and magnitude-time plot of the cluster (lower figures). (a) Catalogue of the absolute location of the events. (b) Catalogue of the relative relocated events. Gray line is the MCT.

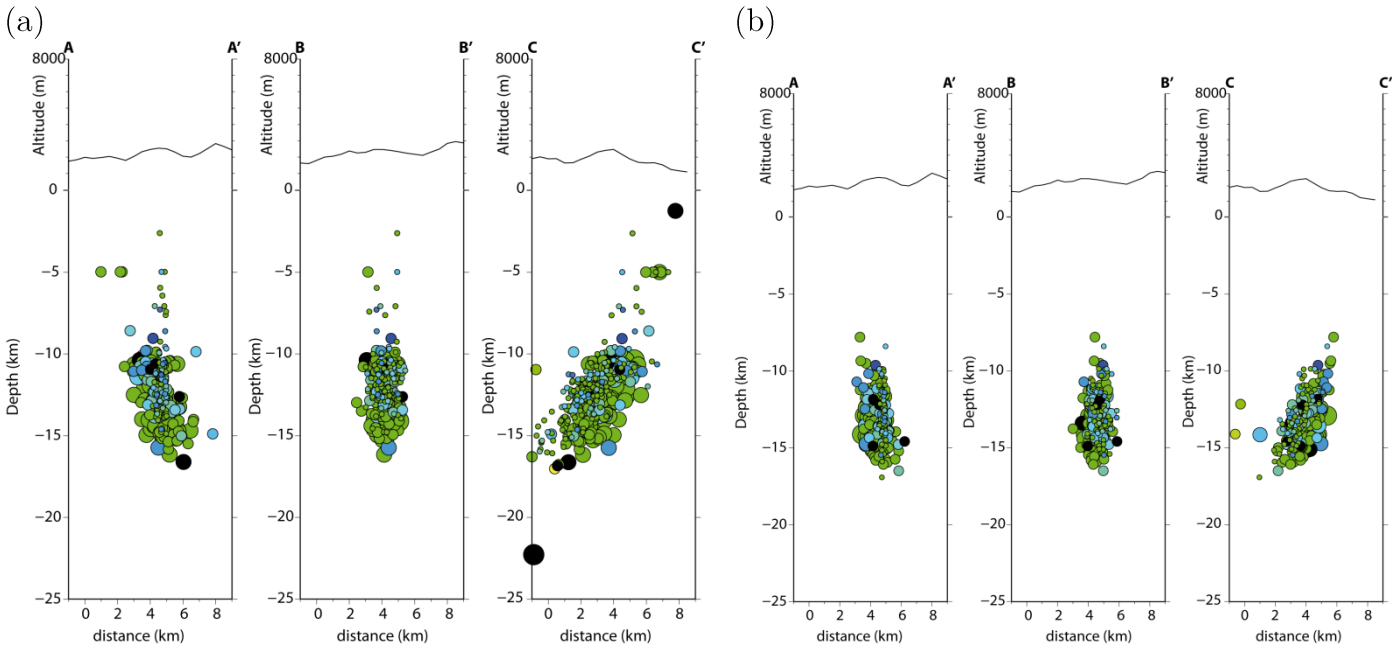

Figure 4.16. Cross-sections within +/- 2km from A-A', B-B' and C-C' (see Figure 4.15). A-A' is 10 km-long striking N030E. B-B' is 10 km-long striking N065E. C-C' is 10 km-long striking N155E. (a) Catalogue of the absolute location of the events. (b) Catalogue of the relative relocated events.

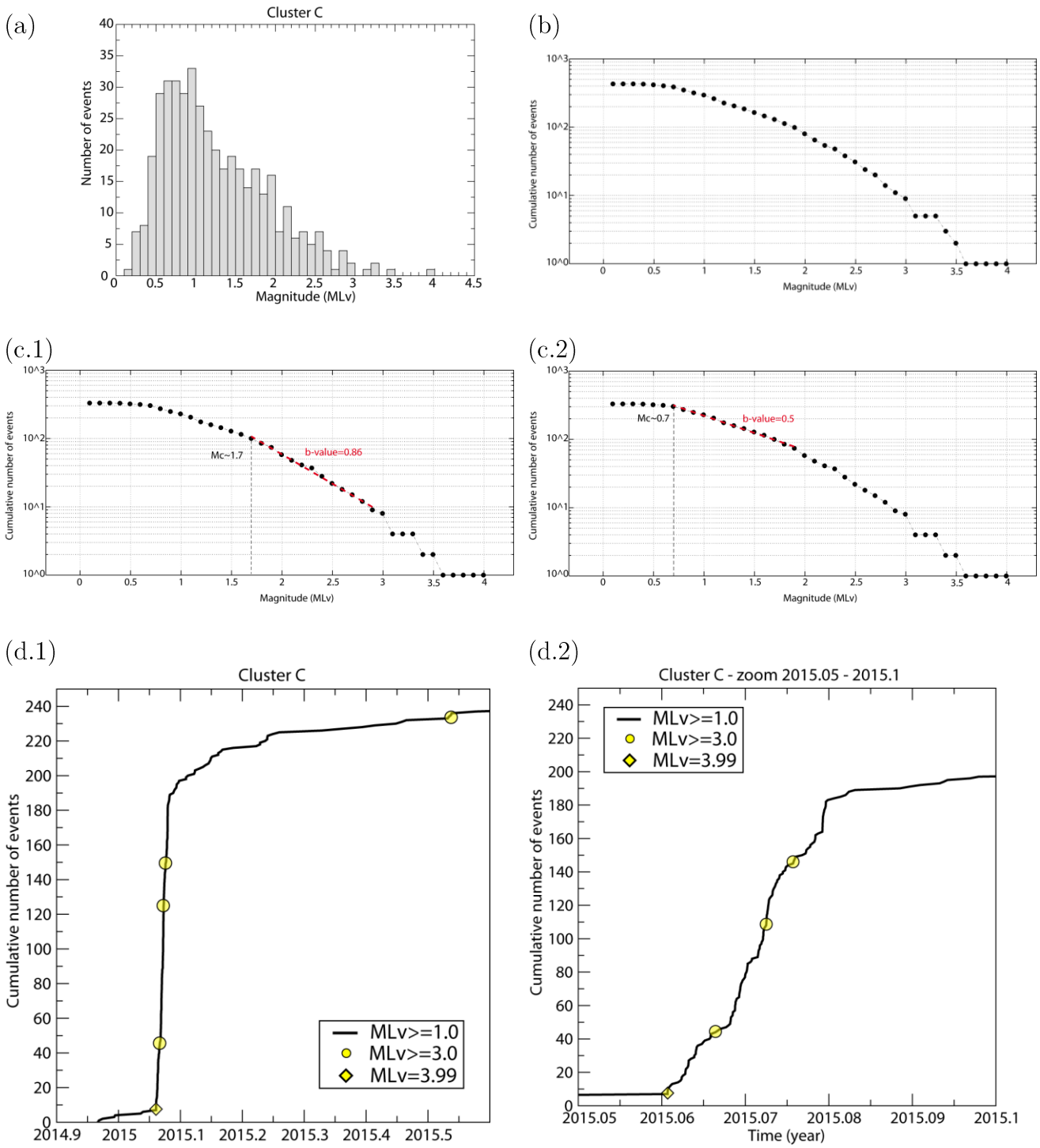

Figure 4.17. Evolution in time of the seismicity above the estimated Mc in cluster C of Figure 4.15.a. (a) Number of events in function of magnitude for the period 01/12/2014 – 10/10/2015. (b) Gutenberg-Richter distribution for the period 01/12/2014 – 10/10/2015. (c) Gutenberg-Richter distribution for the period 03/01/2015 – 01/02/2015 with two trends: (1) b-value=0.86±0.02 and Mc~1.7 and (2) b-value=0.5±0.01 and Mc~0.7. (d) Cumulative number of events with MLv≥1.0 in function of time: (1) the whole period 01/12/2014 – 10/10/2015 and (2) centered on the most active period of cluster C (22/01/2015 – 31/01/2015).

4.1.1.4. Cluster D

Cluster D is located at the southeast extremity of the seismicity of Zone W with BAYN and MA10 as the closest stations. It constitutes the less crowded cluster of the 4 we relocated in this area with ~70 events (almost 50 events were relocated). However, it concentrates 3 events of magnitudes of 4.0≥MLv≥3.0 (Figure 4.18).

In this case, the relocated seismicity presents a completely different geometry than the absolute location (Figure 4.18). In surface, we have the seismicity agglomerated in about 2 km without a clear preference orientation NNW-SSE (Figure 4.18). In depth, the seismicity was originally concentrated between 15 and 18 km (Figure 4.19), after the relocation they are organized vertically between 15 and 20 km (Figure 4.19).

We perform the magnitude-frequency distribution and we observe a continuous slope between 0.9≥MLv≥2.5 with a b-value of 0.72±0.04. The break-in-slope of the GR distribution is MLv~0.9 which might be approximately the Mc. (Figure 4.20.a).

The time sequence of events of magnitude MLv≥0.9 shows from the beginning an emergent seismic activity (Figure 4.20.b). The rapid increase of seismicity is preceded by the occurrence of an event of magnitude MLv=3.4 on 2014 December the 13th. This was not the larger event in the cluster, instead it came 3 days later and had a magnitude MLv=3.7 (Figure 4.20.b). The activity slows down at the end of 2014 and a smaller increase on the activity is noticed from late January to early February. The rest of the months do not show much activity (Figure 4.20.b).

The clustered activity seems to start just after the installation of the stations, though we cannot be sure only with the TSN catalogue that it was already running at the time (Figure 4.20.b). Looking at the RSC catalogue for the same frame of Figure 4.18 but since the beginning of 2014 we confirm that the TSN catalogue has the burst of seismicity since the beginning (Figure 4.20.c). We observe as well that at least two clustered seismicity has taken place since April 2014 before the current cluster. Such time structure describes a pulsed activity in the area in the past 10 months (Figure 4.20.c).

The change of geometry between the absolute location and the relative relocation attracts our attention. *A priori*, we do not have reasons to doubt of its validity because we were confident on the results obtained in Chapter 3. The high depth uncertainty in the absolute location for this cluster could have been solved by the relative relocation (Figure 3.18.b). Or, the fact that the closest stations are all located north-west of the cluster could influence the results. In any case, we are not sure whether the geometry is accurate or not, consequently we prefer do not take the spatial distribution of the seismicity of cluster D into account later on.

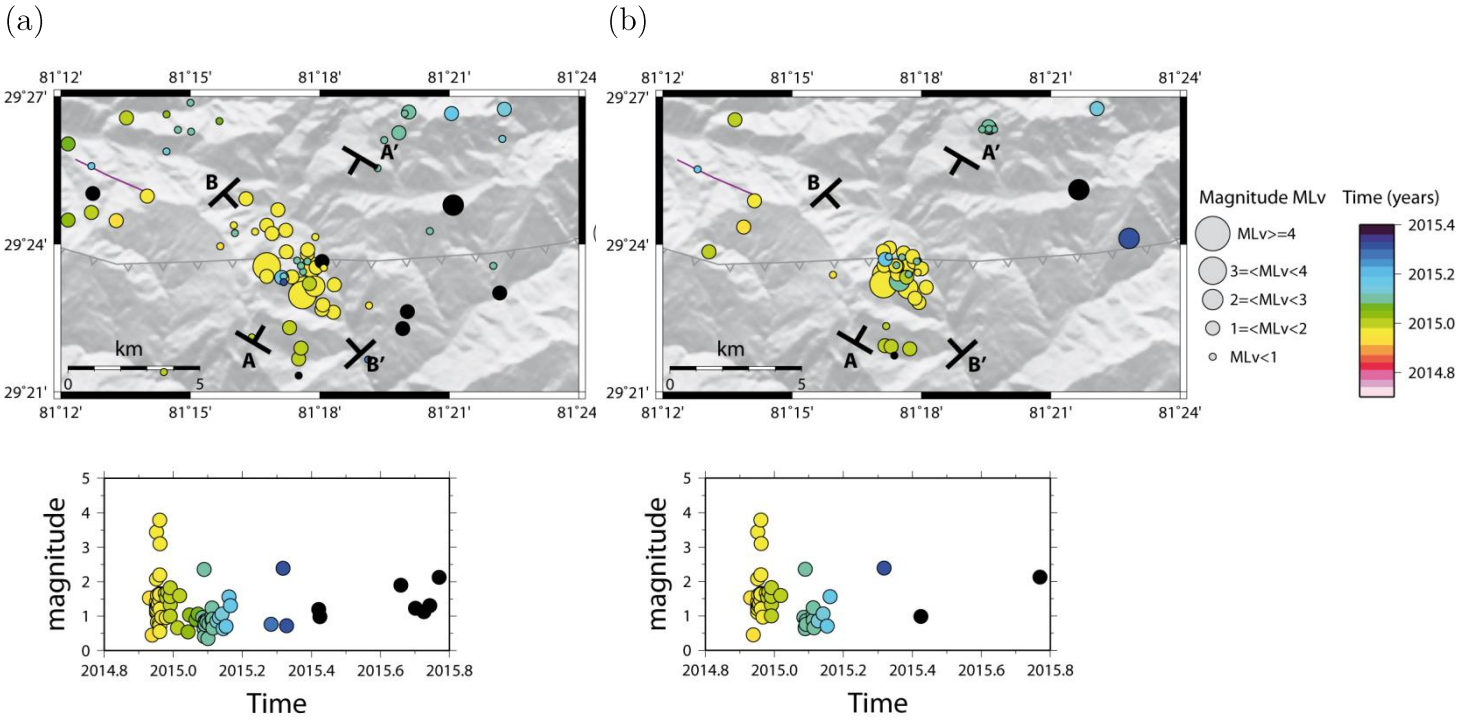

Figure 4.18. Spatio-temporal evolution of cluster D in map view (upper figures) and magnitude-time plot of the cluster (lower figures). (a) Catalogue of the absolute localization of the events. (b) Catalogue of the relative relocated events. Purple lines are the active faults of Nakata, 1982. Gray line is the MCT.

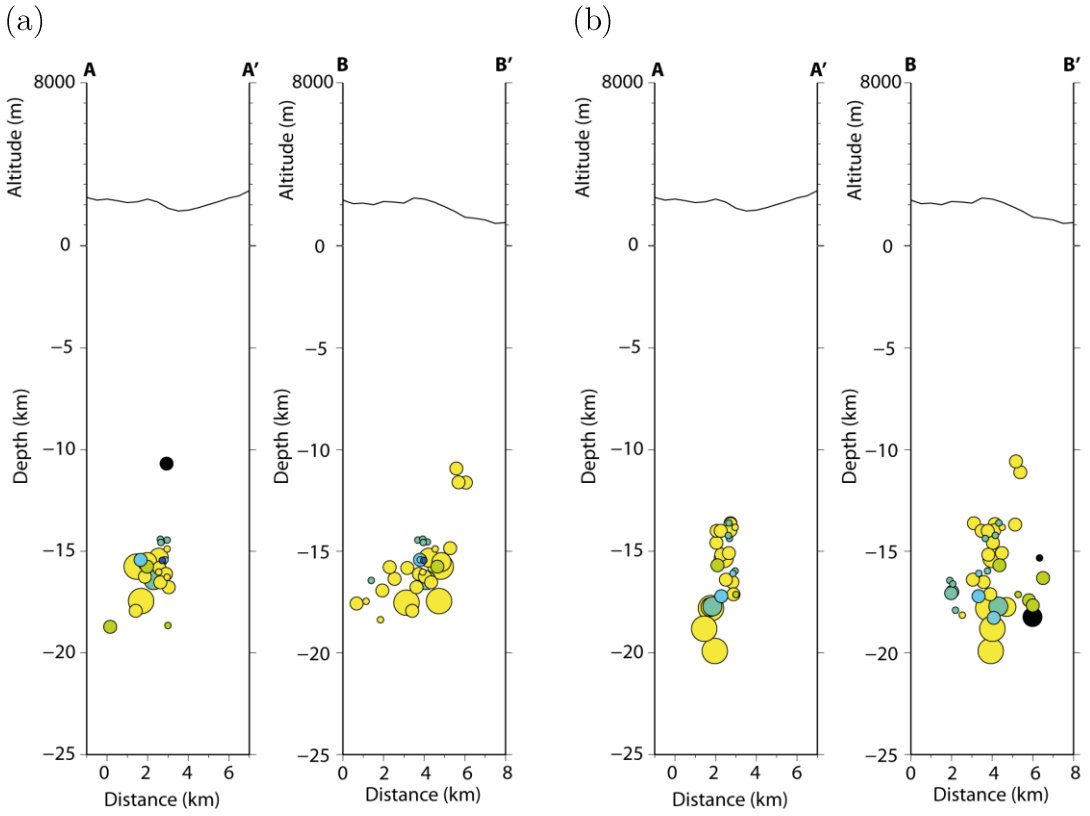

Figure 4.19. Cross-sections within +/- 1 km from A-A' and B-B' (see Figure 4.18). A-A' is 8 km-long striking N030E. B-B' is 8 km-long striking N140E. (a) Catalogue of the absolute location of the events. (b) Catalogue of the relative relocated events.

(a)

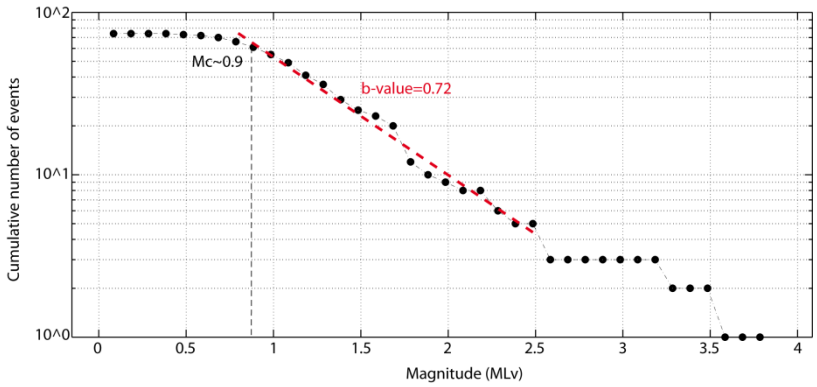

(b)

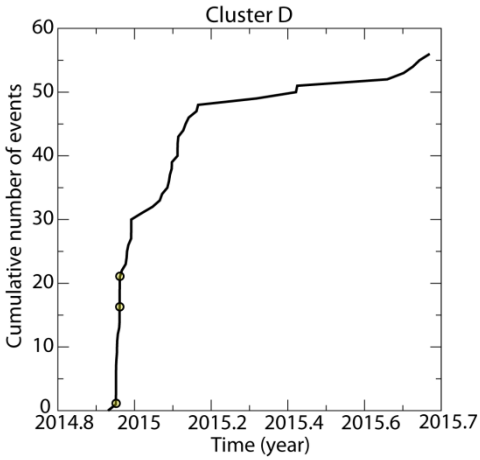

(c)

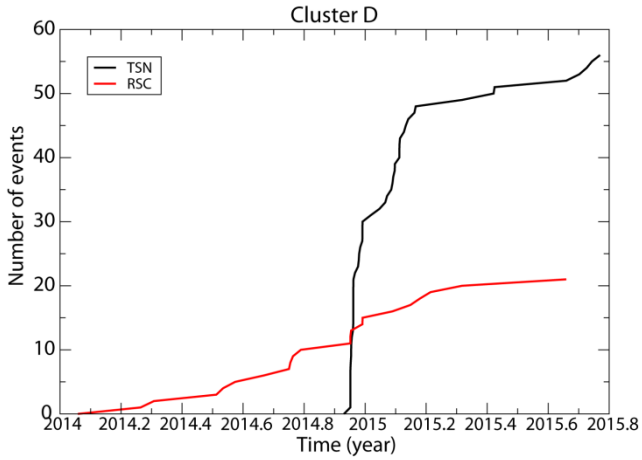

Figure 4.20. Evolution in time of the seismicity above the estimated Mc in cluster D of Figure 4.18.a. (a) Gutenberg-Richter distribution with a b-value=0.72±0.04 and a Mc~0.9. (b) Cumulative number of events with MLv≥0.9 in function time. (c) Comparison between the cumulative number of events of the TSN and the RSC catalogue.

4.1.2. The South Karnali seismic belt

During the period we studied, we have detected 294 events from which 64% are high quality events (Figure 4.21). The seismicity is present under the network all along the experiment distributed in agglomerations of events but also as single ones (Figure 4.21.c). The depth of the events ranges between 5 and 15 km, centered around 10 km (Figure 4.21.b). In addition, the seismicity located northwest is deeper in general than the seismicity located southeast (Figure 4.21.b). This lateral variation is arisen basically by the two clusters (Cluster KS and Cluster DK) (Figure 4.22).

The 85 % of the events recorded have magnitudes 0.1<MLv≤2.0 with a pick of the number of events around MLv=0.7 (Figure 4.23.a). We couple this information with the GR distribution which break-in-slope is MLv~0.8 that might correspond more or less to the Mc of the catalogue for South Karnali seismic belt (Figure 4.23.b). The slope of the GR distribution is constant from MLv=0.8 until MLv~3.0 with a b-value=0.76±0.03 (Figure 4.23.b).

Regarding the cumulative number of events of magnitude MLv≥0.8 as a function of time, we observe from one side a general increase of the seismicity rate from early January 2015 to mid-March followed by a slower increase (Figure 4.24). And from the other side, the time sequence increases in small leaps, clustering groups of events in time (Figure 4.24).

(a)

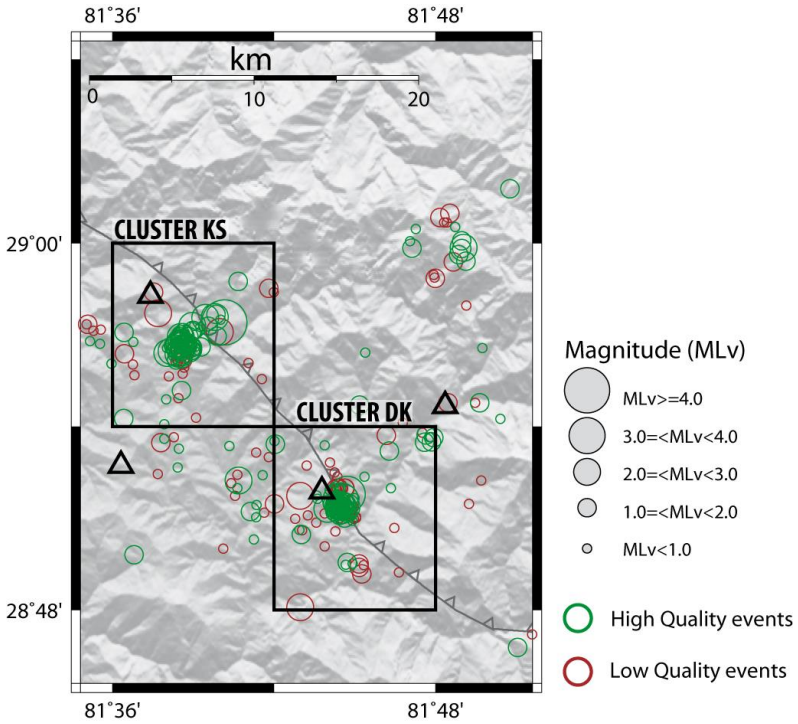

(b)

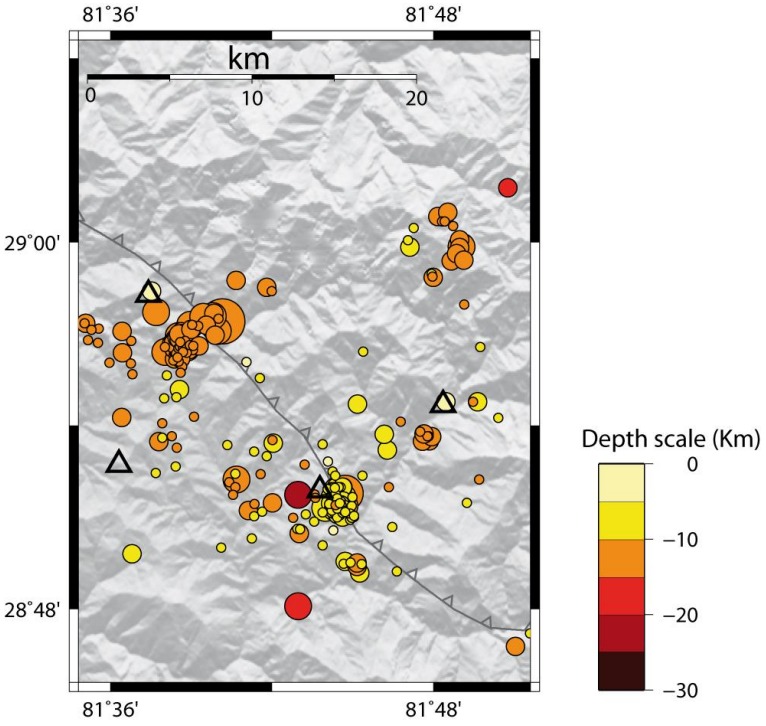

(c)

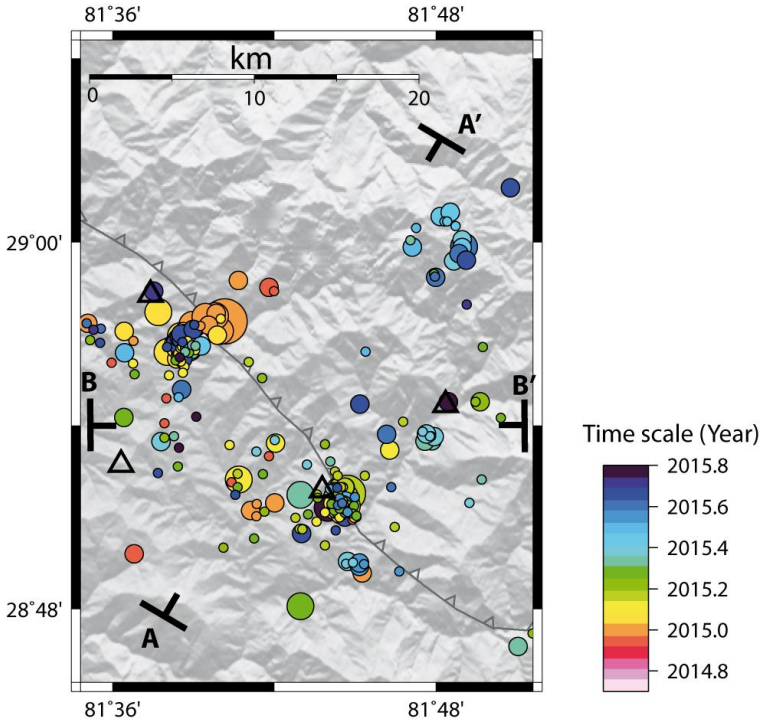

Figure 4.21. Map of the seismicity of South Karnali seismic belt with circle size depending on magnitude MLv. The color of the events depends on (a) their quality: green circles represent the high quality HQ events (6 P-phases, 3 S-phases, RMS ≤ 0.4 and ERH and ERZ ≤ 2 km), brown circles are the low quality events (P-phases < 6, S-phases < 3, RMS > 0.4 seconds and ERH and ERZ > 2 km); (b) their depth and (c) their date of occurrence. A-A' and B-B' are the cross sections through the seismicity represented in Figure 4.22.

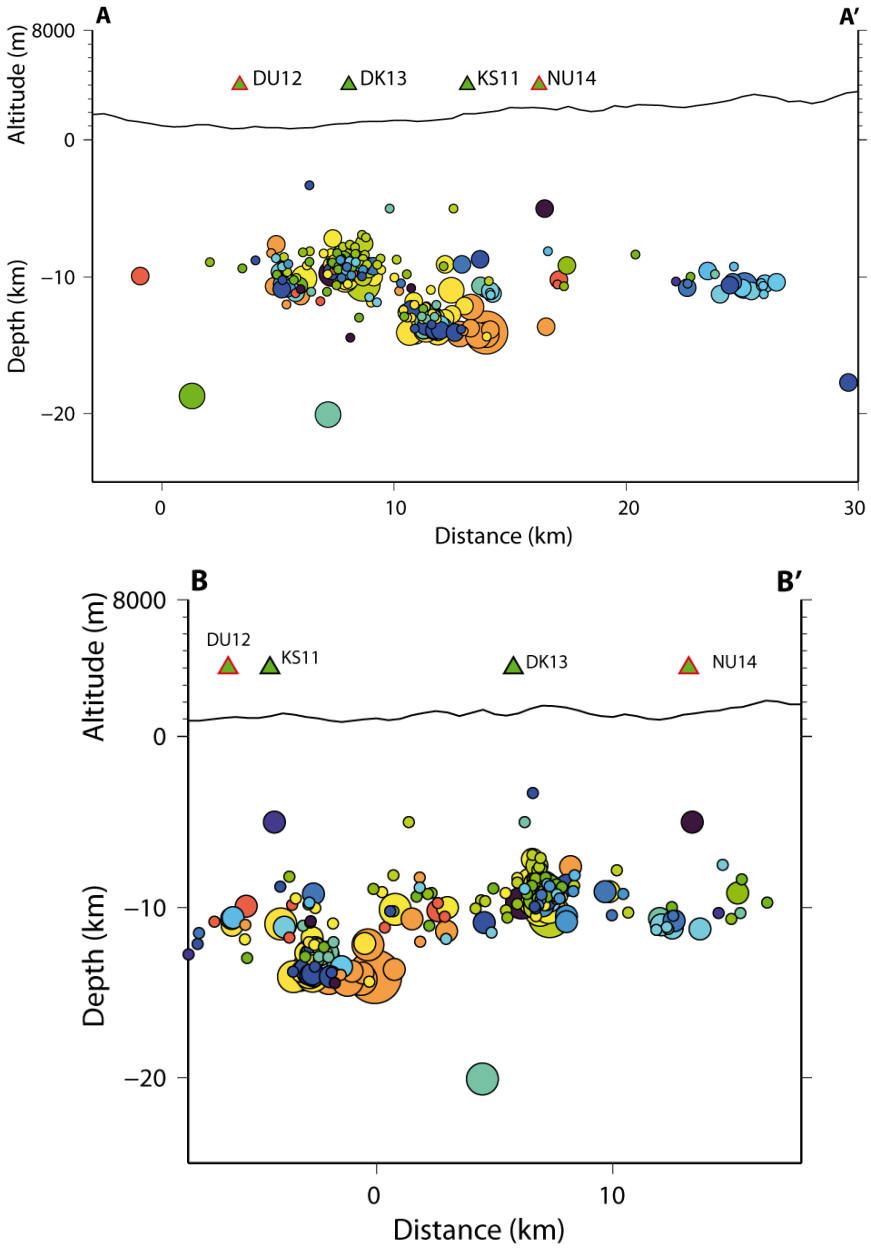

Figure 4.22. Cross-sections within +/-10 km from A-A' and B-B' of Figure 4.21. A-A' strikes N030E. B-B' strikes N090E. See Figure 4.21 for magnitude scale.

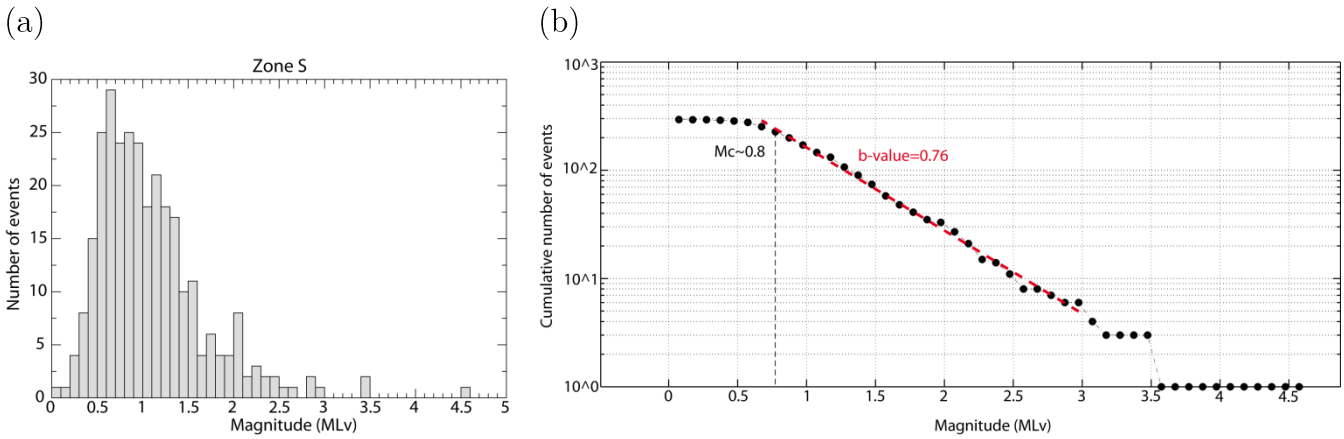

Figure 4.23. Magnitude distribution for South Karnali seismic belt. (a) Magnitude histogram of the events in MLv. (b) Gutenberg-Richter distribution of the zone of study with a b-value=0.76±0.03 and Mc~0.8.

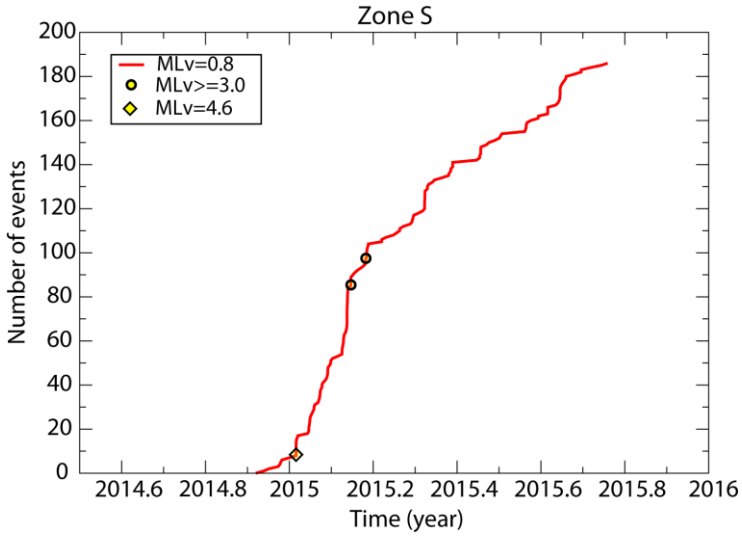

Figure 4.24. Time sequence of the seismic events which MLv≥0.8 in South Karnali seismic belt. Yellow circles are the events which magnitude is MLv≥3.0 and the yellow diamond is the M=4.6 event that occurred the 05/01/2015.

4.1.2.1. Cluster KS

The cluster KS is located nearby KS11 station, northwest of Zone S (Figure 4.21). Contrary to what we expected, it is formed by 96 events (77 events were relocated) divided in two groups: (1) a small cluster that includes the MLv=4.6 occurred the 05/01/2015 and (2) a large numbered cluster active in different periods starting after (1) (Figure 4.25).

They have been processed together because we did not realize that they were two different clusters until we applied the relative-relocation to the area. The smallest cluster is formed by 9 events and we point out that the MLv=4.6 is situated around 12 km depth and the "after" shocks are just above it (Figure 4.25 and 4.26).

The seismicity of cluster (2) distributes along 2 km x 1.5 km thick x ~0.7 km wide dipping ~68° NW (Figure 4.25 and 4.26).

We perform the magnitude-frequency distribution calculation using only the large numbered cluster. The slope of the GR distribution is homogeneous with a b-value=0.61±0.02 from MLv=2.0 until the breaking slope at MLv=0.9 which we estimate to be close to the Mc (Figure 4.27.a).

The activity begins just after cluster (1) and remains active few weeks, after a period of quiescence it develops bursts of seismicity at two occasions (Figure 4.25). Cutting the time sequence to events of magnitudes MLv≥0.9, the first event to come up is the MLv=4.6 event followed by 8 aftershocks (Figure 4.27.b). The small cluster is followed by a burst of seismicity of the larger cluster that lasts approximately two weeks, and then the activity is almost inexistent until the end of April when there is a sudden increase on the seismicity rate but without major events. Once more the activity continues being very low until the end of August when the rate of seismicity rises again (Figure 4.27.b).

The lack of significant-magnitude events and the pulse functioning of the cluster along the year let us think that cluster (2) presents swarm characteristics. On the contrary, the time sequence and the distribution of seismicity of cluster (1) present the characteristics of a mainshock-aftershock sequence.

(a)

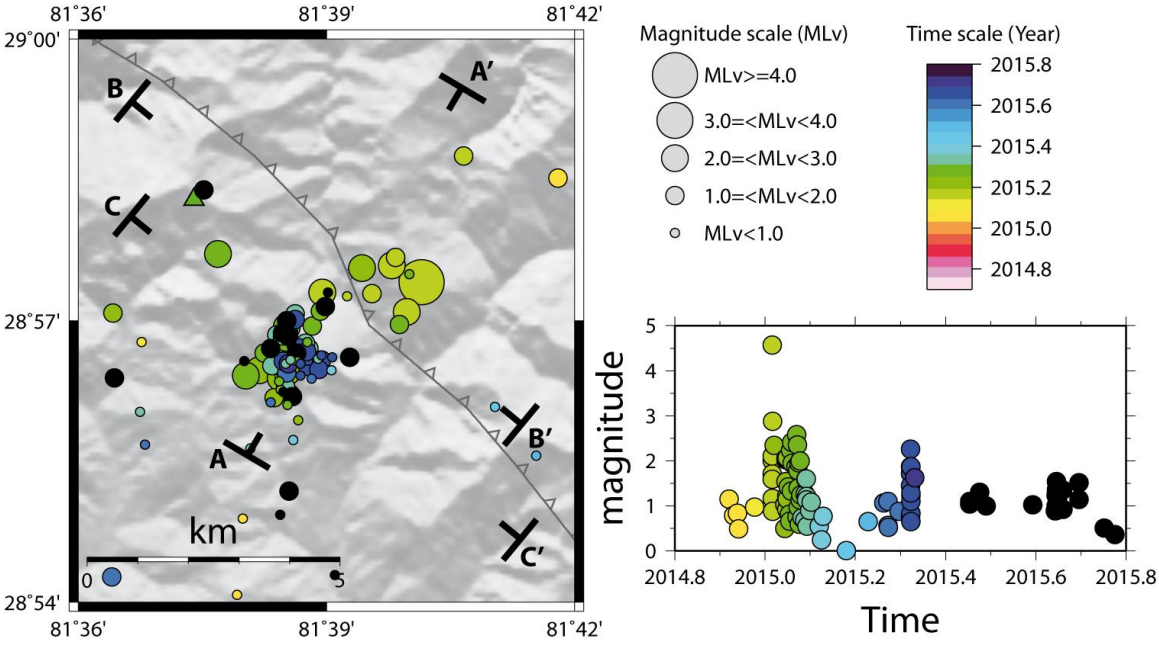

(b)

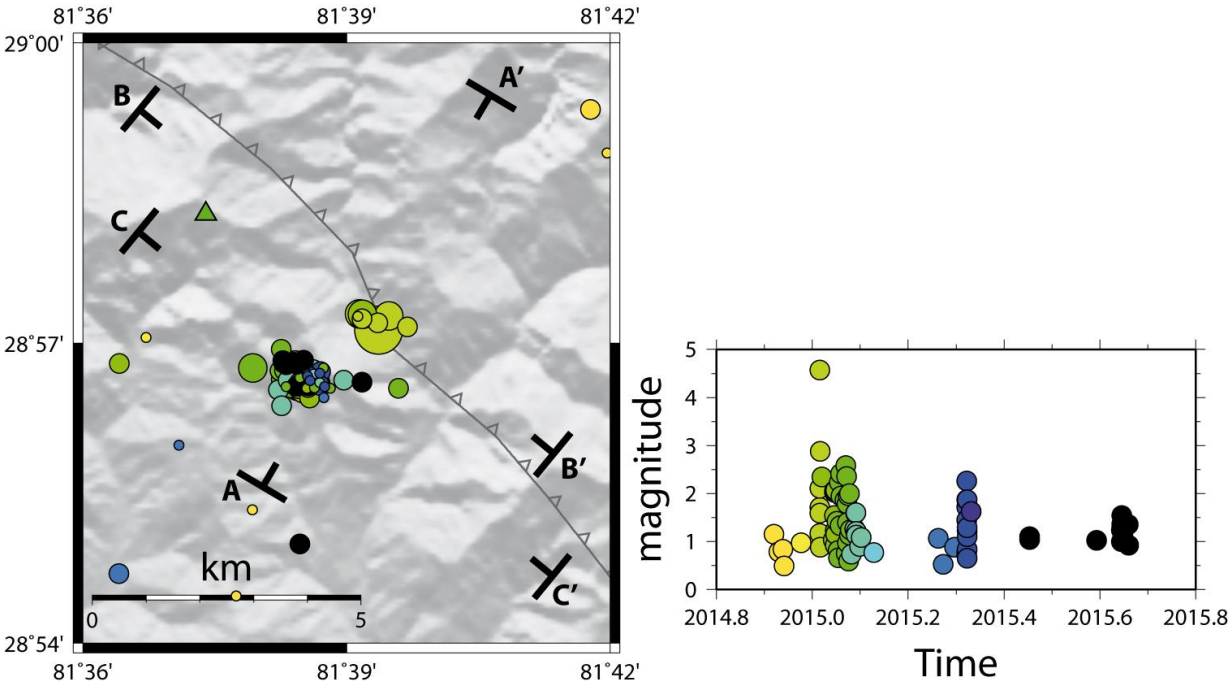

Figure 4.25. Spatio-temporal evolution of seismic cluster KS in map view (left figures) and magnitude-time plot of the cluster (right figures). (a) Catalogue of the absolute localization of the events. (b) Catalogue of the relative relocated events.

(a) (b)

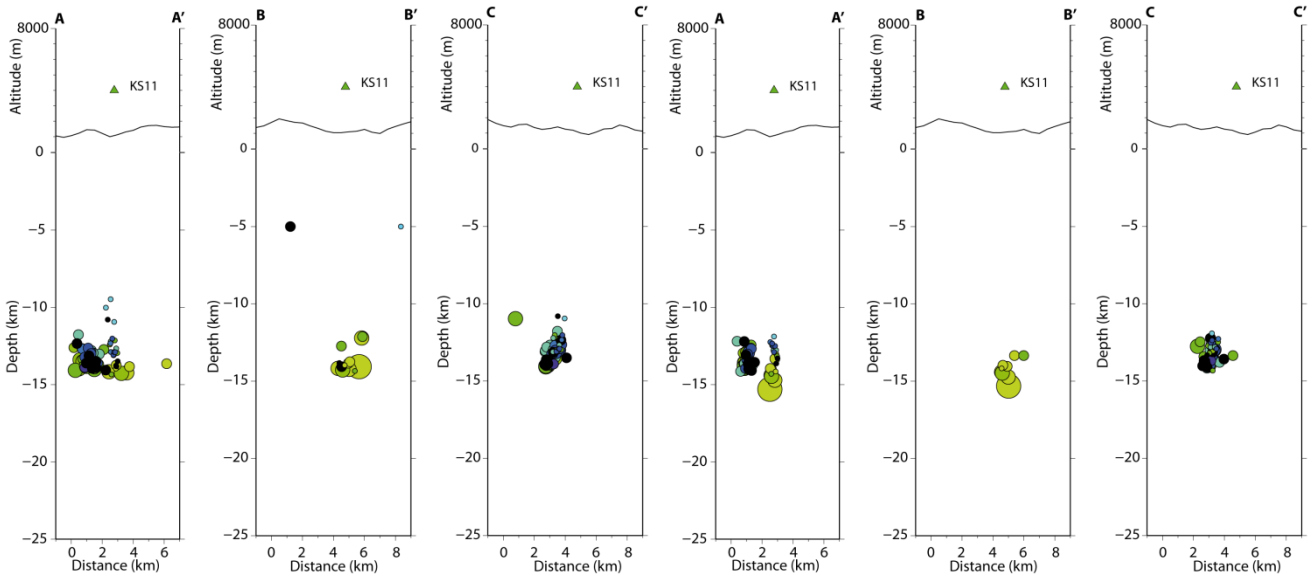

Figure 4.26. Cross-sections within +/- 1km from A-A', B-B' and C-C' (see Figure 4.25). A-A' is 8 km-long striking N030E. B-B' and C-C' are 10 km-long striking N130E. (a) Catalogue of the absolute localization of the events. (b) Catalogue of the relative relocated events. Circle size and color scale are the same as Figure 4.25.

(a) (b)

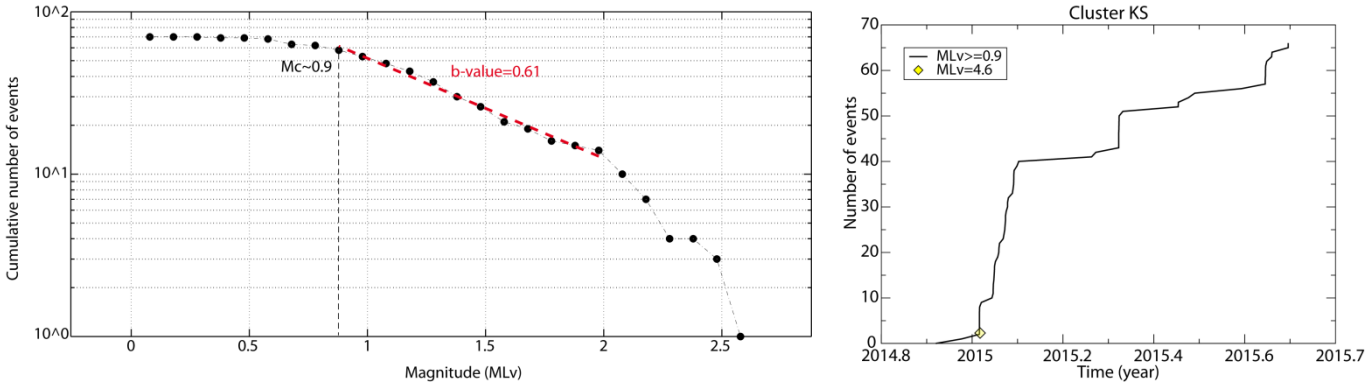

Figure 4.27. Evolution in time of the seismicity above the estimated Mc in cluster KS of Figure 4.25.a. (a) Gutenberg-Richter distribution with a b-value=0.61±0.02 and a Mc~0.9. (b) Cumulative number of events with MLv≥0.9 in function time.

4.1.2.2. Cluster DK

Cluster DK is placed about 1 km southeast from DK13 station as the crow flies (Figure 4.21). It is formed by 139 events (~100 events were relocated) with event magnitudes below MLv=4.0 and mostly active from mid-February to mid-March 2015 (Figure 4.28).

The geometry of the cluster after relocation is a WNW-ESE orientated seismicity for 2 km (Figure 4.28.b). At depth the seismicity distributes on a little bit more than 1 km dipping ~65° NE (Figure 4.29.b). Notice that the largest magnitudes events are located at the deepest part of the cluster whereas the smaller magnitude events are in shallower positions (Figure 4.29.b).

The GR distribution presents a slope or b-value=0.8±0.05 continue from MLv=2.3 until the breaking slope at MLv=0.6 which might be close to the Mc (Figure 4.30.a). Looking at the big picture, the evolution of the seismicity in time is a period of quiescence followed by a sudden increase of the activity from mid-February until mid-March and finally a slow decrease for some months (Figure 4.30.b). At a detailed scale, there is a small increase of the seismicity rate at the beginning before soaring. The drastic raise of seismicity is done at least with two steps (Figure 4.30.b). The first and most significant rise of seismicity includes an event of magnitude MLv≥3.0 at the end of the burst (Figure 4.30.b). The second rise includes also an event of magnitude MLv≥3.0 but this time at the beginning of the burst. From mid-March until early October, the cluster produces small amounts of seismicity by periods (Figure 4.30.b and 4.28).

In this case, the lack of a major earthquake triggering the rapid increase of clustered seismicity and the activity by stages seems to tilt in favor of a swarm activity for cluster DK.

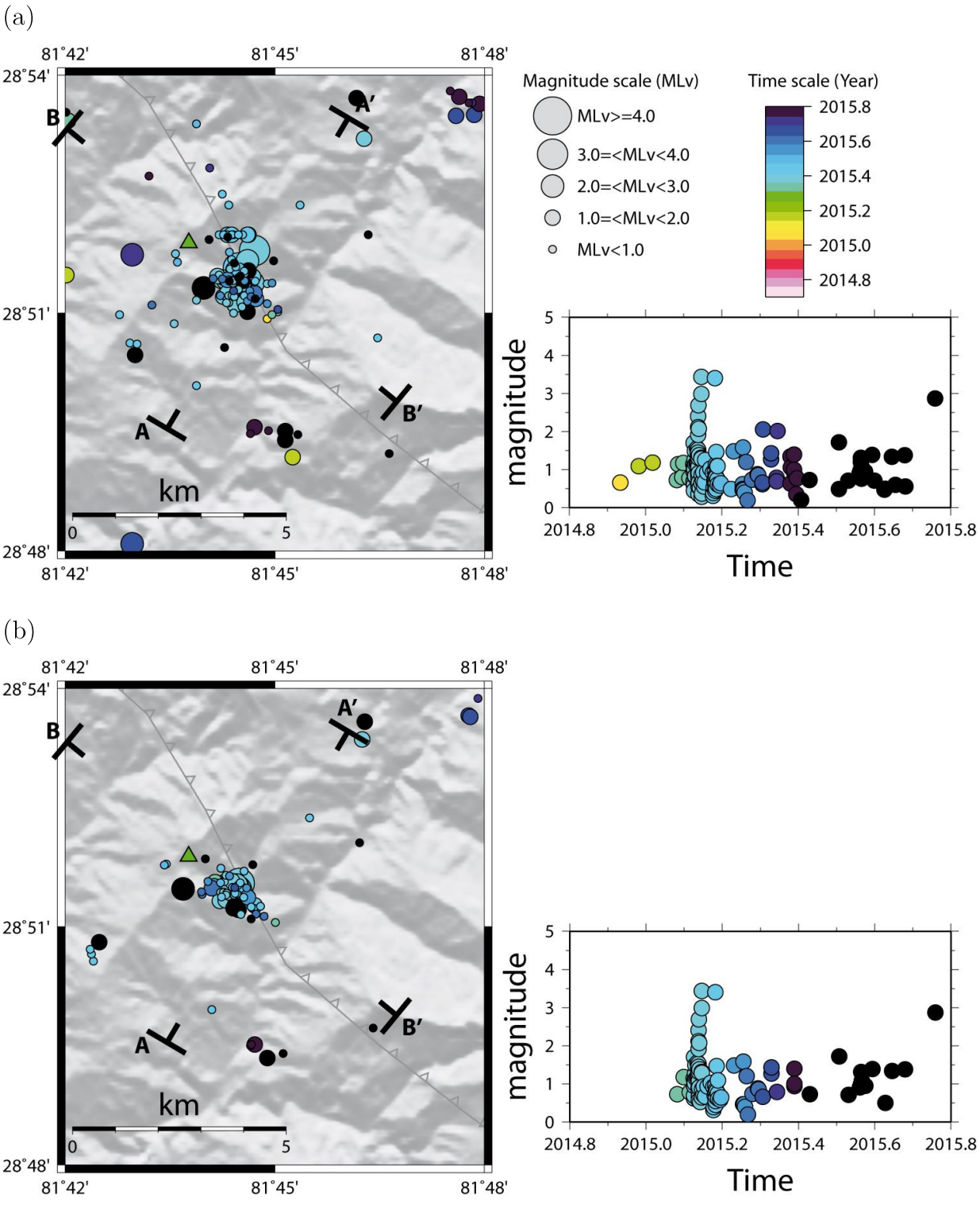

Figure 4.28. Spatio-temporal evolution of seismic cluster DK in map view (left figures) and magnitude-time plot of the cluster (right figures). (a) Catalogue of the absolute localization of the events. (b) Catalogue of the relative relocated events.

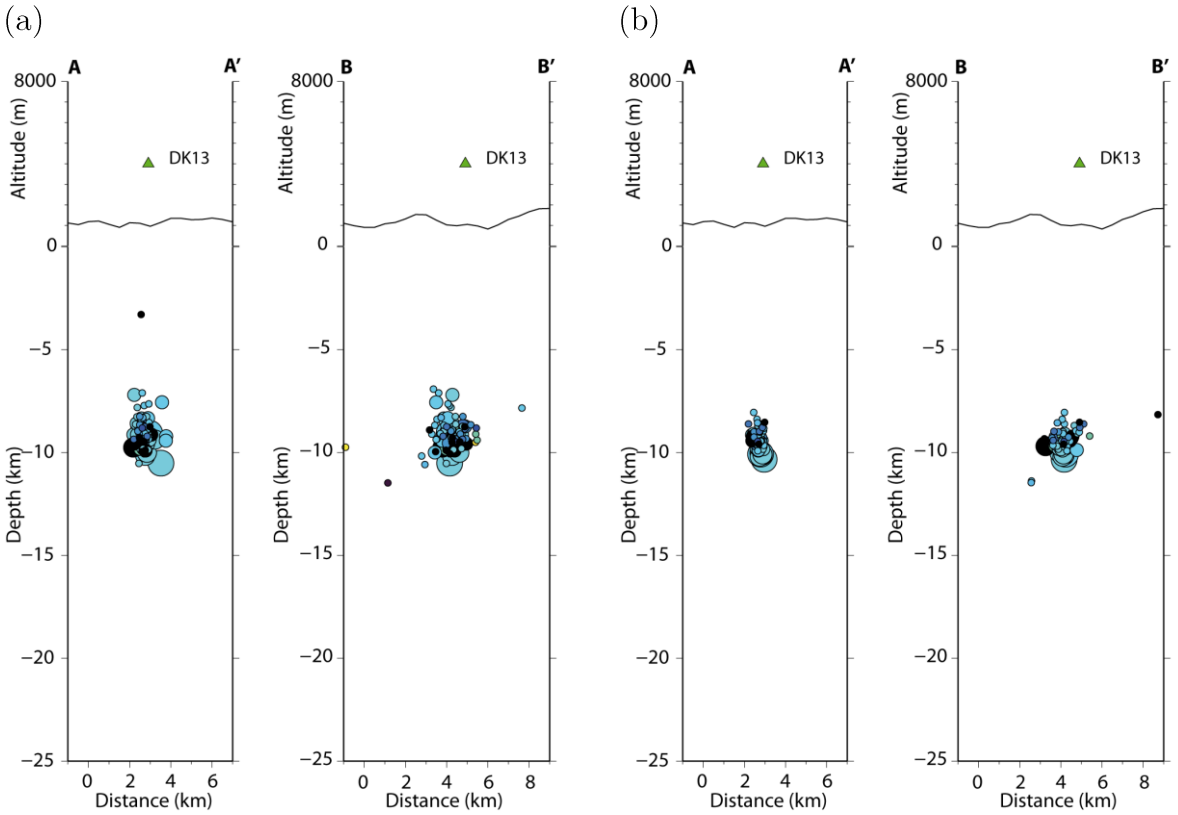

Figure 4.29. Cross-sections within +/- 1km from A-A' and B-B' (see Figure 4.28). A-A' is 8 km-long striking N030E. B-B' is 10 km-long striking N130E. (a) Catalogue of the absolute localization of the events. (b) Catalogue of the relative relocated events.

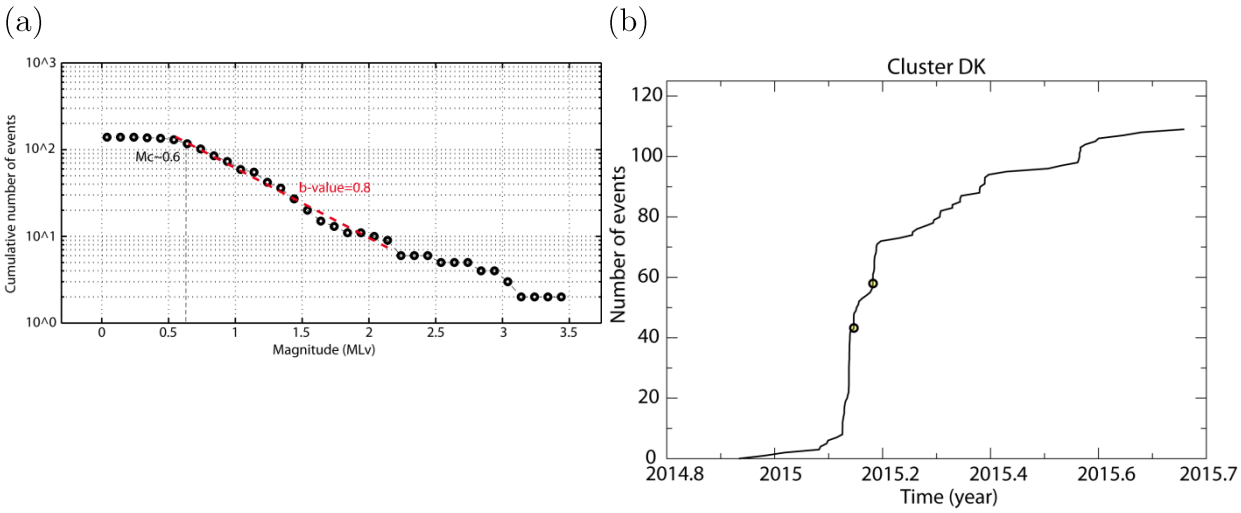

Figure 4.30. Evolution in time of the seismicity above the estimated Mc in cluster DK of Figure 4.28.a. (a) Gutenberg-Richter distribution with a b-value=0.8±0.05 and a Mc~0.6. (b) Cumulative number of events with MLv≥0.6 in function of time.

4.1.3. Main characteristics of the seismic clusters

We have described the results at different scales: the zone of study, the denser seismicity zones with the closest stations and the clusters of seismicity individually.

The densification of stations in certain parts of the zone of the study has influenced results like the location of the best located events (HQ) in Zone W and Zone S principally.

The magnitude of completeness is about Mc~1.4 for the entire catalogue, but it is drastically decreased to 1.0 and 0.7 in Zone W and Zone S, respectively (Table 4.1 and 4.2). However, the relation between the small magnitudes and the bigger magnitudes is more or less stable between the entire catalogue and the Zones W and S with similar values around 0.75. This relation changes locally in the clusters going from 0.69 until 0.86 (Table 4.1 and 4.2).

The seismicity recorded during the first year of the presence of the temporary network is more important in the Bajhang seismicity belt than the South Karnali seismicity belt, as well as the area affected. The average depths of the events become shallower from west (~14 km) to southeast (~10 km). The seismicity in Zone S and Zone W appears as isolated events and also as clustered events. We have focused our interest on the larger scale clusters, but the agglomeration of events is done at a very small scale of 4-5 events too.

We have relocated 6 clusters, 4 in Zone W and 2 in Zone S. We have presented each one individually and we summarize the information in Table 4.1 and Table 4.2.

The geometry of clusters in Zone W is only exploitable for cluster A, B and C because we are not certain how to explain the big difference between the relative relocation and the absolute location of cluster D. Cluster A, B and C present astonishing common characteristics: They are centered between 12 - 14 km depth and present a similar elongation orientation of the seismicity, especially between cluster A and B. Their width and depth are similar, but they differ on the length of the cluster. The most interesting feature is the dip of the seismicity: from one side cluster A and B, contiguous one from the other, presents a subhorizontal dip and from the other side, clusters C is characterized by a 60° dip.

The clusters in Zone S have similar dimensions and are very steep. However, we would like you to note the difference on the depth, about 12.5 km and 9 km from the cluster KS to the cluster DK (west to east) and the different dip orientation (NE and NW respectively).

Finally, the analysis of the time sequence of the catalogue highlights the important activity in west Nepal expressed by the clustered activity during the first months of the experiment. I would like to draw your attention on the similarity on the time sequences

of each one of the clusters. Although we are looking to a small period, their coexistence at close distance as well as at far distances is worthy to be discussed later on.

Clusters Zone W	Zone W	A	B	C	D
Number of events	1451	313	105	431	74
Number of events relocated	-	133	54	304	49
Dimensions (km)	-	3 x 0.5 x 1	1.5 x 0.6 x 0.5-0.7	7 x 1.5-2 x 1.7	2 x 4-5 x 1.2
Surface orientation	-	WNW-SSE (~N110)	NNW-SSE (~N155)	NNW-SSE (~N150)	-
Dip (°)	-	10° WNW	subhorizontal	60° NNW	Vertical
Average depth (km)	14	14	13	14	15
b-value	0.77±0.03	0.85	0.69±0.01	0.5±0.01 0.86±0.02	0.72±0.04
Estimated Mc	1.0	0.5	0.7	1.0	0.9
Maximum activity period	Early December 2014 to mid-March 2015	14/12/2014 to 02/03/2015	01/12/2014 to 13/03/2015	22 – 31 January 2015	13/12/2014 to 27/02/2015
Type of cluster	-	Swarm	Swarm	Swarm	

Table 4.1. Summarize of the results of Zone W and its clusters.

Clusters Zone S	Zone S	KS small	KS big	DK
Number of events	294	8	88	139
Number of events relocated	-	77		101
Dimensions (km)	-	-	2 x 1.5 x 0.7	2 x 1
Surface orientation	-	-	Not clear	WNW-ESE
Dip (°)	-	-	68° NW	65° NE
Average depth (km)	10	-	12.5	9
b-value	0.76±0.03	-	0.61±0.02	0.8±0.05
Estimated Mc	0.7	-	0.9	0.6
Maximum activity period	Early January to mid-March 2015	05/01/2015	15/01/2015 - 02/02/2015 27-28/04/2015 23/08/2015	14/02/2015 to 10/03/2015
Type of cluster	-	Mainshock-aftershock	Swarm	Swarm

Table 4.2. Summarize of the results of Zone S and its clusters.

4.2. Temporal distribution of the clusters

As previously mentioned in Chapter 3, and illustrated in Figure 4.31.a, the distribution of the seismicity between December 2014 and October 2015 shows a maximum during winter months and a minimum during summer months. Part of this seasonal variation, depicting a peak in January 2015 and a low in July 2015, is due to the variations of the catalogue completeness magnitude, higher in summer than in winter (e.g. Bollinger et al., 2007). Two main reasons are responsible for these variations. 1- In summer, the high frequency seismic noise is higher than in winter due to severe summer monsoon flooding and sediment transportation in the rivers (Burtin et al. 2008) as well as landsliding (Burtin et al., 2009). 2- In summer, the heavy rains and cloud cover limit the insolation of the solar panels, while flooding and landsliding cut the road accesses to most of the stations, precluding their servicing. One third of the temporary stations (5 stations) stopped acquiring during summer 2015, limiting significantly the detection capacity of the network in some of the regions covered by the network. Despite these biases, the catalogue seems complete above MLv≥1.4, and therefore interpretable in term of genuine earthquake rates variations above that value, as shown at the beginning of this chapter (Figure 4.3). The RSC network recorded similar variations, still significant above ML 2.6, the completeness magnitude of the RSC catalogue during summer months (Figure 4.31.b). This RSC catalogue covers the few years before the temporary experiment. It depicts similar seasonal variations in 2010-2015 during which three prominent peaks of earthquakes, related to several clusters generations, were recorded during winter months (Figure 4.31).

This ‘genuine’ earthquake rate variation could be part of the general midcrustal variations of the seismicity observed before by Bollinger et al., 2007. This seasonality could be due to the seasonal local water load or masses redistributions which increase the normal stress applied on the MHT during the summer monsoon period, inhibiting then the midcrustal seismicity, or increasing the shear stresses during winter months due to the discharge of the India plate (Bettinelli et al., 2008; Chanard et al., 2014).

Further examinations of the western Nepal earthquake rates detected by the national (RSC catalogue) and global catalogues (ISC) revealed nothing else than increases in earthquake production in 2011, 2013 and 2015 (Figure 4.32).

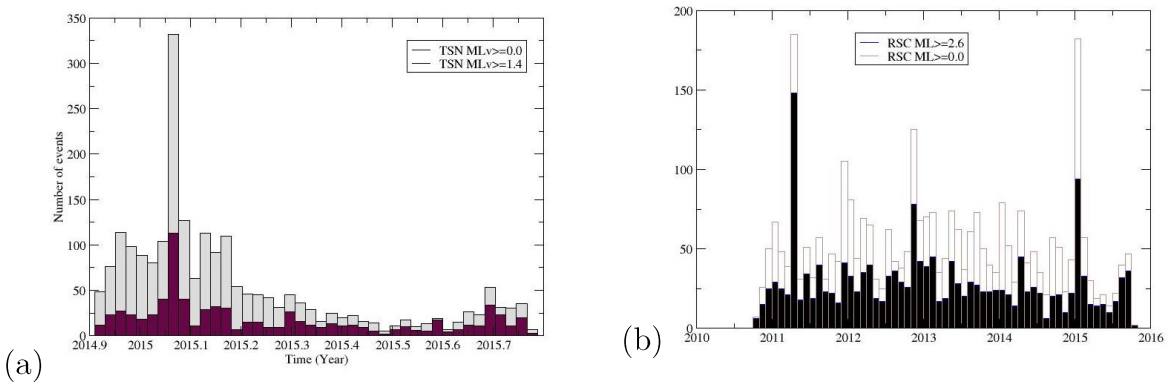

Figure 4.31. Histograms of number of events in function of time for the (a) Temporary Seismic Network during 2014-2015 and for the (b) permanent western Regional Seismic network during 2010-2015. X-scale and Y-scale are the same as (a).

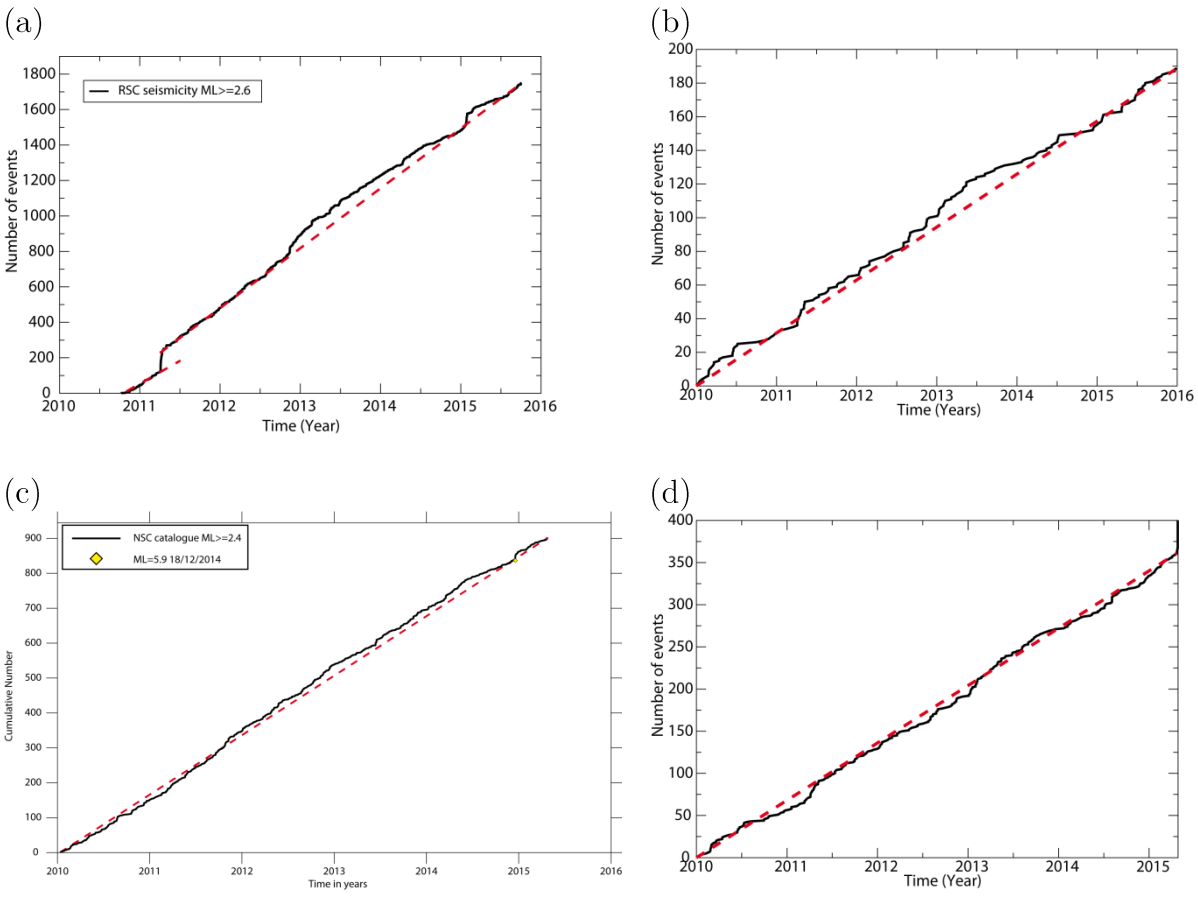

Figure 4.32. Time sequence of the seismicity. (a) RSC catalogue for west Nepal frame. (b) ISC catalogue for west Nepal frame. (c) NSC catalogue of central Nepal. (d) ISC catalogue between 79°E to 88°E and from 26°N to 31°N. Note that no dramatic increase of seismicity was detected in 2015 other than in western Nepal.

A closer look at the winter 2014-2015 seismicity reveals that the seismic burst developed from early December 2014 until March 2015, finishing before the summer monsoon and the loss of the 5 seismic stations that occurred later in 2015. The peak of seismic activity in western Nepal lasted ~3.5 months, contributing to the development of several swarms. Each cluster had a specific productivity and t0 (Figure 4.33). The first swarms that initiated, early December 2014, were clusters A and B (Figure 4.33), which are the northernmost swarms in Bajhang area (Figure 4.5), very close one to the other (~7 km distant) (Figure 4.5). Then, in mid-December 2014, cluster D located 25 km eastwards from clusters A and B, begins its activity followed 3 weeks later by KS cluster but also by the agglomeration of events near Manma (Figure 4.33) (40 and 60 km SSE of cluster D, respectively (Figure 4.5, 4.21 and 4.34). After that, there are two directions on the succession of the burst of the clusters. From one side, the activity begins on cluster C located ~20 km SSW from cluster A and ~10 km SSW from cluster B (Figure 4.5), more than one month after cluster A, B and D (Figure 4.33). From the other side, DK cluster, 12.5 km south-east of KS cluster (Figure 4.21) and shallower as well, gets started mid-February 2015 (Figure 4.33).

(a)

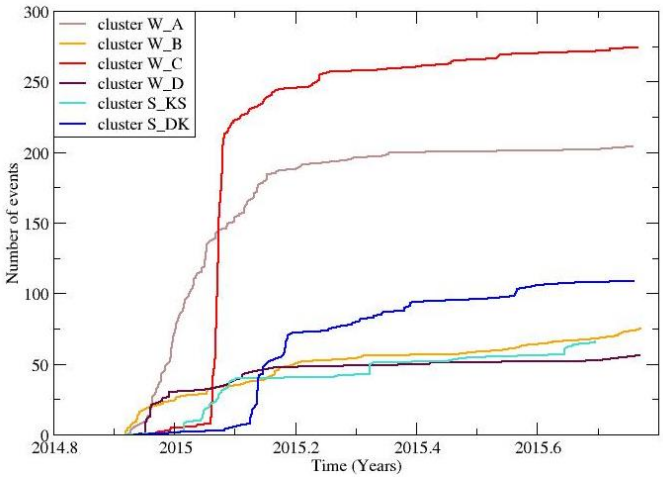

(b)

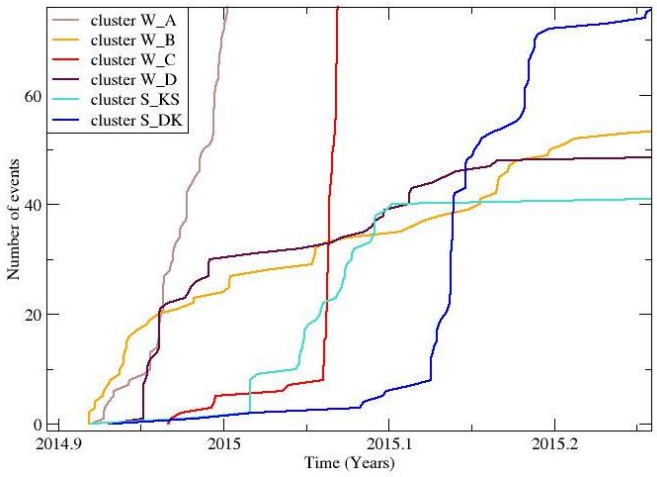

Figure 4.33. Time sequence of indivual clusters (TSN catalogue). (a) The entire time period. (b) Zoom on the starting point of each cluster.

4.3. Seismicity and the geological structures

The distribution of the seismicity in two parallel belts was firstly suspected to be related with the presence of two midcrustal ramps of the MHT, both underlying windows on the lesser Himalaya, north of the Dadeldhura klippe (Pandey et al, 1999). The original DeCelles et al., 1998 cross-section, on which Pandey et al. 1999 based their interpretation on, was located near the west Nepal border stacking the seismicity of the whole region (from 80°E to 82.5°E). However, after few years of work on the regional geology, Robinson et al., 2006 re-balanced the cross section in the area and suggested the presence of a unique ramp right north to the Dadeldhura klippe. However, the idea of a double ramp lived long and has been used as the geometry for the MHT in most of far-western Nepal studies (e.g. Berger et al., 2004; Harvey et al., 2015). Further geological studies have since been conducted and we know now that, in western Nepal, the geological structures vary laterally (Robinson et al., 2006). Among these variations, from west to east, the Dadeldhura klippe and the Lesser Himalayan duplexes surfaces shift towards north, while the position of the mid-crustal ramps and contacts between the Lesser Himalayan slivers within the duplexes vary laterally. The confrontation between the balanced cross section and the relocated catalogue of seismicity could help resolve the relations between the structures at depth and the seismicity.

The seismicity is mostly located within the Lesser Himalayan Zone (Figure 4.34). West of the confluence of the Seti and Karnali rivers (Figure 4.34), the balanced cross-sections documented by DeCelles et al., 2001 and Robinson et al., 2006, place a MHT at depths similar to the depth of the seismicity (Figure 4.35). Most of the hypocenters are located nearby the decollement level or at close distance within its hanging wall over a distance of approximately 30 to 40 km (Figure 4.35). The southern rim of the seismicity coincides with the presence of a ramp in the MHT according to Robinson et al., 2006 (Figure 4.35.a) whereas the seismicity is on the flat of the MHT according to DeCelles et al., 2001 who predicts also a ramp but farther south (Figure 4.35.b). The main difference between the two geologic cross-sections is their interpretation of the structures under the Dadeldhura klippe (Figure 4.35).

On the other side of the Karnali-Seti rivers confluence, the South Karnali seismicity is located in the Lesser Himalayan Zone south of the Dadeldhura klippe (Figure 4.34), and at depth is located nearby the proposed depth of the MHT flat under a suspected blind duplex (Figure 4.36). Northward, the North Karnali seismicity appears less focused along a given structure but falls within the Lesser Himalayan duplex (Figure 4.34). The Lesser Himalaya Duplex extends farther north here than at Bajhang klippe (Figure 4.35 and 4.36). The balanced cross-section proposed by Robinson et al., 2006 document the presence of a ramp, 120 km-north from the MFT, below a complex Lesser Himalayan duplex which coincides approximately with the location of the

midcrustal North Karnali hypocenters (Figure 4.36). The shallower seismicity of the North Karnali region, although not very well constrained at depth, seems to fall at close distances with the contact between the Lesser Himalaya and the Dadeldhura klippe (Figure 4.36).

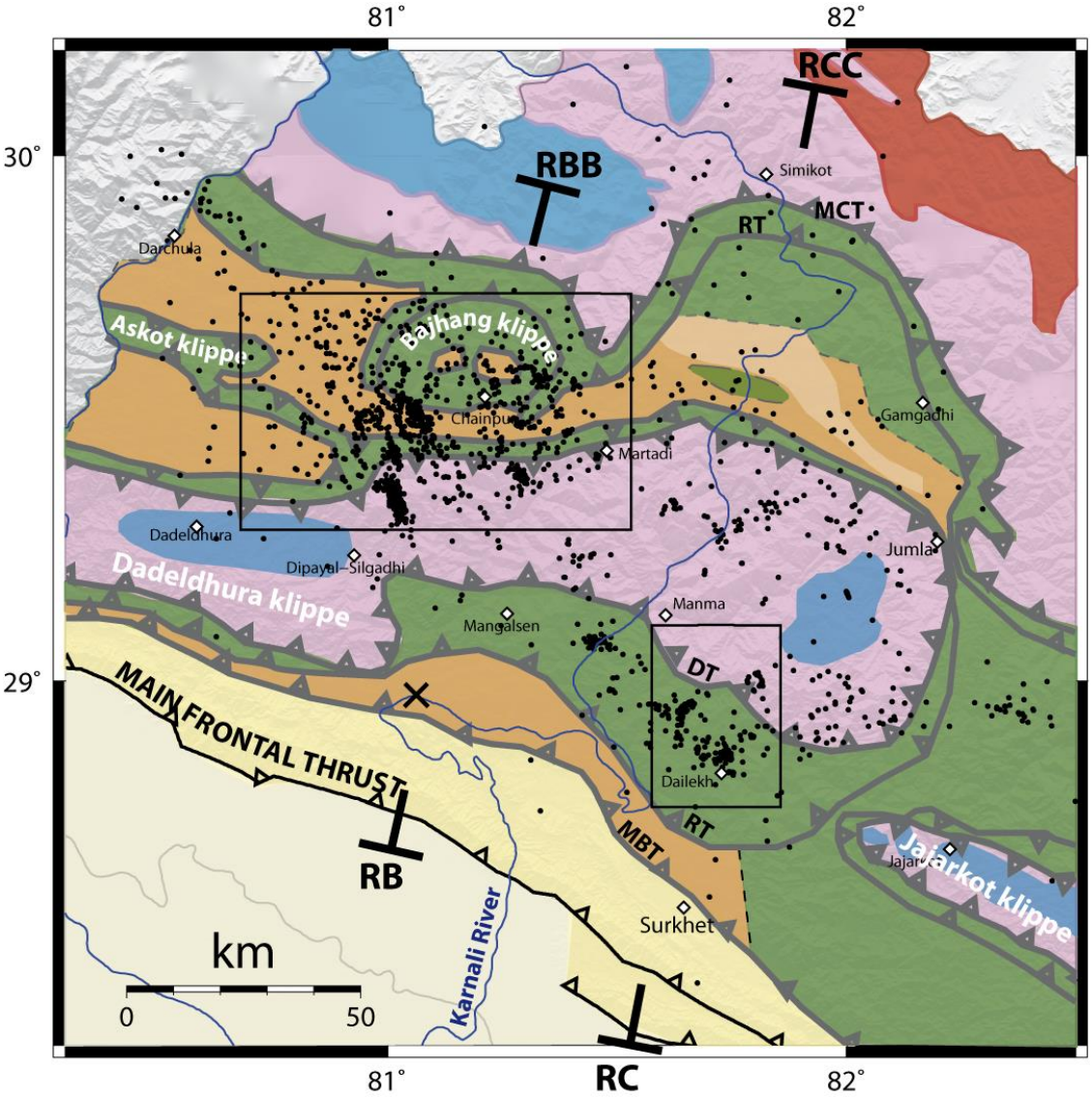

Figure 4.34. Geological map of west Nepal from Robinson et al., 2006 and seismicity of the TSN catalogue. The colors represent the zones: the Subhimalayan Zone (dark yellow), the Lower Lesser Himalayan Zone (green), Upper Lesser Himalayan Zone (orange), the Greater Himalayan Zone (pink and red) and the Tibetan Himalayan Zone (blue). Light yellow correspond to the current sediments of the orogeny. The faults correspond to the Main Frontal Thrust (MFT), the Main Boundary Thrust (MBT), the Ramgarh Thrust (RT), the Dadeldhura Thrust (DT) and the Main Central Thrust (MCT). The black cross on the Karnali River is its confluence with the Seti River. The squares are, from west to east, the zoom areas of Bajhang (Figure 4.37) and South Karnali (Figure 4.39). Cross-section tracks correspond to Figure 4.35 and 4.36.

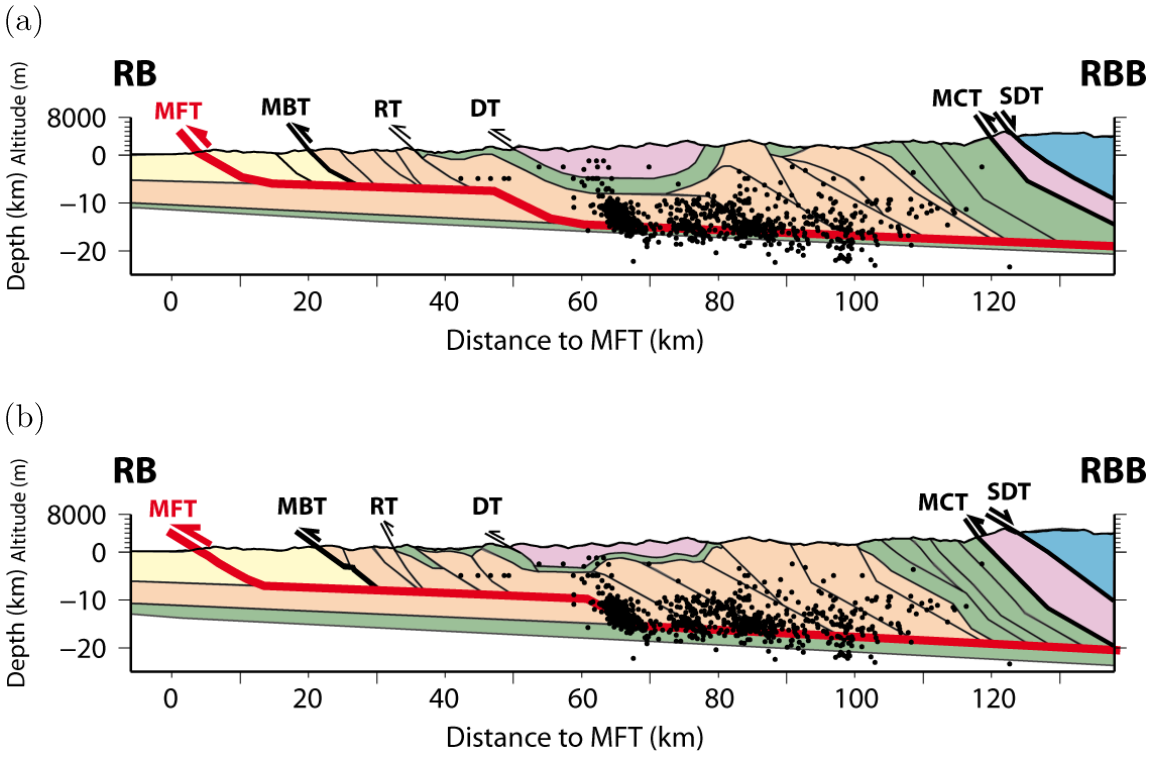

Figure 4.35. Cross-sections RB-RBB across Chainpur (Bajhang) (see Figure 4.34 for location) stacking seismicity 20 km apart. Geology and structures are from (a) DeCelles et al., 2001 and (b) Robinson et al., 2006. Note that cross-section (a) is 5km eastwards from the track. Color scale is the same as Figure 4.34.

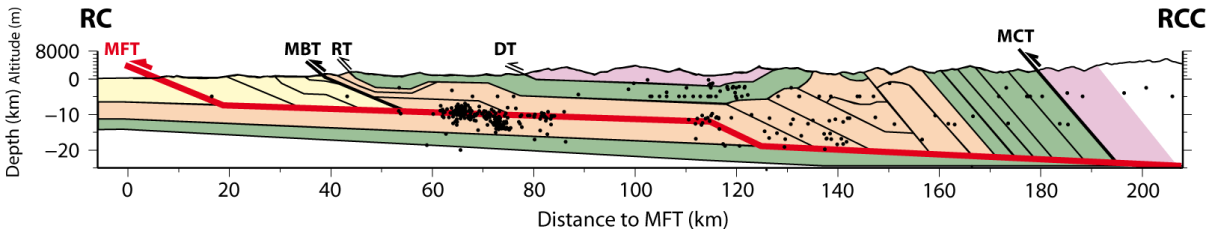

Figure 4.36. Cross-section RC-RCC across Dailekh (Dailekh) and Simikot (Mugu) (see Figure 4.34 for location) stacking seismicity 20 km apart. Geology and structures are from Robinson et al., 2006.

Digging a little deeper, the seismicity and the geology present complexities at local scales. We distinguish four sismotectonic zones: Darchula, Bajhang, North Karnali and South Karnali where the distribution of the seismicity and the geologic structures are different from its neighbors.

4.3.1. Darchula

The duplex in Darchula seismotectonic zone is formed by a succession of duplex horses with an important exposure from south to north (Figure 4.34). Here we observe a parallel relation between the Dadeldhura klippe (Great Himalaya zone), the Askot klippe (Lower Lesser Himalaya) and the Upper Lesser Himalaya outcrops (Figure 4.34) (Amatya and Jnawali, 1994 ; Robinson et al., 2006). These structures continue westwards in the Kumaon-Garhwal Himalayas in India (Srivastava and Mitra, 1996). The seismicity in this area is located near the town of Darchula about 85 km from the MFT and 70 from the MBT (Figure 4.34). The earthquakes hypocenters located in this region fall within a single seismic belt at the foot of the high topography in the vicinity of the midcrustal ramp, in a position similar to the position of the midcrustal cluster located in central Nepal by the NSC. The midcrustal cluster falls at the eastern end of a 200 km long narrow midcrustal seismic belt characterized in Kumaon –Garwhal by Mahesh et al., 2013 with a temporary network deployed between 2005 and 2008.

4.3.2. Bajhang

Eastward (80.8°-81°E), the Askot klippe disappears laterally, the Upper Lesser Himalaya sequence being more exhumed. The Dadeldhura klippe there (~81°E) is preserved further north than elsewhere, suggesting a northward step of the midcrustal ramp and of the core of the Lesser Himalayan duplex (Figure 4.34 and 4.37). This region exposes a succession of Upper Lesser Himalaya slivers and Lower Lesser Himalayas preserved along a klippe of Lower Lesser Himalaya that we will call the Bajhang klippe. This Lower Lesser Himalayas klippe preserved between 81°E and 81.4°E corresponds to the Chainpur culmination in Robinson et al., 2006 (Figure 4.37). The exposure of this last klippe is limited ~50 km east-west and ~20 km north-south and is characterized by the presence of two windows of upper Lesser Himalaya sequence in the middle of the klippe (Figure 4.37)(Amatya and Jnawali, 1994; Robinson et al., 2006).

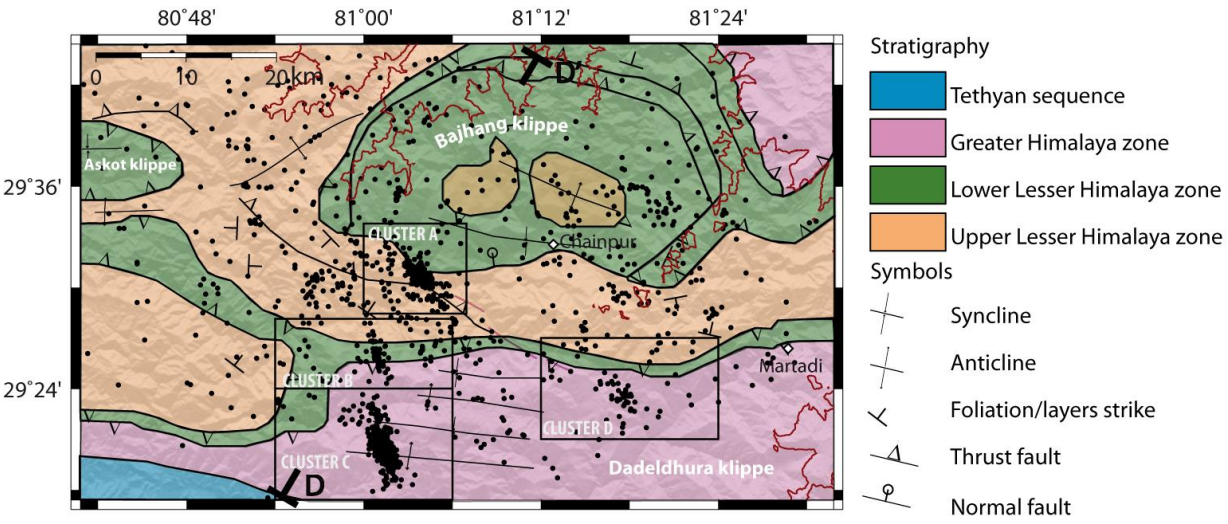

Figure 4.37. Geological map of west Nepal from Robinson et al., 2006 with the seismicity of TSN catalogue in Bajhang area frame (see Figure 4.34). Dark red line represents the 3500 m altitude contour.

Most of the seismicity recorded during the temporary experiment was located within this very complex region, particularly north of Dipayal-Silgadhi, under the Dadeldhura klippe, until the northernmost parts of the Bajhang klippe, and from the eastern parts of the Askot klippe until the easternmost part of the Bajhang klippe (Figure 4.37). The seismic cluster there falls at depth within the Lesser Himalaya Duplex in a region where a complex stack of Lesser Himalayan tectonic slivers have been described (Figure 4.38) (Robinson et al., 2006 and DeCelles et al., 2001). The southern extension of the seismicity falls in the close vicinity of the position of a suspected ramp of the MHT according to the balanced cross sections (Figure 4.38).

In the vicinity of Bajhang, the depth of the hypocenters ranges mainly from 9 to 18 km, a depth similar to the 15 km deep Low Velocity Zone detected in Far West Nepal below CH06, TK08, ML04, DE02 WA07 and BJ01 stations in Bajhang area (Subedi, 2016). This is complementary information to the balanced-cross-sections where the MHT is around 15 km depth at the foot of the ramp (Figure 4.38).

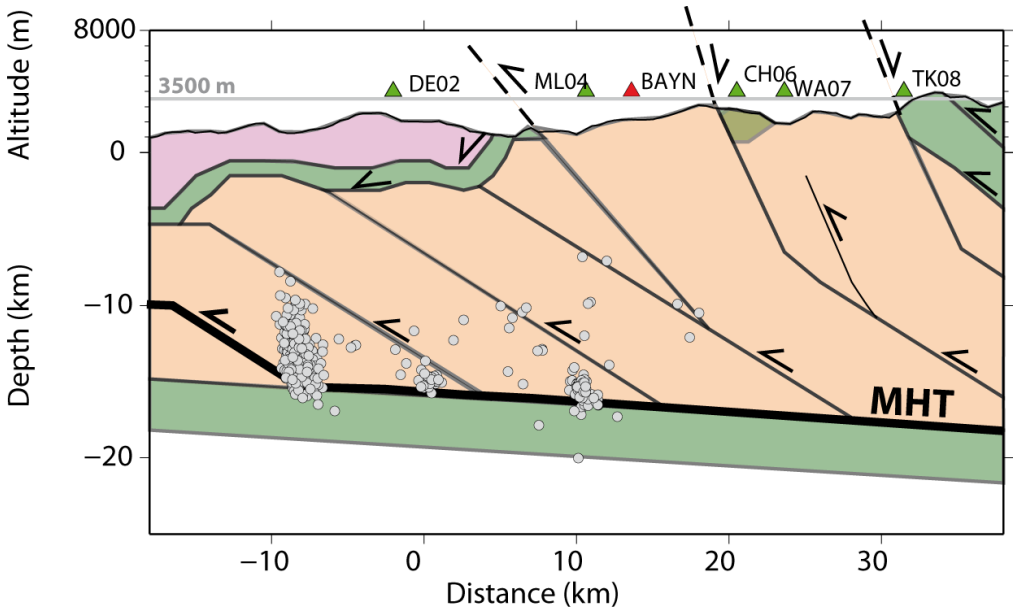

Figure 4.38. Cross-section D-D' of seismicity of Figure 4.37. Cross-section of geological structures is a zoom of RB-RBB of Figure 4.35 from Dadeldhura klippe to Bajhang klippe from Robinson et al., 2006.

In addition to falling at close distance from the Main Himalayan Thrust, the midcrustal seismic clusters were located principally in the vicinity of the contacts between Lesser Himalayan slivers (Figure 4.38). The location southwards of the seismicity from Darchula to Dipayal-Silgadhi could be related to an offset between two or several horses (Figure 4.34). These surface structure offsets are underlined by lateral ramps that have already been observed in a Ramgarh thrust outcrop in the confluence between the Karnali and Seti rivers (Robinson et al., 2006; Bollinger, 2002). These contacts and offsets of MHT create areas of weakness that well orientated could become preferential planes to localize seismicity as we observed with the swarms en-echelon. Indeed, this hypothesis supports the localization in sort of lines of the seismicity of cluster A, B and C; and the subparallel orientation between cluster A and B (Figure 4.37).

4.3.3. South Karnali

The pattern of seismicity revealed in the South Karnali zone with punctual bursts of seismicity (Figure 4.39) contrasts with the almost continuous seismicity from Martadi to Manma located by the RSC catalogue (e.g. Figure 3.1). The lack of resolution of the seismicity depth in the RSC catalogue can induce a more diffuse localization. But also, the catalogue from the permanent network accounts for more than 20 years of data while the TSN catalogue presents almost a year of records. We have barely recorded

seismicity between the southeastern corner of the Bajhang seismicity and the South Karnali seismicity situated in the Lesser Himalaya exposed south of the Dadeldhura klippe (Figure 4.34). This gap of seismicity cannot be interpreted as a long term gap because of the time period covered by our catalogue. However, we want to point out that this area corresponds to the zone where the Dadeldhura klippe and the Lesser Himalayan duplex outcrop further north.

The seismicity locates southwest of Manma towards the east (Figure 4.34). It is mainly parallel with the trace of the contact between the Dadeldhura klippe and the Lower Lesser Himalaya, and is limited south by the Ramgarh thrust surface trace (Figure 4.39). Although the seismicity is still located in the Lesser Himalaya Zone, we are no longer in the Lesser Himalayan Duplex like in Bajhang area.

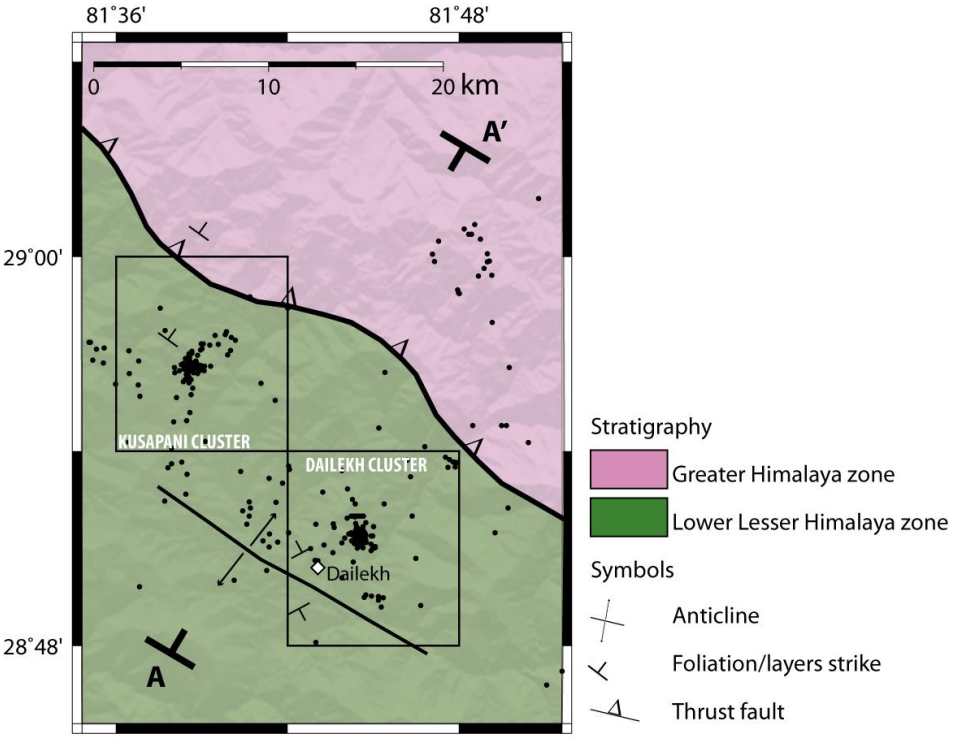

Figure 4.39. Geological map of western Nepal from Robinson et al., 2006 with the seismicity of TSN catalogue in South Karnali area frame (see Figure 4.34).

The seismicity is located principally within three clusters. Two have been relocated (see Chapter 3): the Kusapani or KS cluster and the Dailekh or DK cluster (Figure 4.39). We focus on these two lasts clusters because the hypocentral locations are better resolved. They are distant of 12 km and occurred in a seismic belt almost parallel to the south trace of the Dadeldhura Thrust (Figure 4.39). On average, the hypocenters of the Kusapani cluster were located 12.5 km-deep, 3 km deeper than the earthquakes located below Dailekh (located 9 km-deep) (Figure 4.26 and 4.29). At this emplacement, different structures have been proposed at depth:

1) **Passive duplex.** Robinson et al., 2006, based on the balanced cross-section, proposed the overlapping of two parallel series of Upper Lesser Himalayan formations separated by the MHT, with a suspected duplex on the upper series (Figure 4.40). In this case, the seismicity of the Kusapani cluster is located in the footwall and the seismicity of the Dailekh cluster on the flat of the MHT under the duplex.

2) **Double ramp.** Remnants of uplifted flat surfaces (described at 3000-4000m) were preserved on top of the Dadeldhura klippe while deep canyons entrench its southern and northern rims (Figure 4.40). These observations are consistent with the activity of a flat-ramp-flat-ramp-flat structure at depth related to the recent development of a young duplex horse 60 km from the MFT (Harvey et al., 2015). The South Karnali seismic cluster is then located in the vicinity of the frontal ramp on and along the flat of the MHT.

The geological and geomorphological observations made by Robinson et al., 2006 and Harvey et al., 2015 can be reconciled within a single model involving the development of a duplex beneath the front of the Dadeldhuhra klippe:

3) **Our proposition**. The denudation of the reliefs of the Dadeldhura klippe (Harvey et al., 2015) is focused slightly north of the surface trace of the seismic cluster (Figure 4.40). The cluster falls also in between the southern rim of the Dadeldhura klippe to the north and the axis of an anticlinal fold to the south (Amatya and Jnawali, 1994). This anticlinal fold is mapped precisely between Kusapani and Dailekh clusters, an area along which this anticlinal is prominent (Figure 4.39). This anticlinal and the young duplex horse that is suspected beneath this area may develop above a local ramp. The structure could be at the origin of the anticlinal fold mapped in the area (Figure 4.40). Note that this ramp is in a similar structural position than the ramp mapped along the southern extension of the Gorkha earthquake under the south western extension of the Kathmandu klippe (Khanal and Robinson, 2013; Hubbard et al., 2016) or under the easternmost part of Nepal (Schelling and Arita, 1991). The relations between this ramp, suspected at 10-15 km depths, and the seismic clusters located beneath Dailekh and Kusapani are not easy to ascertain: the seismicity is discontinuous and its hypocenters do not define a clear northward dipping plane but two 60° dipping planes respectively toward the NE and NW for Dailekh and Kusapani. Punctual seismicity would locate in the vicinity of the ramp, for instance the hinge between the flat MHT and above the termination (Figure 4.40). Such scenario situates the seismicity in the vicinity of the intermediate ramp of the MHT principally in the hangingwall (Figure 4.40).

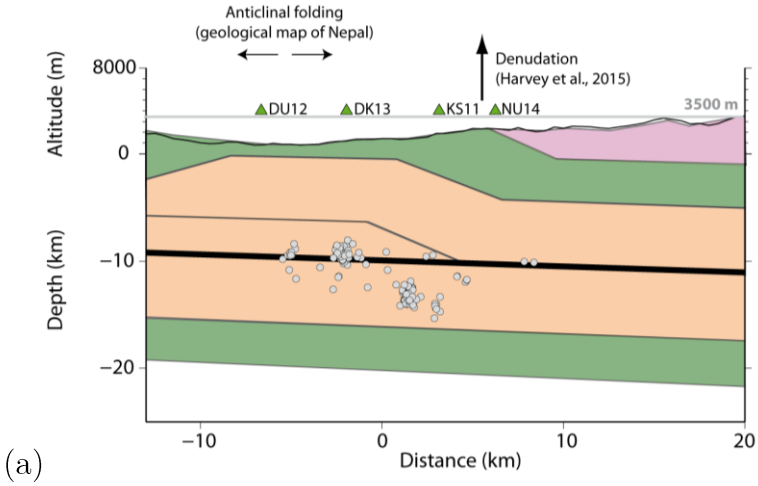

(a)

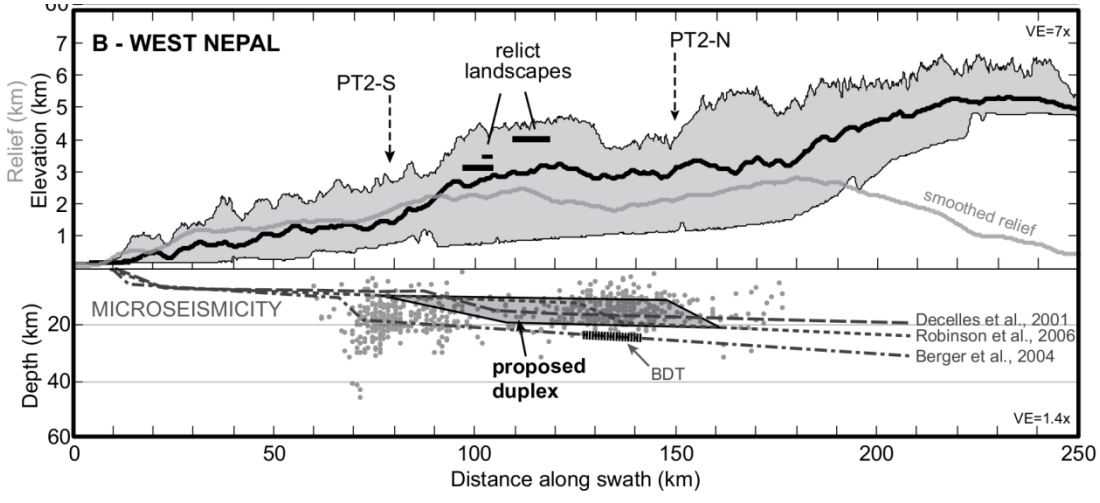

(b)

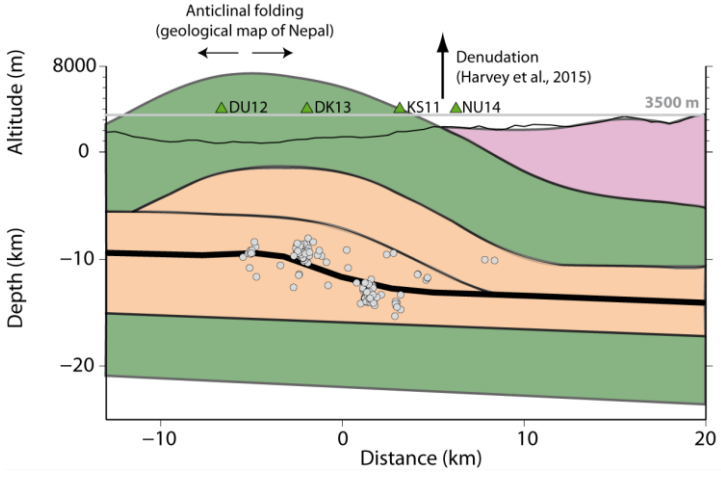

(c)

Figure 4.40. (a) A-A' cross-section of Figure 4.39 with the geological interpretation of Robinson et al., 2006 interpretation. (b) Proposition from Harvey et al., 2015 : recent duplex at depth (dark gray polygon). Points are the seismicity of RSC catalogue relocalized by Ader et al., 2012. Location of the cross-section corresponds approximately to RC-RCC of Figure 4.34. (c) Our proposition of structure on A-A' cross-section of Figure 4.39.

4.3.4. North Karnali

Finally, the limited number of hypocenters located within the North Karnali area (Figure 4.34) during the first year of the experiment precludes more detailed confrontation between hypocenters and the structures than what I already presented at the beginning of section *4.3 Seismicity and the geological structure* and on cross-section of Figure 4.36.

Most of the hypocenters fall either: (1) at small distances from the MHT basal decollement, (2) in the vicinity of a midcrustal ramp suspected to be prominent, 120 km from the MFT, south of the window on the Lesser Himalayan duplex (Robinson et al., 2006) or (3) within their hangingwall.

Two significant instrumental events with magnitudes mb=5.5 and mb=5.3 were located in this region on 27/11/2001. These events were studied by the global Centroid Moment Tensor project yielding pure thrusting focal mechanisms. This confirms the reverse motion of some of the earthquakes in the area. However, note that the northern part of the duplex is also affected by secondary active right lateral strike slip and normal faults that produced paleo- and historical surface ruptures (Nakata et al., 1984; Murphy et al. 2014). These relatively infrequent earthquakes, given the motion on the faults in the area, might add some complexities to the kinematics of the area.

4.4. Interpretation

The relations between the seismicity and the structures at depth in western Nepal suggest that the structures play a major role on the seismicity distribution. However, different forcings can intervene to induce or inhibit seismicity along these structures at depth. We discuss in the following paragraphs the influence of the seismic coupling and stress build up on the seismicity. We finally mention some of the parameters that could influence this seismic coupling and the related stress build up along strike (the seismic coupling being still poorly constrained in Mid and Far Western Nepal regions due to the sparse GPS stations available). The parameters potentially influencing the seismic coupling and/or the stress field at depth include the topography, the thermal structure or the presence of fluids which could play roles on the distribution of the seismicity in the area.

4.4.1. Full or partial locking and related stress build up along the MHT

The large earthquakes that occurred along the Main Himalayan Thrust fault result from the rupture of fault segments given to be fully locked during the interseismic period in early studies (e.g. Bilham et al., 1997; Cattin et Avouac, 2000; Jouanne et al., 2004). The determination of the downdip extension of the locked fault segments, as well as the slip rate on the aseismically creeping lower segments of the MHT are therefore critical to evaluate the seismogenic potential of the fault (e.g. Bilham et al., 1997). The downdip end of the locked MHT, as then deduced from geodetic data first available in central Nepal (e.g. Bilham et al., 1997), falls below the midcrustal seismic cluster (Pandey et al., 1995). Similarly, the extension of the locked fault segments of the MHT was estimated a few years later in Far Western Nepal, from a set of campaign GPS measurements (Bollinger et al., 2004a, Berger et al., 2004; Jouanne et al., 2004; Bettinelli et al. 2006) (Figure 4.41).

Indeed, the interseismic stress build up at the downdip end of the locked fault segment creates a static Coulomb stress change which is positive in the hangingwall of the MHT and a negative lobe in its footwall (Cattin and Avouac, 2000; Vergne et al., 2001). Consequently, the seismicity should be mainly located within the hangingwall, at close distance with the downdip end of the locked fault segments. The seismicity of Bajhang zone seems consistent with that model (Figure 4.35 and 4.38). In South Karnali, the shape of the seismic cluster necessarily depends on the structures at depth and on the seismic coupling, two parameters poorly constrained and therefore debated within competing models (Figure 4.40). However, the cross-sections drawn by Robinson et al., 2006 and Harvey et al., 2015 generate a seismic cluster within the footwall of the MHT (Figure 4.40.a and 4.40.b). Therefore, only our proposition of an intermediate ramp

verifies the production of seismicity by static stress variation at the seismic coupling transition zone (Figure 4.40.c).

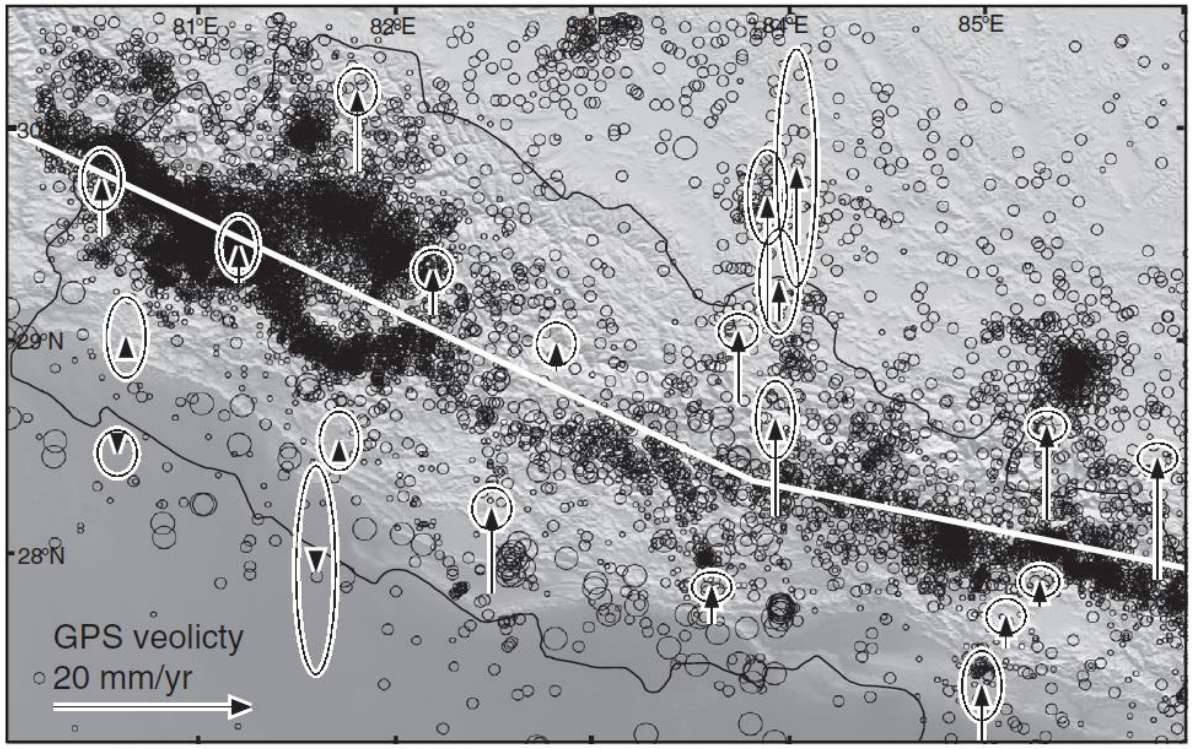

Figure 4.41. Map from Cannon and Murphy, 2014 with the seismicity located by NSC between 1995 and 2000. The downdip extent of the locked segments of the MHT is the thick white line from Jouanne et al., 2004. The vertical component of the velocity field is from Ader et al., 2012.

With the densification of the geodetic data available, more complex kinematic models emerged, involving partial locking of the fault (Ader et al., 2012; Grandin et al., 2015; Stevens and Avouac, 2015, Jouanne et al., 2017). These studies lead to the determination of the seismic coupling along the faults. Some of them suggest that significant transition zones, partially coupled, exist between fully coupled and creeping areas. In Mid and Far West Nepal regions, the transition zone could be larger and explain the wide area where the seismicity is distributed. Moreover, this transition is not necessary related to a particular structure (e.g. a midcrustal ramp), so it could explain the seismicity on the flat of the MHT under the duplex as we have seen in the South Karnali zone with the geologic structure proposed by Robinson et al., 2006 (Figure 4.40.a).

The seismic coupling models proposed so far present (1) a transition zone of narrow extension (Ader et al., 2012; Stevens and Avouac, 2015) (Figure 1.8) or (2) a transition zone larger than the area affected by the midcrustal seismic cluster (Jouanne et al., 2017) (Figure 4.42). In case (1) part of the seismicity is located in the transition zone (part of the seismicity of Bajhang and the seismicity of North Karnali zone), and part

within the locked segment (the seismicity of South Karnali zone and part of the seismicity of Bajhang zone). In case (2) which is the most recent study, the seismicity falls within the transition zone, but mostly on the less coupled transition zone (Figure 4.42).

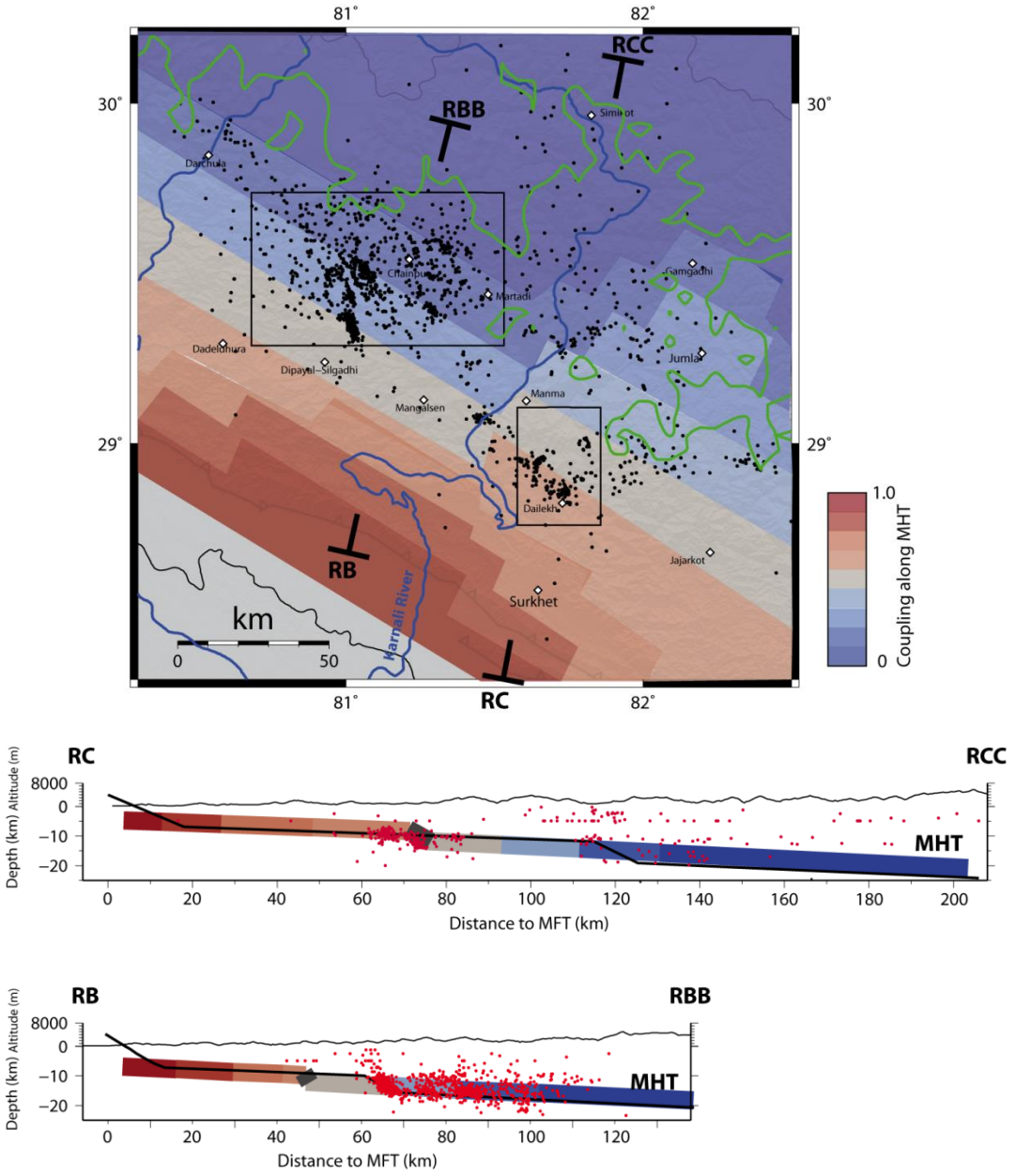

Figure 4.42. Seismic coupling along MHT in Far and Mid Western Nepal regions from Jouanne et al., 2017 in map and cross-section. The MHT geometry is taken from the structural representation of Robinson et al., 2006. Black and red points (respectively in map view and cross-section) correspond to the hypocenters of the TSN catalogue. Rectangles delineate the Bajhang and South Karnali zones. Green line delineates the 3500m topographic contour line (deduced from SRTM resampled at 5 km).

The non-uniqueness of the seismic coupling map which results from the analysis of the GPS velocity field in Far and Mid Western Nepal regions, their model-dependent characteristics, demonstrate that our knowledge of the stress build up in this area is still very limited (e.g. Ader et al., 2012, Stevens and Avouac, 2015; Jouanne et al., 2017 for alternative coupling maps covering the region). However, lateral and frontal variations of the coupling on the MHT might exist in Far and Mid West Nepal to produce such pattern of seismicity.

Part of the uncertainty associated to the determination of the seismic coupling comes from the sparse GPS data available in the area, limiting the resolution of the models. As an illustration, only 3 continuous GPS stations (ie. Bayana, Darchula and Jumla) fall in the vicinity of the seismic clusters and the brittle-ductile transition zone in western Nepal (Figure 4.42).

It is particularly clear that there is a need for more cGPS/levelling/InSAR data in western Nepal.

4.4.2. Behavior of the MHT related to the topography, the thermal structure and fluids

The topography has been identified as a parameter which controls the northern extent of the midcrustal seismic cluster along the MHT (Bollinger et al., 2004a). This relation between the seismicity and the topography is particularly visible in western Nepal where the midcrustal cluster follows the foot of the high range along the 3500 m isocontour, depicting a northward embayment within the North Karnali zone (Figure 4.42).

The topography may influence the seismicity there through several processes:

-The topography modulates significantly the orientation of the stress field at midcrustal depths,

-The topography has therefore an influence on the tectonic regime and orientation of the failure planes at these depths

- and has a most-probable influence on the position of the midcrustal ramps along strike the MHT.

-The topography and kinematics influence also the thermal structure which control the brittle-ductile transition zone

Indeed, along the Himalayas, in the vicinity of the 3500 m topographic contour line, the maximum stress rotates from north-south to vertical inducing a change on the tectonic regime from thrust to normal faults (see article Hoste-Colomer et al., 2017 in Chapter 2).

North of Kathmandu, the midcrustal seismicity is localized right under the high range. The high range is characterized by uplift due to the accretion of slivers of the Indian plate. The underplating (ie. Accretion of sliver at depth) occurs when the midcrustal ramp – located at the front of the high range in the vicinity of the brittle/ductile transition zone – propagates southward.

In Mid and Far West Nepal, the geometry of the Lesser Himalayas is more complex (Figure 1.7, 4.35 and 4.36), particularly when compared to central Nepal (Figure 1.6). Indeed, a larger number of imbricated Lesser Himalayan slivers have been identified within a larger area. As we have seen in Bajhang zone (Figure 4.37 and 4.38), the present-day ramp does not fall immediately below the front of the high range. Indeed, according to the balanced cross-sections published covering this area, the 3500 m topographic contour falls 40 km northwards from the suspected midcrustal ramp. This could help explain the ~40 km spread of the midcrustal seismicity covering the region that extends from the ramp to the front of the high range (Figure 4.38).

The 3500 m contour line of the topography not only coincides with the northern extension of the Bajhang seismicity belt but with the embayment of the seismicity in the Karnali area. In addition, the two seismicity belts located there fall on both sides of a high topography, identified by Harvey et al., 2015 who mapped there surfaces at 3000-4000 m of altitude (visible on figure 4.42). Such a high topography is a potential inhibitor of the midcrustal seismicity (given its influence on the orientation of the stress field at midcrustal depths – among other influences) and may be partly responsible for the double seismicity belt (Figure 4.40 and 4.42).

The topography in the area is therefore probably responsible for some of the lateral variations of the seismicity: through the modulation of the orientation of the failure planes, through the probable control of the position of the midcrustal ramp.

The high topography and its evolution through time (as other kinematical parameters) have also a strong influence on the shape of the 300-400 °C isotherm of the thermal structure at depth (e.g. Henry et al., 1997; Bollinger et al., 2004b). These isotherms fall within close distances from the midcrustal seismic cluster and the brittle-ductile transition zone in central Nepal (Ader et al., 2012). This brittle-ductile transition is given to be controlled mainly by the plasticity of the quartz there. Given the similar nature of the rocks on both walls of the MHT in central and western Nepal, the similar kinematics on the fault, it is therefore likely that the thermal structure in western Nepal has a similar influence as in central Nepal.

The presence of fluids at midcrustal depths along the fault zone may also influence the local seismicity. Indeed, high pore pressure facilitates fault activation trough their influence on the frictional state on the fault plane or promote hydrofracturation.

The results of the analysis of the seismic clusters indicated that most seismic clusters were swarms (except for the sub-cluster of Kusapani) (Table 4.1 and 4.2). The spatiotemporal characteristics of some clusters make us consider the possibility that generation of some earthquakes within the swarms could be related to fluids migration at depth. Indeed, the seismic events which occurred within Cluster A migrated in space as a function of time, migrating both to the SE and NW at the same time (Figure 4.9 and 4.43). Figure 4.43 illustrates that migration, around 50 m/d, which is in the range of velocity migrations observed in the Corinth rift where seismicity is related to fluid circulation at the intersection of fault planes (Pacchiani and Lyon-Caen, 2010; Duverger et al., 2015) (Figure 4.43). Note that several other similar time-structure of the seismicity within swarms have already been observed in other contexts for which migration of fluids were suspected (Jacques et al., 1999; Audin et al., 2002) such as Vosges (France) and Afar (Ethiopy).

Other observations such as the clustered activity in pulses of the time sequences of Cluster D (Figure 4.18 and 4.20) and cluster Kusapani (Figure 4.25 and 4.27) can be related to swarms where fluids triggered part of the seismicity (e.g. Hainzl and Ogata, 2005).

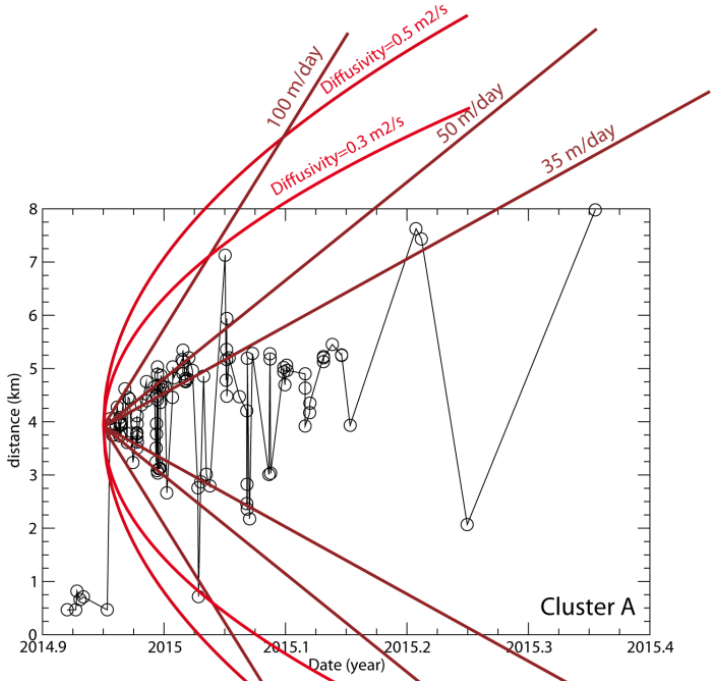

Figure 4.43. Spatio-temporal distribution of Cluster A after HypoDD relocalisation (frame of Figure 4.9.b). The distance corresponds to the distance between a given epicenter and the first event located in the area. Dark red lines correspond to three different migration velocities. Red curve is a poroelastic model of the pore-pressure diffusion (Shapiro et al., 1997) for diffusivity of 0.5 m^2 s^{-1} and 0.3 m^2 s^{-1}.

The presence of fluids was one of the hypotheses to explain the midcrustal Low Velocity Zone described along the MHT in central Nepal by (Nabelek et al., 2009) as presented in Chapter 1. The LVZ coincides with the MHT where the pressure on the fault decreases the permeability and increases the pore pressure inducing the rock fracturing and the fluid-driven slip of a patch (e.g. Chiarraba et al., 2009; Johnson and McEvilly, 1995). This process begins again and becomes a cyclic pressurization of fluids within the fault (Johnson and McEvilly, 1995). Such a periodic process could explain the exceptional bursts of seismicity during winter 2011, 2013 and 2015. If the process observed by Johnson and McEvilly, 1995 is prominent in this part of Nepal; it could explain partially the rather elevated rate of seismicity recorded by the RSC in comparison to other places of this country.

The origin of such fluids can be either meteoric or metamorphic. In both cases, fluids may migrate along the MHT shear zone and the subsidiary faults which are connected to it (MCT, contacts between slivers in the Lesser Himalaya zone). This could explain why some clusters appear located at the junction between the MHT and subsidiary faults.

The circulation of fluids can be certified in surface at the hot springs or *tatopani,* found along the foot of the high range, in the vicinity of the Main Central Thrust surface trace. To date, the studies of the *tatopani* waters in Central Nepal demonstrate that the waters are essentially meteoric waters that have circulated through the first's kilometers of the crust (e.g. Girault et al., 2014). In addition, at depth, along the MHT, the presence of metamorphic fluids (brines, CO_2, among others) is suspected due to the metamorphic reactions occurring at depth. Furthermore, the presence of such fluids is consistent with the presence of a high conductivity layer observed in a magnotellurics survey (Lemonnier et al., 1999) nearby the Low Velocity Zone (Nabelek et al., 2009). These fluids, migrating within the fractured/permeable midcrustal environment of the MHT shear zone as well as along subsidiary faults in its hangingwall, could explain, at least partially, the spatiotemporal evolution of the seismic swarms.

4.5. Implications on the segmentation of the MHT

Midcrustal seismicity as well as the geology presents lateral and frontal variations in western Nepal expressing intrinsically along strike variations of the geometry of the MHT. Significant variations in the deep geometry of the MHT could be responsible for a segmentation of the fault rupturing at depth; the presence of barriers that could influence the rupture dynamics in a similar way than what has been described after 2015 Gorkha earthquake (e.g. Elliott et al., 2016; Hoste-Colomer et al., 2017; Hubbard et al., 2016).

We have several reasons to think that large and great earthquakes might coexist in west Nepal, like they coexist in central Nepal where large and great earthquakes partially (1833AD, 2015AD) or totally rupture the MHT (1255AD, 1344AD, 1934AD) (e.g. Bollinger et al., 2016). Indeed, the region ruptured during the great earthquake (M8+) in 1505AD. This event generated a coseismic slip sometime greater than 20 meters and a rupture identified at three paleoseismological sites excavated from the Nepal-India border until near Jajarkot klippe, along more than 200 km-long stretch of the range , 50 to 100 km from the brittle-ductile transition zone (Figure i.4). This region also ruptured during smaller earthquakes including the 1916 M7 earthquake (Bilham et al., 2017).

These observations are consistent with ruptures affecting large segments.

In Central Nepal, some structures at depth interfered with the progression of the coseismic rupture of the Gorkha earthquake (see *Chapter 2*, Hoste-Colomer et al., 2017). Among these structures, deep ramps along the MHT controlled the Gorkha earthquake rupture extent (Hubbard et al., 2016). The pluri-kilometric MHT deep ramps which develop under the Karnali (see section *4.3. Seismicity and geological structure*), below the southern extent of the Dadeldhura klippe or the southern extent of the north Karnali window are therefore structures that most likely control the extent of intermediate and/or large ruptures.

Three distinct segments / MHT flats are therefore delineated in Karnali region (K1, K2, K3 on Figure 4.44). The ramps between North and South Karnali areas (between K1 and K2 and K2 and K3) would likely influence a frontal progression of an earthquake in a similar way as the southern deep ramp that was described along the southern extension of the Gorkha earthquake rupture.

West of the Karnali region, in Bajhang area, the structural segmentation is less pronounced. The area is more complex, comprising significant lateral variations affecting the geometry of the Lesser Himalaya Duplex, lateral ramps and a complex succession of seismic clusters (see beginning of *Chapter 4*), suggesting that this region is a transition zone between the Darchula and Karnali regions. Despite this apparent complexity in terms of structural inheritance and seismicity, the region could be segmented in two patches (B1 and B2 on Figure 4.44).

The surfaces of each of these segments (i.e. K1, K2, K3, B1 and B2) are approximately comprised between the surfaces ruptured by the Kodari and the Gorkha earthquakes (Figure 4.44). The coseismic slip deficit likely accumulated since the last great earthquake in 1505AD is around 10 m. Large or great earthquakes rupturing partially or totally the MHT in the area would respectively produce earthquakes of magnitude ~7.9≤Mw≤~8.2 and Mw~8.5 depending on the number of segments ruptured (according to the relations of Kanamori, 1977 between seismic moment – rupture surface – slip and seismic moment – seismic moment magnitude) (Figure 4.44). A larger earthquake,

but more infrequent, rupturing more than the stretch of the Himalaya on which our study focuses, must also be considered. All these scenarios should be integrated in future seismic hazard studies in order to better assess the seismic risks in the region.

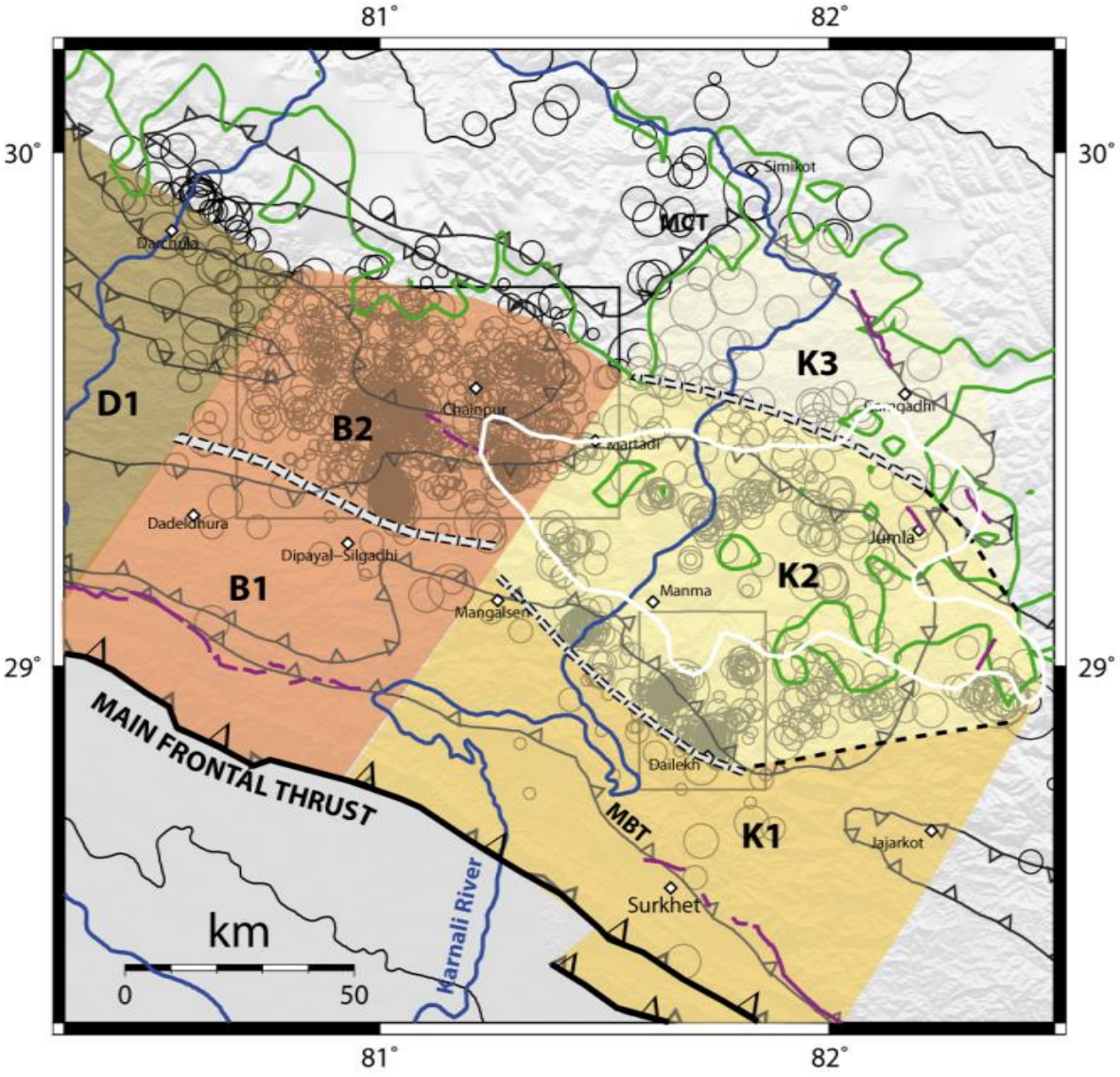

Figure 4.44. Schematic proposition of the segmentation patches in Far and Mid Western Nepal regions. Ochre patch (D1) includes Darchula seismotectonic zone and develops from the main midcrustal cluster at the foot of the high range to the MFT. Orange patches in the trace of the Bajhang seismic zone is divided in two: (B1) a frontal part including the upper flat of the MHT, fully locked during last years and (B2) a deeper flat underlying the Bajhang seismicity belt which falls within a transition zone (partially locked and/or affected by fluid migrations and connected to the Karnali Zone). The yellow patches (K1, K2, K3) in the Karnali zone correspond to the 3 flats of the MHT, separated by suspected midcrustal ramps (white and black bold lines). Purple lines are the active faults of Nakata, 1982. Green line is the topographic contour of 3500m smoothed to 5 km. White line represents the surface (slip ≥ 2m) de Grandin et al., 2015 ruptured by Mw7.8 Gorkha earthquake as a reference of magnitude – rupture area relationship.

Conclusions et Perspectives

La sismicité micrustale localisée le long du méga-chevauchement himalayen (*Main Himalayan Thrust* ou MHT), au voisinage de l'extension profonde de la zone sismogène, présente des variations latérales significatives. J'ai étudié ces variations au Centre Népal, la zone la plus étudiée de l'Himalaya et au travers de l'ouest du Népal, une région à la sismicité encore très mal connue. Les catalogues de sismicité issus des bulletins sismologiques publiés par le *National Seismological Centre* (NSC) et le *Regional Seismological Centre* (RSC) depuis 1994 m'ont permis de constater que la sismicité de l'ouest du Népal présentait les plus fortes variations spatiales. Pour autant, les incertitudes de localisation associées aux hypocentres dans la région sont importantes. La profondeur de la sismicité y reste peu résolue. L'association de cette sismicité à des structures locales comme l'examen détaillé de la structure spatiotemporelle de la sismicité y étaient donc particulièrement délicats. Un réseau sismologique temporaire de 15 stations, en complément des 9 stations du RSC, a donc été déployé au-dessus des ceintures de sismicité du Grand Ouest Népal pour la période 2014-2016 –dans le cadre de ma thèse et de l'ANR-Bhutanepal. Ce réseau a permis (1) de bénéficier d'un seuil de détection plus bas et (2) d'obtenir une meilleure résolution de la localisation hypocentrale des séismes par rapport à celle du catalogue de sismicité du RSC :

- Du 1er décembre 2014 au 10 octobre 2015, le RSC a localisé 513 séismes dont 468 en commun avec notre catalogue. Pour la même période, nous avons détecté automatiquement plus de 6500 séismes dont 2245 pointés manuellement avec Seiscomp3. 2190 de ces évènements sont présents dans notre zone d'étude. 2154 des séismes ont été relocalisés avec Hypo71 (relocalisation absolue). 40% des événements présentent des localisations de bonne qualité (nombre de phases (nP>=6, nS>=3), RMS<=0.4 et erreur horizontale et verticale <= 2 km). Une partie importante de cette sismicité (1158 séismes) est localisée au sein de 6 essaims de sismicité. 718 événements de ces séismes ont été relocalisés avec HypoDD (relocalisation relative) afin d'estimer au mieux l'évolution spatio-temporelle de la sismicité au voisinage des structures tectoniques locales.
- Les différences de localisation épicentrale des évènements des catalogues du réseau national et du réseau local temporaire sont typiquement comprises entre 5 et 15 km. Cette différence est pour partie liée à la profondeur hypocentrale des événements, très mal résolue par le réseau national dans l'ouest Népal du fait de sa géométrie et de la relativement grande distance entre les stations et la sismicité. En effet, pour exemple, un nombre important d'événements présentent des hypocentres RSC à 2 km et 25 km de profondeur (Figure c.1), des

profondeurs fixées par les analystes. Ces mêmes séismes sont localisés à des profondeurs de 10 à 16 km dans le catalogue TSN (Figure c.1). Il y a une différence systématique aux alentours de 10 km entre la profondeur RSC et TSN (Figure c.1).

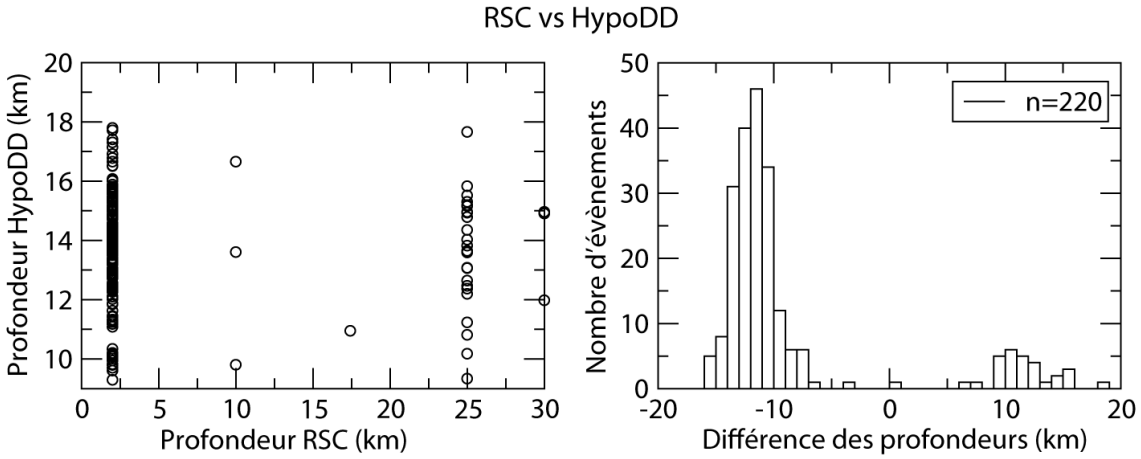

Figure c.1. Comparaison des profondeurs des évènements communs au catalogue RSC et au catalogue TSN relocalisé avec HypoDD. (a) Profondeur du TSN en fonction de la profondeur RSC. (b) Histogramme des $\Delta profondeur = profondeur\ RSC - profondeur\ TSN$.

A l'échelle régionale, les résultats obtenus confirment la forte variation latérale de la distribution de la sismicité de l'ouest du Népal. Les épicentres du catalogue TSN dessinent une géométrie similaire, en fourche, à celle de la distribution des séismes du catalogue RSC depuis 1994. Cette variation spatiale de la sismicité est concordante avec les variations latérales de structures géologiques. De la zone de Bajhang –à l'ouest de la région couverte par le réseau- à la zone Karnali Nord –plus au nord est-, nous observons un décalage vers le nord de la sismicité micrustale cohérent avec l'exposition plus au nord d'un Duplex de Moyen Pays.

La confrontation entre la sismicité relocalisée et la structure géologique de l'Himalaya issue de coupes équilibrées démontre que la sismicité du Grand Ouest Népal est localisée en profondeur à proximité du MHT principalement dans son compartiment supérieur (10–18/20 km pour Bajhang ; 8-15 km pour Karnali Sud). Une partie de cette sismicité est localisée à la jonction entre le MHT et les contacts entre écailles de moyen pays et une autre partie le long des structures héritées dans le moyen pays. La sismicité de la zone Karnali Sud se situerait quant à elle à proximité d'une rampe intermédiaire de faible extension latérale (3-4 km d'extension verticale et probablement plus de 20 km d'extension latérale, à une profondeur d'environ 10 km). La distribution de la sismicité a révélé la présence de variations latérales de géométrie du chevauchement principal (plats, rampes dont des rampes latérales, …) et de structures dans son compartiment chevauchant (contacts entre écailles du duplex …).

Ces variations de structure du MHT en profondeur influencent très certainement les ruptures cosismiques des forts séismes. En effet, la rupture du séisme de Gorkha (25/04/2015), au centre du Népal, a été perturbée (variations de glissement ou arrêt de la rupture) par des structures d'extension plus faible que les structures décrites dans l'ouest Népal. Parmi ces structures, une avait été révélée par l'analyse de la sismicité intersismique présente au nord-ouest de Katmandou. Contrairement à la rampe micrustale décrite plus au sud, au droit du Mahabarat, cette structure n'a pas été en capacité d'arrêter la rupture de 2015 mais l'a perturbée significativement (présente au droit d'une forte variation de glissement cosismique). A l'ouest du Népal, les variations latérales de structures et de sismicité intersismique associées sont beaucoup plus marquées. Cela pourrait traduire une influence plus conséquente des structures sur la segmentation des ruptures cosismiques dans une région qui produit des séismes intermédiaires (M7+, 1916) comme des méga-séismes (M8+ , 1505), des événements qui viennent probablement rompre partiellement / totalement la zone bloquée du méga-chevauchement.

Nous avons aussi exploré les variations temporelles des catalogues (RSC, NSC et TSN). La génération de sismicité intersismique est permanente le long du pied de la haute chaîne au Népal (40-70 séismes de magnitude ML≥3.0 par an d'après le NSC et le RSC). Néanmoins elle apparait modulée par des évènements transitoires à l'échelle régionale (essaims de sismicité locaux) comme à une plus grande échelle (existence d'un regain d'activité en hiver, développement d'essaims de sismicité simultanés). Les essaims les plus développées ont été détectés en 1996-1997. L'étude des essaims principaux de 1996-1997 a révélé qu'ils présentaient des structures temporelles similaires malgré la grande distance qui les sépare. Dans les deux cas, il semble possible qu'une perturbation affectant le MHT soit à l'origine de la sismicité.

Les séries temporelles GPS n'ont pour le moment pas capturé d'épisodes de glissements transitoires significatifs. Il est possible que la résolution du réseau GPS actuel au Népal ne soit pas suffisante pour enregistrer des perturbations de faible ampleur à 15 km de profondeur. La détection/ caractérisation de crises sismiques transitoires pourrait permettre de se focaliser spécifiquement sur les régions touchées afin de travailler à des études de détectabilité spécifiques.

De même, les variations de couplage sismique à l'ouest du Népal ne sont pas bien contraintes. L'étude dédiée à la sismicité de l'ouest Népal suggère qu'il existe des variations latérales de couplage sismique le long du MHT. Ces variations latérales de couplages sont très mal résolues par le réseau GPS actuel, qui ne présente pas la densité suffisante. Le déploiement d'un réseau dédié et une couverture InSAR de la déformation de la région pourraient permettre de travailler sur les variations de glissement au voisinage de la zone de transition fragile-ductile.

Les variations de couplage sismique, comme les variations latérales de sismicité pourraient refléter l'influence de la topographie, de la structure tectonique locale, de la structure thermique, ou de migrations de fluides le long de plans de failles préexistants. L'influence de ces migrations de fluides est suspectée, particulièrement au cœur des essaims de sismicité localisés. Elle reste toutefois à démontrer.

L'exploitation des données du réseau sismologique temporaire dans le cadre de ce travail de thèse nous permet de bénéficier d'une vision précise de la sismicité et de sa relation aux structures dans la zone de Bajhang et Karnali Sud. Le catalogue de sismicité n'est pas comparable pour la zone Karnali Nord, une région qui n'était pas couverte par suffisamment de stations au cours des premiers mois de l'expérience sismologique. L'exploitation de la deuxième année de signaux enregistrés par le réseau sismologique temporaire permettrait d'arriver à un niveau de détail supérieur parce que la station de Simikot (SM15), ouvrant le réseau au nord de l'essaim de Karnali Nord, est présente toute cette seconde année. Cette seconde année est par ailleurs très intéressante parce qu'une crise sismique abondante, présentant un séisme principal de magnitude mb=5.3, s'y est développée en décembre 2015.

Des travaux préliminaires à la détermination d'un nouveau modèle de vitesse sismique ont été effectués (stage de M2 d'Angélique Benoit). Une partie des signaux a été utilisée pour imager la structure profonde (Moho, *Low Velocity Zone* micrustale) au droit des stations dans le cadre du stage de M2 et du CDD de Shiba Subedi. Des travaux dans la continuité de ces deux études pourraient permettre d'aller plus loin dans la compréhension des relations entre la sismicité et les structures géologiques locales.

Toutes ces études devraient permettre de bénéficier d'une réinterprétation fine de la sismicité et de son association éventuelle aux structures tectoniques locales ou régionales. Ces structures influent sur la segmentation du méga-chevauchement. Leur cartographie devrait permettre, à terme, de mieux estimer cette segmentation, une donnée importante dans les études d'aléa sismique.

References

Acton, C.E., Priestley, K., Mitra, S. and Gaur, V.K., 2011. Crustal structure of the Darjeeling-Sikkim Himalaya and southern Tibet, Geophysical Journal International, 184, 829-852, doi:10.1111/j.1365-246X.2010.04868.x.

Ader, T., Avouac, J.P., Liu-Zeng, J., Lyon-Caen, H., Bollinger, L., Galetzka, J., Genrich, J., Thomas, M., Chanard, K., Sapkota, S.N., Rajaure, S., Shrestha, P., Ding L. and Flouzat, M., 2012. Convergence rate across the Nepal Himalaya and interseismic coupling on the Main Himalayan Thrust: Implications for seismic hazard, Journal of Geophysical Research, 117, B04403, doi: 10.1029/2011JB009071.

Adhikari, L.B., Gautam, U.P., Koirala, B.P., Bhattarai, M., Kandel, T., Gupta, R.M., Timsina, C., Maharjan, N., Maharjan, K., Dahal, T., Hoste-Colomer, R., Cano, Y., Dandine, M., Guilhem, A., Merrer, S., Roudil, P. and Bollinger, L., 2015. The aftershock sequence of the 2015 April 25 Gorkha-Nepal earthquake, Geophysical Journal International, 203, 2119-2124, doi: 10.1093/gji/ggv412.

Akaike, H., Petrov, B. N. and Csaki, F., 1973. Information theory and an extension of the maximum likelihood principle.

Allen, R., 1982. Automatic phase pickers: their present use and future prospects, Bulletin of the Seismological Society of America, 72 (6), S225-S242.

Ambraseys, N. N. and Douglas, J., 2004. Magnitude calibration of north Indian earthquakes, Geophysical Journal International, 159(1), 165-206.

Amatya and Jnawali, 1994. Geological map of Nepal 1:1000000, Department of Mines and Geology.

Ando, M., 1975. Source mechanisms and tectonic significance of historical earthquakes along the Nankai trough, Japan, Tectonophysics, 27, 119 – 140.

Audin, L., Avouac, J. P., Flouzat, M. and Plantet, J. L., 2002. Fluid-driven seismicity in a stable tectonic context: The Remiremont fault zone, Vosges, France, Geophysical research letters, 29(6).

Avouac, J-P., Bollinger, L., Lavé, J., Cattin, R. and Flouzat, M., 2001. Le cycle sismique en Himalaya, C. R. Acad. Sci. Paris, Sciences de la Terre et des planets, 333, 513-529.

Avouac, J.P., Meng, L., Wei, S., Wang, T. and Ampuero, J.P., 2015. Lower edge of locked Main Himalayan Thrust unzipped by the 2015 Gorkha earthquake, Nature Geoscience, 8, 708-711.

Baillard, C., Crawford, W. C., Ballu, V., Hibert, C. and Mangeney, A., 2014. An automatic kurtosis-based P-and S-phase picker designed for local seismic networks, Bulletin of the Seismological Society of America, 104(1), 394-409.

Baillard, C., Lyon-Caen, H., Bollinger, L., Rietbrock, A., Letort, J. and Adhikari, L.B., 2017. Automatic analysis of the Gorkha earthquake aftershock sequence: evidences of structurally segmented seismicity, Geophysical Journal International, 209, 1111-1125, doi:10.1093/gji/ggx081.

Banerjee, P. and Burgman, R., 2002. Convergence across the northwest Himalaya from GPS measure- ments, Geophysical Research Letters, 29(13), 1652, doi:10.1029/2002GL015184.

Berger, A., Jouanne, F., Hassani, R. and Mugnier, J.L., 2004. Modelling the spatial distribution of present-day deformation in Nepal : how cylindrical is the Main Himalayan Thrust in Nepal ?, Geophysical Journal International, 156, 94-114, doi:10.1111/j.1365-246X.2004.02038.x.

Bettinelli, P., Avouac, J.P., Flouzat, M., Jouanne, F., Bollinger, L., Willis, P. and Chitrakar, G.R., 2006. Plate motion of India and interseismic strain in Nepal Himalaya from GPS and DORIS measurements, Journal of Geodesy, 80, 567-589, doi:10.1007/s00190-006-0030-3.

Bettinelli, P., Avouac, J.P., Flouzat, M., Bollinger, L., Ramillien G., Rajaure S. and Sapkota S., 2008. Seasonal variations of seismicity and geodetic strain in the Himalaya induced by surface hydrology, Earth and Planetary Science Letters, 266, 332-344, doi:10.1016/j.epsl.2007.11.02110.

Bilham, R., Larson, K., Freymueller, J. and Project Idylhim members, 1997. GPS measurements of present-day convergence across the Nepal Himalaya, Nature, 386, 61-64.

Bilham, R., 2004. Urban earthquake fatalities: a safer world, or worse to come? Seismological Research Letter, 75, 706–712.

Bilham R., 2009. The seismic future of cities. Twelfth Annual Mallet-Milne Lecture. Bull Earthquake Eng, 2009, 1–49. doi:10.1007/s10518-009-9147-0

Blaser, L., Krüger, F., Ohrnberger, M. and Scherbaum, F., 2010. Scaling relations of earthquake source parameter estimates with special focus on subduction environment, Bulletin of the Seismological Society of America, 100 (6), 2914-2926, doi:10.1785/0120100111.

Bollinger, L., 2002. Déformation de l'Himalaya du Népal, Université de Paris IX.

Bollinger, L., Avouac, J.P., Cattin, R. and Pandey, M.R., 2004a. Stress buildup in the Himalaya, Journal of Geophysical Research, 109, B11405, doi:10.1029/2003JB002911.

Bollinger, L., Avouac, J.P., Beyssac, O., Catlos, E.J., Harrison, T.M., Grove, M., Goffé, B. and Sapkota, S., 2004b. Thermal structure and exhumation history of the Lesser Himalaya in central Nepal, Tectonics, 23, TC5015, doi:10.1029/2003TC001564.

Bollinger, L., Henry, P. and Avouac, J.P., 2006. Mountain building in the Nepal Himalaya: Thermal and kinematic model, Earth and Planetary Science Letters, 244, 58-71.

Bollinger, L., Perrier, F., Avouac, J.P., Sapkota, S., Gautam, U, and Tiwari, D.R., 2007. Seasonal modulation of seismicity in the Himalaya of Nepal, Geophysical Research Letters, 34, L08304, doi:10.1029/2006GL029192.

Bollinger, L., Sapkota, S.N., Tapponnier, P., Klinger, Y., Rizza, M., Van der Woerd, J., Tiwari, D.R., Pandey, R., Bitri, A. and Bes de Berc, S., 2014. Estimating the return times of great Himalayan earthquakes in eastern Nepal: Evidence from the Patu and Bardibas strands of the Main Frontal Thrust, Journal of Geophysical Research: Solid Earth, 10.1002/2014JB010970.

Bollinger, L., Tapponnier, P., Sapkota, S.N. and Klinger, Y., 2016. Slip deficit in central Nepal: omen for a repeat of the 1344 AD earthquake?, Earth, Planets and Space, 68:12, doi:10.1186/s40623-016-0389-1.

Bondár, I. and Storchak, D., 2011. Improved location procedures at the International Seismological Centre, Geophysical Journal International, 186(3), 1220-1244.

Burtin, A., Bollinger, L., Vergne, J., Cattin R. and Nábělek J. L., 2008. Spectral analysis of seismic noise induced by rivers: A new tool to monitor spatiotemporal changes in stream hydrodynamics, Journal of Geophysical Research, 113, B05301, doi:10.1029/2007JB005034.

Burtin, A., Bollinger, L., Cattin, R., Vergne, J. and Nábělek, J.L., 2009. Spatiotemporal Sequence of Himalayan Debris Flow from Analysis of High-Frequency Seismic Noise, Journal of Geophysical Research, doi:10.1029/2008JF001198.

Caldwell, W.B., Klemperer, S.L., Lawerence, J.F., Rai, S.S. and Ashish, 2013. Characterizing the Main Himalayan Thrust in the Garhwal Himalaya, India with receiver function CCP stacking, Earth and Planetary Science Letters, 367, 15-27.

Cannon, J.M. and Murphy, M.A., 2014. Active lower crustal deformation and Himalayan seismic hazard revealed by stream channels and regional geology, Tectonophysics, 633, 34-42, doi:10.1016/j.tecto.2014.06.031.

Cattin, R. and Avouac, J.P., 2000. Modeling mountain building and seismic cycle in the Himalaya of Nepal, Journal of Geophysical Research, 105(B6), 13389-13407.

Chanard, K., Avouac, J. P., Ramillien G. and Genrich J., 2014. Modeling deformation induced by seasonal variations of continental water in the Himalaya region: Sensitivity

to Earth elastic structure, Journal of Geophysical Research: Solid Earth, 119, doi:10.1002/2013JB010451.

Chen, W. P., and Molnar, P., 1977. Seismic moments of major earthquakes and the average rate of slip in central Asia, Journal of Geophysical Research, 82(20), 2945-2969.

Chiarabba, C., Piccinini, D. and De Gori, P., 2009. Velocity and attenuation tomography of the Umbria Marche 1997 fault system: evidence of a fluid-governed seismic sequence, Tectonophysics, 476(1), 73-84.

DeCelles, P.G., Gehrels, G.E., Quade, J., Ojha, T.P., Kapp, P.A. and Upreti, B.N., 1998. Neogene foreland basin deposits, erosional unroofing, and the kinematic history of the Himalayan fold-thrust belt, western Nepal, Geological Society of America Bulletin, 110 (1), 2-21, doi: 10.1130/0016-7606.

DeCelles, P.G., Robinson, D.M., Quade, J., Ojha, T.P., Garzione, C.N., Copeland, P. and Upreti, B.N., 2001. Stratigraphy, structure, and tectonic evolution of the Himalayan fold-thrust belt in western Nepal, Tectonics, 20 (4), 487-509.

De la Torre, T.L., Monsalve, G., Sheehan, A.F., Sapkota, S. and Wu, F., 2007. Earthquake processes of the Himalayan collision zone in eastern Nepal and the southern Tibetan Plateau, Geophysical Journal International, 171, 718-738, doi:10.1111/j.1365-246X.2007.03537.x.

Dhital, M.R., 2015. Geology of the Nepal Himalaya. Regional Perspective of the Classic Collided Orogen, Springer.

Diehl, T., Singer, J., Hetényi, G., Grujic, D., Clinton, J., Giardini, D., Kissling, E. and GANSSER Working Group, 2017. Seismotectonics of Bhutan: Evidence for segmentation of the Eastern Himalayas and link to foreland deformation, Earth and Planetary Science Letters, 471, 54-64.

Duputel, Z., Vergne, J., Rivera, L., Wittlinger, G., Farra, V. and Hetényi, G., 2016. The 2015 Gorkha earthquake: A large event illuminating the Main Himalayan Thrust fault, Geophysical Research Letters, 43, doi: 10.1002/2016GL068083.

Duverger, C., Godano, M., Bernard, P., Lyon-Caen, H. and Lambotte, S., 2015. The 2003-2004 seismic swarm in the western Corinth rift: Evidence for multiscale pore pressure diffusion process along a permeable fault system, Geophysical Research Letters, 42, 7374-7382, doi:10.1002/2015GL065298.

Elliott, J.R., Jolivet, R., Gonzalez, P.J., Avouac, J.P., Hollingsworth, J., Searle, M.P. and Stevens, V.L., 2016. Himalayan megathrust geometry and relation to topography revealed by Gorkha earthquake, Nature geoscience, 9, doi:10.1038/NGEO2623.

Fan, W. and Shearer P.M., 2015. Detailed rupture imaging of the 25 April 2015 Nepal earthquake using teleseismic P waves, Geophysical Research Letters, 42, 5744-5752, doi: 10.1002/2015GL064587.

Gansser, A. 1964. Geology of the Himalayas: London Wiley Interscience, 289.

Galetzka, J., Melgar, D., Genrich, J. F., Geng, J., Owen, S., Lindsey, E. O., Xu, X., Bock, Y., Avouac, J-P., Adhikari, L.B., Upreti, B. N., Pratt-Sitaula, B., Bhattarai, T.N., Sitaula, B., Moore, A., Hudnut, K.W., Szeliga, W., Normandeau, J., Fend, M., Flouzat, M., Bollinger, L., Shrestha, P., Koirala, B., Gautam, U., Bhatterai, M., Gupta, R., Kandel, T., Timsina, C., Sapkota, S.N., Rajaure, S. and Maharjan, N., 2015. Slip pulse and resonance of the Kathmandu basin during the 2015 Gorkha earthquake, Nepal, Science, 349(6252), 1091-1095.

Girault, F., Bollinger, L., Bhattarai, M., Koirala, B. P., France-Lanord, C., Rajaure, S., Gaillardet, J., Fort, M., Sapkota, S.N. and Perrier, F., 2014. Large-scale organization of carbon dioxide discharge in the Nepal Himalayas, Geophysical Research Letters, 41(18), 6358-6366.

Grandin, R., Doin, M-P., Bollinger, L., Pinel-Puyssegur, B., Ducret, G., Jolivet, R. and Sapkota, S.N., 2012. Long-term growth of the Himalaya inferred from interseismic InSAR measurement, Geology, 40, 12, 1059-1062, doi:10.1130/G33154.1.

Grandin, R., Vallée, M., Satriano, C., Lacassin, R., Klinger, Y., Simoes, M., and Bollinger, L., 2015. Rupture process of the Mw=7.9 2015 Gorkha earthquake (Nepal): insights into Himalayan megathrust segmentation, Geophysical Research Letters, 42, doi: 10.1002/2015GL066044.

Gualandi, A., Avouac, J-P., Galetzka, J., Genrich, J.F., Blewitt, G., Adhikari, L.B., Koirala, B.P., Gupta, R., Upreti, B.N., Pratt-Sitaula, B. and Liu-Zeng, J., 2016. Pre- and post-seismic deformation related to the 2015, Mw 7.8 Gorkha earthquake, Nepal, Tectonophysics, doi:10.1016/j.tecto.2016.06.014 (In Press).

Hainzl, S. and Ogata, Y., 2005. Detecting fluid signals in seismicity data through statistical earthquake modeling, Journal of Geophysical Research, 110, B05S07, doi:10.1029/2004JB003247.

Hanks, T.C. and Kanamori, H., 1979. A moment magnitude scale, Journal of Geophysical Research, 84, 2348-2350.

Harvey, J.E., Burbank, D.W. and Bookhagen, B., 2015. Along-strike changes in Himalayan thrust geometry: topographic and tectonic discontinuities in western Nepal, Lithosphere, doi:10.1130/L444.1.

Hauck, M.L., Nelson, K.D., Brown, L.D., Zhao, W. and Ross, A.R., 1998. Crustal structure of the Himalayan orogeny at ~90° east longitude from Project INDEPTH deep reflection profiles, Tectonics, 17 (4), 481-500.

Henry, P., Le Pichon, X. and Goffe, B., 1997. Kinematic, thermal and petrological model of the Himalayas: Constraints related to metamorphism within the underthrust Indian crust and topographic elevation, Tectonophysics, 273, 31 – 56.

Herman, F., Copeland, P., Avouac, J-P., Bollinger, L., Mahéo, G., Le Fort, P., Rai, S., Foster, D., Pêcher, A., Stüwe, K. and Henry, P., 2010. Exhumation, crustam deformation, and thermal, structure of Nepal Himalaya derived from inversion of thermochronological and thermobarometric data and modeling of topography, Journal of Geophysical Research: Solid Earth, 115, B06407, doi:10.1029/2008JB006126.

Hetényi, G., Cattin, R., Bruntet, F., Bollinger, L., Vergne, J., Nabelek, J.L. and Diament, M., 2007. Density distribution of the India plate beneath the Tibetan plateau: Geophysical and petrological constraints on the kinetics of the lower-crustal eclogitization, Earth and Planetary Science Letters, 264, 226-244, doi:10.1016/j.epsl.2007.09.036.

Hoste-Colomer, R., Bollinger, L., Lyon-Caen, H. and Burtin, A., 2017. Lateral structure variations and transient swarm revealed by seismicity along the Main Himalayan Thrust North of Kathmandu, Tectonophysics, http://dx.doi.org/10.1016/j.tecto.2016.10.004.

Hubbard, M.S. and Harrison, T.M., 1989. 40Ar/39Ar age constraints on deformation and metamorphism in the Main Central Thrust zone and Tibetan slab, eastern Nepal Himalaya, Tectonics, 8 (4), 865-880.

Hubbard, J., Almeida, R., Foster, A., Sapkota, S.N., Bürgi, P. and Tapponnier, P., 2016. Structural segmentation controlled the 2015 Mw 7.8 Gorkha earthquake rupture in Nepal, Geology, 44 (8), 639-642, doi:10.1130/G38077.1.

International Seismological Centre, On-line Bulletion, http://www.isc.ac.uk, International Seismological Centre, Thatcham, United Kingdom, 2017.

Jackson, M., and Bilham, R., 1994. Constraints on Himalayan deformation inferred from vertical velocity fields in Nepal and Tibet, Journal of Geophysical Research: Solid Earth, 99(B7), 13897-13912.

Jackson, J., 2006. Fatal attraction: living with earthquakes, the growth of villages into megacities, and earthquake vulnerability in the modern world. Phil Trans R Soc A, 364, 1911–1925.

Jacques, E., Ruegg, J. C., Lépine, J. C., Tapponnier, P., King, G. C. P. and Omar, A., 1999. Relocation of M≥ 2 events of the 1989 Dôbi seismic sequence in Afar: evidence for earthquake migration, Geophysical Journal International, 138(2), 447-469.

Johnson, P. A. and McEvilly, T. V. (1995). Parkfield seismicity: Fluid-driven?, Journal of Geophysical Research: Solid Earth, 100(B7), 12937-12950.

Jouanne, F., Mugnier, J.L., Gamond, J.F., Le Fort, P., Pandey, M.R., Bollinger, L., Flouzat, M. and Avouac, J.P., 2004. Current shortening across the Himalayas of Nepal, Geophysical Journal International, 157, 1-14, doi: 10.1111/j.1365-246X.2004.02180.x.

Jouanne, F., Awan, A., Madji, A., Pêcher, A., Latif, M., Kausar, A., Mugnier, J.L., Khan, I. and Khan, N.A., 2011. Postseismic deformation in Pakistan after the 8 October 2005 earthquake: Evidence of afterslip along a flat north of the Balakit-Bagh thrust, Journal of Geophysical Research, 116, B07401, doi:10.1029/2010JB007903.

Jouanne, F., Mugnier, J.L., Sapkota, S.N., Bascou, P. and Pecher, A., 2017. Estimation of coupling along the Main Himalayan Thrust in the central Himalaya, Journal of Asian Earth Sciences, 133, 62-71, doi:10.1016/j.jseaes.2016.05.028.

Kanamori, H. and Anderson, D. L., 1975. Theoretical basis of some empirical relations in seismology, Bulletin of the seismological society of America, 65(5), 1073-1095.

Kanamori, H., 1977. The Energy Release in Great Earthquakes, Journal of Geophysical Research, 82(20), 7B0286, 2981-2987.

Kaneda, H., Nakata, T., Tsutsumi, H., Kondo, H., Sugito, N., Awata, Y., Akhtar, S.S., Majid, A., Khattak, W., Awan, A.A., Yeats, R.S., Hussain, A., Ashraf, M., Wesnousky, S.G. and Kausar, A.B., 2008. Surface rupture of the 2005 Kashmir, Pakistan, earthquake and its active tectonic implication, Bulletion of the Seismological Society of America, 98 (2), 521 – 557, doi:10.1785/0120070073.

Kennett and Engdahl, 1991. Traveltimes for global earthquake location and phase identification, Geophysical Journal International, 105, 429-465.

Khanal, S. and Robinson, D.M., 2013. Upper crustal shortening and forward modeling of the Himalayan thrust belt along the Budhi-Gandaki River, central Nepal, International Journal of Earth Science (Geol Rundsch), 102, 1871-1891.

Kobayashi, T., Morishita, Y. and Yarai, H., 2015. Detailed crustal deformation and fault rupture of the 2015 Gorkha earthquake, Nepal, revealed from ScanSAR-based interferograms of ALOS-2, Earth, Planets and Space, 67, 201, doi: 10.1186/s40623-015-0359-z.

Lavé, J. and Avouac, J.P., 2000. Aactive folding of fluvial terraces across the Siwaliks Hills, Himalayas of central Nepal, Journal of Geophysical Research, 105 (B3), 5735-5770.

Lavé, J., Yule, D., Sapkota, S., Basant, K., Madden, C., Attal, M. and Pandey, R., 2005. Evidence for the Great Medieval Earthquake (~1100 A.D.) in the Central Himalayas, Nepal, Science, 307(5713), 1302 – 1305, doi:10.1126/science.1104804.

Lee, W.H.K., and Lahr, J.C., 1975. Hypo71 (revised): a computer program for determining hypocenter, magnitude and first motion pattern of local earthquakes, U.S. Geological Survey Open-File Report 75-311, 1-113.

Lemonnier, C., Marquis, G., Perrier, F., Avouac, J. P., Chitrakar, G., Kafle, B., Sapkota, S.N., Gautam, U., Tiwari, D. and Bano, M., 1999. Electrical structure of the Himalaya of central Nepal: High conductivity around the mid-crustal ramp along the MHT, Geophysical Research Letters, 26(21), 3261-3264.

Leroux-Mallouf, R., Ferry, M., Ritz, J-F., Berthet, T., Cattin, R. and Drukpa, D., 2016. First paleoseismic evidence for great surface rupturing earthquakes in Bhutan Himalayas, Journal of Geophysical Research: Solid Earth, 121, 7271-7283, doi:10.1002/2015JB012733.

Letort, J., Guilbert, J., Cotton, F., Bondár, I., Cano, Y. and Vergoz, J., 2015. A new, improved and fully automatic method for teleseismic depth estimation of moderate earthquakes (4.5< M< 5.5): application to the Guerrero subduction zone (Mexico), Geophysical Journal International, 201(3), 1834-1848.

Letort, J., Bollinger, L., Lyon-Caen, H., Guilhem, A., Cano, Y., Baillard, C. and Adhikari, L.B, 2016. Teleseismic depth estimation of the 2015 Gorkha-Nepal aftershocks, Geophysical Journal International, 207, 1584-1595, doi:10.1093/gji/ggw364.

Lyon-Caen, H. and Molnar, P., 1985. Gravity anomalies, flexure of the Indian plate, and the structure, support and evolution of the Himalaya and Ganga Basin, Tectonics, 4, 513-538.

Mahesh, P., Rai, S.S., Sivaram, K., Paul, A., Gupta, S., Sarma, R. and Gaur, V.K., 2013. One-dimensional reference velocity model and precise locations of earthquake hypocenters in the Kumaon-Garhwal Himalaya, Bulletin of the Seismological Society of America, 103 (1), 328-329, doi:10.1785/0120110328.

McCaffrey, R., Wallace L.M. and Beaven,J., 2008. Slow slip and frictional transition at low temperatures at the Hikurangi subduction zone, Nature Geoscience, 1, 316 – 320, doi:10.103B/ngeo178.

MolnarP. and Tapponnier, P., 1975. Cenozoic Tectonics of Asia: Effects of a Continental Collision, Science, 189, 4201.

Monsalve, G., Sheehan, A., Schulte-Pelkum, V., Rajaure, S., Pandey, M.R. and Wu, F., 2006. Seismicity and one-dimensional velocity structure of the Himalayan collision zone: Earthquakes in crust and upper mantle, Journal of Geophysical Research, 111, B10301, doi:10.1029/2005JB004062.

Mugnier, J-L., Gajurel, A., Huyghe, P., Jayangondaperumal, R., Jouanne, F. and Upreti, B., 2013. Structural interpretation of the great earthquakes of the last

millennium in the central Himalaya, Earth-Science Reviews, 127, 30-47, doi: 10.1016/j.earscirev.2013.09.003.

Murphy, M. A., Taylor, M. H., Gosse, J., Silver, C. R. P., Whipp, D. M. and Beaumont, C., 2014. Limit of strain partitioning in the Himalaya marked by large earthquakes in western Nepal, Nature Geoscience, 7(1), 38-42.

Nábělek, J., Hetényi, G., Vergne, J., Sapkota, S.N., Kafle, B., Jiang, M., Su, H., Chen, J., Huang, B-S. and Hi-CLIMB team, 2009. Underplating in the Himalaya-Tibet Collision Zone Revealed by the Hi-CLIMB Experiment, Science, 325, 1371-1374.

Nakata, T., 1982. A photogrammetric study on active faults in Nepal Himalayas, Journal of Nepal Geological Society, 2, special issue, 67-80.

Nakata, T., Iwata, S., Yamanaka, H., Yagi, H. and Maemoku, H., 1984. Tectonic Landforms of several active faults in the western Nepal Himalayas, Journal of Nepal Geological Society, 4 (special issue), 177-200.

Ni, J. and Barazangi, M., 1984. Seismotectonics of the Himalayan collision zone: geometry of the underthrusting India plate beneath the Himalaya, Journal of Geophysical Research, 89 (B2), 1147-1163.

Pacchiani, F. and Lyon-Caen, H., 2010. Geometry and spatio-temporal evolution of the 2001 Agios Ioanis earthquake swarm (Corinth Rift, Greece), Geophysical Journal International, 180, 59-72, doi:10.1111/j.1365-246X.2009.04409.x.

Pandey, M.R., 1985. Seismic model of central and eastern lesser Himalaya of Nepal, Journal of Nepal Geological Society, 3(1-2), 1-11.

Pandey, M.R. and Nicolas, M., 1991. The aftershock sequence of the Udaypur (Nepal) earthquake of August 20, 1988, Journal of N.G.S, 7 (special issue), 19-29.

Pandey, M.R., Tandukar, R.P., Avouac, J.P., Lavé, J. and Massot, J.P., 1995. Interseismic strain accumulation on the Himalayan Crustal Ramp (Nepal), Geophysical Research Letters, 22, 751-754.

Pandey, M.R., Tandukar, R.P., Avouac, J.P., Vergne, J. and Héritier, T., 1999. Seismotectonics of the Nepal Himalayas from a local seismic network, Journal of Asian Earth Sciences., 17(5-6), 703-712.

Paul, J., Bürgmann, R., Gaur, V. K., Bilham, R., Larson, K. M., Ananda, M. B., Jade, S., Mukal, M., Anupama, T.S., Satyal, G. and Kumar, D., 2001. The motion and active deformation of India, Geophysical Research Letters, 28(4), 647-650.

Pearson, O.N. and DeCelles, P.G., 2005. Structural geology and regional tectonic significance of the Ramgarh thrust, Himalayan fold-thrust belt of Nepal, Tectonics, 24, TC4008, doi: 10/1029/2003TC001617.

Qiu, Q., Hill, E.M., Barbot, S., Hubbard, J., Feng, W., Lindsey, E.O., Feng, L., Dai, K., Samsonov, S.V. and Tapponnier, P., 2016. The mechanism of partial rupture of a locked megathrust: role of fault morphology, Geology, doi:10.1130/G38178.1.

Richter, C. F., 1935. An instrumental earthquake magnitude scale, Bulletin of the Seismological Society of America, 25(1), 1-32.

Robinson, D.M., DeCelles, P.G. and Copeland, P., 2006. Tectonic evolution of the Himalayan thrust belt in western Nepal: Implications for channel flow models, Geological Society of America Bulletin, 118 (7/8), 865-885, doi:10.1130/B25911.1.

Sakai, H., Sakai, H., Yahagi, W., Fujii, R., Hayashi, T. and Upreti, B. N., 2006. Pleistocene rapid uplift of the Himalayan frontal ranges recorded in the Kathmandu and Siwalik basins, Palaeogeography, Palaeoclimatology, Palaeoecology, 241(1), 16-27.

Saijo, K., Kimura, K., Dongol, G., Komatsubara, T. and Yagi, H., 1995. Active faults in south western Kathmandu basin, central Nepal, Journal of Nepal Geological Society, 11, 217-224.

Sapkota S.N. ,2011. Surface rupture of 1934 Bihar-Nepal earthquake: implications for seismic hazard in Nepal Himalaya, Ph.D thesis, Institut de Physique du Globe de Paris,France. pp 2-292.

Sapkota, S.N., Bollinger, L., Klinger, Y., Tapponnier, P., Gaudemer, Y. and Tiwari, D., 2013. Primary surface ruptures of the great Himalayan earthquakes in 1934 and 1255, Nature Geoscience, 6, 71-76, doi:10.1038/NGEO1669.

Sapkota, S.N., Bollinger, L. and Perrier, F., 2016. Fatality rates of the Mw~8.2, 1934, Bihar-Nepal earthquake and comparison with the April 2015 Gorkha earthquake, Earth, Planets and Space, 68:40, doi: 10.1186/s40623-016-0416-2.

Schelling, D. and Arita, K., 1991. Thrust tectonics, crustal shortening, and the structure of the Far-Eastern Nepal Himalaya, Tectonics, 10, 5, 851-862.

Scholz, C.H.,1990. The mechanics of earthquakes and faulting. Cambrige university press.

Schulte-Pelkum, V., Monsalve, G., Sheehan, A., Pandey, M.R., Sapkota, S., Bilham, R. and Wu, F., 2005. Imaging the Indian subcontinent beneath the Himalaya, Nature Letters, 435, doi:10.1038/nature03678.

Shapiro, S.A., Huenges, E. and Borm, G., 1997. Estimating the crust permeability from fluid-injection-induced seismic emission at the KTB site, Geophysical Journal International, 131(2), F15-F18, doi:10.1111/j.1365-246X.1997.tb01215.x.

Seiscomp3, 2013. GFZ Potsdam, gempa GmbH, http://www.seiscomp3.org, access date: March 29th 2017.

Srivastava, P., & Mitra, G. (1994). Thrust geometries and deep structure of the outer and lesser Himalaya, Kumaon and Garhwal (India): Implications for evolution of the Himalayan fold-and-thrust belt, Tectonics, 13(1), 89-109.

Stevens,V.L. and Avouac, J.P, 2015. Interseismic coupling on the main Himalayan thrust, Geophysical Research Letters, 42, 5828–5837, doi:10.1002/2015GL064845.

Stevens, V.L. and Avouac, J-P., 2016. Millenary Mw>9 earthquakes required by geodetic strain in the Himalaya, Geophysical Research Letters, 43, 1118 – 1123, doi:10.1002/2015GL067336.

Subedi, S., 2016. Seismic imaging in western Nepal: a receiver function approach, IPGP, stage M2.

Upreti, B. N., 1999. An overview of the stratigraphy and tectonics of the Nepal Himalaya. Journal of Asian Earth Sciences, 17(5), 577-606.

Vergne, J., Cattin, R. and Avouac, J-P., 2001. On the use of dislocations to model interseismic strain and stress build-up at intracontinental thrust faults, Geophysical Journal International, 147, 155-162.

Waldhauser, F. and Ellsworth, W.L., 2000. A double-difference earthquake location algorithm: method and application to the Northern Hayward Fault, California, Bulletin Seismological Society of America, 90 (6), 1353-1368.

Weber, B., Becker, J., Hanka, W., Heinloo, A., Hoffmann, M., Kraft, T., Pahlke, D., Reinhardt, J. and Thoms, H., 2007. SeisComP3—Automatic and interactive real time data processing. In Geophysical Research Abstracts, 9, 09219.

Wells, D.L. and Coppersmith, K.J., 1994. New empirical Relationships among magnitude, rupture length, rupture width, rupture area, and surface displacement, Bulletin of the Seismological Society of America, 84 (4), 974-1002.

Wesnousky, S.G., Kumar, S., Mohindra, R. and Thakur, V.C., 1999. Uplift and convergence along the Himalayan Frontal Thrust of India, Tectonics, 18 (6), 967-976.

Wesnousky, S.G., Kumahara, Y., Chamlagain, D., Pierce, I.K., Karki, A. and Gauta, D., 2017. Geological observations on large earthquakes along the Himalayan frontal fault near Kathmandu, Nepal, Earth and Planetary Science Letters, 457, 366-375, doi:10.1016/j.epsl.2016.10.006.

Xu, X., Wen, X., Yu, G., Chen, G., Klinger, Y., Hubbard, J. and Shaw, J., 2009. Coseismic reverse- and oblique-slip surface faulting generated by the 2008 Mw 7.9 Wenchuan earthquake, China.

Yule, D., Dawson, S., Lavé, J., Sapkota, S., and Tiwari, D., 2006. Possible evidence for surface rupture of the Main Frontal Thrust during the great 1505 Himalayan earthquake, far-western Nepal, in AGU Fall Meeting Abstracts, S33C-05, 1, 5.

Zhao, W., Nelson, K.D. and Project INDEPTH Team, 1993. Deep seismic reflection evidence for continental underthrusting beneath southern Tibet, Nature, 366, 557- 559.

ANNEXES

Annexe A : Adhikari, L.B., Gautam, U.P., Koirala, B.P., Bhattarai, M., Kandel, T., Gupta, R.M., Timsina, C., Maharjan, N., Maharjan, K., Dahal, T., Hoste-Colomer, R., Cano, Y., Dandine, M., Guilhem, A., Merrer, S., Roudil, P. and Bollinger, L., 2015. The aftershock sequence of the 2015 April 25 Gorkha-Nepal earthquake, Geophysical Journal International, 203, 2119-2124, doi: 10.1093/gji/ggv412. _____ p.179

Annexe B: Matériel supplémentaire de l'article: Hoste-Colomer, R., Bollinger, L., Lyon-Caen, H. and Burtin, A., 2017. Lateral structure variations and transient swarm revealed by seismicity along the Main Himalayan Thrust North of Kathmandu, Tectonophysics, http://dx.doi.org/10.1016/j.tecto.2016.10.004._____ p.187

Annexe C: Station field sheets of deployment mission (November – December 2014)_____ p.203

Annexe A:

Adhikari, L.B., Gautam, U.P., Koirala, B.P., Bhattarai, M., Kandel, T., Gupta, R.M., Timsina, C., Maharjan, N., Maharjan, K., Dahal, T., Hoste-Colomer, R., Cano, Y., Dandine, M., Guilhem, A., Merrer, S., Roudil, P. and Bollinger, L., 2015. The aftershock sequence of the 2015 April 25 Gorkha-Nepal earthquake, Geophysical Journal International, 203, 2119-2124, doi: 10.1093/gji/ggv412.

Geophysical Journal International

Geophys. J. Int. (2015) **203,** 2119–2124
GJI Seismology

doi: 10.1093/gji/ggv412

The aftershock sequence of the 2015 April 25 Gorkha–Nepal earthquake

L.B. Adhikari,[1] U.P. Gautam,[1] B.P. Koirala,[1] M. Bhattarai,[1] T. Kandel,[2] R.M. Gupta,[1] C. Timsina,[1] N. Maharjan,[1] K. Maharjan,[2] T. Dahal,[2] R. Hoste-Colomer,[3,4] Y. Cano,[3] M. Dandine,[3] A. Guilhem,[3] S. Merrer,[3] P. Roudil[3] and L. Bollinger[3]

[1] *National Seismological Centre, Department of Mines and Geology, Lainchaur, Kathmandu, Nepal. E-mail: adhikari.research@gmail.com*
[2] *Regional Seismological Centre, Department of Mines and Geology, Surkhet-Birendranagar, Nepal*
[3] *CEA, DAM, DIF, F-*91297 *Arpajon, France*
[4] *Laboratoire de Géologie, Ecole Normale Supérieure, CNRS,* 24 *rue Lhomond, F-*75004 *Paris, France*

Accepted 2015 September 24. Received 2015 September 24; in original form 2015 July 13

SUMMARY

The *M* 7.8 2015 April 25 Gorkha earthquake devastated the mountainous southern rim of the High Himalayan range in central Nepal. The main shock was followed by 553 earthquakes of local magnitude greater than 4.0 within the first 45 days. In this study, we present and qualify the bulletin of the permanent National Seismological Centre network to determine the spatio-temporal distribution of the aftershocks. The Gorkha sequence defines a ∼140-km-long ESE trending structure, parallel to the mountain range, abutting on the presumed extension of the rupture plane of the 1934 *M* 8.4 earthquake. In addition, we observe a second seismicity belt located southward, under the Kathmandu basin and in the northern part of the Mahabarat range. Many aftershocks of the Gorkha earthquake sequence have been felt by the 3 millions inhabitants of the Kathmandu valley.

Key words: Earthquake source observations; Seismicity and tectonics; Asia.

1 INTRODUCTION

On 2015 April 25 at 11 h 56 local time, a M_w 7.8 (M_L 7.6) earthquake struck central Nepal devastating the region at the rim of the High Himalayan range and affecting Kathmandu valley, causing 8700+ deaths and leaving hundreds of thousands homeless. The regions affected by the main shock are located above the Main Himalayan Thrust fault (MHT), a shallow dipping megathrust accommodating half the India–Eurasia convergence where most of the shortening between India plate and the Tibetan plateau occurs (e.g. Bilham *et al.* 1997; Bettinelli *et al.* 2006).

While the northern deep portion of the thrust, under the high Himalayan range, continuously slips at 18 mm yr^{-1} during the interseismic period, its southern and shallowest segment is fully locked (e.g. Bollinger *et al.* 2004; Ader *et al.* 2012; Grandin *et al.* 2012). The locked portion of the fault system is estimated to extend over a distance of approximately 80 km from the surface trace of the Main Frontal Thrust that merges at depth on the MHT to the brittle–ductile transition, which falls at 15–20 km depth, under the southern slope of the high topography (Ader *et al.* 2012).

This segment partially ruptured during past large earthquakes. Such events include the $M \sim 7.5$ 1833 A.D. earthquake known by its macroseismic effects (Bilham 1995; Ambraseys & Douglas 2004; Szeliga *et al.* 2010), which suggest a partial rupture of the MHT, north of Kathmandu. In 1934, the larger Bihar–Nepal earthquake ($M \sim 8.2$–8.4) ruptured up to the surface along a minimum 150-km-long segment of the MHT, in eastern Nepal (Fig. 1; Sapkota *et al.* 2013).

Despite the significant documentation of these past events, their aftershock distribution is poorly known. This inhibits any detailed analysis of the seismic hazards following a large Himalayan earthquake, and prevents any discussion about the post-main shock slip potency. The recent Gorkha earthquake sequence helps toward better understanding the faulting conditions of the region. Here, we examine the aftershock sequence of the Gorkha earthquake recorded by the Nepal seismological network. We evaluate the quality of the early bulletins published by the National and Regional Seismological Centres. We then describe a homogeneous catalogue of aftershocks between 2015 April 25 and June 8, and we study their spatio-temporal distribution. We confront it to the available data from the 1833 and 1934 events. Such rapid earthquake catalogue is

© The Authors 2015. Published by Oxford University Press on behalf of The Royal Astronomical Society. This is an Open Access article distributed under the terms of the Creative Commons Attribution License (http://creativecommons.org/licenses/by/4.0/), which permits unrestricted reuse, distribution, and reproduction in any medium, provided the original work is properly cited.

Downloaded from http://gji.oxfordjournals.org/ at Commissariat A L'Energie Atomique on November 6, 2015

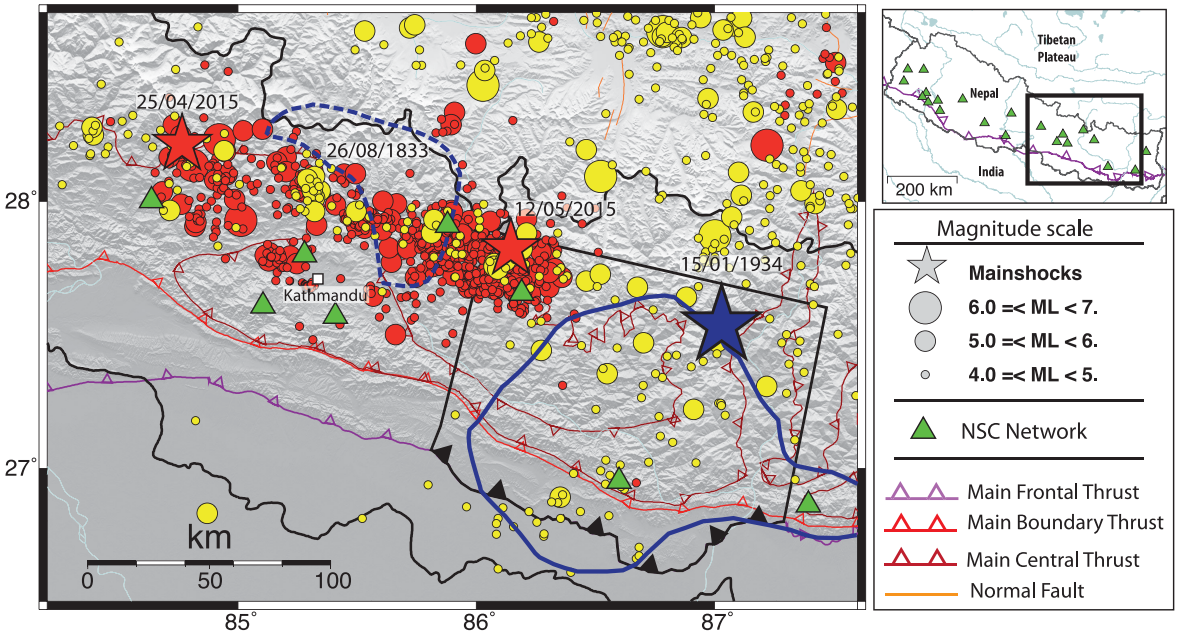

Figure 1. General map of the principal aftershocks (red dots) of the April 25th Gorkha earthquake located by NSC within the 45 days following the earthquake (red dots). Green triangles correspond to the national seismic network stations. The most western red star corresponds to the epicentre of the Gorkha earthquake while the eastern red star locates the epicentre of the May 12th event. In yellow, earthquake epicentres of the seismic events recorded during the twenty years preceding the main shock. Blue polylines correspond to the macroseismic isoseimals MSK64-VIII of the great 26/08/1833 and 15/01/1934 earthquakes (respectively dashed and plain polylines) deduced from Ambraseys and Douglas (2004) (Sapkota 2011). The blue star locates the relocated instrumental 1934 epicentre (Chen & Molnar 1977). Black rectangular polyline corresponds to the suspected extent of that earthquake rupture as suggested by (a) the macroseismic isoseismals and (b) the minimum stretch of 1934 MFT surface rupture represented by the black teethed polyline (Sapkota *et al.* 2013; Bollinger *et al.* 2014).

aimed to serve as a basic constraint to develop improved static and dynamic source models of the Gorkha earthquake, ultimately leading to a better understanding of strain and stress accommodation and release during the 2015 sequence.

2 METHODS AND BULLETIN ANALYSIS

2.1 Seismic data

In this study, we analyse seismic signals recorded by the Nepal nationwide seismological network (e.g. Pandey *et al.* 1995, 1999). 21 short period (1 s) vertical component stations (ZM500) and two broad-band (0.1–120 s) stations are operated by the Department of Mines and Geology (DMG) in collaboration with the Département Analyse Surveillance Environnement (DASE, France). These seismic stations are telemetered to, and processed at two independent seismic centres: the National Seismological Centre (NSC) and the Regional Seismological Centre (RSC). The NSC, which is located in Kathmandu, monitors the central and eastern Nepal seismicity with 12 analogous seismic stations deployed between 1978 and 1994. These records are digitized at the seismological centre. The RSC, based in Surkhet-Birendranagar, monitors the western Nepal seismicity with nine analogous stations deployed between 1994 and 1999 and later replaced in 2014 by digital stations. The records are all integrated, at both seismic centres, into the Jade-Onyx acquisition-treatment software suite. A three-layer 1-D velocity model is used for routine localisation processing. The *P*- and *S*-wave velocities in the three layers are, respectively (5.56, 6.50, 8.10) and (3.18, 3.71, 4.63) km s^{-1} with depth interfaces at 23 and 55 km for the Moho discontinuity (Pandey 1985; Pandey *et al.* 1995).

2.2 Magnitudes and locations

The local magnitude (M_L) is estimated on the maximum amplitude [$A(i)$] of the Sg, Sn or Lg seismic phases measured at station i on the 0.3–7 Hz bandpass filtered seismic signals following:

$$M_L_\mathrm{NSC}(i) = \mathrm{LOG}[A(i)/T] + B[\mathbf{\Delta}(i)] + C(i), \quad (1)$$

where T is the period, B the attenuation law, and $C(i)$ a station correction term. The attenuation law is expressed as a function of the epicentral distance ($\mathbf{\Delta}$) and include a geometrical spreading correction and an anelastic attenuation term such that

$$B(\mathbf{\Delta}) = -1.85 + 0.854\ \log 10(\mathbf{\Delta}) + 0.00102\ \mathbf{\Delta}. \quad (2)$$

Only stations with epicentral distances greater than 100 km are considered for this magnitude determination, in order to avoid source and path effects. However, because the seismic signal saturates at most of the closest NSC stations during the largest earthquakes of the sequence, the measurement of the magnitude is limited to the stations located at the periphery of NSC network or to the stations of the RSC network.

Overall, 4401 events were manually picked and located within the 45 days following the main shock (between 2015 May 25 and June 8). 1802 events have M_L greater than 3.0 including 553 events with M_L greater than 4.0.

Regarding the events with M_L greater than 3.0, we estimate that their location is globally well constrained. Indeed, an average of 15–20 seismic phases was picked at NSC per event (Fig. 2). The minimal epicentral distance is lower than 31 km for 75 per cent of the events (Fig. 2a). Because of the geometry of the seismic cluster within the network, the maximal gap between two stations for a given event is preferentially 180–185° (Fig. 2b). However, origins of the easternmost epicentres (i.e. beyond longitude 86°)

Downloaded from http://gji.oxfordjournals.org/ at Commissariat A L'Energie Atomique on November 6, 2015

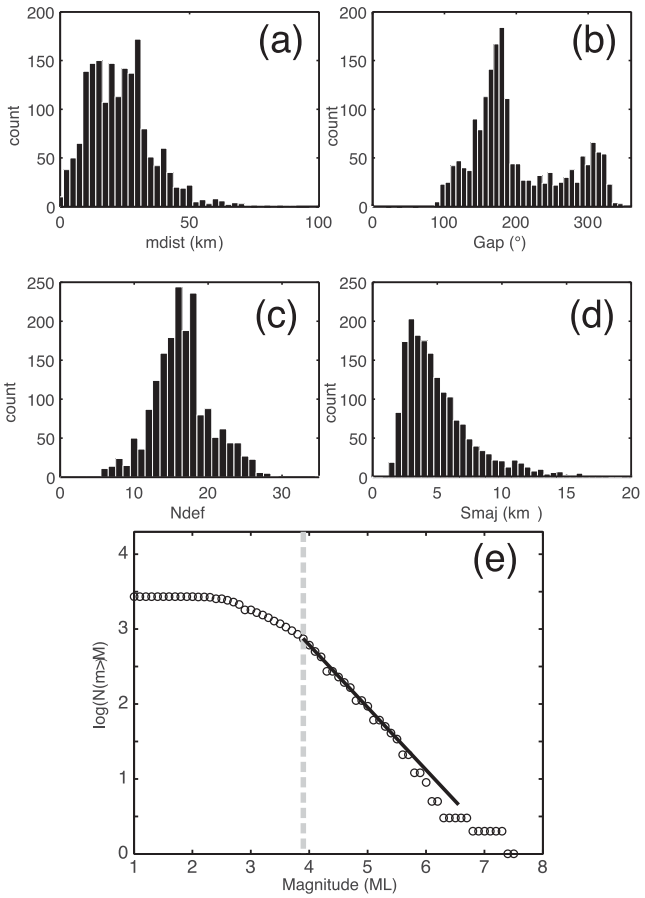

Figure 2. (a) Distance between the epicentre and the closest station. (b) Maximum azimuthal gap. (c) Number of phases pointed by events. (d) Major semi axis of the location uncertainty in kilometres. (e) Gutenberg–Richter plot of the cumulative number of events located by NSC analysts during the first 45 d after the Gorkha-earthquake main shock. The straight-line portion of the curve yields a *b*-value of 0.80 ± 0.05, while the progressive flattening of the curve below M_L 4 is the result of the incompleteness of the seismic catalogue below this value.

have an azimuthal gap around 300–310° between April 27 and May 28, due to a technical issue on a relay transmitting the easternmost stations (TAPN/ODAN/RAMN). Consequently, uncertainties on the locations of the earthquake cluster associated to the *M* 7.3 aftershock that followed on 2015 May 12 are larger than during the rest of the sequence. All those characteristics lead to a major semi axis of the location uncertainty ellipse with a median value at 4.7 km and a 95th percentile at 11.5 km (Fig. 2d). In total, analysts at DMG manually picked 55 778 phases, mainly Pg and Sg, through June 8 (Fig. 2c). The distribution of Pg and Sg time residuals show that the observed arrival times are consistent with the 1-D velocity model (Fig. S2). The average *Vp*/*Vs* ratio based on the entire catalogue is estimated at 1.70 ± 0.20 using *Ts*–*Tp* time difference. This value fits well with the theoretical *Vp*/*Vs* ratio used in the velocity model (i.e. *Vp*/*Vs* = 1.75).

RSC provided also bulletins of the sequence. These bulletins were merged to NSC's. However, because all the RSC stations recorded the events within a narrow azimuth/distance range of about [280 ± 20°; 400 ± 100 km], their addition in the location process introduces a location bias that translates the epicentres by [−5; 30] km southward (Fig. S3). Longitudinal variations of the relocation vectors are smaller than latitudinal variations (i.e. in the [−5; +5] km range) and show no apparent regional trend. This potential bias could possibly be corrected after adding station corrections or by considering another velocity model. Such corrections are however outside of the scope of the present work. Here, we only exploit RSC bulletins regarding the magnitude associated to each event. Initial depths are obtained using the 1-D-layer model. As a result, the preliminary depth estimations clearly depict a layered structure consistent with the default depths of the location processing (originally set at 2/10/25/30/40/50 km and lately complemented for some events with additional values at 6/15 and 20 km). To obtain a clearer image of the aftershocks cluster at depth, we perform a relocation of the seismic sequence using ISClocator (Bondár & Storchak 2011) and taking into account the RSTT velocity model, a 3-D model including regional phase traveltime corrections (Myers *et al.* 2010). The relocation of the 4401 events studied, using ISClocator with RSTT and allowing for phase reallocation differs by 2.5 ± 4.2 km (median value) from the original NSC location. The main differences in term of earthquake locations between the two catalogues are illustrated on Figs S4–S6. The relocation confirms that most aftershocks are located in the hangingwall of the Main Himalayan Thrust.

2.3 Gutenberg–Richter distribution of the Gorkha sequence

Despite the 4401 events located by the seismic analysts, the seismic catalogue is clearly incomplete below M_L = 4.0 (Fig. 2e), which corresponds approximately to the magnitude of completeness (M_c). This magnitude is greater than the M_c determined during the interseismic period (i.e. $M_c \sim 2.0$) according to Pandey *et al.* (1999), even considering its season variations of ±0.5 magnitude unit due to the seismic noise of the rivers and landslides (Bollinger *et al.* 2007). The current M_c of the Gorkha sequence can be explained by (i) the high seismic noise level during the first hours following the main shock (Fig. S1), and (ii) the high number of seismic alerts during the early sequence. Indeed, NSC has for mission to provide rapid seismic alerts to the Nepalese authorities for all M_L 4.0+ earthquakes. Such requirements precluded picking arrivals for events smaller than M_L 4.0.

On the Gutenberg–Richter plot of the aftershocks (Fig. 2e), the straight portion of the cumulative number of seismic events as a function of the magnitude yields a *b*-value of 0.80 ± 0.05. This post-earthquake *b*-value is smaller than the average *b*-value of 1 observed worldwide, but identical within uncertainties to the average value of 0.83 ± 0.05 estimated between 1995 and 2015 in the same area from 2102 events of magnitude greater than 2.4, including 110 greater than M_L 4. We notice that there is a small overlap of the interseismic and post-seismic magnitude bands considered in the magnitude distributions that does not help for discussing in greater details the pre- and post-earthquake *b*-values.

3 SPATIO-TEMPORAL VARIATIONS OF THE SEISMICITY

The main shock was immediately followed by a string of aftershocks from its epicentre, near Barpak-Gorkha, to a region about 120 km to the east, within a trace width of about 40 km (Fig. 3). Altogether, more than 120 events with M_L greater than 4.0 were located there within the 12 hr following the main shock. The rate of the seismicity over the next 18 days showed a typical decay, and the aftershocks

Downloaded from http://gji.oxfordjournals.org/ at Commissariat A L'Energie Atomique on November 6, 2015

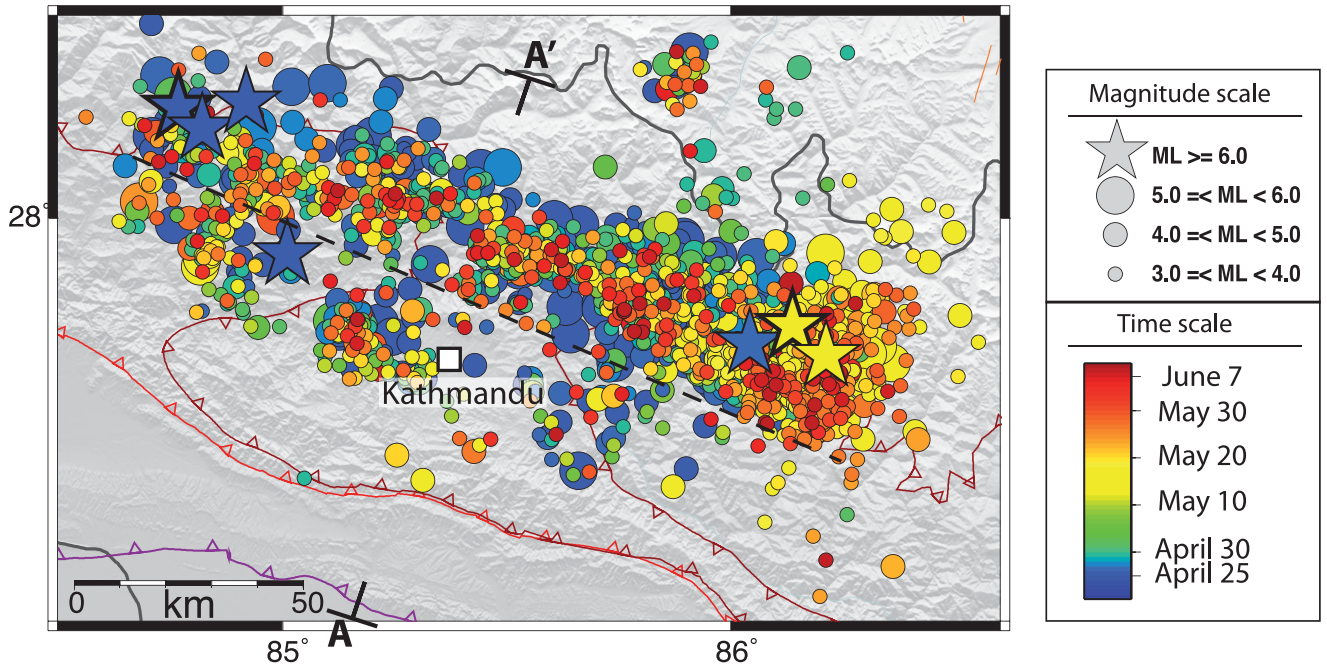

Figure 3. Map of the main shock and aftershocks of the Gorkha earthquake colour coded as a function of their time of occurrence. The dashed line divides the earthquake epicentres colour-coded in green (north) and red (south) on Fig. 4. Included on the map is the location of the A–A′ profile through the aftershocks (Figs S5a and b).

occurred within a relatively restricted area. The largest early aftershocks were located within the first 2 days at both the west and east termini of the main shock rupture (Fig. 3). Two large aftershocks with $M_L \geq 6.0$ immediately followed the main shock (i.e. 4 and 34 min, respectively) in its immediate vicinity at the western end of the cluster (Fig. 4). Its eastern end was also the place of two additional events of similar size ~3 and 25 hr, respectively after the main shock. The first of these events was located about 10 km east of its eastern rim, and was followed by a small cluster of events (Fig. 4).

Seventeen days later, on May 12, the largest aftershock (M_w 7.3, M_L 6.9) ruptured the easternmost region. This event was followed by an important number of aftershocks. We indeed counted almost 70 M_L 4+ events within the first 24 hr of the M 7.3 earthquake. These events were spread along a 60-km-long segment centred on the M 7.3 epicentre. In addition, a significantly denser cluster developed asymmetrically within a 30-km-large area, from about 10 km to the west to 20 km to the east of the epicentre (Fig. 4). The following large M_L 6.3 aftershock was recorded in this area about 30 min after. This seismic cluster remained very productive during the following weeks (Fig. 4).

The space–time distribution of all aftershocks within the first 45 days of the sequence reveals a clustering of activity within the main shock rupture zone (Fig. 4a). Because the clusters do not extend continuously from the downdip to the updip ends of the seismicity, we choose to separately divide the seismic area into two regions (see Fig. 3): a region to the south, comprising the trace of the Kathmandu basin and northern Mahabarat range, and another region to the north, covering the area devastated by the main shock (Figs 3 and 4). The temporal behaviour of seismicity in both areas (red for southern seismicity and green for the northern seismicity in Fig. 4) shows no significant differences. The clusters south of Kathmandu develop from the first day of the sequence, and depict a temporal decay similar to the one observed for the northern clusters (Fig. 4).

4 DISCUSSION – CONCLUSION

Most of the 3000 aftershocks located by NSC within the first 45 days following the Gorkha earthquake are concentrated in a narrow 40-km-wide band at midcrustal to shallow depths (i.e., between 2 and 25 km) along the strike of the southern slope of the high Himalayan range. The westernmost seismicity of the sequence near the M 7.8 epicentre seems to abut on a topographical high. Eastward, the seismicity develops within 160 km in two main clusters: (1) a large 120 × 40–50 km seismic patch, that activated immediately after the main shock and that encompassed significant spatial variations in term of seismicity rate, including a central area with a low rate of events and (2) a second smaller but denser patch (20 km × 30 km) located at the eastern end of the seismic cluster that mainly occurred following the May 12 earthquake (Figs 3 and 4). While the downdip end of the seismicity band along strike coincides broadly with the downdip end of the interseismic midcrustal cluster (Fig. 1), its updip extension develops significantly farther south. It is particularly true for the trace of the first, larger patch, where an embayment of the seismicity reaches the Chandragiri hills, ~50 km south from the onset of the seismicity. This first patch appears to coincide with the main fault segment and centred on the Kathmandu klippe. Teleseismic source inversions coupled with cGPS and DinSAR models show that the M 7.8 earthquake ruptured this segment (e.g. Avouac *et al.* 2015; Galetzka *et al.* 2015; Grandin *et al.* 2015), which may have also previously ruptured during the 1833 A.D. earthquake as suggested from the macroseismic trace of that 182-yr-old event (Martin *et al.* 2015 and Fig. 1). The second, smaller patch marks a deeper structural rupture further to the east that borders the north westernmost extent of the great 1934 AD earthquake (Fig. 1).

The characteristics of the main rupture that (1) is centred on the Kathmandu klippe, (2) probably occurred in a similar region as a past earthquake and (3) showed a two-step activation with along strike variations of the updip-end of the seismicity advocate for a potential midcrustal structure controlling the rupture extension

Downloaded from http://gji.oxfordjournals.org/ at Commissariat A L'Energie Atomique on November 6, 2015

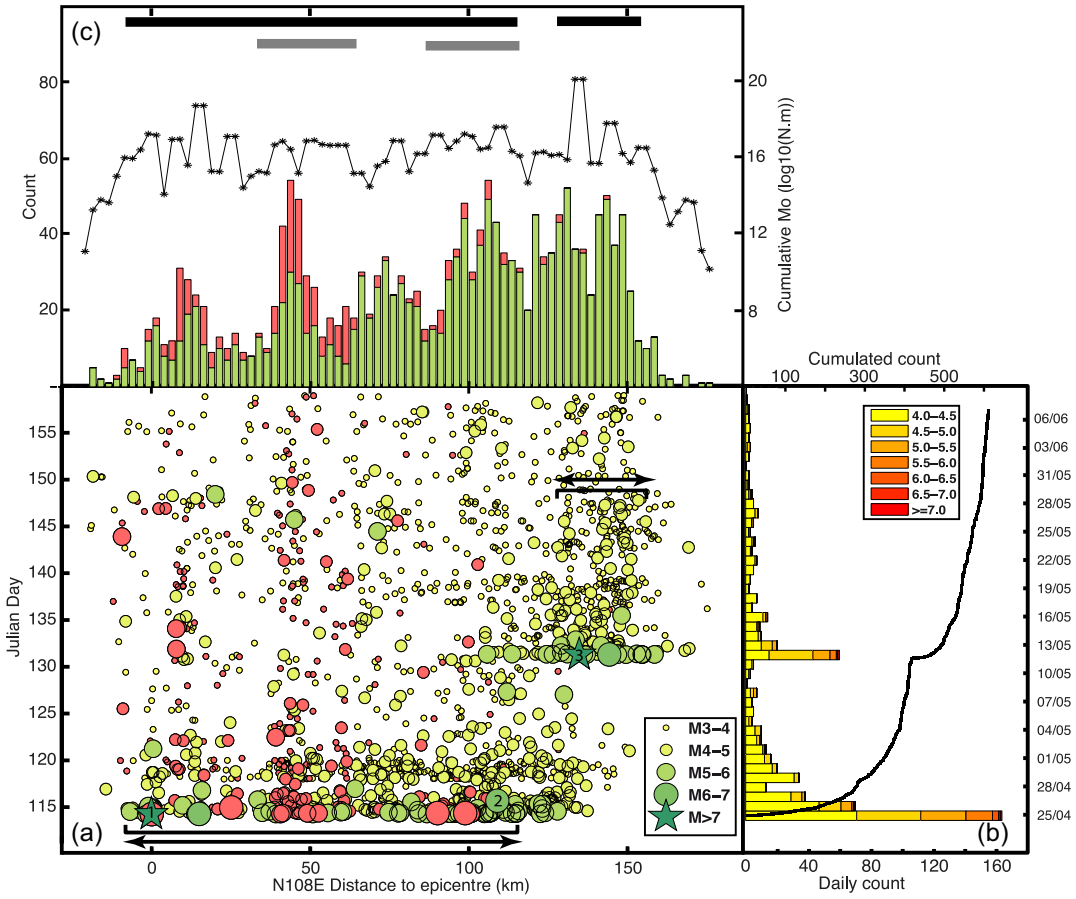

Figure 4. Spatio-temporal variation of the aftershocks. (a) Time sequence of the aftershocks. The events colour coded in red and green are respectively located south and north from the dashed line on Fig. 3. Numbers 1, 2 and 3 correspond, respectively, to the main shock epicentre, to the easternmost $M_L > 6.0$ event located within the supposed trace of the main shock and to the epicentre of the May 12th earthquake (underlined by the double arrows). (b) Daily and cumulated number of aftershocks with M_L greater than 4.0 (respectively histogram and black curve). (c) Lateral variations of the number of events (histogram) and moment released by the aftershocks.

of the earthquakes in this region of central Nepal. Moreover, the uneven along-strike distribution of aftershocks may reflect second-order structural features and/or lateral variations of co- and post-seismic slip (e.g. Avouac *et al.* 2015; Grandin *et al.* 2015). Both need to be better understood given their potential control on future rupture extensions.

After 45 days of aftershock activity, the rate of events with magnitudes above the present completeness magnitude (i.e. $M_c \sim 4$) has remained high (>1 per day) compared to the rate of five events of similar size recorded per year in the last 20 yr for the area covered by the post-seismic activity (Fig. 1). This present-day rate is, however, consistent with a typical temporal decay of the number of events. Analysis of the catalogue shows that the $M4+$ aftershock rate, $R(t)$, as a function of time, t, since the main shock follows a modified Omori law such as:

$$R(t) = k(t + c)^{-p}, \tag{3}$$

where $p = 0.8 \pm 0.4$, $c = 0.019 \pm 0.015$ and $k = 30.92 \pm 2.97$ for the main cluster, and $p = 0.78 \pm 0.07$, $c = 0.004 \pm 0.012$ and $k = 11.21 \pm 1.44$ within the trace of M 7.3 May 12 aftershock. We find that k, which is normalized to the surface considered, appears larger within the trace of that aftershock. We also stress that c is probably ill-defined due to the fact that some M_L 4+ aftershocks were almost certainly missed during the day following the main shock given the high level of background seismic noise (Fig. S1) and the saturation of the seismic stations. p is similar within the uncertainty for the two patches and well within the range of p values 0.6–2.5 previously reported (Utsu & Ogata 1995), smaller than the value of 1.15 obtained for Muzzafarabad-2005 (Tahir & Grasso 2013). These values of the p parameter are within typical average values for thrust faults [i.e. around 0.8 according to Tahir (2011)].

However, because both MHT fault segments located (i) south to the Gorkha rupture and (ii) west of it are capable of generating large earthquakes, monitoring the behaviour of the seismicity around the Kathmandu valley will remain crucial. In the meantime, additional work on the aftershock activity, preferentially focusing on the generation of a catalogue of smaller sized earthquakes and on their precise relocations, will be important to assess and understand eventual migration of seismicity on the MHT and on surrounding splay faults that may add to the regional seismic hazards.

ACKNOWLEDGEMENTS

The authors are most grateful to Mr Sarbajit Prasad Mahato, director of DMG and Soma Nath Sapkota, Deputy Director General in charge of the Geoscience division as well as to all the staff of the DMG and DASE who have contributed to the national seismological network. Eric Sauvage and JeanBaptiste Leblanc, which collaborated in maintaining the network during the seismic crisis

Downloaded from http://gji.oxfordjournals.org/ at Commissariat A L'Energie Atomique on November 6, 2015

are also thanked. We also thank Susan Hough and Pascal Bernard for their constructive reviews as well as Helene Lyon-Caen, Jean Letort and Christian Baillard for useful discussions.

REFERENCES

Ader, T. *et al.*, 2012. Convergence rate across the Nepal Himalaya and interseismic coupling on the Main Himalayan Thrust: implications for seismic hazard, *J. geophys. Res.,* **117,** B04403, doi:10.1029/2011JB009071.

Ambraseys, N.N. & Douglas, J., 2004. Magnitude calibration of north Indian earthquakes, *Geophys. J. Int.,* **159,** 165–206.

Avouac, J.P., Meng, L., Wei, S., Wang, T. & Ampuero, J.P., 2015. Lower edge of locked Main Himalayan Thrust unzipped by the 2015 Gorkha earthquake, *Nat. Geosci.,* **8,** 708–711.

Bettinelli, P., Avouac, J.P., Flouzat, M., Jouanne, F., Bollinger, L., Willis, P. & Chitrakar, G.R., 2006. Plate motion of India and interseismic strain in the Nepal Himalaya from GPS and DORIS measurements, *J. Geod.,* **80**(8–11), 567–589.

Bilham, R., 1995. Location and magnitude of the 1833 Nepal earthquake and its relation to the rupture zones of contiguous great Himalayan earthquakes, *Curr. Sci.,* **69,** 101–128.

Bilham, R. *et al.*, 1997. GPS measurements of present-day convergence across the Nepal Himalaya, *Nature,* **386**(6620), 61–64.

Bollinger, L., Avouac, J.P., Cattin, R. & Pandey, M.R., 2004. Stress build up in the Himalaya, *J. geophys. Res.,* **109,** B11405, doi:10.1029/2003JB002911.

Bollinger, L., Perrier, F., Avouac, J.P., Sapkota, S., Gautam, U. & Tiwari, D.R., 2007. Seasonal modulation of seismicity in the Himalaya of Nepal, *Geophys. Res. Lett.,* **34,** L08304, doi:10.1029/2006GL029192.

Bollinger, L. *et al.*, 2014. Estimating the return times of great Himalayan earthquakes in Eastern Nepal: evidence from the Patu and Bardibas strands of the Main Frontal Thrust, *J. geophys. Res.,* **119**(9), 7123–7163.

Bondár, I. & Storchak, D., 2011. Improved location procedures at the International Seismological Centre, *Geophys. J. Int.,* **186**(3), 1220–1244.

Chen, W.-P. & Molnar, P., 1977. Seismic moments of major earthquakes and the average rate of slip in Central Asia, *J. geophys. Res.,* **82,** 2945–2969.

Galetzka, J. *et al.*, 2015. Slip pulse and resonance of Kathmandu basin during the 2015 M_w 7.8 Gorkha earthquake, Nepal imaged with geodesy, *Science,* **349,** 1091–1095.

Grandin, R., Doin, M.P., Bollinger, L., Pinel-Puyssegur, B., Ducret, G., Jolivet, R. & Sapkota, S.N., 2012. Long-term growth of the Himalaya inferred from interseismic InSAR measurement, *Geology,* **40**(12), 1059–1062.

Grandin, R., Vallée, M., Satriano, C., Lacassin, R., Klinger, Y., Simoes, M. & Bollinger, L., 2015. Rupture process of the $M_w = 7.9$ 2015 Gorkha earthquake (Nepal): insights into Himalayan megathrust segmentation, *Geophys. Res. Lett.,* doi:10.1002/2015GL066044.

Martin, S., Hough, S., Bilham, R. & Hung, C., 2015. Ground Motions from the 2015 M7.8 1 Gorkha, Nepal, Earthquake Constrained by a Detailed Assessment of Macroseismic Data, Accepted at Seismological Research Letters, special issue on Gorkha earthquake.

Myers, S.C. *et al.*, 2010. A crust and upper mantle model of Eurasia and North Africa for Pn travel-time calculations, *Bull. seism. Soc. Am.,* **100,** 640–656.

Pandey, M.R., 1985. Seismic model of central and eastern lesser Himalaya of Nepal, *J. Nepal geol. Soc.,* **3**(1–2), 1–11.

Pandey, M.R., Tandukar, R.P., Avouac, J.P., Lavé, J. & Massot, J.P., 1995. Interseismic strain accumulation on the Himalayan Crustal Ramp (Nepal), *Geophys. Res. Lett.,* **22,** 751–754.

Pandey, M.R., Tandukar, R.P., Avouac, J.P., Vergne, J. & Héritier, T., 1999. Seismotectonics of the Nepal Himalayas from a local seismic network, *J. Asian Earth Sci.*, **17**(5–6), 703–712.

Sapkota, S.N., 2011. Surface rupture of 1934 Bihar-Nepal earthquake: implications for Seismic Hazard in Nepal Himalaya, *Unpublished thesis,* IPGP, pp. 1–292.

Sapkota, S.N., Bollinger, L., Klinger, Y., Tapponnier, P., Gaudemer, Y. & Tiwari, D., 2013. Primary surface rupture of the great Himalayan earthquakes of 1934 and 1255, *Nat. Geosci.,* **6,** 71–76.

Szeliga, W., Hough, S., Martin, S. & Bilham, R., 2010. Intensity, magnitude, location, and attenuation in India for felt earthquakes since 1762, *Bull. seism. Soc. Am.,* **100**(2), 570–584.

Tahir, M., 2011. Aftershock properties and its triggering mechanism, *PhD thesis,* Grenoble University, France.

Tahir, M. & Grasso, J.R., 2013. Aftershock patterns of $M_s > 7$ earthquakes in the India–Asia collision belt: anomalous results from the Muzaffarabad Earthquake sequence, Kashmir, 2005, *Bull. seism. Soc. Am.*, **104**(1), 1–23.

Utsu, T. & Ogata, Y., 1995. The centenary of the Omori formula for a decay law of aftershock activity, *J. Phys. Earth,* **43**(1), 1–33.

SUPPORTING INFORMATION

Additional Supporting Information may be found in the online version of this paper:

Figure S1. Time–frequency diagram of the power spectral density (in acceleration) at GKN. SHZ raw signals between day 100 and 150.

Figure S2. (a, b) Respectively histograms of the Pg and Sg residues in seconds (c) *Vp*/*Vs* estimation from t_S–t_P time difference.

Figure S3. Illustration of RSC/NSC bulletin fusions on the location of the epicentres (a) Map of the relocation vectors generated after the RSC/NSC bulletin fusion (b) Histograms of the latitudinal and longitudinal components of the relocation vectors.

Figure S4. Map view of hypocentre locations. (a) Using the default parameters (b) After relocation using ISClocator (Bondár & Storchak 2011) and taking into account the RSTT velocity model, a 3-D model including regional phase traveltime corrections (Myers *et al.* 2010). A–A′ locate the cross-section through the aftershocks Fig. S5. Note the deeper aftershocks along the trace of the eastern segment, ruptured on 2015 May 12.

Figure S5. Cross-sections through the aftershocks along A–A′ profiles (see location on Figs 3 and S4). All hypocentres within 20 km from the N18E profile going through Kathmandu are represented.

Figure S6. Hypocentres depth histograms (a) for the original bulletin and (b) After relocation using ISClocator (Bondár & Storchak 2011) and taking into account the RSTT velocity model, a 3-D model including regional phase traveltime corrections (Myers *et al.* 2010).

Table S1. Original NSC seismic catalogue of all aftershocks greater than M_L 4.0 for the 45 days following the Gorkha-Nepal earthquake.

Table S2. Seismic catalogue of all aftershocks greater than M_L 4.0 for the 45 days following the Gorkha-Nepal earthquake relocated using ISClocator taking into account RSTT velocity model—see paper for further details and references.

Table S3. GSE2 bulletin for the 45 days following the Gorkha-Nepal earthquake. This bulletin incorporates the Phasepicks/arrivals at each NSC station for all events with $M_L \geq 4.5$ (http://gji.oxfordjournals.org/lookup/suppl/doi:10.1093/gji/ggv412/-/DC1).

Please note: Oxford University Press is not responsible for the content or functionality of any supporting materials supplied by the authors. Any queries (other than missing material) should be directed to the corresponding author for the paper.

Downloaded from http://gji.oxfordjournals.org/ at Commissariat A L'Energie Atomique on November 6, 2015

Annexe B:

Matériel supplémentaire de l'article: Hoste-Colomer, R., Bollinger, L., Lyon-Caen, H. and Burtin, A., 2017. Lateral structure variations and transient swarm revealed by seismicity along the Main Himalayan Thrust North of Kathmandu, Tectonophysics, http://dx.doi.org/10.1016/j.tecto.2016.10.004.

Supplementary Material for "Lateral structure variations and transient swarm revealed by seismicity along the Main Himalayan Thrust North of Kathmandu"

R. Hoste-Colomer[(1)(2)], L. Bollinger[(1)], H. Lyon-Caen[(2)], A. Burtin[(3)], L.B. Adhikari[(4)]

[(1)] CEA, DAM, DIF, F-91297 Arpajon, France.

[(2)] Laboratoire de Géologie, Ecole Normale Supérieure/CNRS UMR 8538, PSL Research University, Paris 75005, France.

[(3)] Institut de Physique du Globe de Paris, Sorbonne Paris Cité, Université Paris Diderot, UMR 7154 CNRS, Paris, France.

[(4)] Department of Mines and Geology, National Seismological Center, Kathmandu, Nepal.

---

1. Seismological Network

The Nepalese Seismological Network is monitored by two centers, the NSC and RSC. The National Seismological Centre monitors the east and central Nepal and the Regional Seismological Centre monitors the western part of the country. The area of our study being north of Kathmandu, we used the NSC network plus 3 temporary stations deployed between 1995 and 1996 (Figure S1).

Figure S1. Map of the permanent stations and the 1995-1996 temporary network. NSC: National Seismological Network. RSC: Regional Seismological Network.

2. Location uncertainties

The relative relocation in this study is performed using the NSC data and the temporary network data. The uncertainties on the longitude and latitude before relocation are well-reported in the bulletin (Figure S2). However, the depth uncertainty in most cases is not given because the depth is not well resolved (Figure S3 and S4). After relative relocation is performed, the results show clustering of the events and a decrease of the horizontal uncertainties (Figure S5, S6, and S7).

Figure S2. Map of the seismicity of the National Seismological Centre of Nepal before relative relocation with the horizontal uncertainties in the location.

Figure S3. Cross-section A-A' of Figure S1. Earthquakes with error bars equal to zero are those which uncertainties were default value (-999).

Figure S4. Cross-section B-B' of Figure S1. Earthquakes with error bars equal to zero are those which uncertainties were default value (-999).

Figure S5. Map of the seismicity of the National Seismological Centre of Nepal after relative relocation performed in this article with the relative location uncertainties.

Figure S6. Cross-section A-A' of Figure S4.

Figure S7. Cross-section B-B' of Figure S4.

3. Coulomb Stress Change

The schema of the Coulomb stress change in Figure 7B is computed with Coulomb 3.4 software (Toda et al., 2005; Lin and Stein, 2004). Table S1 and S2 describe the input parameters. The results shows the areas where seismicity should be trigged in yellow to red colors and areas where seismicity should be inhibited in blue colors in the receiving faults due to the static stress change induced by the tear fault (Figure S8 to S11).

Tear Fault Parameters	Values
Fault length (km)	20
Fault width (km)	6
Fault depth (km)	16
Strike (°)	155
Dip (°)	90
Rake (°)	180

Table S1. Parameters of the tear fault to compute the Coulomb stress change.

	Strike (°)	Dip (°)	Rake (°)	Depth of observation (km)
Backthrust fault	250	80	90	22
Thrust Fault	110	7	90	15

Table S2. Parameters of the receiving faults to compute the Coulomb stress change.

Figure S8. Map of the Coulomb stress change (bar) for the backthrust as the receiving fault at a depth of 22 km induced by a slip of 50 cm on the tear fault. The slip considered for the calculation is scaled based on the dimensions of the source (20x6 km). We use Okada (1992)

formulation for plane dislocation in an elastic half-space with elastic moduli Lambda= mu = $0.33.10^{11}$ N/m^2.

Figure S9. Cross-section A-B of Figure S8 of the Coulomb stress change (bar) for the backthrust as the receiving fault induced by the tear fault. Dotted line indicates the depth of observation of Figure S8.

Figure S10. Map of the Coulomb stress change (bar) for the thrust receiving fault at a depth of 15 km induced by a slip of 50 cm on the tear fault. The slip considered for the calculation is scaled based on the dimensions of the source (20x6 km). We use Okada (1992) formulation for plane dislocation in an elastic half-space with elastic moduli Lambda= mu = $0.33.10^{11}$ N/m^2.

Figure S11. Cross-section A-B of Figure S10 of the Coulomb stress change (bar) for the thrust as the receiving fault induced by the tear fault. Dotted line indicates the depth of observation of Figure S10.

References

Lin, J. and R.S. Stein, 2004. Stress triggering in thrust and subduction earthquakes, and stress interaction between the southern San Andreas and nearby thrust and strike-slip faults, Journal of Geophysical Research, 109, B02303, doi:10.1029/2003JB002607.

Toda, S., R. S. Stein, K. Richards-Dinger and S. Bozkurt, 2005. Forecasting the evolution of seismicity in southern California: Animations built on earthquake stress transfer, Journal of Geophysical Research, 110, B05S16, doi:10.1029/2004JB003415.

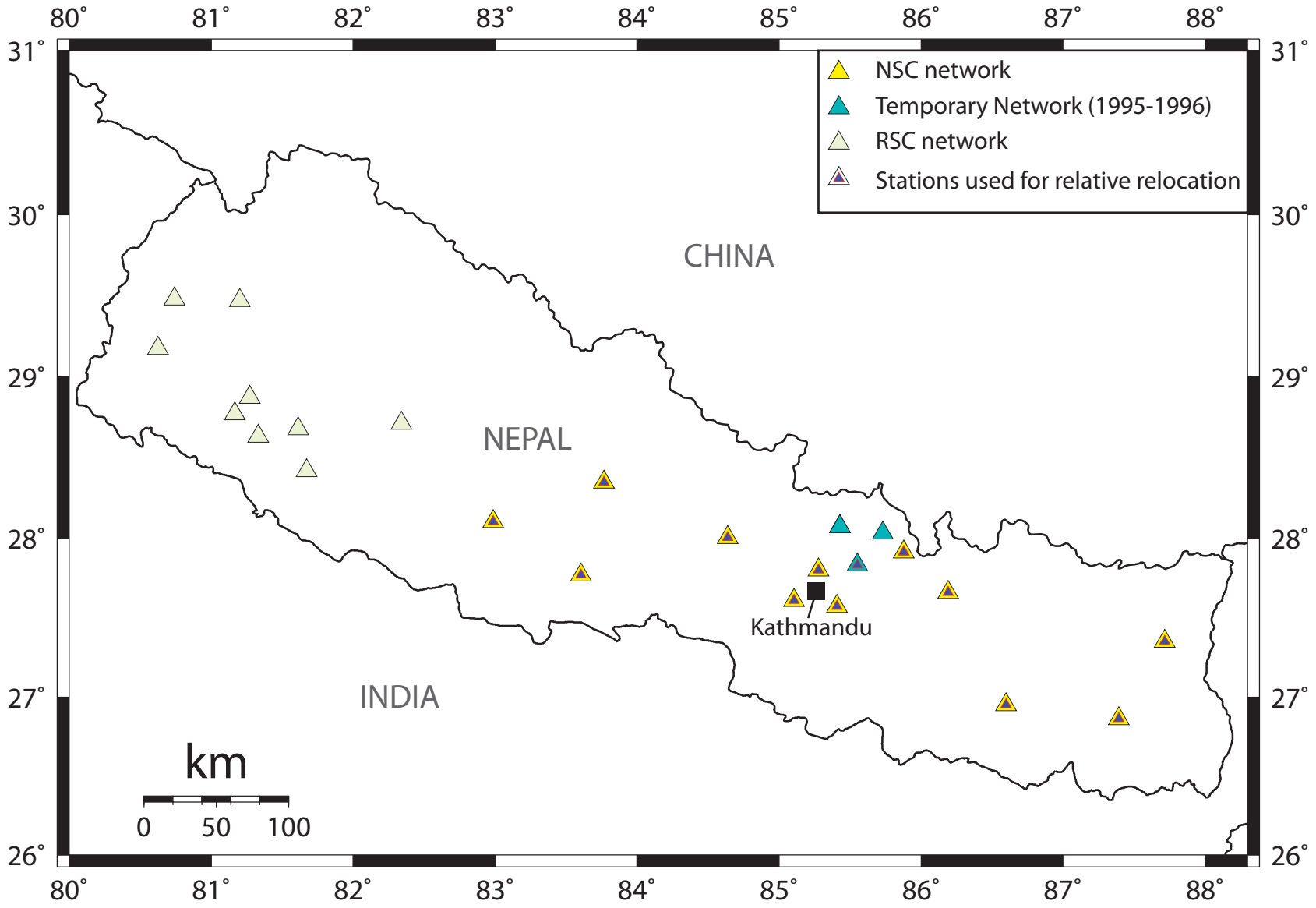
80°
81°
82°
83°
84°
85°
86°
87°
88°
31°
30°
29°
28°
27°
26°
NSC network
Temporary Network (1995-1996)
RSC network
Stations used for relative relocation
CHINA
NEPAL
INDIA
Kathmandu
km
0
50
100

Figure S1

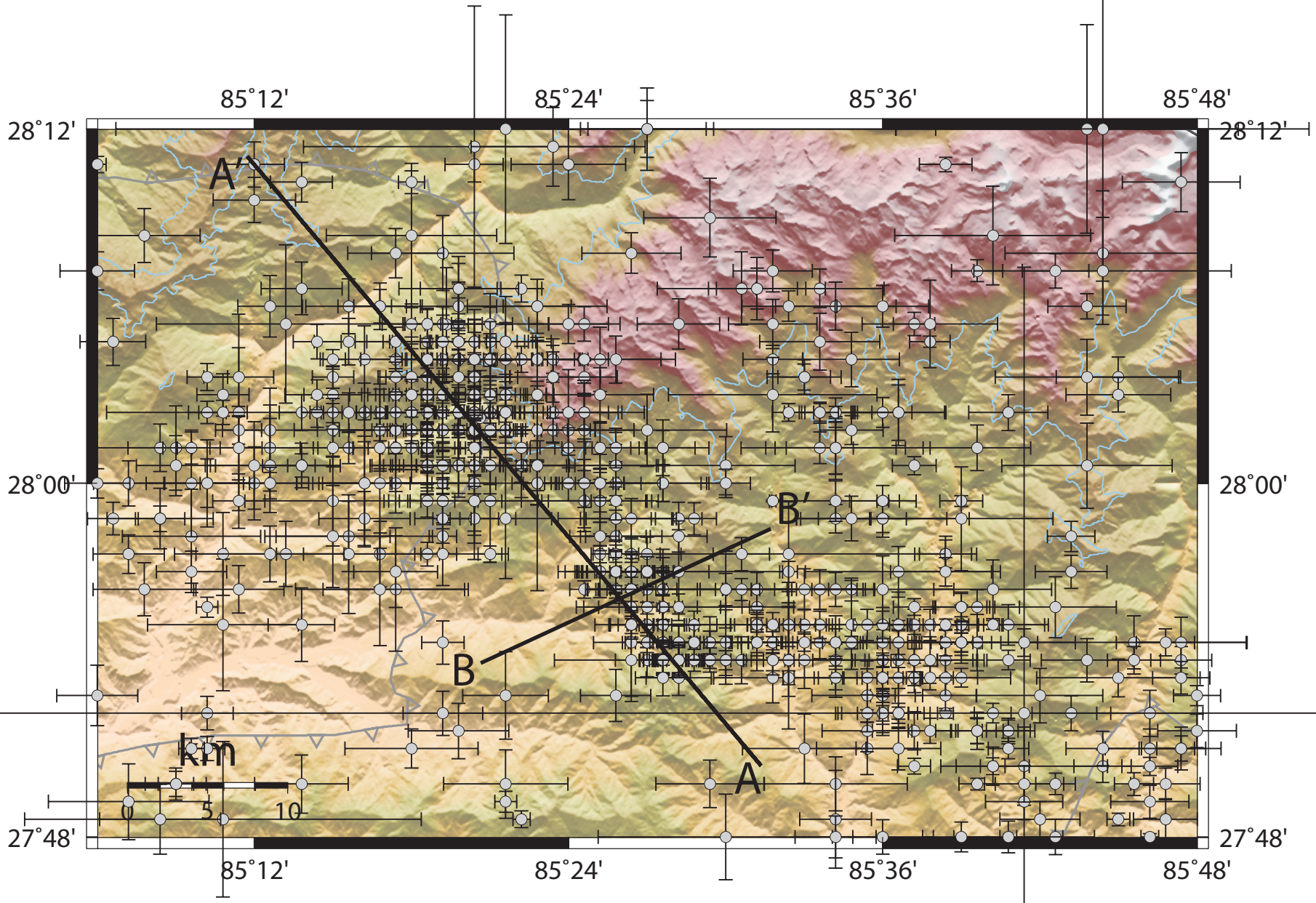

Figure S2

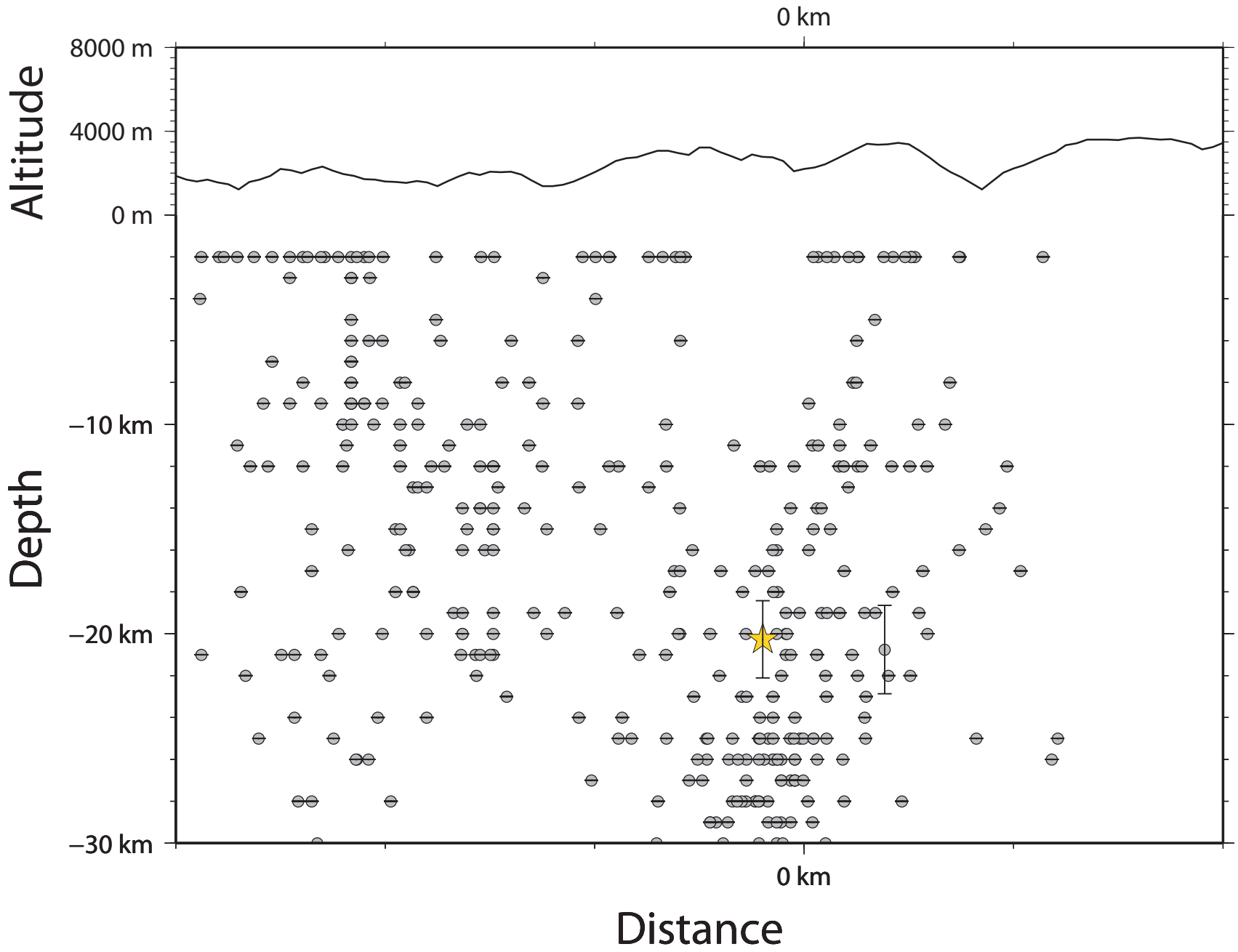
0 km
8000 m
4000 m
0 m
Altitude
−10 km
−20 km
−30 km
Depth
0 km
Distance

Figure S3

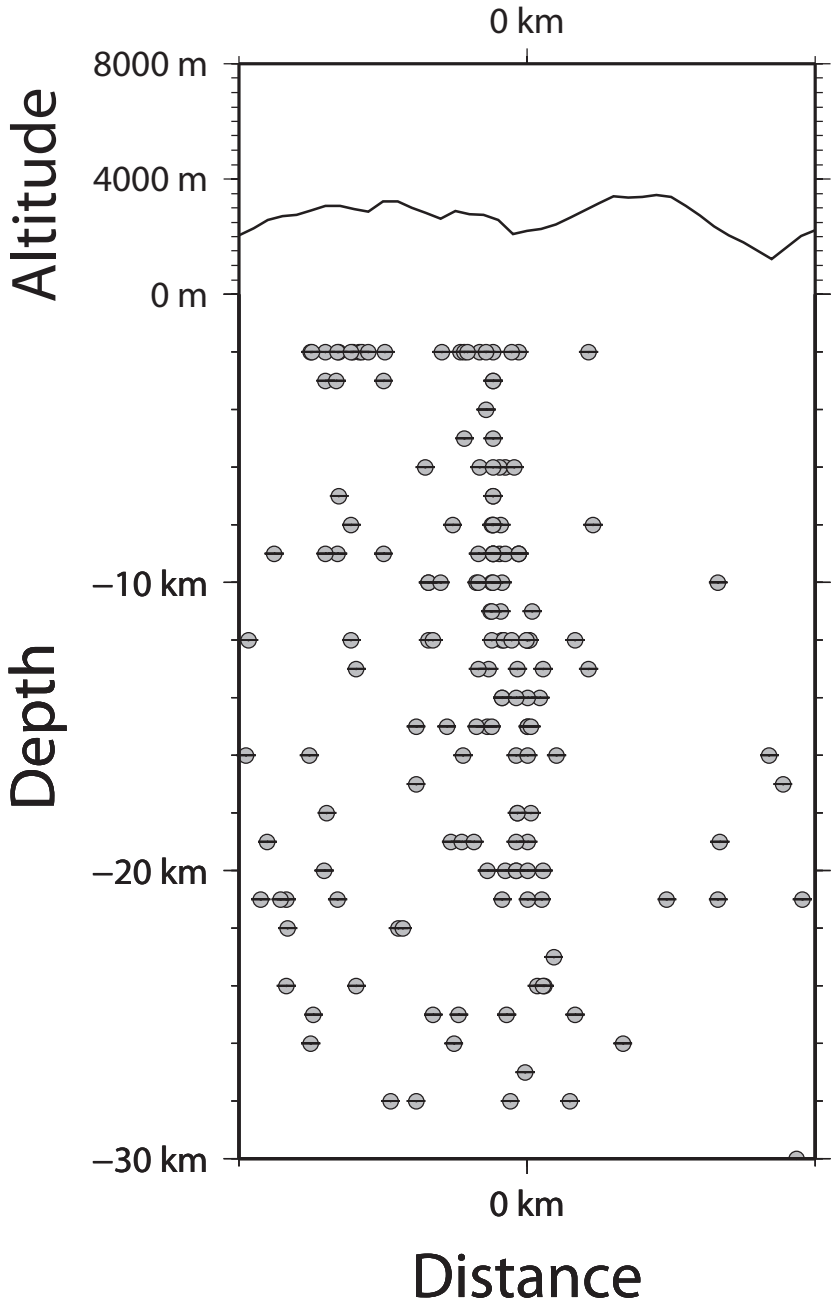
0 km
8000 m
4000 m
0 m
Altitude
–10 km
–20 km
–30 km
Depth
0 km
Distance

Figure S4

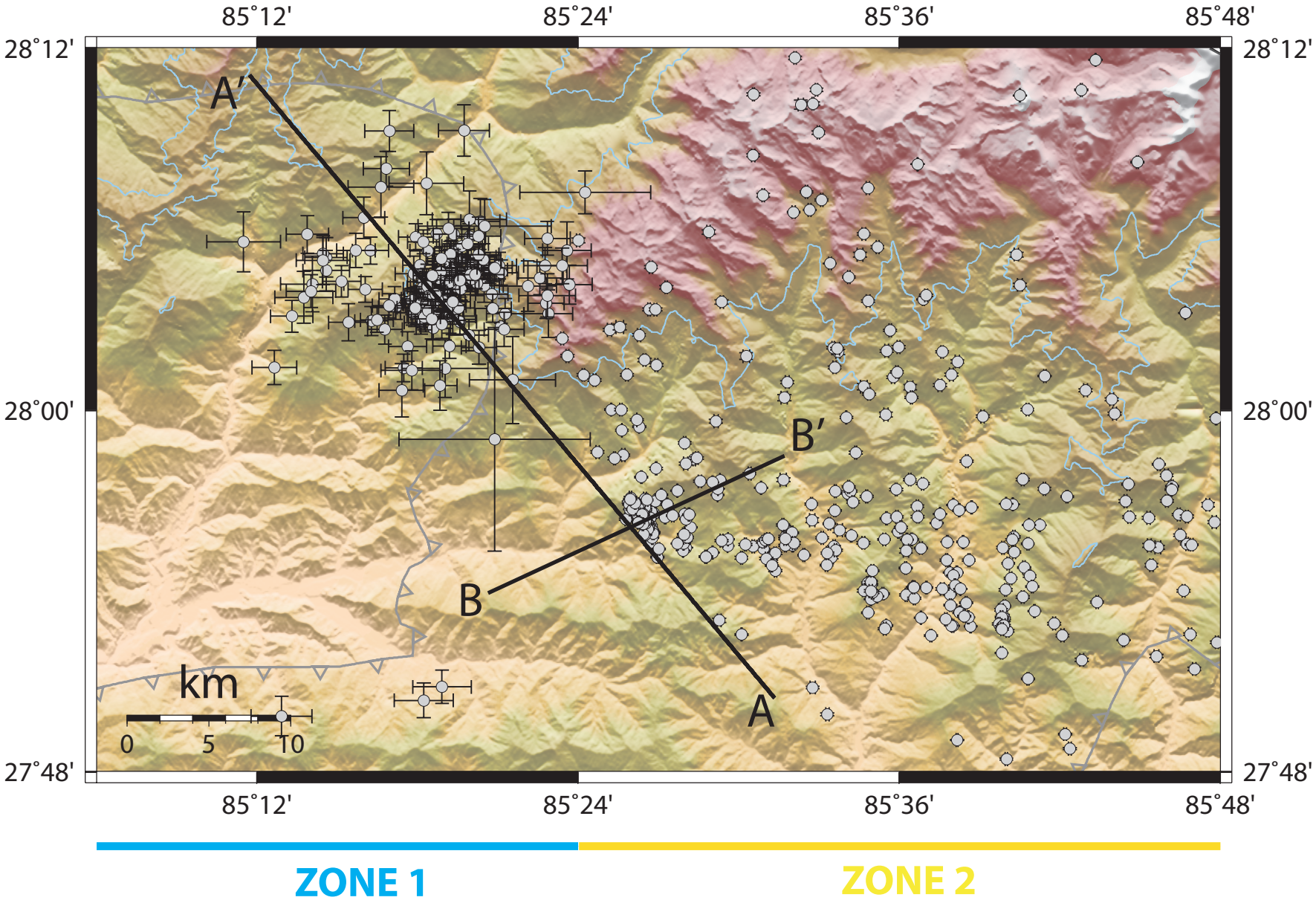

Figure S5

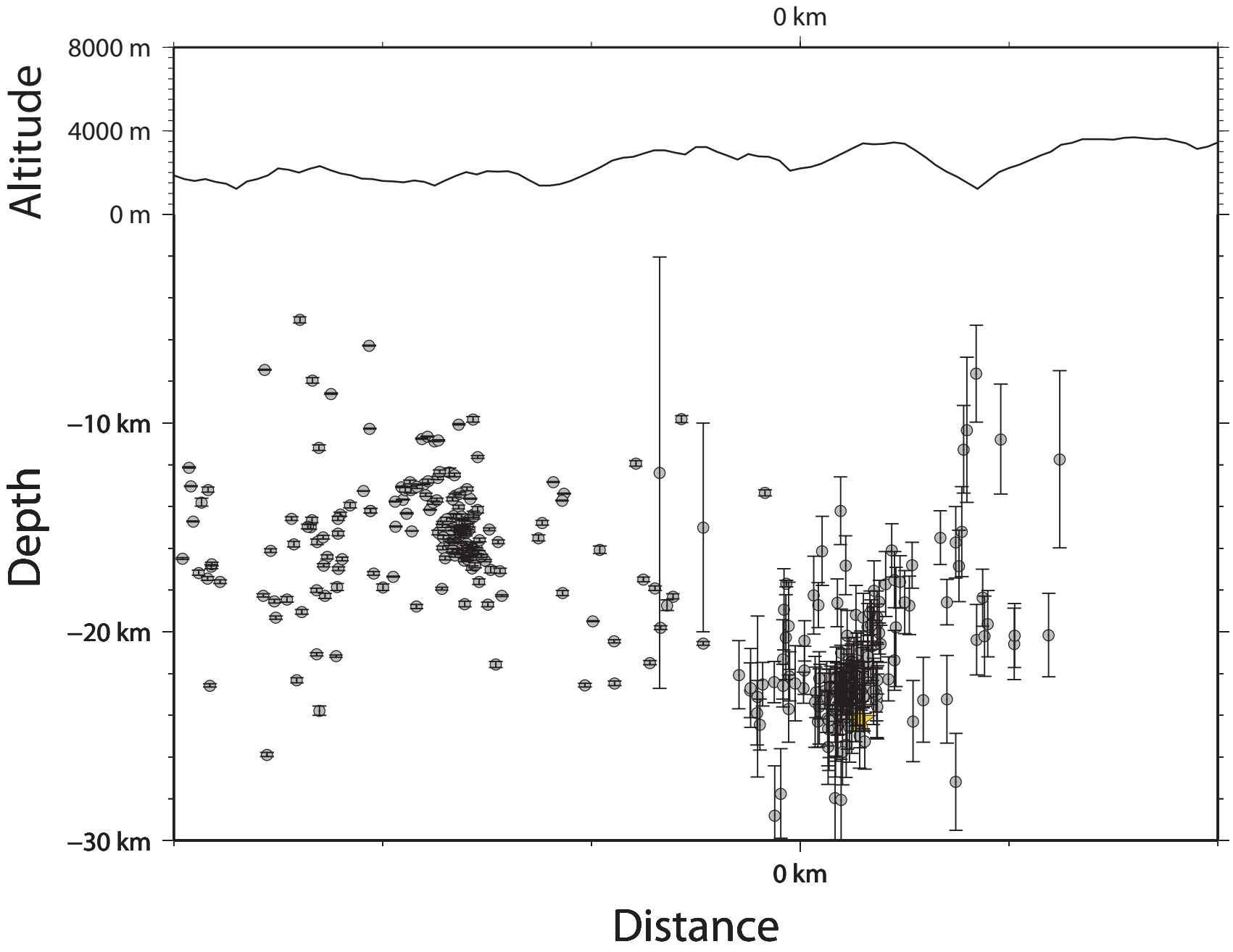
0 km
8000 m
4000 m
0 m
Altitude
–10 km
–20 km
–30 km
Depth
0 km
Distance

Figure S6

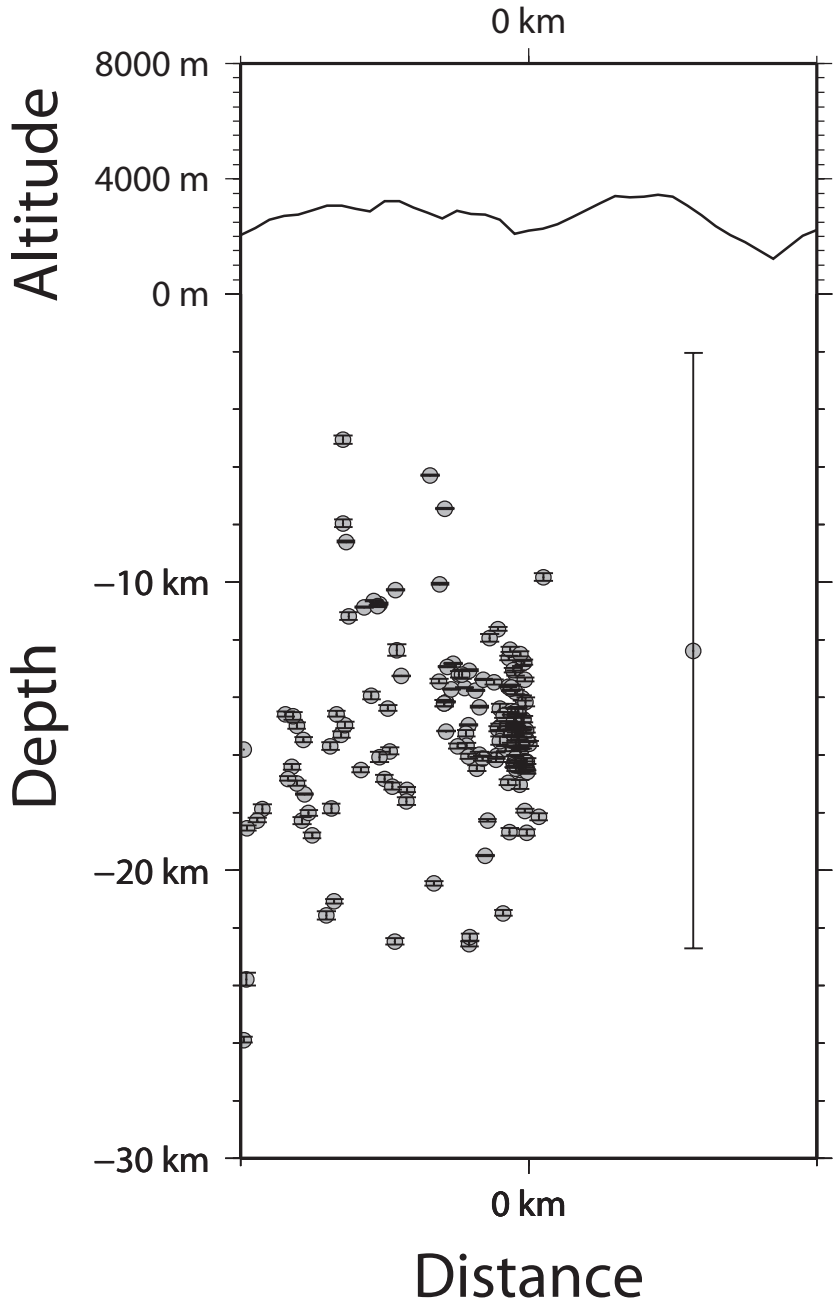
0 km
8000 m
4000 m
0 m
Altitude
−10 km
−20 km
−30 km
Depth
0 km
Distance

Figure S7

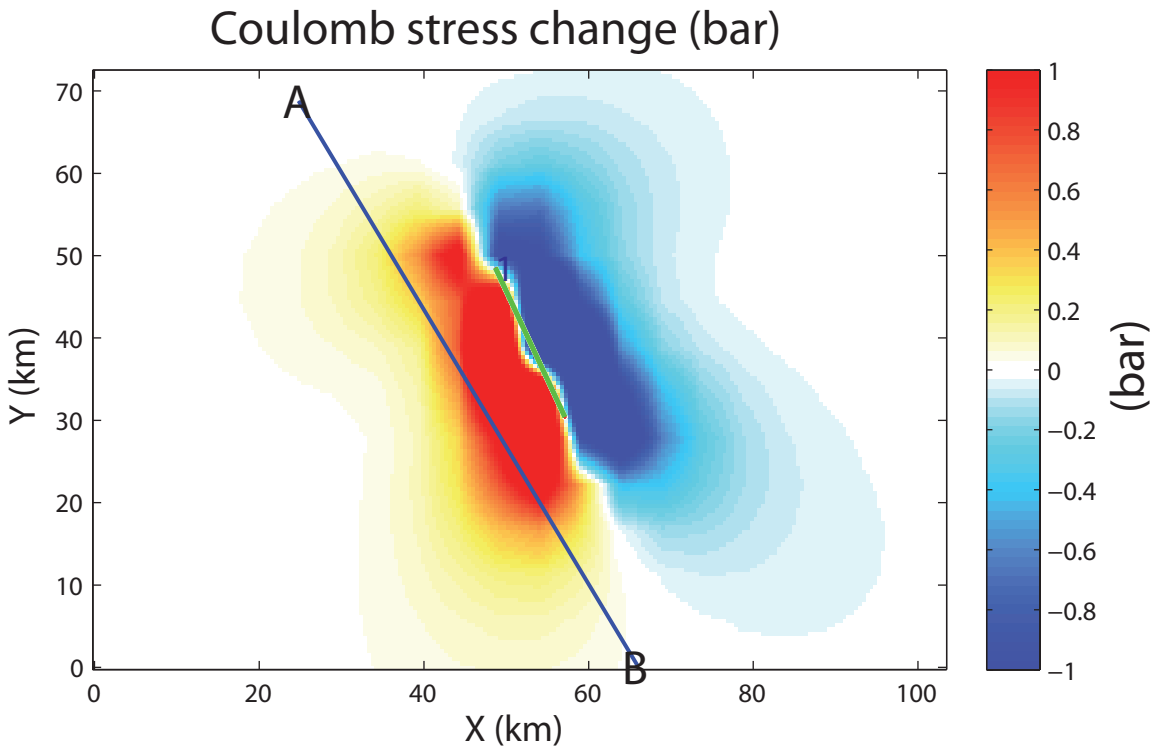
Coulomb stress change (bar)
A
B
Y (km)
X (km)
0
10
20
30
40
50
60
70
0
20
40
60
80
100
1
0.8
0.6
0.4
0.2
0
−0.2
−0.4
−0.6
−0.8
−1
(bar)

Figure S8

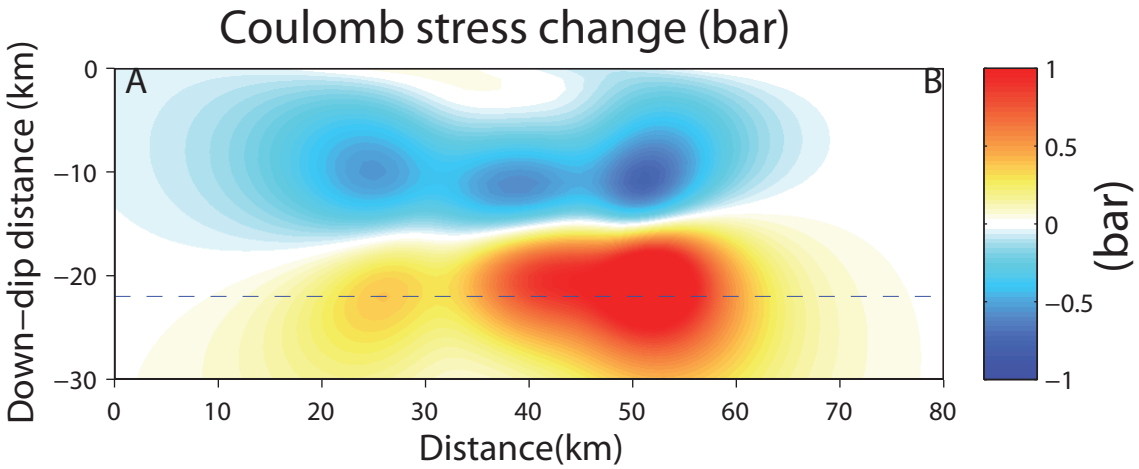
Coulomb stress change (bar)
A
B
Down−dip distance (km)
0
−10
−20
−30
0
10
20
30
40
50
60
70
80
Distance(km)
1
0.5
0
−0.5
−1
(bar)

Figure S9

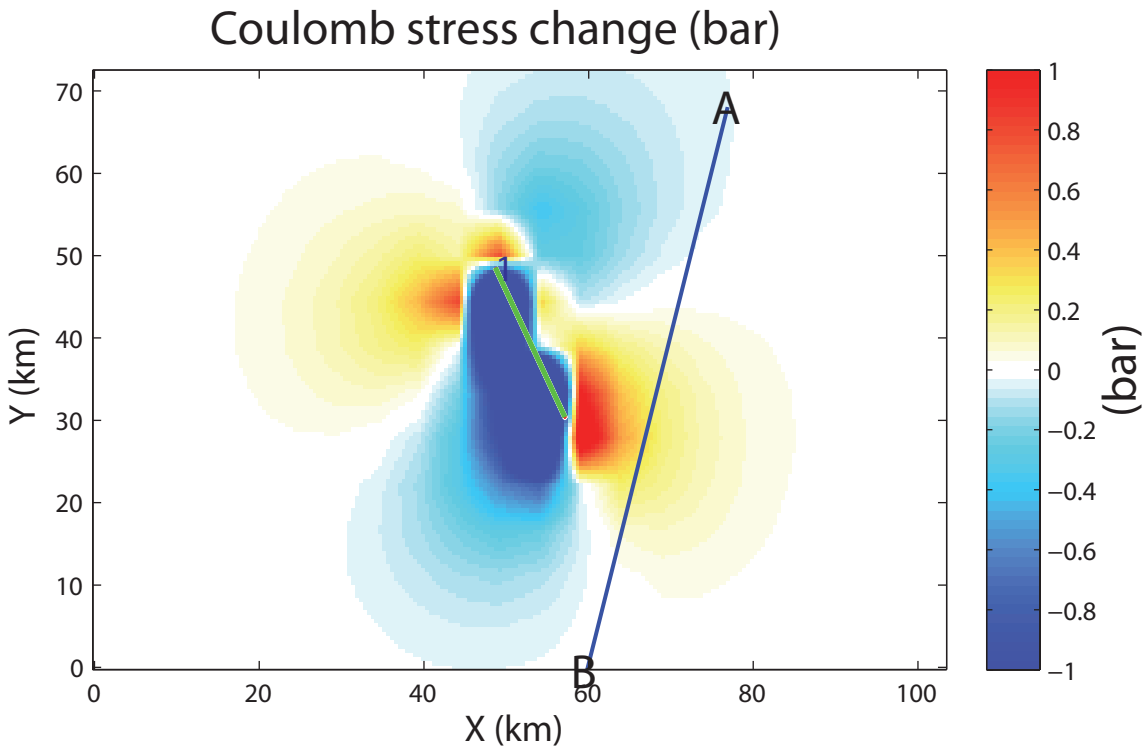
Coulomb stress change (bar)
A
B
1
Y (km)
X (km)
(bar)
0
10
20
30
40
50
60
70
0
20
40
60
80
100
1
0.8
0.6
0.4
0.2
0
−0.2
−0.4
−0.6
−0.8
−1

Figure S10

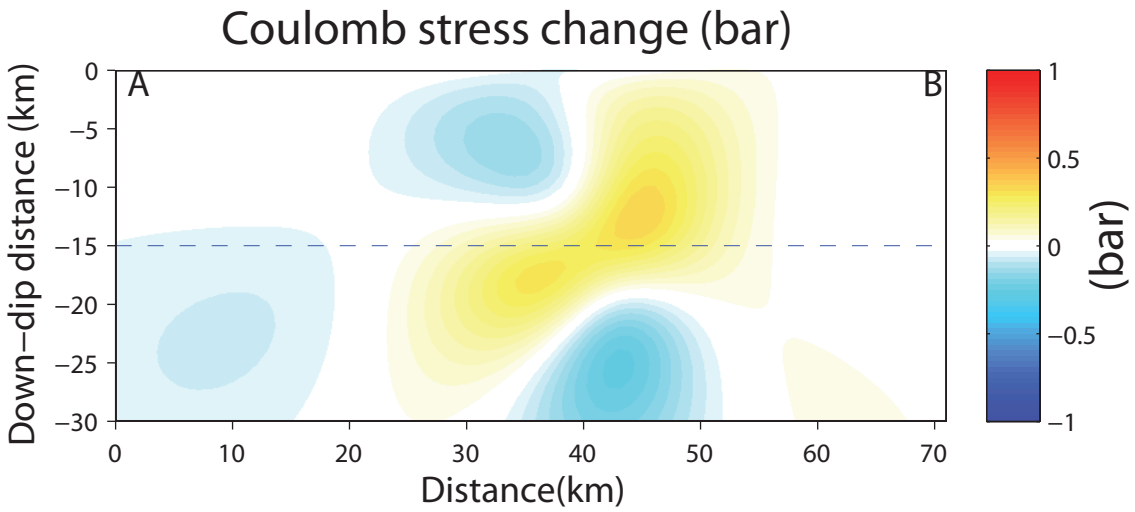
Coulomb stress change (bar)
A
B
Down−dip distance (km)
0
−5
−10
−15
−20
−25
−30
0
10
20
30
40
50
60
70
Distance(km)
1
0.5
0
−0.5
−1
(bar)

Figure S11

Annexe C:

Fiches de station de la mission de déploiement (Novembre – Décembre 2014)

Contenu Annexe C

Zone 0 ____ p. 205

- BJ01 ____ p. 205
- DE02 ____ p. 207
- ML04 ____ p. 209
- CH06 ____ p. 211
- WA07 ____ p. 213
- TK08 ____ p. 215

Zone 1 ____ p. 217

- KS11 ____ p. 217
- DU12 ____ p. 219
- DK13 ____ p. 221
- NU14 ____ p. 223

Zone 2 ____ p. 226

- MA10 ____ p. 226
- SM15 ____ p. 228
- GH25 ____ p. 229
- SJ26 ____ p. 231
- JL27 ____ p. 233

Zone 0

BIJGADA STATION: BJ01

Station Site

STATION NAME	BJ01
INSTALLATION DATE	01/12/2014
STATION LOCATION	**N 29.5969 °** **E 80.8672 °** **Altitude: 1257 m**

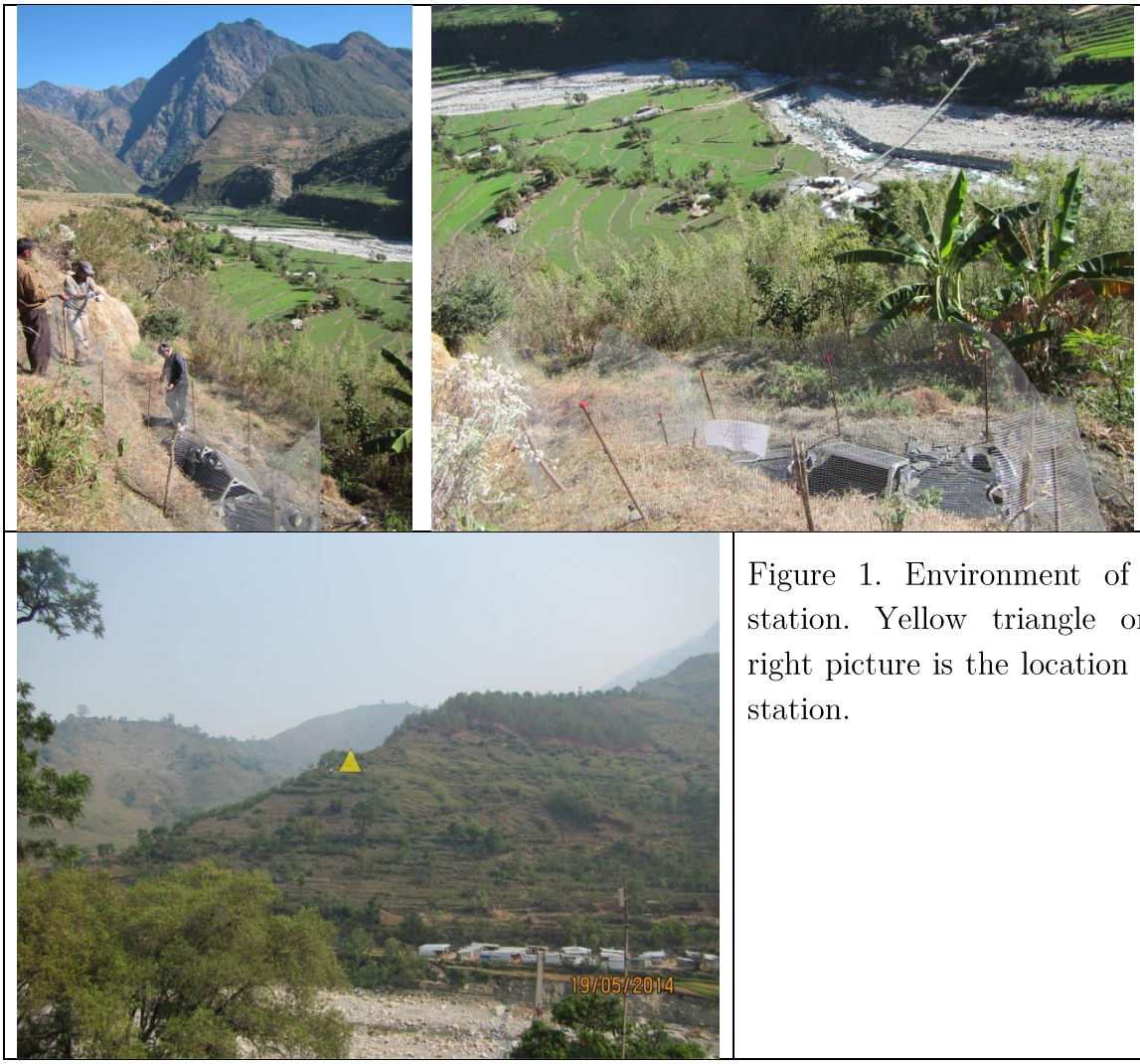

Figure 1. Environment of BJ01 station. Yellow triangle on the right picture is the location of the station.

General description		
Village name:	Pipal Dhara, Bijgada, Khiratadi VDC	
Time needed to go to the station	~ 15 min	
How to go to the emplacement of the station?	Cross the bridge, turn right at the end of the Bazar and then take a trail going behind the Bazar. When reaching the school (on the left down), take the trail going steep up of the mountain. Go on until the house.	
Field description	Small non cultivated field (~ 1.5mX8m), East-West direction, facing South. It is next to the bedrock. Slope of the mountain profile around 50°	
	Bedrock:	Dark gray slates. Orientation: 290/18
	Field dimensions:	~ 1.5 X 5 m
Logistics	Water supply:	Owner's House
	Cement:	Surkhet
	Sand for concrete:	
	Solar panels orientation:	East panel towards SE. West panel towards S.
Comments	Important river in the valley. The noise in the waveform screen seems higher than other stations.	

Technical part specific to this site	
Hole	
Cement/concrete	
Solar panels	They are located in line with the hole of the seismometer.
Fence	Fence behind the station is up on the slope. Space available very limited.

Climate conditions	
Weather	Sunny and cold.
Insulation time	08:00 – 16:00

DEURA STATION: DE02

Station Site

STATION NAME	DE02
INSTALLATION DATE	27/11/2014
STATION LOCATION	**N 29.4625** **E 80.9015** **Altitude: 1017m**

Figure 2. Environment of the station DE02. Yellow triangle on the right picture is the location of the station.

General description		
Village name:	Khairadi, Rawan VDC	
Owner:	Mr. Bhandari	
Time needed to go to the station	~ 20 mintues	
How to go to the emplacement of the station?	Before Deura there is a village with a Bridge. Take a path just before the village, go up until the bedrock peak, and just below there is a group of 3 houses.	
Field description	Cultivated field. NE-SW orientation (030°-210°), facing SE. Bedrock found 30 cm when digging the hole for the seismometer. It is exposed on the house.	
	Bedrock:	Mica Phylite
	Field dimensions:	~ 3 X 3 m
Logistics	Water supply:	Owner's house
	Cement:	Surkhet
	Sand for concrete:	
	Solar panels orientation:	West panel towards S. East panel towards SE.
Comments	All instruments of the station have been installed inside the fence. Important number of cattle in the house, so high level of noise could be recorded.	

Technical part specific to this site	
Hole	Dug mainly in the bedrock (30 cm of soil only)
Cement/concrete	
Solar panels	We asked to keep a big tree as free as possible of leaves in order to not disturb the solar panels.
Fence	

Climate conditions	
Weather	Sunny and clear. Big river in the valley, it could be humid.
Insulation time	07:00 – 16:00

MATELA STATION: ML04

Station Site

STATION NAME	ML04
INSTALLATION DATE	26/11/2014
STATION LOCATION	**N 29.5016** **E 81.0848** **Altitude: 1143 m**

Figure 3. Environment of the station ML04. Yellow triangle on the right picture is the location of the station.

General description		
Village name:	Matela	
Owner:	Prema Giri	
Time needed to go to the station	20 minutes	
How to go to the emplacement of the station?	From Bagargau go west direction along the road until a path that crosses the water channel. Follow this path going up, pass through the first village and go on up until a group of 5-6 houses.	
Field description	Cultivated terrace, E-W towards S.	
	Bedrock:	Dolomite limestone on the lateral position of the field E-W orientation and dipping more or less south.
	Field dimensions:	~ 2 X 2 m
Logistics	Water supply:	Owner's house
	Cement:	Surkhet
	Sand for concrete:	Bagargau
	Solar panels orientation:	East panel towards SSE. West panel towards SSW.
Comments	The site is surrounded by trees, especially behind. We asked to cut the few trees that could disturb the solar panels.	

Technical part specific to this site	
Hole	
Cement/concrete	Extra cement solution to stick the slab to the concrete.
Solar panels	
Fence	

Climate conditions	
Weather	Sunny and humid (Site in the Seti River valley)
Insulation time	07:00 – 17:00

CHAINPUR STATION: CH06

Station Site

STATION NAME	CH06
INSTALLATION DATE	02/12/2014
STATION LOCATION	**N 29.5458** **E 81.2012** **Altitude: 1373 m**

Figure 4. Environment of the station CH06. Yellow triangle on the right picture is the location of the station.

General description		
Village name:	Army Camp of Chainpur. Hemanta, Pades VDC	
Owner:	Ministry	
Time needed to go to the station	45 min	
How to go to the emplacement of the station?	Take the main road of Chainpur (NEN-SSW direction), go straight ahead until the road divides in two, straight-right and straight-left. Take the small road on your right and go on until the bridge. Cross the bridge and follow straight crossing the village. When arriving to a wicker baskets shop you must turn right to take the "steepy" trail. Go up always on the right side (river must be seen). Then you have the possibility to go up or to go on on the right without going up, take the second option that must take you until the plateau with cultivated fields. Cross the fields until the entrance of the Army Camp. Station is located behind the meteorological station.	
Field description	Grass field. Training field between outer and inner fence of army camp. Close to the outer fence, there are cultivated fields.	
	Bedrock:	Made of Quartzite highly metamorphic and folded.
	Field dimensions:	1.5 X 3 m
Logistics	Water supply:	Army Camp
	Cement:	Surkhet
	Sand for concrete:	Chainpur
	Solar panels orientation:	East panel towards SW. West panel towards S.
Comments		

Technical part specific to this site	
Hole	
Cement/concrete	
Solar panels	
Fence	Meteorological station is fenced. So we used this fence to fix our fence.

WARIANA STATION WA07

Station Site

STATION NAME	WA07
INSTALLATION DATE	28/11/2014 – 29/12/2014
STATION LOCATION	**N 29.6040** **E 81.1497** **Altitude: 1886 m**

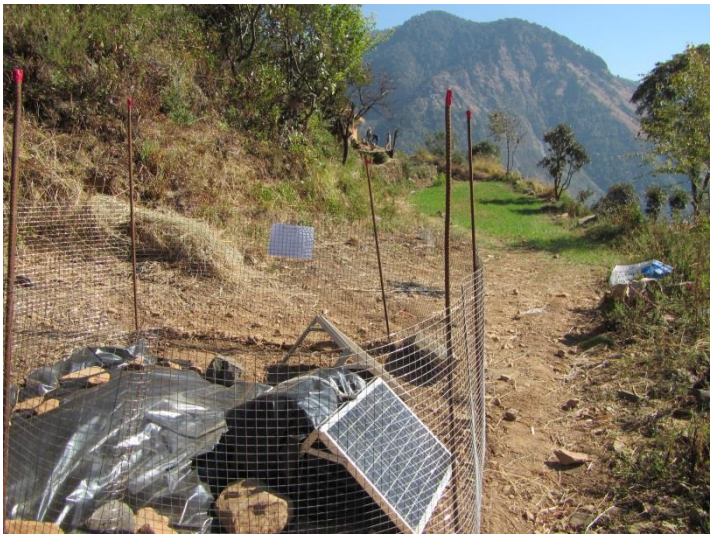

Figure 5. Environment of the station WA07. Yellow triangle on the right picture is the location of the station.

General description		
Village name:	Kaflin, Daulichour VDC.	
Owner:	Dhauliya Kumar Bohara contact person in village: Ramesh Kumar Bohara, contact person by phone: Sher Bahadur Bohara 9848436969	
Time needed to go to the station	5h walking from Chainpur.	
How to go to the emplacement of the station?	In Chainpur, a secondary river reverses to the Seti River, this valley goes to Wariana. There are two ways to reach Wariana, using the left bank trail or the right bank trail. This time we walked along the left bank looking upstream until the hydroelectric power station. Cross the river. Continue upstream along the right bank and at the end climb the first terrace. Go on climbing until the head of the landslide and reach the village. Cross the fields on your right and take the path climbing the hill. Climb until a fountain and go on until the first house on your left.	
Field description	Station is situated at the end of a cultivated field, next to the cliff. Field orientation: SE-NW	
	Bedrock:	Dolomite. Some meters depth of the field, it is possible to see it from the village. Good view of dolomite bedrock
	Field dimensions:	2 X 2 m
Logistics	Water supply:	Owner's house
	Cement:	Surkhet
	Sand for concrete:	River banks of the closest river
	Solar panels orientation:	East panel: ~ E-W towards S West panel: WNW-SSE towards SWS.
Comments		

Climate conditions	
Weather	Sunny and clear. Very cold at night.
Insulation time	08:00 – 17:30

TALKOT STATION: TK08

Station Site

STATION NAME	TK08
INSTALLATION DATE	24/11/2014 – 25/11/2014
STATION LOCATION	**N 29.6152** **E 81.2895** **Altitude: 1895 m**

General description		
Village name:	Dhamena	
Owner:		
Time needed to go to the station	Jeep: 2h Walking from Jeep to village: 45 min	
How to go to the emplacement of the station?	From Rithe Tole (terminus of the Mahindra Jeeps connecting Chainpur to Talkot) walk few meters north and then take one of the paths on the left climbing up the mountain. Reach the school and take the stairs on the right. Go on climbing until you arrive on relatively big fields and go on towards your right until the village. Cross the village, turn right after few meter from the fountain, pass in front of 2 houses and you will arrive to the owner's house. The site is behind the house on a chili field.	
Field description	Cultivation field on an old landslide	
	Bedrock:	Laterally it is not very far. In deep, I don't know. I found it on the road. Look at the map for meters precision. Mica Phylite to clorite. Schistosity N-S 24°NE and lineation E-W.
	Field dimensions:	2 m^2
Logistics	Water supply:	In village
	Cement:	Surkhet
	Sand for concrete:	On the way from Chainpur to Talkot (private house)
	Solar panels orientation:	E-W facing S
Comments	School teacher and villagers know about the station, do not hesitate to ask them to show you the way to the site. The first day, in owner's absence we had teacher's and villagers' permission to start the installation.	

Figure 6. Environment of the station TK08. Yellow triangle on the right picture is the location of the station.

Technical part specific to this site	
Hole	
Cement/concrete	
Solar panels	Orientation of solar panels E-W towards S and SSE.
Fence	

Climate conditions	
Weather	Sunny and cold.
Insulation time	07:30 – 15:30

Zone 1

KUSAPANI STATION: KS11

Station Site

STATION NAME	KS11
INSTALLATION DATE	19/11/2014
STATION LOCATION	**N 28.9715** **E 81.6233** **Altitude: 1863 m**

Figure 7. Environment of the station KS11.

General description		
Village name	Urapanichaur Kusapani VDC	
Owner	Lok Prasad Kandel. Tel: 9748057265	
Contract witness	Ram Prasad Adhikari	
Time needed to go to the station	~ 30 min from owner's house. 1h From Khambagade 2h From the place where the car blocked: N 28° 57' 07.2'' E 081° 37' 27.7'' Altitude: 1576 m	
How to go to the emplacement of the station?	Difficult. Exposed road to the owner's house. Stop the car before difficulties. From Dullu, take the road going to Kusapani. Continue until the car blocks. Then reach Khambagade Bazar. Take the path going up through the ridge of the mountain. On the top, turn left and take the path on the ridge. The house is the last before the slope of the mountain becomes very steep.	
Field description	Cultivated terrace	
	Bedrock:	Colluvium (quartzite + schist) under cultivated terrace
	Field dimensions:	
Logistics	Water supply:	Available (100 m)
	Cement:	
	Sand for concrete:	
	Solar panels orientation:	SE + S
Comments		

DULLU STATION: DU12

Station Site

STATION NAME	DU12
INSTALLATION DATE	18/11/2014
STATION LOCATION	**N 28.8789** **E 81.6052** **Altitude: 1372 m**

Figure 8. Environment of the station DU12.

General description		
Village name:	Dhulu Municipality, Jimaldanda	
Owner:	Himal Singh 9848279769	
Time needed to go to the station	5 minutes	
How to go to the emplacement of the station?	Coming from Dullu, turn right towards Baleswar Temple, pass the temple and reach the place where the other temple is, park under the big tree on the road. Two houses are on the other side of the road, the owner lives in the left house.	
Field description	Mountain ridge	
	Bedrock:	Is just under the field. Appears on the hill limitating the field. Composition: Phyllite important oxidation. Field direction: ESE-WNW.
	Field dimensions:	~ 2 X 4 m
Logistics	Water supply:	Owner's house
	Cement:	Surkhet
	Sand for concrete:	Dailekh
	Solar panels orientation:	Facing S.
Comments		

Technical part specific to this site	
Hole	
Cement/concrete	
Solar panels	They are placed in line with the seismometer emplacement.
Fence	We needed 2m extra fence, so 8 m for the whole fence.

Climate conditions	
Weather	Sunny and dry. A little bit windy.
Insulation time	

DAILEKH STATION: DK13

Station Site

STATION NAME	DK13
INSTALLATION DATE	16/11/2014
STATION LOCATION	**N 28.86479 °** **E 81.72949 °** **Altitude: 1496 m**

Figure 9. Environment of the station DK13.

Technical part specific to this site	
Hole	~ 50 cm far from the slope of the cultivated terrace above and 1.5m far from the limit of the terrace. Dimensions: - Long: ~ 60cm - Width: ~ 60cm - Depth: 70-80 cm
Cement/concrete	The volume of concrete used is 3 times the plate used for mixing. Mixture: 1/3 stones 2x2cm, 1/3 sand, 1/3 cement In last mixture: 2-3 “taps/bouchons” of quick liquid cement. This time, concrete has had the entire night to get dry.
Solar panels	Solar panels were put in front of the seismometer location. Orientation: both striking NE-SW towards SE
Fence	6m fence with 6 iron rods.

Climate conditions	
Weather	Clear and dry weather. Warm during day time.
Insulation time	7 a.m to 3:30 p.m.

NAUMULE STATION: NU14

Station Site

STATION NAME	NU14
INSTALLATION DATE	17/11/2014
STATION LOCATION	**N 28.9113 °** **E 81.80589 °** **Altitude: 1309 m**

Figure 10. Environment of the station NU14. Yellow triangle on the right picture is the location of the station.

General description		
Village name:	Dhansar, Baluwatar VDC	
Owner:		
Time needed to go to the station	45 min	
How to go to the emplacement of the station?	From Naumule, follow the river upstream from the main road until you find a stream ~ 1m wide crossing the main road. Then follow the stream on the same direction from the left bank and cross the stream following the trail. Go on climbing the mountain using this same trail. [If the trail splits in 2 trails of the same size, take the trail on your right]. Pass trough 2 big trees on a man made basis, reach the school. Behind the school, turn left. Follow the trail always on the same altitude and the third house belongs to the field's owner. The station field is the 4rth terrace from the house.	
Field description	It is a rice cultivation field, so two drainage ditch are dug (E and W of the station) to drain water away.	
	Bedrock:	Micaschist to gneiss with quartz veins. It appears fresh on an outcrop in the house; however it is very weathered on the fields.
	Field dimensions:	~ 3 X 4 m
Logistics	Water supply:	Owner's house
	Cement:	Surkhet
	Sand for concrete:	Dailekh
	Solar panels orientation:	East solar panel towards SE-S. West solar panel towards S.
Comments	There are a lot of monkeys on the area.	

Technical part specific to this site		
Hole	It is situated in a cultivated field. About 1.5m far from the slope of the cultivated terrace above and the limit of this terrace.	
	Dimensions:	
	Long	~ 90cm on surface, ~60cm on the bottom
	Width	~ 90cm on surface, ~60cm on the bottom
	Depth	~ 1m
Cement/concrete	The volume of concrete used is 3 times the plate used for mixing. Mixture: 1/3 stones 2x2cm, 1/3 sand, 1/3 cement, 2-3 lids measures of quick liquid cement. Concrete drying time: ~ 2h	
Solar panels	Solar panels were situated in front of the seismometer hole. Orientation: East panel: towards SE-S West panel: towards S	

Fence	6m of fence has been used around the station with 6 rods. An extra fence has been put on the top to protect monkeys to come in. We have put electric tape on the top of the iron rods to protect from thunder storms.

Climate conditions	
Weather	
Insulation time	From 8h to ~ 17h

Zone 2

MARTADI STATION : MA10

Station Site

STATION NAME	MA10
INSTALLATION DATE	07/12/2014
STATION LOCATION	**N 29.4520** **E 81.4749** **Altitude: 1696 m**

Figure 11. Environment of the station MA10.

General description		
Village name:	Martadi Army Camp	
Owner:	Ministry	
Time needed to go to the station	30 min from the hotel to the army camp.	
How to go to the emplacement of the station?	The site is located on the western most part of the army camp. In the entrance, take the path that goes close to the temple and some buildings. At the end of the nice path, turn left, walk behind the building and the station is one terrace downwards on your right.	
Field description	Terrace in a rockslide deposit. Field orientation: NNE-SSW	
	Bedrock:	Mica phyllite.
	Field dimensions:	~ 4 X 3 m
Logistics	Water supply:	Army Camp
	Cement:	Surkhet
	Sand for concrete:	Army Camp
	Solar panels orientation:	West panel towards S. East panel towards SSW.
Comments	Strong wind coming from downstream SW direction towards NE direction.	

Climate conditions	
Weather	Sunny, cold and windy.
Insulation time	

Simikot Station: SM15

STATION NAME	SM15
INSTALLATION DATE	25/04/2015
STATION LOCATION	**N 29.4520** 29°58’16’’ **E 81.4749** 81°48’40’’ **Altitude: 1696 m**

Date	25/04/2015	Time		Site name	SM15	
Operator	Jean Letort	Taurus S/N	2283	Sensor S/N	Lenartz: Le3D05 0025	
Latitude	29°58’16’’	Longitude	81°48’40’’	Altitude	3226 m	
Sensor Type	Lenartz					

GAMGHADI STATION GH25

Station Site

STATION NAME	GH25
INSTALLATION DATE	26/11/2014
STATION LOCATION	**N 29.5199°** **E 82.1502°** **Altitude: 2629 m**

Figure 12. Environment of the station GH25.

General description		
Village name:	Talcha	
Owner:		
Time needed to go to the station	10 minutes	
How to go to the emplacement of the station?	From the road under the airport	
Field description	Garden	
	Bedrock:	Anthropic terrace
	Field dimensions:	
Logistics	Water supply:	
	Cement:	
	Sand for concrete:	
	Solar panels orientation:	
Comments		

SINJA STATION: SJ26

Station Site

STATION NAME	SJ26
INSTALLATION DATE	25/11/2014
STATION LOCATION	**N 29.40874°** **E 82.02383°** **Altitude: 2473 m**

Figure 13. Environment of the station SJ26. Yellow triangle on the right picture is the location of the station.

General description		
Village name:	Sinja	
Owner:	Area Police Station	
Time needed to go to the station	10 minutes	
How to go to the emplacement of the station?	Take the bridge in Sinja. Climb the stairs to go to the temple. 100 m before reaching the temple, the police station is on the right. The site is the terrace right under.	
Field description		
	Bedrock:	Anthropic terrace made on colluvium,.
	Field dimensions:	
Logistics	Water supply:	
	Cement:	
	Sand for concrete:	
	Solar panels orientation:	
Comments		

JUMLA STATION: JL27

Station Site

STATION NAME	JL27
INSTALLATION DATE	29/11/2014
STATION LOCATION	**N 29.27782°** **E 82.19262°** **Altitude: 2390 m**

Figure 14. Environment of the station JL27.

General description		
Village name:	Jumla	
Owner:	Karnali Zone Police office	
Time needed to go to the station	10 minutes	
How to go to the emplacement of the station?	The Karnali Zone Police Office is on the top of the first hill facing the airport.	
Field description	The seismological station is installed in the immediate vicinity of the GPS station at the opposite of the entrance of the police headquarter.	
	Bedrock:	Schist and micashcist.
	Field dimensions:	
Logistics	Water supply:	
	Cement:	
	Sand for concrete:	
	Solar panels orientation:	
Comments		

Résumé

La sismicité présente le long du méga-chevauchement himalayen, dans la trace du fort séisme de 1505, des variations spatiales qui restaient peu résolues. Nous y avons déployé un réseau sismologique temporaire de 15 stations pour la période 2014-2016, en complément du réseau national. Nous avons effectué une détection automatique Seiscomp3 puis un pointé manuel des séismes enregistrés par le réseau, suivi par une localisation absolue Hypo71 et une relocalisation relative d'essaims HypoDD. Le catalogue résultant compte 2154 évènements dans notre zone d'étude dont les profondeurs (8-16 km) sont bien résolues. Les variations temporelles de la sismicité suggèrent des migrations de fluides. La confrontation de la sismicité avec des coupes géologiques équilibrées montre que les séismes se localisent dans le compartiment supérieur à proximité du Grand Chevauchement Himalayen au voisinage de rampes ou contacts suspectés entre écailles de moyen pays. Les variations latérales de structures associées à cette sismicité sont susceptibles de contrôler pour partie les ruptures cosismiques de séismes intermédiaires, qui viennent rompre partiellement le chevauchement, comme l'ont démontré les études du séisme de Mw7.8 de Gorkha-Népal, 2015. La segmentation qui en résulte est une donnée importante dans les études d'aléa sismique.

Mots Clés

Sismicité, cycle sismique, Himalaya, chevauchement, relocalisation, réseau sismologique temporaire.

Abstract

The seismicity located along the Himalayan mega-thrust, within the trace of the great M8+ 1505AD earthquake, displays striking spatial variations which remained poorly resolved. In order to better constrain and understand these variations, we deployed a 15-stations temporary seismological network for 2 years (2014-2016) as a complement to the national network. We first processed the data with an automatic detection with Seiscomp3, then a manual picking of earthquakes recorded by the network, followed by a Hypo71 absolute localization and HypoDD relative relocation of clustered events. The resulting catalogue contains 2154 local events, shallow to midcrustal (8 – 16 km). The seismicity presented temporal variations suggesting fluid migrations. The confrontation between the seismicity and the geologic balanced cross-sections shows that most earthquakes happen within the hangingwall of the Main Himalayan Thrust fault nearby ramps or suspected contacts between Lesser Himalayan slivers. The lateral variations of some of the structures associated to this seismicity are likely to partially control the extent of the coseismic ruptures during intermediate earthquakes that break partly the locked fault zone, in a similar way as what was reported after the Mw7.8 2015 Gorkha-Nepal earthquake. Better characterizing the segmentation of such faults is an important input for seismic hazard studies.

Keywords

Seismicity, seismic cycle, Himalaya, thrust, relocation, temporary seismological network.